The Hashemite Kingdom of Jordan   Scientific Research Support Fund   The Hashemite University

JJEES

Jordan Journal of Earth and Environmental Sciences

Volume (13) Number (3)

Cover photo © Prof. Khaled Al Tarawneh

JJEES is an International Peer-Reviewed Research Journal

ISSN 1995-6681   jjees.hu.edu.jo   September 2022

Jordan Journal of Earth and Environmental Sciences (JJEES)

JJEES is an International Peer-Reviewed Research Journal, Issued by Deanship of Scientific Research, The Hashemite University, in corporation with, the Jordanian Scientific Research Support Fund, the Ministry of Higher Education and Scientific Research.

Submission address:

Manuscripts should be submitted electronically to the following e-mail:

jjees@hu.edu.jo

For more information and previous issues:

www.jjees.hu.edu.jo

Hashemite Kingdom of Jordan

Scientific Research Support Fund

Hashemite University

Jordan Journal of Earth and Environmental Sciences

JJEES

An International Peer-Reviewed Scientific Journal

Financed by the Scientific Research Support Fund

Volume 13 Number (3)

http:// jjees.hu.edu.jo/

ISSN 1995-6681

*Variegated sandstone in Umm Ishrin Sandastone in Petra.
Photographed by Prof. Khaled Al Tarawneh

JJEES

Jordan Journal of Earth and Environmental Sciences

PAGES	PAPERS

JJEES

JJEES (2022) 13 (3): 146-157
ISSN 1995-6681

Jordan Journal of Earth and Environmental Sciences

Temporal–Spatial Dew Formation Potential in Jordan – Identification of Dew Formation Zones

Nahid Atashi [1,2], Tareq Hussein [1,3*]

[1] University of Helsinki (UHEL), Faculty of Science, Institute for Atmospheric and Earth System Research (INAR/Physics), Helsinki, Finland
[2] Faculty of Geographical Science and Planning, University of Isfahn, Isfahan, Iran
[3] The University of Jordan, School of Science, Department of Physics, Amman, Jordan

Received 29th May 2021; Accepted 29th January 2022

Abstract

Jordan is the fourth country in the world suffering from freshwater shortages. Therefore, this research aims to investigate the dew formation potential as an alternative source of water in Jordan. We performed gridded model simulations to estimate the dew yield during 1979–2018. We also utilized cluster analysis to identify the dew formation zones in Jordan. Our investigation revealed that dew can occur almost everywhere in Jordan during the winter (~75 days). As expected, summer is the driest season with the least number of dew days (~37 days). According to the cluster analysis, we distinguished three dew formation zones, which were closely related to the climate zones: Dew zone A (eastern desert), Dew zone B (Jordan Valley), and Dew Zone C (central heights Plateau). Zone A receives the least dew formation potential (on average 0.05 L/m^2/day), which mainly occurs during the winter, and Zone B receives the highest dew formation potential (on average 0.15 L/m^2/day), which occurs throughout the year. The average yearly dew yield in dew zone A, B, and C was about 18, 55, and 28 L/m^2. The outcomes of this study are ought to be useful for managing and planning local feasibility studies for dew harvesting and a better understanding of the feedback processes between the water cycle and climate change in Jordan.

Keywords: *Dew formation, heat-transfer balance, cluster analysis, long-term analysis.*

1. Introduction

Jordan has been one of the countries that suffered from the climate change impacts on water resources and supplies. This disruption imposed socio-economic consequences that might take many years to recover. Like many other countries, Jordanians will suffer from freshwater shortage by the year 2025 (Lindblom et al., 2006). Accordingly, awareness, international agreements, and national strategies must be built up to wisely manage and restore water resources in Jordan (Lekouch et al., 2011). For example, technological advancement (e.g. water desalination, enhanced rain programs, dew, and fog harvesting) plays an important role in decreasing the effects of climate change on water resources (Khalil et al., 2016; MaestreValero et al, 2011; Mileta et al., 2019; Agam et al., 2006; Kidron et al., 2002; Nikolayev et al., 1996; Nilsson et al., 1994; Rajvanshi, 1981; Jumikis, 1965; Hamed et al., 2010).

Water is continuously re-circulated and transported between oceans, land, and the atmosphere forming the so-called Earth's hydrologic cycle. Besides, vertical convection of water vapor and cloud formation, water vapor might transport nearby the Earth's surface and end up forming fog, smog, and mist as well as the condensation on cooled surfaces (i.e., dew formation). In fact, dew and fog formation is a very complex phenomenon that has been understood as a two-step process (Beysens et al., 2003, 2005 and 2006a; Beysens 1995 and 2006; Muselli et al., 2002; Raman et al., 1973): (1) formation of droplets on obstacles (particle, surface, etc.) via nucleation of water vapor and (2) droplet growth due to condensation of water vapor.

The amount and quality of harvested dew water have been given growing attention (Alnaser et al. 2006; Beysens et al., 2006b and 2007; Galek et al., 2012 and 2015; Lekouch et al., 2010; Odeh et al 2017; Polkowska et al., 2008). Several groups have developed different methods and tools to harvest dew in different environments (Odeh et al., 2017; Clus et al., 2008; Muselli, et al., 2009; Richards, 2019; Sharan et al., 2007 and 2019; Ye et al., 2007; Vuollekoski et al., 2015; Tomaszkiewicz et al., 2015). The most common experimental methods included passive condensers, radiative cooling, roofs (made of different materials, and surfaces made of a material that enhances the yield of dew. However, sustainable and long-term experimental studies about dew formation seem to be almost impossible. Therefore, the potential of dew formation has been investigated using model simulation. The simplest and most applicable models are those based on the semi-empirical approaches to implementing heat-mass transfer and energy balance (Nikolayev et al., 1996 2001; Beysens et al., 2003 and 2005; Vuollekoski et al., 2015; Tomaszkiewicz et al., 2015 and 2016; Monteith, 1957; Beysens, 2016; Gandhisam et al., 2005; Pedro et al., 1981; Nilsson, 1996; Jacobs et al., 2008; Jorge Ernesto et al., 2016). In Jordan, there have been only three investigations about dew water (Jiries, 2001; Odeh et al., 2017; Atashi et al., 2020, Al-Shuaibi, 2021). The first one reported some elemental and ion concentrations in dew water (Jiries, 2001). In the second one, Odeh et al.

* Corresponding author e-mail: t.hussein@ju.edu.jo

(2017) collected 15 samples of dew water on a substrate (during March–July 2015) in an urban area in Amman and reported the collected amount and quality by applying chemical and physical analysis. The third investigation included long-term model simulations for dew potential at ten selected locations reflecting the different climate zones in Jordan (Atashi et al. 2020). The most recent research on dew water harvesting quantity and quality was conducted at an urban site in Jordan (Al-Shuaibi R. 2021). However, dew formation zones have never been assessed theoretically in Jordan.

In this study, we performed gridded model simulations to estimate the dew yield during 1979–2018 aiming at distinguishing the dew formation zones in Jordan. The model simulations were made by adapting the global model, which was developed by Vuollekoski et al. (2015), to accommodate the environmental conditions in different environments in Jordan. The outcomes of this study are ought to be useful for managing and planning local feasibility studies for dew harvesting and a better understanding of the feedback processes between the water cycle and climate change in Jordan.

2. Data and Methods

2.1 An overview of the climate and water resources in Jordan

Jordan is a small country (29.4°–33° North and 35°–39.5° East, (~89,000 km^2, population ~11 million in 2021) with limited water sources and diverse habitats, ecosystems, and biota. The summer season (May–September) is hot-dry with a mean temperature of ~32 °C. The winter (November–March) is relatively cool with a mean temperature of ~13 °C and frequent showers and occasional snowfall in some elevated areas. Geographically, Jordan comprises a wide variety of topography that defines its climate spatial variation (Abdulla, 2020; Freiwan and Kadioglub, 2008): (1) semi-arid climate in the Jordan Valley with a hot dry summer, warm winter, and precipitation less than 200 mm/yr.; (2) arid climate in the Eastern Desert (also known as Badia) characterized by a sharp change in temperature between day and night and between summer and winter; and (3) Mediterranean climate on the Mountains Heights Plateau (including highlands above the Jordan Valley, mountains of the Dead Sea, Wadi Araba, and Ras Al-Naqab) with a hot-dry summer and cool-wet winter and two short transitional seasons. The Mountains Heights Plateau receives Jordan's highest amounts of precipitation (more than 300 mm/year), which falls from October to May with the peak usually during winter (December–February).

Jordan is the fourth country in the world suffering from freshwater shortages (Hamdy et al., 1999; Hadadin, 2015). The available water per capita has declined considerably during the past century; it was about 3600 m^3 in 1946 and it is expected to be as low as 100 m^3 in 2025 (Hadadin, 2015). Jordan's water demand was estimated to be about 940 MCM (63% agriculture, 32% domestic, and 5% industry) in 2007 and it increased to about 1600 MCM in 2010. The main sources of water include safe abstraction of groundwater, recycling wastewater, surface runoff water, and desalination. The annual mean water amount received in the form of rainfall is about 8300 million cubic meters (MCM) (Hamdy et al., 1999).

2.2 Meteorological input data

The meteorological input data-base includes horizontal and vertical wind components (U10 and V10) at 2 m, surface roughness (z0), ambient temperature and dew point (Ta and DP) at 2 m, and short-wave and long-wave surface solar radiation (R_{sw} and R_{lw}). The input database was downloaded from the European Centre for Medium-Range Weather Forecast (ECMWF) Interim Reanalysis (ERA-Interim), which is a global atmospheric reanalysis that is available from 1 January 1979 to 31 August 2019 (Berrisford et al., 2011; Dee et al., 2011). ERA-Interim has a native resolution of 0.75° (approximately 80 km) and 60 vertical levels. In this study, we considered the time during 1979- 2018 and input data interpolated to a grid resolution of 0.25 (~ 30 km) over a domain covering all parts of Jordan. The ERA-Interim is differentiated into two main categories: analysis fields and forecast fields (i.e. instantaneous and accumulated forecast). The analysis fields were available every 6 h (00:00, 06:00, 12:00, and 18:00 UTC) and the forecast fields were available every 3 h; hence, they can be used to fill in the gaps between the analysis. In our case, U10, V10, Ta, and DP were obtained from both analysis (i.e. at 00:00, 06:00, 12:00, and 18:00 UTC) and instantaneous forecast fields (i.e. at 03:00, 09:00, 15:00, and 21:00 UTC) and obtained the short-wave and long-wave (R_{sw} and R_{lw}) surface radiation as accumulated forecast fields. In the ERA-Interim database, the horizontal wind components (U_{10} and V_{10}) are provided at 10 m. Therefore, the wind speed at 2 meters was calculated by using a logarithmic wind profile as follows:

$$WS = \frac{log\left(\frac{2+z_0}{z_0}\right)}{log\left(\frac{10+z_0}{z_0}\right)} \sqrt{U_{10}^2 + V_{10}^2} \quad \text{......} (1)$$

where z_0 (as instanton forecast parameter) is the surface roughness and U_{10} and V_{10} are the horizontal wind speed components at 10 m.

2.3 Dew formation model

A global dew formation model, which was developed by Vuollekoski et al. (2015), was downscaled to simulate the dew formation potential in Jordan (Figure 1). The substrate (i.e., condenser material) was assumed a horizontally aligned sheet (at 2 m height and thermally insulated from the ground) of a suitable material such as low-density polyethylene (LDPE) or polymethylmethacrylate (PMMA). The detailed model description is presented in Supplementary Material (which I didn't see in the article). In brief, the model describes the water phase change based on mass and heat balance Equation:

$$\frac{dT_c}{dt}(C_c m_c + C_w m_w + C_i m_i) = P_{rad} + P_{cond} + P_{conv} + P_{lat} \quad ... (2)$$

where $dT_c/_{dt}$ is the change rate in the condenser temperature. C_c, C_w, and C_i are the specific heat capacity of condenser, water, and ice; respectively. Here, m_c, m_w, and m_i are mass of condenser, water, and ice; respectively. The right-hand side describes the heat exchange involved in the heat exchange processes: P_{rad} is the net radiation, P_{cond} is the conductive heat exchange between the condenser surface and the ground, P_{conv} is the convective heat exchange, and P_{lat} is the latent heat released by the condensation or desublimation of water. The model reads all input data (described in section 2.2) for a given grid point and solves the mass and heat balance equations using a fourth-order Runge–Kutta algorithm with a 10 s time step. The output is the cumulative daily dew yield in mm/m^2. All terms in Equation (S1) are described in more detail in Tables S1 and S2 (see Appendix).

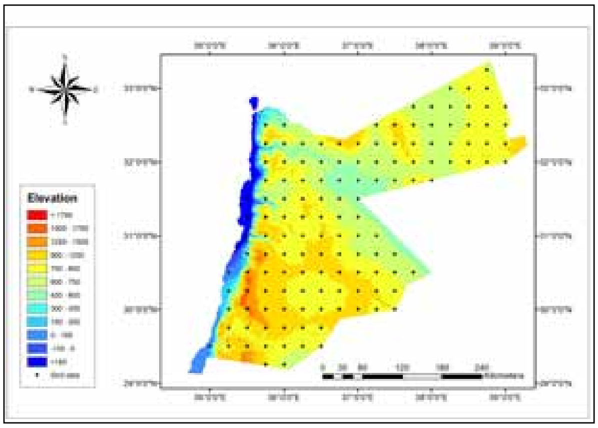

Figure 1. A map of Jordan illustrating the geographical topography and the domain of the grid points used in the model simulation.

Table 1. Dew formation zones and their climate features (i.e., mean (min-max) values for meteorological parameters (T, Td, RH)) as well as statistical analysis for overall mean daily cumulative dew yield (i.e., std, 25, 50, 75th, and 99th percentile as daily max aa well as yearly max dew yield).

	Zone A	Zone B	Zone C
T_{mean} [°C]	20 [19-2]	19 [12-26]	19 [12-26]
$T_{d\ mean}$ [°C]	4 [3-6]	8 [5-11]	6 [4-8]
RH_{mean} [%]	42 [36-51]	57 [49-66]	49 [42-58]
Mean dew yield ± std [L/m^2/day]	0.05 ± 0.05	0.15 ± 0.03	0.08 ± 0.04
25 % [L/m^2]	0.03	0.11	0.05
Median [L/m^2]	0.04	0.14	0.07
75% [L/m^2]	0.06	0.18	0.10
99% [L/m^2]	0.09	0.26	0.15
Mean [L/m^2/year]	18	55	28
Max [L/m^2/year]	26	66	36

2.4 Cluster Analysis

To identify the major dew formation zones in Jordan we applied Cluster Analysis (CA) to the long-term gridded model simulation. CA is an effective statistical technique that groups similar data points in the same group so that the objects in one group (called a cluster) are more similar to each other than in the other groups. There are two main clustering methods: hierarchical and non-hierarchical cluster analysis (Bunkers and Miller, 1996; Yim and Ramdeen,2015). In this study, we used hierarchical agglomerative clustering which consists of four main steps (HAC, Nielsen, 2016).

1. calculating the distance measured between all entries (data points);
2. merging the two closest entries as a new cluster;
3. recalculating the distance between all entries;
4. repeat steps 2 and 3 until all entries are grouped into distinct groups (i.e., clusters). The details of the clustering method used in this study are described in the supplementary material (section S2). After calculating all the steps and visualizing the results, three clusters were chosen as an optimal number of clusters for Jordan.

3. Discussion and Results

3.1 Dew potential – Long-Term Simulation and Analysis

The model simulation results revealed that dew can occur almost everywhere in Jordan, even in the driest areas in the eastern part of the country. Figure 2 illustrates the frequency of seasonal dew occurrence as a fraction of days for any dew yield. The average frequency of dew was about 84% (~ 75 days) in wintertime (December– February, Figure 2a). After winter with the most frequency of dewy days, spring (March-May) with 52% (~ 48 days, Figure 2b) and autumn (September–November) with 57% (~ 52 days, Figure 2d) have a modest frequency, respectively. As expected, summer (June–August) was the driest season with the least number of dew days in Jordan (40%, ~ 37 days, Figure 2c).

From the spatial point of view, in all cases, the dry eastern part has the minimum number of dew occurrences and the northwest part has the maximum. However, by limiting the dew occurrence analysis to dew yield > 0.1 L/m^2/day, the frequency of dew days was reduced by about 30% (~ 25 days) in all seasons. Specifically, by considering this threshold (> 0.1 L/m^2/day), the frequency of dew occurrence was about 15% (~ 14 days), 25% (~ 23 days), 32% (~29 days), and 57% (~ 51 days) and in the summer and spring, dew occurrence shrank to include mainly the western half of the country (Figure 1).

The seasonal mean of daily cumulative and also monthly dew yield is presented in Figure 3 and Figure 4; respectively. The seasonal mean of daily dew yield shows the same temporal and spatial pattern as the frequency map with the highest yields in winter (~0.13 L/m^2/day, Figure 3a), and the lowest yields in summer (~0.03 L/m^2/day, Figure 3c). These amounts for the transition months (i.e. autumn and spring) are about 0.07 and 0.05 L/m^2/day. In spatial scale, the highest values are along with the highlands in the northwestern part of Jordan. The lowest values were belonging to the dry lands and deserts in the southeastern parts of the country.

A closer look at the spatial and temporal variation of dew yield can be seen from the monthly cumulative dew reflects the seasonal pattern (Figure 4). Based on the monthly analysis, dew can occur from October–March in almost whole areas with the highest yields in December and January whereas, from April–September except for the western areas (i.e. Jordan valley and coastal dead sea areas), dew almost vanishes in the rest parts of the country. High air temperature, low relative humidity, and long day duration in the warm seasons prevent dew condensation in most areas in Jordan, in turn, during the cold seasons by decreasing the air temperature and injecting moisture by the prevailing westerly winds, the difference between temperature and dew point temperature declines and the initial condition is provided for the formation of dew in the almost whole country.

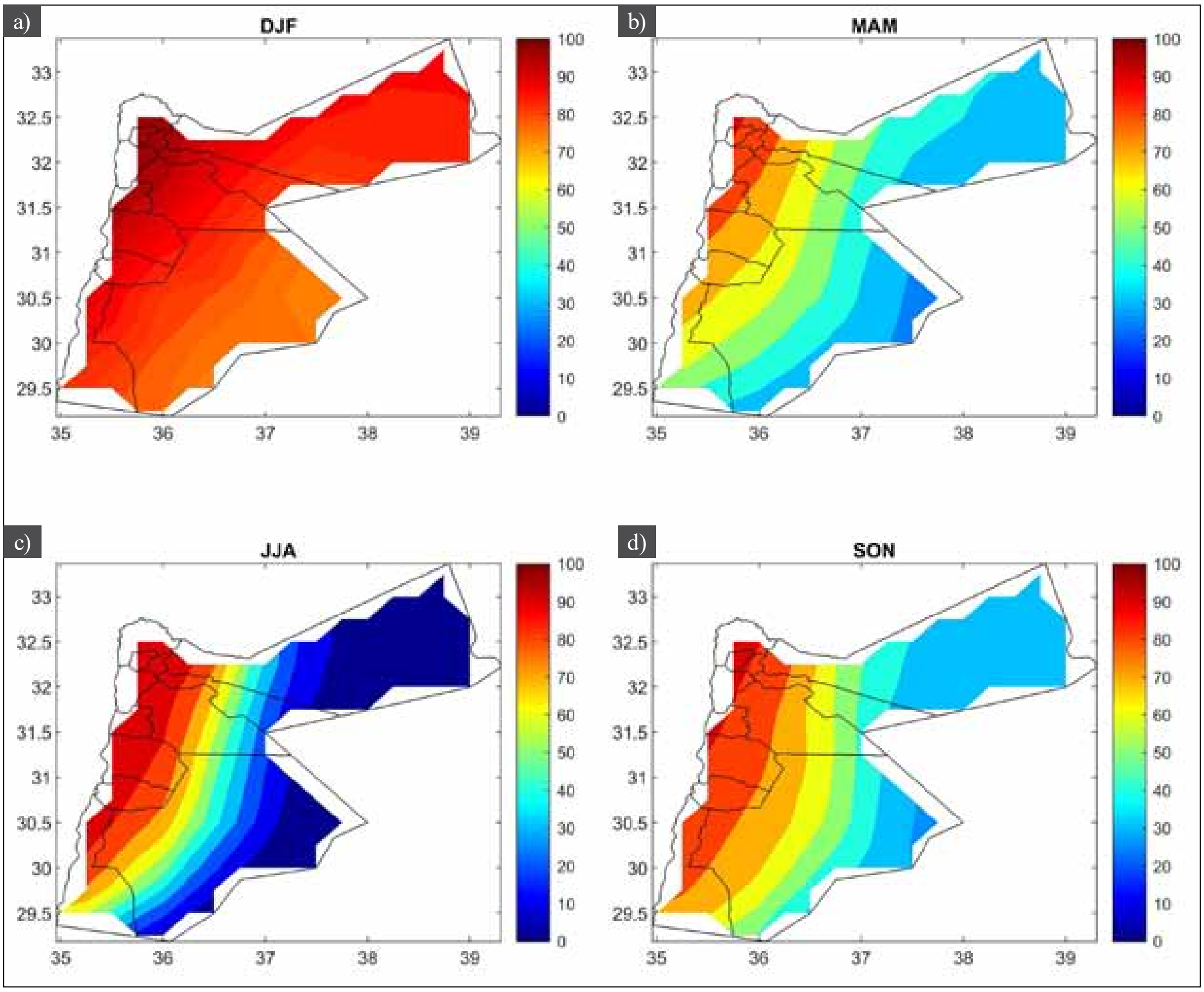

Figure 2. Frequency of dew occurrence as a fraction of days presented as an overall seasonal mean during 1979–2018. (a) winter (December, January, and February), (b) spring (March, April, and May), (c) summer (June, July, and August), and (d) autumn (September, October, and November).

3.2 Dew formation zones – Spatial Variation of Dew Potential

3.2.1 Dew zones – a general overview

According to the cluster analysis, we identified three dew formation zones in Jordan (Figure 5). The amount of daily dew yield (i.e. mean, max (99th percentile), std) and the important climatological parameters related to dew formation (e.g., temperature, dew point temperature, and relative humidity) are listed in Table 1. The percentiles of daily dew yield (i.e. 25th, median, 75th, and 99th percentile) are calculated in Table 1, and the 25th and 75th percentiles are illustrated in Figure 6. Eventually, the distribution of the dew formation zones in Jordan is aligned with topography, sources of moisture, and climate zones. Therefore, we named the dew zones similar to the climate zones.

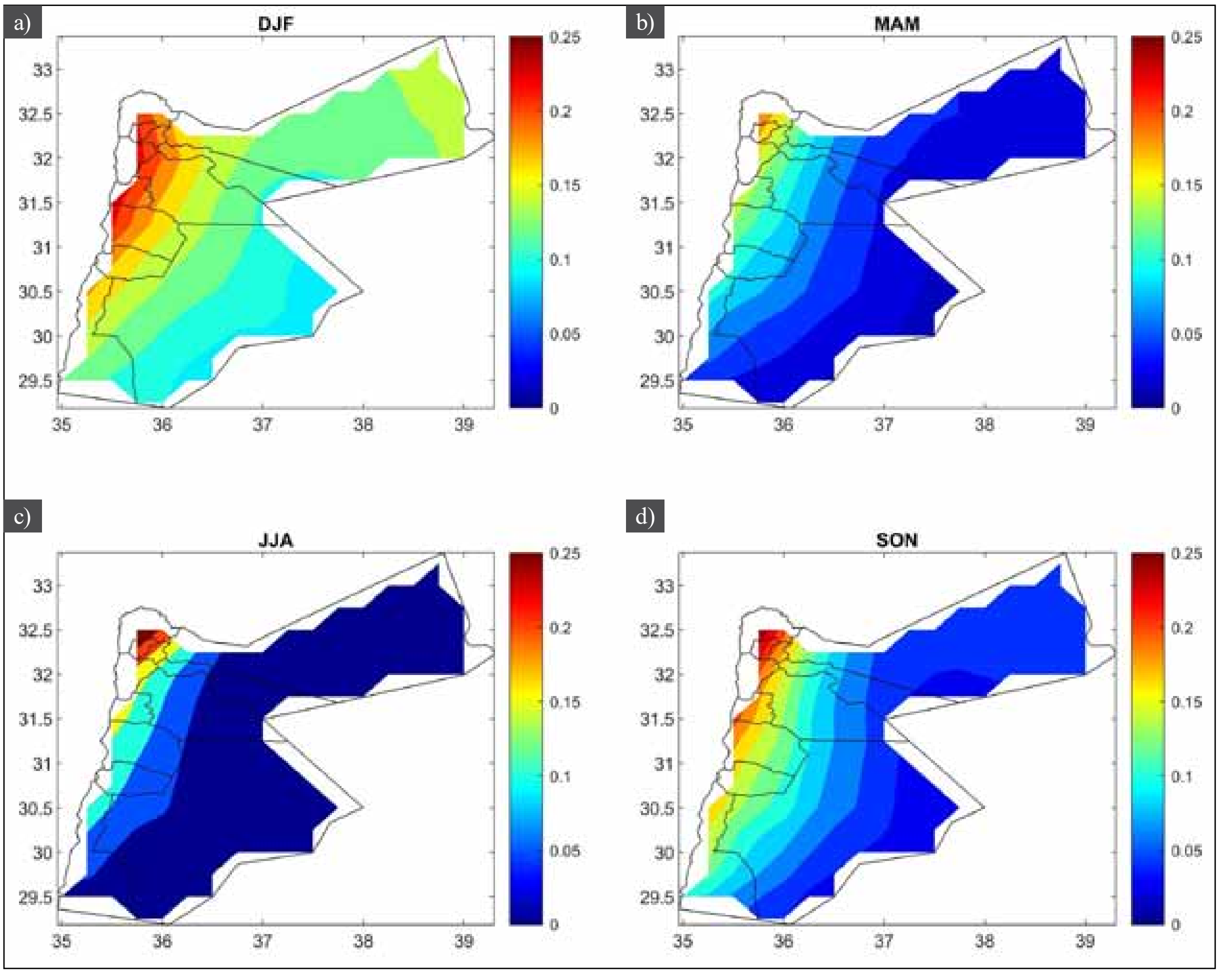

Figure 3. Cumulative dew yield [L/m2/day] presented as an overall seasonal mean during 1979–2018. (a) winter (December, January, and February), (b) spring (March, April, and May), (c) summer (June, July, and August), and (d) autumn (September, October, and November).

3.2.2 Dew zone A – Eastern desert

We identified the first dew zone (i.e. dew zone A) as the "Eastern desert". This zone including 50% of all the grid points in Jordan is the largest dew formation. However, it has the least amount of dew occurrence and dew yields in the country. By considering the minimum harvestable dew water from the condenser (> 0.1 L/m^2/day), the number of dew occurrences in this zone is about 80 days per year and the overall mean daily dew yield was ~0.05±0.05 L/m^2/day, which is the lowest among other dew zones in Jordan (Figure 6 and Table 1).

The Dew period in this zone starts from October and continues through winter until the spring (namely April). However, only 80 days of this period dew can be collectible (> 0.1 L/m^2/day) and for the rest of the days, the amount of dew yield is very little. From May– September dew vanished (almost Zero) in this zone (Figure 6). Indeed, this zone is characterized as the arid-hyper arid area with high temperature, no source of moisture, and low relative humidity; therefore, T_a–T_d is high (about 18°C most of the time (Table 1)). Furthermore, during the warm season, high surface temperature leads to the form of thermal low-pressure systems, which cause turbulence and an intense wind speed. As such, condensation cannot occur over a long period of the year. Only during late autumn and winter due to a decrease in the temperature and domination of prevailing westerly winds that bring the moisture from the Mediterranean Sea into the country, T_a–T_d is reduced and dew can form in this zone. As such, the peak of dew yield (about 0.15 L/m^2/day) is also in wintertime (December–January). The mean yearly dew yield in this zone was about 18 L/m^2 and the maximum was about 26 L/m^2 (Table 1).

3.2.3 Dew zone B – Jordan Valley

Dew zone B includes the Jordan Valley and the mountain heights plateau, which are mainly situated in the western region starting at the northern part parallel to the Jordan Valley and extending to the south approaching Wadi Rum.

Although, this zone is the smallest dew zone (including 20% of the al grid points) it has the highest potential of dew yield (overall mean daily 0.15 L/m^2/day) in Jordan (Figure 6 and Table 1). Furthermore, this zone has the longest dew formation period which spans over the whole year with a significant amount of dew yield. The mean frequency of dew occurrence (> 0.1 L/m^2/day) is more than 330 days/year (Figure 6 and Table 1). The mean yearly dew yield in this zone is estimated at 55 L/m^2 and the maximum was about 66 L/m^2 which is the highest in the country (Table 1). The high potential of dew formation and yield in this region is related to the fact that initial conditions for dew formation are provided during the year. For instance, this zone is located in the height mountains area so that, has a high diurnal variation of the temperature, receiving high short-wave radiation during the day and reflecting it in the form of long-wave radiation during the night. Therefore, air temperature declines very quickly in the nighttime resulting in a reduction in T_a–T_d. Furthermore, this zone benefits the efficient water bodies (e.g. Dead Sea, Mediterranean Sea, Sea of Galilee) through the westerlies or sea breeze which favors dew formation in this zone.

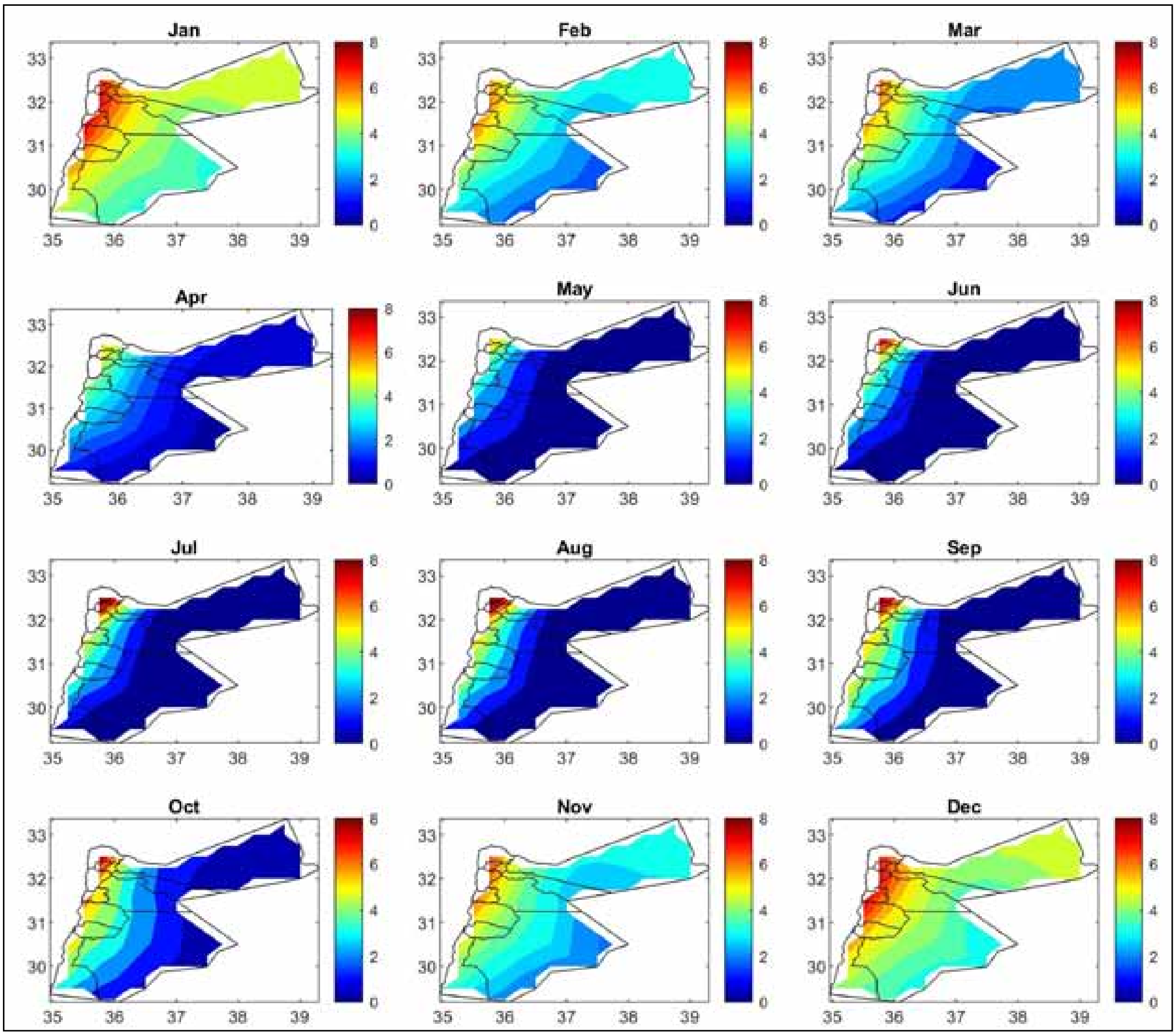

Figure 4. Cumulative dew yield [L/month] presented as an overall monthly mean during 1979–2018 in Jordan.

3.2.4 Dew zone C –Central heights Plateau

The third dew zone (dew zone C) covers the central part of Jordan from north to south including about 30% of all grid points and is geographically called East Bank Plateau. The overall mean daily dew yield in this zone is about 0.08 L/m^2/day (Table 1). Although the frequency of dew occurrence in this zone is throughout the year in most cases the amount of dew is very little and negligible and the days with dew yield > 0.1 L/m^2 are about 120 days (Figure 6 and Table 1). The annual cycle of dew yield is clear in this zone as it was in the first dew zone with the highest yields in winter (December–January) and the lowest in late spring to late autumn (May–September). The mean yearly dew yield is about 28 L/m^2 and the maximum is about 36 L/m^2/year (Table 1). In comparison, the potential for dew formation in this zone is more than in the first dew zone but less than in the second dew zone. However, the daily and seasonal variations are more similar to the eastern desert dew zone. Indeed, this dew zone is suffering from high temperature and low humidity, and therefore T_a–T_d rises. This condition is almost valid most of the time, only during the cold season due to a decline in temperature and increase in relative humidity dew can form on the condenser surface.

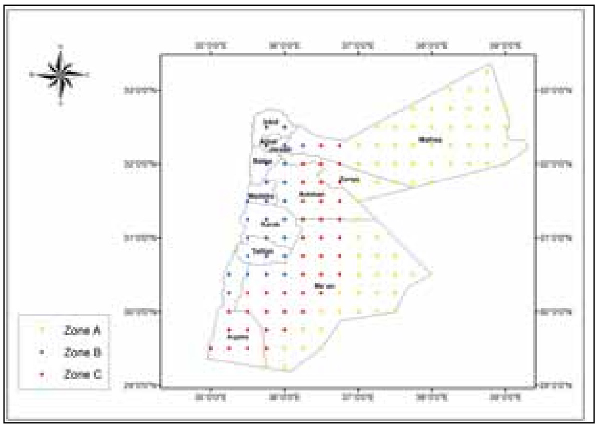

Figure 5. Dew formation zones in Jordan based on the cluster analysis of the daily cumulative dew yield during 1979–2018.

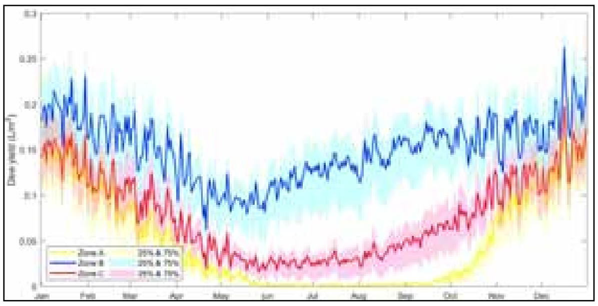

Figure 6. long-term mean seasonal variation of the cumulative daily dew yield over 40 years (1079-2018). Note that the color coding on this figure is the same and corresponds to the dew formation zones in Figure 6: (yellow) dew zone A (arid and semi-arid region), (blue) Zone B (coastal region), and (red) Zone C (central heights Plateau). The shaded parts around the lines represent the 25th and 75th percentile of daily dew yields for each cluster, and the colors are the same as clusters.

4. Discussion

Jordan is located in an arid and semi-arid region and has been suffering from fresh water scarcity over the last decades. This problem is getting even more serious with a growing population, therefore looking for a renewable source of water is vital. The atmosphere can be considered a huge reservoir of water that can be extracted in the form of dew or fog, especially in dry conditions. Based on our model simulation results to estimate the potential of dew formation in Jordan, the average dew yield was in the range of 0.05- 0.15 L/m^2/ day. The outcomes are in agreement with previous observational studies that have been conducted in similar climates as Jordan (i.e. arid and semi-arid, desert, Mediterranean climates). For instance, the reported values for average daily dew yield for a semi-arid Mediterranean climate were 0.04 L/m^2 in Zadar (France; Muselli et al., 2009), 0.09 L/m^2 in Komiža (Croatia; Muselli et al., 2009), 0.04 L/m^2 in Beirut (Lebanon; Tomaszkiewicz et al., 2015), 0.06–0.19 L/m^2 in a semi-arid coastal area in southwestern Madagascar (Hanisch et al., 2015), and 0.13 L/m^2 in Beiteddine village (Lebanon; Tomaszkiewicz et al., 2017). The results are also in agreement with the desert areas in the neighboring countries, for instance, Israel (mean: 0.09 L/m^2; Kidron, 1999); Dhahan, Saudi Arabia (mean: 0.22 L/m^2/day; Gandhisan and Abualhamayel, 2005).

It should be noted that similar to all numerical models, this model also has some limitations that cause some uncertainties in the results, and it is expected to overestimate dew yield. However, these uncertainties caused by the model assumptions do not affect the main conclusions of this study (spatial (dew zones) and temporal variation) since it has been conducted over 40 years and averaging on a long-term smoothens the differences in daily scale.

5. Conclusions

Jordan is a country with limited water sources and comprises a wide variety of topography that defines its climate spatial variation (semi-arid, arid, and Mediterranean). It is the fourth country in the world suffering from freshwater shortages. Therefore, it is a challenging topic to find alternative sources of water for drinking and agricultural application. Dew and fog harvesting can be one of these alternative sources. However, there have been very few investigations about dew water in Jordan. In this study, we performed gridded model simulations to estimate the dew yield during 1979–2018 aiming at investigating the spatial-temporal variation of dew formation. We also applied cluster analysis to distinguish the dew formation zones in Jordan.

Our investigation revealed that dew can occur almost everywhere in Jordan during the winter (about ~75 days during December–February). As expected, summer is the driest season with the least number of dew days in Jordan (~37 days during June–August). According to the cluster analysis, we distinguished three dew formation zones, which were closely related to the climate zones: Dew zone A (eastern desert), Dew zone B (Jordan Valley), and Dew zone C (central heights Plateau). Zone A receives the least dew formation potential, which mainly occurs during the winter, and Zone C receives the highest dew formation potential, which occurs throughout the year.

The outcomes of this study are ought to be useful for managing and planning local feasibility studies for dew harvesting and a better understanding of the feedback processes between the water cycle and climate change in Jordan.

Acknowledgment

This research was supported by the Deanship of Scientific Research at the University of Jordan, Finnish Academy (Flagship funding (grant number 337549), Center of Excellence program (CoE-ATM, grant no. 307331)), University of Isfahan is acknowledged to facilitate the research visit abroad for graduate students. Tareq Hussein acknowledges support from the Eastern Mediterranean and the Middle East—Climate and Atmosphere Research (EMME-CARE) project, which has received funding from the European Union's Horizon 2020 Research and Innovation Program (grant agreement no. 856612) and the Government of Cyprus. The European Union is not responsible for any use that may be made of the information contained therein. The sole responsibility of this publication lies with the author.

References

Abdulla, F. 21st Century Climate Change Projections of Precipitation and Temperature in Jordan. 1st International Conference on Optimization-Driven Architectural Design (OPTARCH 2019). Proced. Manuf. 2020, 44, 197–204.

Al-Shuaibi R. (2021) Investigation of Dew Water Harvesting Quantity and Quality at Selected Sites in Jordan. Master Thesis, Faculty of Science, Department of Geology, The University of Jordan. Unpublished M.Sc. Thesis.

Atashi, N.; Rahimi, D.; Al Kuisi, M.; Jiries, A.; Vuollekoski, H.; Kulmala, M.; Vesala, T.; Hussein, T. "Modeling Long-Term Temporal Variation of Dew Formation in Jordan and Its Link to Climate Change." Water, 2020, 12, 21–86.

Beysens, D. Dew nucleation, and growth. C. R. Phys. 2006, 7, 1082–1100.

Beysens, D. Estimating dew yield worldwide from a few meteo data. Atmos. Res. 2016, 167, 146–155.

Beysens, D. The formation of dew. Atmos. Res. 1995, 39, 215–237.

Beysens, D.; Clus, O., Mileta, M.; Milimouk, I.; Muselli, M.; Nikolayev, VS. Collecting dew as a water source on small islands: The dew equipment for water project in (Croatia).

Energy 2007, 32, 1032–1037.

Beysens, D.; Milimouk, I.; Nikolayev, V.; Muselli, M.; Marcillat, J. Using radiative cooling to condense atmospheric vapor: A study to improve water yield. J. Hydrol. 2003, 276, 111.

Beysens, D.; Muselli, M.; Milimouk, I.; Ohayone, C.; Berkowicz, S.M.; Soyeuxg, E.; Mileta, M.; Ortega, P. Application of passive radiative cooling for dew condensation. Energy 2006a, 31, 1967–1979.

Beysens, D.; Muselli, M.; Nikolayev, V.; Narhe, R.; Milimouk, I. Measurement, and modelling of dew in island, coastal and alpine areas. Atmos. Res. 2005, 73, 122.

Beysens, D.; Ohayon, C.; Muselli, M.; Clus, O. Chemical and biological characteristics of dew and rainwater in an urban coastal area (Bordeaux, France). Atmos. Environ. 2006b, 40, 3710–3723.

Berrisford, P.; Dee, D.; Poli, P.; Brugge, R.; Fielding, K.; Fuentes, M.; Kallberg, P.; Kobayashi S.; Uppala, S.; Simmons, A. ERA report series, The ERA-Interim archive, version 2, Shinfield Park, Reading, available at: https://www.ecmwf.int/en/elibrary/8174-era-interim-archive-version-20 (last access: 7 August 2021), 2011.

Bunkers, M. J.; Miller Jr, J. R. Definition of climate regions in the Northern Plains using an objective cluster modification technique, J. Climate, 1996, 9, 130–146, https://doi.org/10.1175/1520- 0442(1996)009<0130: DOCRIT>2.0.CO;2.

Clus, O.; Ortega, P.; Muselli, M.; Milimouk, I.; Beysens, D. Study of dew water collection in humid tropical islands. J. Hydrol. 2008, 361, 159–171.

Dee, D. P.; Uppala, S. M.; Simmons, A. J.; Berrisford, P.; Poli, P.; Kobayashi, S.; Andrae, U.; Balmaseda, M. A.; Balsamo, G.; Bauer, P.; Bechtold, P.; Beljaars, A. C. M.; van de Berg, L.; Bidlot, J.; Bormann, N.; Delsol, C.; Dragani, R.; Fuentes, M.; Geer, A. J.; Haimberger, L.; Healy, S. B.; Hersbach, H.; Hólm, E. V.; Isaksen, L.; Kållberg, P.; Köhler, M.; Matricardi, M.; McNally, A. P.; Monge-Sanz, B. M.; Morcrette, J.-J.; Park, B.-K.; Peubey, C.; de Rosnay, P.; Tavolato, C.; Thépaut, J.-N.; and Vitart, F. The ERA-Interim reanalysis: configuration and performance of the data assimilation system, Q. J. Roy. Meteorol. Soc. 2011, 137, 553–597. https://doi.org/10.1002/qj.828.

Freiwan, M.; Kadioglub, M. Climate variability in Jordan. Int. J. Climatol. 2008, 28, 69–89.

Galek, G.; Sobik, M.; Blas, M.; Polkowska, Z.; Cichala-Kamrowska, K. Dew formation and chemistry near a motorway in Poland. Pure Appl. Geophys. 2012, 169, 1053–1066.

Gałek, G.; Sobik, M.; Błaś, M.; Polkowska, Ż.; Cichała-Kamrowska, K.; Wałaszek, K. Dew and hoarfrost frequency, formation efficiency and chemistry in Wroclaw, Poland. Atmos. Res. 2015, 151, 120–129.

Gandhisan, P.; Abualhamayel, H.I. Modelling and testing of a dew collection system. Desalination 2005, 18, 47–51.

Hadadin, N. Dams in Jordan current and future perspective. Can. J. Pure Appl. Sci. 2015, 9, 3279–3290.

Hamdy, A.; Lacirignola, C. Mediterranean water resources: Major challenges towards the 21st century. In Proceedings of the International Seminar on Mediterranean Water Resources: Major Challenges Towards the 21st Century, Egypt, Cairo, 1–5 March 1999.

Hamed, A.M.; Kabeel, A.E.; Zeidan, E.S.B.; Aly, A.A. A technical review on the extraction of water from atmospheric air in arid zones. Int. J. Heat Mass Trans. 2010, 4, 213–228.

Hanisch, S.; Lohrey, C.; Buerkert, A. Dewfall, and its ecological significance in semi-arid coastal southwestern Madagascar, J. Arid. Environ. 2015, 121, 24–31, https://doi.org/10.1016/j.jaridenv.2015.05.007.

Jacobs, A.F.G.; Heusinkveld, B.G.; Berkowicz, S.M. Passive dew collection in a grassland area, The Netherlands. Atmos. Res. 2008, 87, 377–385.

Jiries, A. Chemical composition of dew in Amman, Jordan. Atmos. Res. 2001, 57, 261–268.

Jorge Ernesto, A.T.; Jose Jasson, F.P. Winter dew harvest in Mexico City. Atmosphere 2016, 7, 2.

Jumikis, A.R. Aerial wells: Secondary source of water. Soil Sci. 1965, 100, 83–95.

Khalil, B.; Adamowski, J.; Shabbir, A.; Jang, C.; Rojas, M.; Reilly, K.; OzgaZielinski, B. A review: Dew water collection from radiative passive collectors to recent developments of active collectors, Sustain. Water Resource. Manag. 2016, 2, 71–86.

Kidron, G. J. Altitude dependent dew and fog in the Negev Desert, Israel, Agr. Forest. Meteorol. 1999, 96, 1–8, https://doi.org/10.1016/S0168-1923(99)00043-X.

Kidron, G.J.; Herrnstadt, I.; Barzilay, E. The role of dew as a moisture source for sand microbiotic crusts in the Negev Desert, Israel. J. Arid Environ. 2002, 52, 517–533.

Lekouch, I.; Mileta, M.; Muselli, M.; Milimouk-Melnytchouk, I.; Šojat, V.; Kabbachi, B.; Beysens, D. Comparative chemical analysis of dew and rainwater. Atmos. Res. 2010, 95, 224–234.

Lekouch, I.; Muselli, M.; Kabbachi, B.; Ouazzani, J.; MelnytchoukMilimouk, I.; Beysens, D. Dew, fog, and rain as supplementary sources of water in southwestern Morocco. Energy 2011, 36, 2257–2265.

Lindblom, J.; Nordell, B. Water production by underground condensation of humid air. Desalination 2006, 189, 248–260.

MaestreValero, J.F.; MartinezAlvarez, V.; Baille, A.; MartínGórriz, B.; GallegoElvira, B. Comparative analysis of two polyethylene foil materials for dew harvesting in a semiarid climate. J. Hydrol. 2011, 410, 84–91.

Mileta, M.; Beysens, D.; Nikolayev, V.; Milimouk, I.; Clus, O.; Muselli, M. Fog, and Dew Collection Projects in Croatia. Available online: https://arxiv.org/ftp/arxiv/papers/0707/0707.2931.pdf. (accessed on 22 November 2019).

Monteith, J.L. Dew. Q. J. R. Meteorol. Soc. 1957, 83, 322–341.

Muselli, M.; Beysens, D.; Marcillat, J.; Milimouk, I.; Nilsson, T.; Louche, A. Dew water collector for potable water in Ajaccio (Corsica Island, France). Atmos. Res. 2002, 64, 297–312.

Muselli, M.; Beysens, D.; Mileta, M.; Milimouk, I. Dew and rainwater collection in the Dalmatian Coast, Croatia. Atmos. Res. 2009, 92, 455–463.

Nielsen, F. Introduction to HPC with MPI for Data Science, in: chap. 8: Hierarchical Clustering, Springer, Switzerland, 2016.

Nikolayev, V.S.; Beysens, D.; Gioda, A.; Milimouka, I.; Katiushin, E.; Morel, J.P. Water recovery from dew. J. Hydrol. 1996, 182, 19–35.

Nikolayev, V.S.; Beysens, D.; Muselli, M. A computer model for assessing dew/frost surface deposition. In Proceedings of the Second International Conference on Fog and Fog Collection, St John's, NL, Canada, 15–20 July 2001; pp. 333–336.

Nilsson, T. Initial experiments on dew collection in Sweden and Tanzania. Sol. Energy Mater. Sol. Cells 1996, 40, 23–32.

Nilsson, T.M.J.; Vargas, W.E.; Niklasson, G.A.; Granqvist, C.G. Condensation of water by radiative cooling. Ren. Energy 1994, 5, 310–317.

Odeh, I.; Arar, S.; Al-Hunaiti, A.; Sa'aydeh, H.; Hammad, G.; Duplissy, J.; Vuollekoski, H.; Korpela, A.; Petäjä, T.; Kulmala, M.; et al. Chemical investigation and quality of urban dew collection with dust precipitation. Environ. Sci. Pollut. Res. 2017, 24, 12312–12318.

Pedro, M.J., Jr.; Gillespie, T.J. Estimating dew duration. I. Utilizing micrometeorological data. Agric. Meteorol. 1981, 25, 283–296.

Polkowska, Ż.; Błaś, M.; Klimaszewska, K.; Sobik, M.; Małek, S.; Namieśnik, J. Chemical characterization of dew water collected in different geographic regions of Poland. Sensors 2008, 8, 4006–4032.

Rajvanshi, A.K. Large scale dew collection as a source of fresh water supply. Desalination 1981, 36, 299–306.

Raman, C.R.V.; Venkatraman, S.; Krishnamurthy, V. Dew ver India and Its Contribution to Winter-Crop Water Balance. Agric. For. Meteorol. 1973, 11, 17–35.

Richards, K. Observation and simulation of dew in rural and urban environments. Prog. Phys. Geogr. 2004, 28, 76–94.

Sharan, G. Dew Yield from Passive Condensers in a Coastal Arid Area: Kutch. Available online: http://vslir.iima.ac.in:8080/jspui/bitstream/11718/6362/1/2005-01-05gsharan.pdf. (accessed on 22 November 2019).

Sharan, G.; Shah, R.; Millimouk-Melnythouk, I.; Beysens, D. Roofs as Dew Collectors: Corrugated Galvanized Iron Roofs in Kothara and Suthari (NW India). In Proceedings of the Fourth International Conference on Fog, Fog Collection and Dew, La Serena, Chile, 22–27 July 2007.

Tomaszkiewicz, M.; Abou Najm, M.; Beysens, D.; Alameddine, I.; El-Fadel, M. Dew as a sustainable non-conventional water resource: A critical review. Environ. Rev. 2015, 23, 425–442.

Tomaszkiewicz, M.; Abou Najm, M.; Beysens, D.; Alameddine, I.; Zeid, E.B.; El-Fadel, M. Projected climate change impacts upon dew yield in the Mediterranean basin. Sci. Total Environ. 2016, 566, 1339–1348.

Tomaszkiewicz, M.; Abou Najm, M.; Zurayk, R.; El-Fadel, M. Dew as an adaptation measure to meet water demand in agriculture and reforestation, Agr. Forest. Meteorol. 2017, 232, 411–421, https://doi.org/10.1016/j.agrformet.2016.09.009.

Vuollekoski, H.; Vogt, M.; Sinclair, V.A.; Duplissy, J.; Järvinen, H.: Kyrö, E.; Makkonen, R.; Petäjä, T.; Prisle, N.L.; Räisänen, P.; et al. Estimates of global dew collection potential on artificial surfaces. Hydrol. Earth Syst. Sci. 2015, 19, 601–613.

Ye, Y.; Zhou, K.; Song, L.; Jin, J.; Peng, S. Dew amount and its correlation with meteorological factors in urban landscapes of Guangzhou, China. Atmos. Res. 2007, 86, 21–29.

Yim, O.; Ramdeen, K. T. Hierarchical cluster analysis: comparison of three linkage measures and application to psychological data, Quant. Meth. Psychol. 2015, 11, 8–21, https://doi.org/10.20982/tqmp.11.1.p008.

Appendix: "Supplementary Material"

Long-Term Model Simulation and a Spatial-Temporal Investigation for Dew Potential in Jordan

Nahid Atashi and Tareq Hussein

S.1. Model Description

The model describes the water phase change based on mass and heat balance Equation

$$\frac{dT_c}{dt}(C_c m_c + C_w m_w + C_i m_i) = P_{rad} + P_{cond} + P_{conv} + P_{lat} \quad \text{... (S1)}$$

where dT_c/dt is the change rate in the condenser temperature. C_c, C_w, and C_i are the specific heat capacity of condenser, water, and ice; respectively. Here, m_c, m_w, and m_i are mass of condenser, water, and ice; respectively. The right-hand side describes the heat exchange involved in the heat exchange processes: P_{rad} is the incoming and outgoing radiation, P_{cond} is the conductive heat exchange between the condenser surface and the ground, P_{conv} is the convective heat exchange, and P_{lat} is the latent heat released by the condensation or desublimation of water. The model reads all input data for a given grid point and solves equations. using a fourth-order Runge–Kutta algorithm with a 10 s time step. All terms in Equation (S1) are described in more detail in Tables S1 and S2.

The model was set up so that it assumes similar conditions for the phase-change of pre-existing water or ice on the condenser sheet. For instance, if the water on the condenser is in the liquid phase (i.e., $m_w > 0$) and the condenser temperature $T_c < 0$ °C, then the sheet is losing energy (i.e., the right-hand side of Equation (S1) is negative). In that case, instead of solving Equation (S1), Tc is assumed constant and the lost mass from the liquid phase of water is transferred to the cumulated mass of ice; i.e., the water is transformed from liquid phase to solid phase. Consequently, Equation (S1) is replaced by

$$L_{wi}\frac{dm_w}{dt} = P_{rad} + P_{conv} + P_{lat}, \quad \text{...... (S2)}$$

where L_{wi} [J kg^{-1}] is the latent heat of fusion. If the water on the condenser is in the solid phase (i.e., $m_i > 0$) and the condenser temperature $T_c > 0$ °C, a similar equation is assumed for the change rate of ice mass (m_i).

Note that Equation (S2) is not related to the condensation of water; it only describes the phase change of the already condensed water or ice on the condenser. For the water condensation rate, which is assumed independent of Equation (S2), the mass-balance equation is then assumed to be

$$\frac{dm}{dt} = \max[\ 0\ ,\ S_c k(\ P_{sat}(T_d) - P_c(T_c)\ )\ ], \quad \text{...... (S3)}$$

where m represents either the mass of ice (m_i) or water (m_w) depending on weather Tc is below or above 0 °C. $P_{sat}(T_d)$ is the saturation pressure at the dew point temperature whereas $P_c(T_c)$ is the vapor pressure over the condenser sheet. $k = h/L_{vw}\gamma = 0.622h/C_a p$ is the mass transfer coefficient, where L_{vw} [J kg^{-1}] is the specific latent heat of water vaporization, γ is the psychrometric constant, C_a is the specific heat capacity of air, and p is the atmospheric air pressure. Here, $h = 5.9 + 4.1\,u\,(511 + 294)/(511+T_a)$ is the heat transfer coefficient, where u and Ta are the prevailing horizontal wind speed and the ambient temperature at 2 m from the ground.

In practice, the wettability of the surface affects vapor pressure P_c directly above it. In other words, P_c is lower over a wet surface; thus, condensation may take place even if $T_c > T_d$ (e.g., [15]). According to the model setup, Equation (S3) assumes irreversible condensation; i.e., there is no evaporation or sublimation during daytime even if $T_c > T_a$. Furthermore, the model simulation resets the cumulative values for water and ice condensation at noon. and takes the preceding maximum value of $m_w + m_i$ as the representative daily yield. This way, the model simulation replicates the daily manual dew water collection of the condensed water around sunrise; i.e., after which T_c is often above the dew point temperature.

Table S1. Description of the dew formation model by listing the terms in Equation (S1).

Term	Unit	Description
dT_c/dt	K s^{-1}	The change rate of the condenser temperature
T_c	K	The temperature of the condenser
T	s	Time. Here the time step in the model was 10 s
C_c	J kg^{-1} K^{-1}	Specific heat capacity of the condenser. For low-density polyethylene (LDPE) and polymethylmethacrylate (PMMA) it is 2300 J kg^{-1} k^{-1}
C_i	J kg^{-1} K^{-1}	Specific heat capacity of ice (2110 J kg^{-1} k^{-1})
C_w	J kg^{-1} K^{-1}	Specific heat capacity of water (4181.3 J kg^{-1} k^{-1})
m_c	kg	Mass of the condenser given by $m_c = \rho_c S_c \delta_c$ where ρ_c, S_c, and δ_c are the density (here it is 920 kg m^{-3}), surface area (here it is 1 m^2), and thickness of the condenser (here it is 0.39 mm)
m_i	kg	Mass of ice
m_v	kg	Mass of water, representing the cumulative mass of water that has
P_{rad}	W	Heat exchange due to incoming and outgoing radiation $P_{rad} = (1 - a)S_cR_{sw} + \varepsilon_c S_c R_{lw} - S_c \varepsilon_c \sigma T_c^4$ where a is the condenser short-wave albedo (here it is 0.84), S_c is the condenser surface area (here it is 1 m^2), ε_c is the emissivity of the condenser (here it is 0.94), σ is Stephan-Boltzmann constant (5.67 × 10^{-8} W m^{-2} K^{-4}), T_c [K] is the temperature of the condenser, and R_{sw} and R_{lw} [W m^{-2}] are the incoming short-wave radiation (i.e., surface solar radiation downwards) and incoming long-wave radiation (i.e., surface thermal radiation downwards)
P_{cond}	W	Conductive heat exchange between the condenser surface and the ground. For simplicity, we assumed that the condenser is perfectly insulated from the ground; i.e., $P_{cond} = 0$
P_{conv}	W	Convective heat exchange $P_{conv} = S_c (T_a - T_c)\, h$ where S_c is the condenser surface area (here it is 1 m^2), T_a [K] is the ambient temperature at 2 m from the ground, T_c [K] is the temperature of the condenser, and h [W m^{-2} K^{-1}] is the heat transfer coefficient that is estimated based on a semi-empirical equation [37] $h = 5.9 + 4.1\, WS\, (511 + 294)/(511 + T_a)$ and here WS [m s^{-1}] is the prevailing horizontal wind speed at 2 m from the ground.
P_{lat}	W	Latent heat released by the condensation or desublimation of water $P_{lat} = \begin{cases} L_{vw}\dfrac{dm_w}{dt} & T_c > 0\,^oC \\ L_{vi}\dfrac{dm_i}{dt} & T_c < 0\,^oC \end{cases}$ where L_{vw} [J kg^{-1}] is the specific latent heat of water vaporization and L_{vi} [J kg^{-1}] is specific latent heat of water desublimation. Here, dm_w/dt is the change rate of water whereas dm_i/dt is the change rate of ice

Table S2. A list of nomenclature.

Parameter	Unit	Description
α		Albedo of the condenser sheet
C_a	J kg^{-1} K^{-1}	Specific heat capacity of air
C_c	J kg^{-1} K^{-1}	Specific heat capacity of the condenser
C_i	J kg^{-1} K^{-1}	Specific heat capacity of ice
C_w	J kg^{-1} K^{-1}	Specific heat capacity of water
DP	K	Dew point temperature
h	W K^{-1} m^{-2}	Heat transfer coefficient
k	Per s^{-1}	Mass transfer coefficient
L_{vi}	J kg^{-1}	Specific latent heat of desublimation for water
L_{vw}	J kg^{-1}	Specific latent heat of vaporization for water
L_{wi}	J kg^{-1}	Latent heat of fusion
m_c	kg	Mass of the condenser
m_i	kg	Mass of ice
m_w	kg	Mass of water
p	Pa	Atmospheric air pressure
p_c	Pa	Vapour pressure over condenser
p_{sat}	Pa	Saturation pressure of water
P_{cond}	W	Conductive heat exchange between the condenser surface and the ground
P_{conv}	W	Convective heat exchange
P_{lat}	W	Latent heat released by the condensation or desublimation of water
P_{rad}	W	Heat exchange due to incoming and outgoing radiation
R_{lw}	W m^2	Surface thermal radiation downwards
R_{sw}	W m^2	Surface solar radiation downwards
S_c	m^2	Surface area of condenser
T_a	K	Ambient temperature at 2 m
T_c	K	The temperature of the condenser
U_{10}	m s^{-1}	Horizontal wind speed component at 10 m
V_{10}	m s^{-1}	Horizontal wind speed component at 10 m
WS	m s^{-1}	Prevailing horizontal wind speed at 2 m
z_0	m	Surface roughness
c	mm	Condenser sheet thickness
c		Emissivity of condenser sheet
	Pa K^{-1}	Psychrometric constant
	W m^{-2} k^{-4}	Stefan–Boltzmann constant

S2. Cluster analysis

We used hierarchical agglomerative clustering which consists of four main steps:

1. calculating the distance measured between all entries (data points);
2. merging the two closest entries as a new cluster;
3. recalculating the distance between all entries;
4. repeat steps 2 and 3 until all entries are grouped into distinct groups (i.e., clusters).

Similarity measurement is a critical step in the hierarchical approach which influences the shape of the clusters [62]. The "Euclidean distance" is the most common distance metric and is widely used in atmospheric science. The Euclidean distance between two objects i and j in a two-dimensional data matrix X (here the number of rows represented the number of spatial grid points in the model simulation domain and the number of columns represented the cumulative daily dew yield) is simply the squared difference between them for each of p variables, summed over the variables and k is the number of clusters [63]. This can be written as

$$d_{ij} = \sqrt{\sum_{k=1}^{p}(x_{ik} - x_{jk})^2}$$

The next step is merging the two closest entries (grid points) to form a new cluster based on a linkage criterion. There are some commonly used linkage criteria: single linkage, complete linkage, average distance, and Ward's minimum variance methods, which differ in how the distances between entries are calculated and how the two closest entries are defined [64]. Here, we used Ward's method for further analysis [65], which is the most frequent clustering technique used in climate research and it gives the most consistent clusters [61,66–68]. It calculates the means of all variables (the amount of dew) within each cluster, then calculates the Euclidean distance to the cluster mean of each case, and finally sums across all grid points [69]. In any CA, the optimal number of clusters is an important issue; however, there is no reliable and universally accepted method to decide the number of clusters and it can be a limitation when using CA, because the number of clusters also determines the amount of variance in each group. Therefore, the number of clusters should be selected so that both the number of groups and the variance within the groups are minimal. There are a few suggestions about the optimum number of clusters [69–71]. Although, this information can be used as an indicator to decide the number of clusters a visual check of the result can still help to make the right decision.

JJEES

JJEES (2022) 13 (3): 158-167
ISSN 1995-6681

Jordan Journal of Earth and Environmental Sciences

Land Suitability Evaluation Using FAO Approach and Spatial Analysis for Mujib Basin – Jordan

Abd Al-azeez Hdoush[1], Zeyad Makhamreh[2], Radwan Al-Weshah[3], Deya Qutishat[4]

1- Dr, the Department of Geography, University of Jordan, Amman- 11942 Jordan.
2- Professor, the Department of Geography, University of Jordan, Amman, Jordan.
3- Professor, Department of Civil Engineering, the University of Jordan, Amman, Jordan.
4- Dr, Engineering Department, Arab University College of Technology, Amman Jordan.

Received 20 May 2021; Accepted 14 February 2022

Abstract

The objective of this study is to investigate the suitability of land use for different purposes in the Mujib Basin in Jordan by using the FAO suitability approach. The current land use was assessed by using the supervised classification which was applied on multi-spectral sentinel satellite images to identify the land use types. The potential land use was evaluated based on different utilization types such as field crops, vegetables, tree crops, forests, and rangelands. The suitability degree was derived by using spatial overlay techniques which were applied to specific criteria for each land utilization type. This study shows that the northern parts of the region have the highest suitability degree due to the high rainfall quantities, good soil quality, and gentle slope. It is also highlighted that these areas are embedded by urban expansion which led to a loss of fertile lands. The study shows as well that the highest suitability area in the basin is for field crops and vegetables while the lowest suitability area is for the forest and irrigated crops. It is recommended to orient the urban expansion in the southern part of the basin to preserve existing fertile lands.

Keywords: *FAO approach, Land evaluation, optimal land use, spatial analysis, supervised classification, Jordan.*

1. Introduction

The inappropriate land use practices lead to the degradation of existing land resources. However, utilization of the soil and land resources based on their capabilities can support the resources over a long time without negative environmental impact (Makhamreh, 2019). The process of determining the degree of land suitability for specific land use is closely related to the physical conditions of the region which includes topography, vegetation, climatic characteristics, and soil properties, in addition to the socio-economic factors (FAO 1983).

The Mujib basin is in the southeast of the Dead Sea and it is characterized by arid dry climatic conditions (MWI, 2018). It suffers from water scarcity which is considered a major constraint for agricultural production, and it is subjected to increased desertification risks due to the climate change impacts (RSCN, 2019), in addition to the effect of the population growth and increased urban expansion on the available agricultural land resources (Ministry of Agriculture, 2017). All these factors increased the pressure on the natural resources and decrease the possibilities of achieving sustainable development in the basin.

Land suitability mapping can only be used as an initial step in spatial planning since actual suitability can only be judged based on a detailed investigation (Proske et al, 2005). The geographic information system is one of the important techniques in analyzing the extent of land suitability for urban growth through its reliance on a multi-criteria analysis approach by combining several criteria to form an evaluation indicator. This is an effective method that helps planners and decision-makers analyze all data before reaching a final decision of determining a specific land use type in the presence of competition between different types of uses.

Remote sensing data can be integrated with a geographical information system to perform agricultural land use classification (Makhamreh, 2018), and land suitability for various uses (Abdel Rahman et al, 2016). Also, remote sensing can be used for general suitability analysis (Vazquez et al, 2020), agriculture suitability evaluation (Shalaby et al, 2006; Majumdar, 2020), and land suitability analysis for urban and industrial development and other land use analysis (Ramamurthy et al, 2020). In this context, the high spatial resolution Sentinel-2B images were used to enable accurate classification of land use types, mapping of land cover types (Ngo et. al, 2020), and use classification (Tong et, al, 2020; Brinkhoff et al, 2020) and identification of land use pattern under agricultural landscapes (Abdi, 2019). In Jordan, many studies had been conducted using the FAO approach to investigate the agricultural land use suitability and land vulnerability to land degradation (MOA, 1995; Hatten, 1998, Makhamreh, 2005; Mazahreh, et al., 2018; Makhamreh 2019). Therefore, the objective of this study is to integrate remote sensing techniques and spatial analysis to assess land suitability based on the FAO approach in the Mujjb basin.

* Corresponding author e-mail: azeezpower2012@yahoo.com

2. Materials and Methods

2.1 Study area:

The Mujib basin is located between latitudes 30°39'09", 31°51'37"north, and longitudes 35°32'38", 36°32'58"east. it covers an area of 6585 km^2 which constitutes about 7% of the total area of Jordan as shown in figure 1.

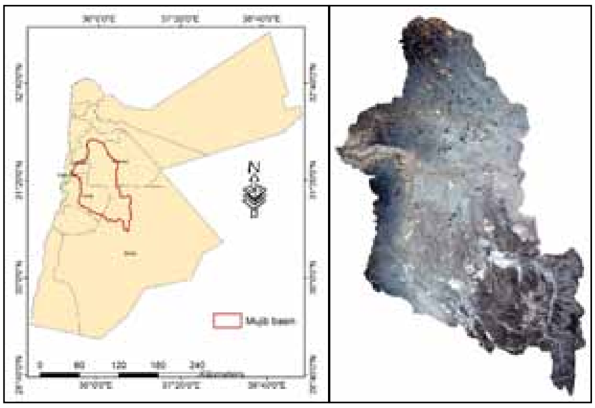

Figure 1. Location map of Mujib basin in Jordan

Mujib basin is a major source of water production for drinking and irrigation purposes in Jordan. It is characterized by semi-arid to arid conditions with low amounts of rainfall, particularly in the eastern parts of the basin. The rainfall begins in October and lasts until May, but most of the precipitations occur during December and January, and annual rainfall decreases from 450 mm in the western parts of the basin to less than 100 mm in the eastern part (DOS, 2018). Hydrologically, the basin comprises two watersheds, one is known as upper Mujib with an area of 4485 km^2 and the other is Wala with an area of 2100 km^2, which is drained by a distributed stream network (Ijam and Al-Tarawneh 2012). More than 80% of the basin is covered by rangeland; bare land and 20% is occupied by agricultural and built-up activities (Abu-Allaban et al. 2015).

2.2 Methodology

Figure 2 shows the methodological approach which uses the optimal land use in the Mujib basin. In this study, a high-resolution Sentinel-2B satellite image for October 2018 with a spatial resolution of 10m was uploaded from European Space Agency (ESA) (website: https://scihub.copernicus.eu) and used in the study. The supervised classification approach was used to derive the map of current land uses for the Mujib basin. The Digital elevation model (DEM) was downloaded from USGS with a spatial resolution of 30m, it was used to derive the slope map and extract the basin hydrological properties. The climate and groundwater data were obtained from the Ministry of Water and Irrigation which include rainfall, well information... etc. The soil data were obtained from the Ministry of Agriculture which include soil texture, soil depth, erosion severity, stones size…etc.

The criteria of different land attributes were classified based on the ranges as indicated in tables (1-7), then a convenient weight was given for each criterion and based on a limitation factor method (FAO, 1983: Makhamreh, 2019). Accordingly, identification of suitability level was identified. Each land use suitability map was classified into four classes according to the land suitability classification method (FAO, 1976). Then the resulting raster maps were derived using the sum overlay weighted analysis to determine the optimal land use map for the Mujib basin.

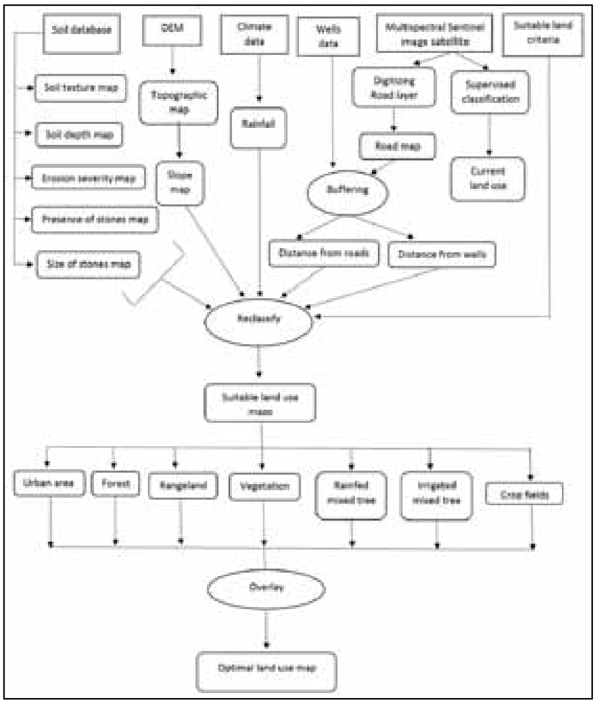

Figure 2. The methodological approach used to derive the optimal land use in the Mujib basin

2.3 Suitability for agricultural land use

The lands use suitability for agricultural production were divided according to the FAO evaluation approach into four categories (FAO, 1976), namely:

i. Highly suitable: lands having no significant limitations and level of production is high with the lowest possible costs.
ii. Moderately suitable: lands having moderate limitations which will reduce production levels but are still physically and economically suitable for agricultural use.
iii. Marginally suitable: lands having a series of limitations that will reduce production levels such that it is economically marginal for agricultural use.
iv. Not suitable: Lands not suitable for agricultural production.

A set of land characteristics has been selected to perform the suitability analysis for determining the optimal suitability degree of each type of agricultural land use. Some criteria are considered limiting factors such as climate, soil depth, and erosion type. However, some other criteria that can be altered or changed by low cost and effort are considered as not-limiting factors such as the presence of stones and road construction. A set of criteria was selected to evaluate suitable sites for different land utilization type in the Mujib basin as shown in Tables (1-7). The list of land utilization types that have been selected to perform the suitability analysis is field crops, irrigated mixed tree crops, rain-fed mixed trees, vegetables, rangelands, forests, and urban expansion. The criteria which have been used to derive the suitability degree for each land utilization type are related mainly to soil climate and topography. The most important criteria are the soil texture, considering soil's main classes: sand, silt, and clay which are important to determine the water holding capacity and soil moisture content, etc. The second factor is soil depth, which is important for plant growth. Soil texture and depth maps are derived using the Inverse distance weighted method based on a set of field samples taken by the Ministry of Agriculture. The slope degree was derived from the DEM raster data, which is a critical factor in determining the suitability class and risk of soil erosion. The rainfall has a direct effect on crop growth and the success of agricultural production while the erosion processes lead to soil losses with reduced depth and fertility and the presence of stones limits the workability and diversity of crop utilization. The weighted average percentage for each criterion is as follows: The soil criteria are 30%, the topography (slope) is 30%, the stones are 5%, and the road accessibility is 5%. The water availability is represented in two criteria either climate for Rainfed agriculture or groundwater for irrigated land use. In both cases, the weighted average percent for climate (rainfall) is 30%, and for groundwater is 30%. Accordingly, the summation of percentages is 100%. The justification for these weighted percentages is that the influence of soil, topography, and water availability on agricultural land use in Jordan is equally contributed and for this reason, it is given the same percentage which is 30% each. Also, we have to recognize that water availability is represented either by climate or groundwater availability according to the land use types. In addition, the 10 % left which is 5% for the stones and road accessibility criteria are important for tillage and ease of accessibility.

Table 1. Land criteria for evaluation of field crops in the Mujib basin

Indicator	Sub-indicator	Unit	Highly suitable	Moderately suitable	Marginally suitable	Not suitable
Soil	Soil texture	Class	Silty, Silty loam	Loam, silty clay	Sandy clay	Sand, clay
	Soil depth	Cm	>75	50-75	25-50	<25
	Erosion severity	Class	Nil	slight	moderate	Severe
Topography	Slope	Degree	<3	3-6	6-12	>12
Climate	Rainfall	Mm	>350	250-350	200-250	<200
Stones	Presence of stones	%	<5	5-20	20-35	>35
	Size of stones	Class	very small	small	moderate	Large
Roads	Distance from roads	M	<1000	10003000-	30005000-	>5000

(Makhamreh, 2005; MOA, 1995; JAZPP, 2000)

Table 2. Land criteria for evaluation of irrigated mixed tree crops in the Mujib basin

Indicator	Sub-indicator	Unit	Highly suitable	Moderately suitable	Marginally suitable	Not suitable
Soil	Soil texture	Class	Silty loam	Loam, silty clay	Sandy clay	Sand, clay
	Soil depth	cm	>90	60-90	30-60	<30
	Erosion severity	Class	nil	slight	moderate	Severe
Topography	Slope	Degree	<5	58-	8-16	>16
Stones	Presence of stones	%	<10	10-20	20-35	>35
	Size of stones	Class	very small	small	moderate	Large
Groundwater	Distance from wells	m	<500	5001000-	10002500-	>2500
Road	Distance from roads	m	<1000	10003000-	30005000-	>5000

(Makhamreh, 2005; MOA, 1995; Hatten, 1998)

Table 3. Land criteria for evaluation of rain-fed mixed trees in the Mujib basin

Indicator	Sub-indicator	Unit	Highly suitable	Moderately suitable	Marginally suitable	Not suitable
Soil	Soil texture	Class	Silty loam	Loam, silty clay	Sandy clay	Sand, clay
	Soil depth	cm	>120	80 – 120	50-80	<50
	Erosion severity	Class	nil	slight	moderate	Severe
Topography	Slope	Degree	<16	16-25	25-40	>40
Climate	Rainfall	mm	>400	300-400	250-300	<250
Stones	Presence of stones	%	<10	10-20	20-35	>35
	Size of stones	Class	very small	small	moderate	Large
Road	Distance from roads	m	<1000	10003000-	30005000-	>5000

(Makhamreh, 2005; MOA, 1995; Hatten, 1998)

Table 4. Land criteria for evaluation of vegetables in the Mujib basin

Indicator	Sub-indicator	Unit	Highly suitable	Moderately suitable	Marginally suitable	Not suitable
Soil	Soil texture	Class	Silty loam	Loam, silty clay	Sandy clay	Sand, clay
	Soil depth	cm	>75	40-75	<40	
	Erosion severity	Class	nil	slight	moderate	Severe
Topography	Slope	Degree	<2	2-4	4-8	>8
Stones	Presence of stones	%	<5	5-20	20-35	>35
	Size of stones	Class	very small	small	moderate	Large
Groundwater	Distance from wells	m	<500	5001000-	10002500-	>2500
Roads	Distance from urban areas	m	<1000	10003000-	30005000-	>5000

(MOA, 1995; JAZPP, 2000)

Table 5. Land criteria for evaluation of rangelands in Mujib Basin

Indicator	Sub-indicator	Unit	Highly suitable	Moderately suitable	Marginally suitable	Not suitable
Soil	Soil texture	Class	Sand, sandy loam	Silty loam, silty	Clay loam, silty clay	Clay
	Soil depth	cm	<25	25-40	>40	
	Erosion severity	Class	slight ، nil	moderate	severe	
Topography	Slope	Degree	<25	25-50	>50	
Climate	Rainfall	mm	>300	200-300	<200	
Stones	Presence of stones	%	<20	20-40	>40	
	Size of stones	Class	very small	small	moderate	Large
Roads	Distance from roads	m	>2500	50002500-	<5000	

(Jafari, 2010; JAZPP, 2000)

Table 6. Land criteria for evaluation of forests in Mujib Basin

Indicator	Sub-indicator	Unit	Highly suitable	Moderately suitable	Marginally suitable	Not suitable
Soil	Soil texture	Class	Silty loam	Loam, silty clay	Sandy clay	Sand, clay
	Soil depth	cm	>90	60-90	30-60	<30
	Erosion severity	Class	nil	slight	moderate	Severe
Topography	Slope	Degree	<15	3015-	>30	
Climate	Rainfall	mm	>400	400-300	200-300	<200
Stones	Presence of stones	%	<5	5-20	20-35	>35
	Size of stones	Class	very small	small	moderate	Large

(MOA, 1995; Hatten, 1998)

Table 7. Land criteria for evaluation of urban expansion in Mujib Basin

Indicator	Sub-indicator	Unit	Highly suitable	Moderately suitable	Marginally suitable	Not suitable
Soil	Soil texture	Class	Sand, Loamy sand	Silty, silty loam	Silty clay	Clay
	Soil depth	cm	<25	25-40	40-50	>50
Topography	Slope	Degree	>15	10-15	5-10	<5
Climate	Rainfall	mm	>350	250-350	<250	
Stones	Presence of stones	%	<5	5-20	20-35	>35
	Size of stones	Class	large	moderate	small	very small
Roads	Distance from services	m	<500	500-1000	1000-2500	>2500
Urban areas	Distance from urban areas	m	<1000	10003000-	30005000-	>5000

(Aburas et al,2017; Park,2011; Hossain et al, 2009)

3. Results and Discussion

The land use suitability for agricultural activities has been investigated. The main agricultural activities which have been tested for their suitability in the study area cultivation of field crops, irrigated vegetables, forests, rangelands, and irrigated and rain-fed mixed trees.

3.1 Current land use

The supervised classification was applied on the multi-spectral Sentinel-2b satellite image to identify the land use types in the study area. The result shows that 12 types of classes were classified and determined, including bare rock, basalt rock, soil, water, crops (olive tree, mixed tree, field crop, and vegetables), urban area, streams valleys, forest, and rangeland.

Figure 3 shows the spatial distribution of the land cover and land use types in the Mujib basin. The results show that the northern part of the basin includes the urban areas and it includes also the existing forest and main agricultural lands within the urban vicinity. The presence of water bodies is limited to the Mujib and Wala dam. It is noticed that the agricultural lands are concentrated in the northern part of the basin and it decreases in density when moving towards the southern and eastern parts of the basin. However, the southern parts of the basin include other types of land cover such as rangeland, bare soil, and rocks. It is noticeable that the cultivation of fruit and olive trees is spreading out in the basin and is characterized by varying densities, and the presence of field crops and vegetables is related to the rainfall and water resources.

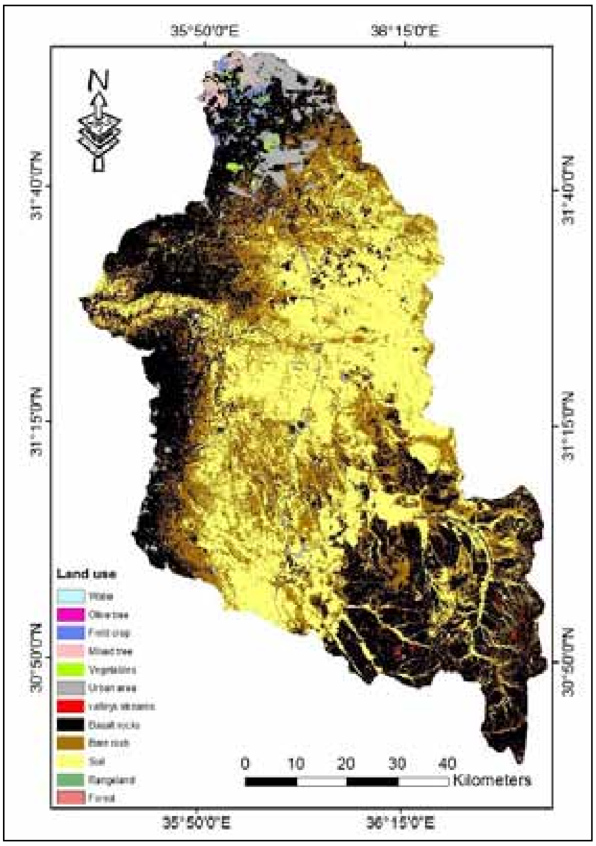

Figure 3. The spatial distribution of land use types in the Mujib basin

Table 8. Land use types in the Mujib basin

Land use	Area (km^2)	Percentage (%)
Water	2.41	0.04
Olive tree	10.36	0.16
Field crops	18.75	0.28
Mixed tree	2.30	0.03
Vegetables	38.61	0.59
Urban area	299.13	4.54
Valleys streams	9.75	0.15
Basalt rocks	1862.12	28.29
Bare rock	2057.58	31.25
Soil	2194.91	33.33
Rangeland	86.54	1.31
Forest	2.14	0.03
Total Area	6584.6	100

Table (8) lists the area and percentage of each land use type in the Mujib basin. The result shows that the bare rock and bare soil are dominating large proportions of the basin, with an area of 6114.6 km^2 which comprises 92.8% of the total area. The agricultural land consists of olive trees, fruit trees, summer vegetables of all kinds, and field crops reaching 1%, with an area of 70 km^2, urban areas occupied 4.5%, rangelands 0.36%, valleys streams 0.15%, water 0.04%, forests 0.03% of the basin area.

3.2 Land use suitability for field crops

Figure 4 shows the suitability map for field crops in the Mujib basin. The highest suitability areas are distributed spatially in the northern and western areas. This is because of the existence of fertile soil with good depth, low slope, and high amount of rainfall. The existing urban area and the Rocky land were masked from the analysis as shown on all suitability maps. The lowest degree of suitability is shown in the southern areas of the basin due to inadequacy of land characteristics such as soil texture, presence of basalt rocks, limited soil depth, high slope degree, and low amounts of precipitation. The total areas highly suitable for cultivation of field crops reach 639 km^2, with a percentage of 27%, moderately suitable areas of 734 km^2 with a percentage of 31% and marginally suitable areas of 804 km^2 with a percentage of 34%, and not suitable areas of 189 km^2 with a percentage of 8% of the total area of Mujib Basin.

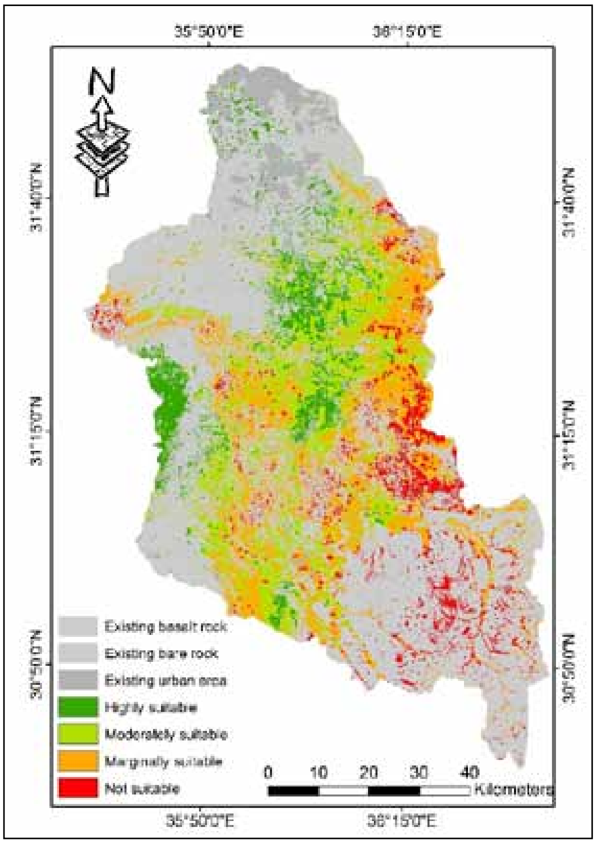

Figure 4. Suitability map of field crops in the Mujib basin

3.3 Land use suitability for irrigated mixed trees

Mixed trees grow well, and their roots stabilize properly when soil depth is deep enough and fertility is of good quality. This help in meeting the water and nutritional needs of the trees.

Figure 5 shows the suitability map of irrigated mixed trees in the Mujib basin. The areas suitable for this type of cultivation are characterized by the presence of fertile soil, deep soil, relatively high slope, and proximity to groundwater wells. The highly suitable areas for cultivation of field crops reach 781 km^2 with a percentage of 33%, and moderate suitable area of 923 km^2 with a percentage of 39% and marginally suitable area of 520 km^2 with a percentage of 22%, and not suitable areas of 142 km^2 with a percentage of 6% from the total area of Mujib Basin.

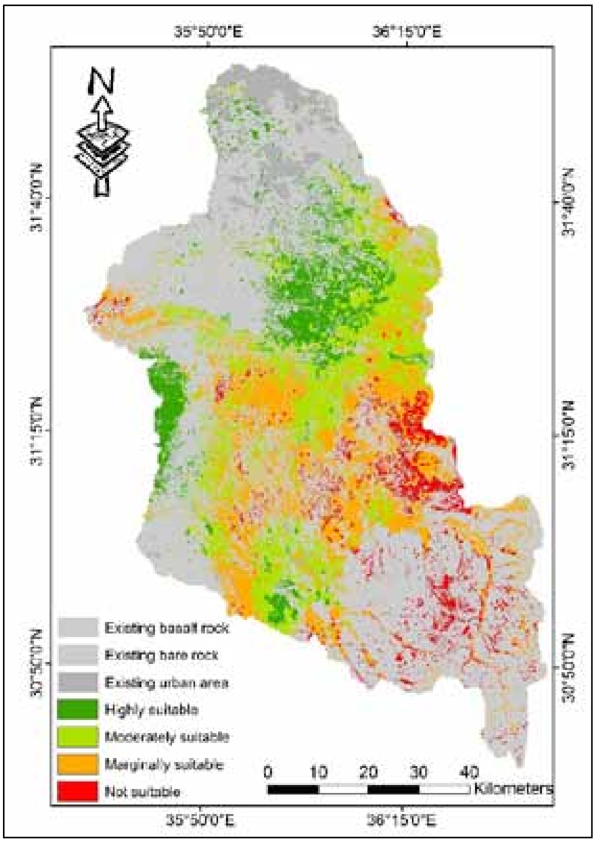

Figure 5. Suitability map of irrigated mixed trees in Mujib basin

3.4 Land use suitability for rainfed mixed trees

Mujib Basin has extremely dry climatic conditions for six successive months starting from May and lasting until October. This drought period has a bad consequence on the growth of tree crops since the amount of available water in soils doesn't meet crop water requirements during the summer months. This leads to low productivity of these trees; therefore, rainfall amounts play a limiting factor for rain-fed tree utilization.

Figure 6 shows the suitability map of the rain-fed mixed trees in Mujib Basin. The suitable sites for this type of rain-fed agriculture are small and confined to the northern and some western regions. These parts are characterized by fertile soil with adequate depths, a high amount of rainfall reaching 300mm, and a low slope. The highly suitable areas for rain-fed mixed trees reach 71 km^2 with a percentage of 3%, and moderate suitable area of 284 km^2 with a percentage of 12% and marginally suitable area of 1278 km^2 with a percentage of 54%, and not suitable areas of 733 km^2 with a percentage of 31% of the total area of Mujib Basin.

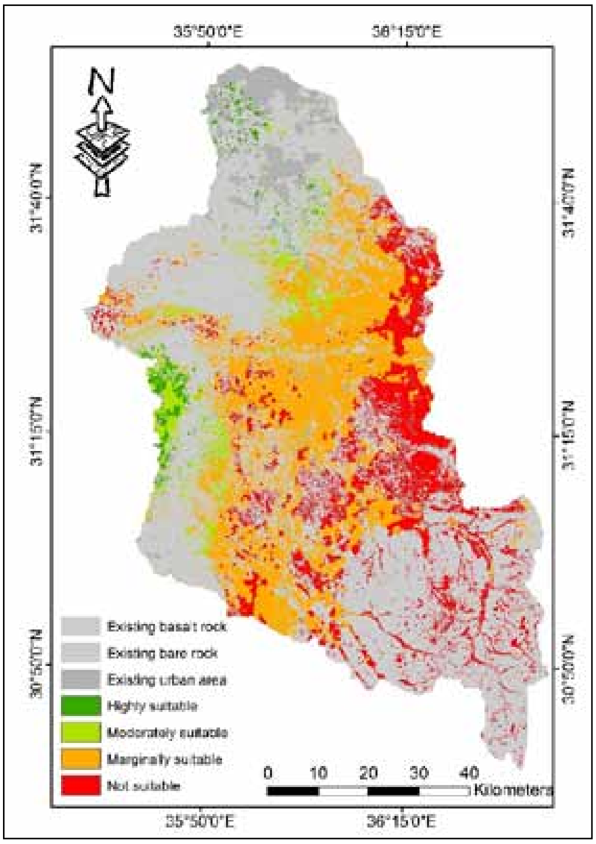

Figure 6. Suitability map of rain-fed mixed trees in the Mujib basin

3.5 Land use suitability for vegetables

Vegetables need a set of specific conditions to grow well and give high productivity. A set of indicators have been chosen that work to achieve these suitable conditions for production.

Figure 7 shows the suitability map for vegetables in the Mujib Basin. The areas suitable for the cultivation of vegetables are concentrated in the northern and western parts of the basin, because of high soil depth, high amount of rainfall, and appropriate soil fertility. The highly suitable area for vegetables reaches 591 km^2 with a percentage of 25%, a moderate suitable area of 805 km^2 with a percentage of 34%, and marginally suitable area of 568 km^2 with a percentage of 24%, and not suitable areas of 402 km^2 with a percentage of 17% of the total area of Mujib Basin.

3.6 Land use suitability for rangelands

Rangelands are characterized by their low requirements and their ability to adapt to a different land and climatic conditions.

Figure 8 shows the possibility of establishing rangelands and expanding existing rangelands in different areas of Mujib Basin. The results show that a highly suitable area reaches 331 km^2 with a percentage of 14%, a moderate suitable area of 1112 km^2 with a percentage of 47%, and marginally suitable area of 710 km^2 with a percentage of 30%, and not suitable area of 213 km^2 with a percentage of 9% of the total area of Mujib Basin.

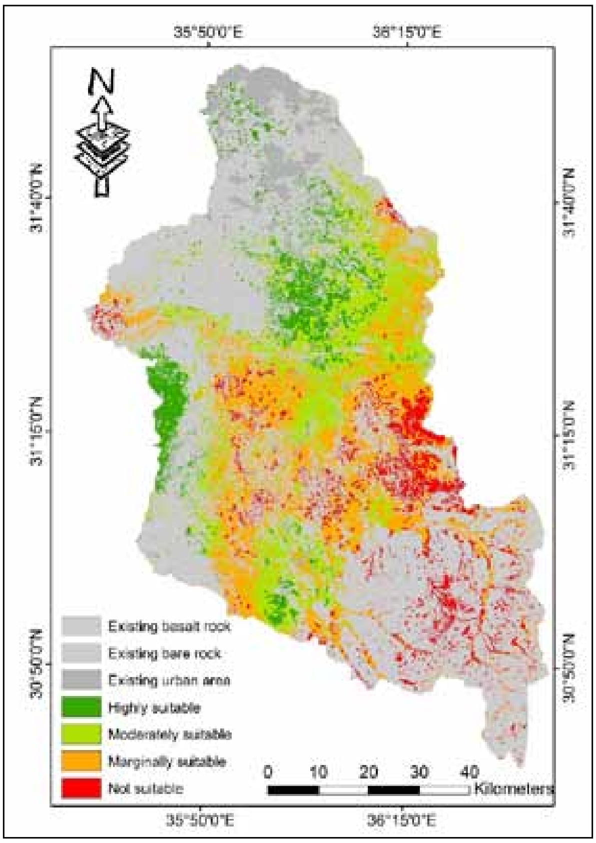

Figure 7. Suitability map of vegetables in the Mujib basin

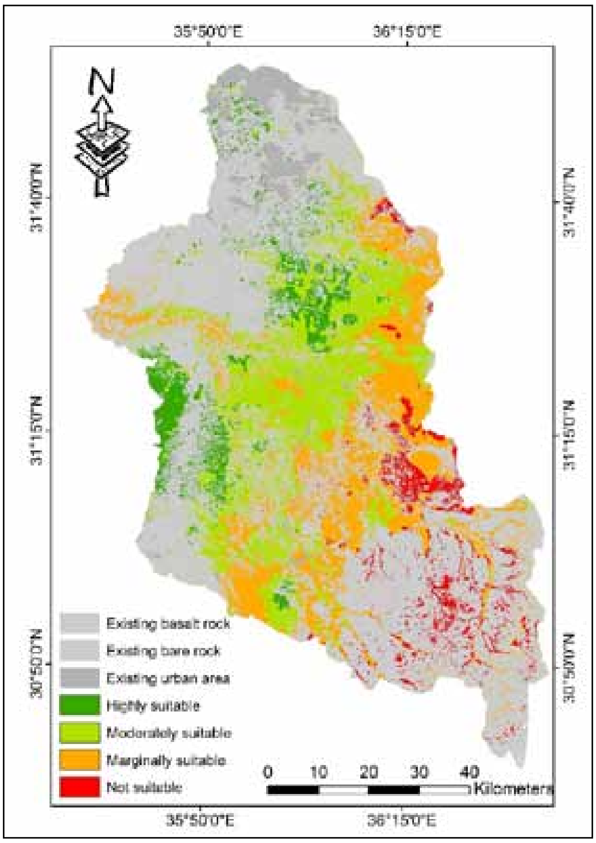

Figure 8. Suitability map for establishment rangelands in the Mujib basin

3.7 Land use suitability for Forests

Forests in Jordan are important for conserving the biodiversity level and contributing to maintaining the environmental balance. Therefore, Forests must be preserved and expanded where possible.

Figure 9 shows the spatial distribution of the suitability map for forests in the Mujib Basin. It is noticed that the suitable areas for forests are small and confined to specific locations in the northern and western areas of the basin. The most limiting factor in growing the forest is the rainfall amounts. The locations of the highly suitable areas for forests reach 95 km^2 with a percentage of 4%, and moderate suitable area of 757 km^2 with a percentage of 32%, and marginally suitable area of 1254 km^2 with a percentage of 53%, and not suitable areas of 260 km^2 with a percentage of 11% from the total area of Mujib Basin

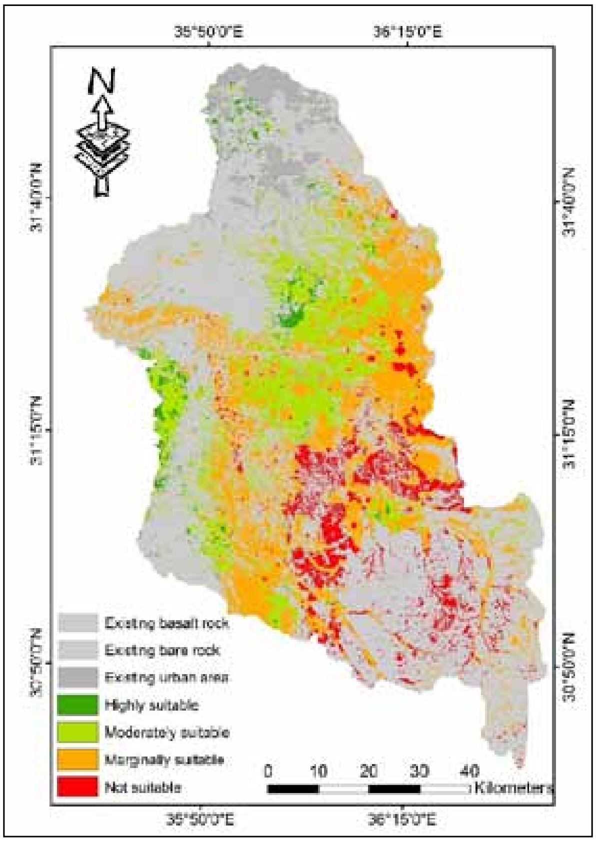

Figure 9. Suitability map for the presence of forests in the Mujib basin

3.8 Land use suitability for urban expansion

One of the most important issues in urban planning and management is determining the directions and locations of appropriate areas for urban expansion. It is vital to maintain the balance between the need to develop residential, commercial, and industrial sectors and the desire to preserve agricultural land ecosystems, biodiversity, and landscapes, especially in a small country like Jordan.

The efforts to achieve sustainable development have faced many challenges mainly related to the costs of agricultural lands due to rapid population growth and urban expansion.

Figure 10 shows the spatial distribution of the suitability map for urban expansion in the Mujib Basin. The highly suitable area for urban areas reaches 548 km^2 with a percentage of 9%, and moderately suitable area of 1382 km^2

with a percentage of 22%, and marginally suitable area of 2156 km^2 with a percentage of 34%, and not suitable areas of 2200 km^2 with a percentage of 35% from the total area of Mujib Basin after excluding the area of urban class area.

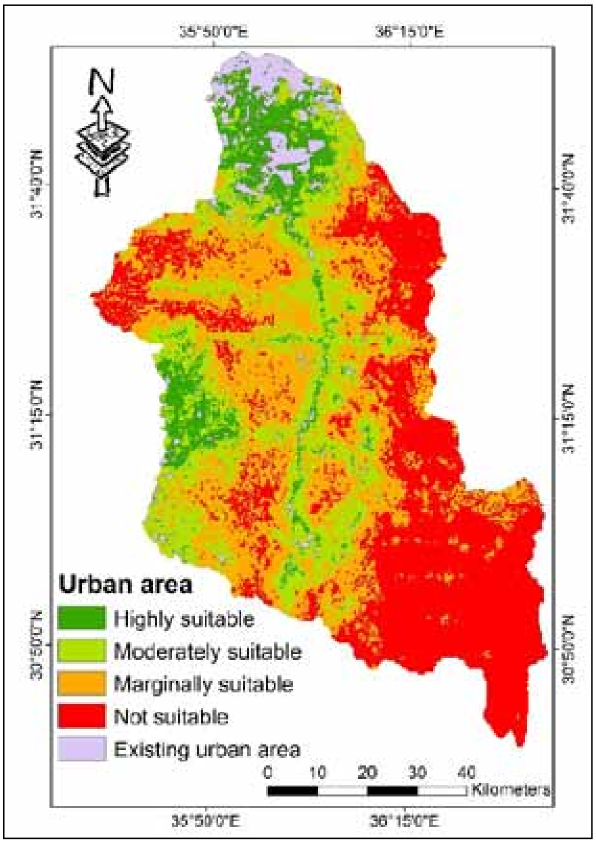

Figure 10. Suitability map for urban expansion in the Mujib basin basin

3.9 Optimal land use in the Mujib basin

The land suitability classification process is defined as an assessment of specific land in terms of its suitability for specific use. Classification of land use according to its capabilities and suitability to plan a specific use is vital to reach optimal use. The importance of planning for the best use of the land is to achieve objectives of sustainability, increase land productivity and reach food security. It also conserves the resources from degradation and deterioration, especially with increasing population pressure and climatic changes effects. After performing the suitability analysis for different land utilization types such as vegetables, field crops, irrigated and rain-fed mixed trees, rangeland, forests, and urban expansion, a map of optimal use was derived for the Mujib Basin.

Figure 11 shows the optimal land use map for the Mujib basin. The final map shows there is a capability that some land units could be used for more than one land use, which provides a good basis to choose the most appropriate land use for the basin.

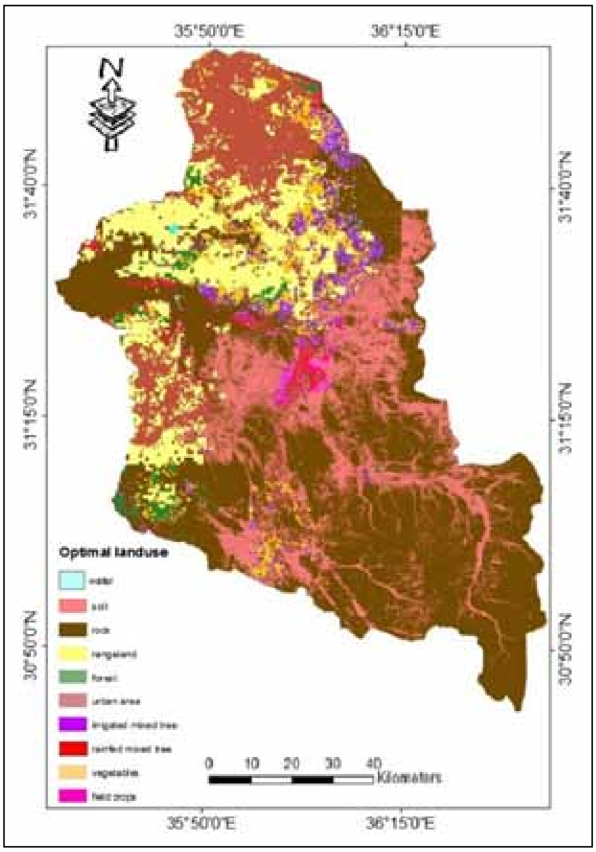

Figure 11. Optimal land use in the Mujib basin

4. Conclusions

Based on this analysis the following conclusions can be made:

i- Land suitability evaluation is employed to determine the appropriateness of land for specific use. It is a complex and multidisciplinary process, involving knowledge of the land's natural characteristics, including land use and land cover, which requires the integration of a wide range of data to develop a spatial analyzing system to determine the land suitability for each use.

ii- Suitability maps have been derived into their classes based on the following main land characteristics which are slope degree, slope depth, rainfall amounts, and existing land use map.

iii- The results of the analysis for each land utilization type are shown below:

- Land use suitability for the cultivation of vegetables showed that the areas of suitability classes are 25% for highly suitable areas, 34% for moderately suitable areas, 24% for marginally suitable areas, and 17% for not suitable areas.
- Land use suitability for field crops showed that the areas of suitability classes are 27% for highly suitable areas, 31% for moderately suitable areas, 34% for marginally suitable areas, and 8% for not suitable areas.
- Land use suitability for rain-fed mixed trees showed that the areas of suitability classes are 3% for highly suitable areas, 12% for moderately suitable areas, 54% for marginally suitable areas,

and 31% for not suitable areas.

- Land use suitability for irrigated mixed trees showed that the areas of suitability classes are 33% for highly suitable areas, 39% for moderately suitable areas, 22% for marginally suitable areas, and 6% for not suitable areas.
- Land use suitability for rangelands showed that the areas of suitability classes are 14% for highly suitable areas, 47% for moderately suitable areas, 30% for marginally suitable areas, and 9% for not suitable areas.
- Land use suitability for forests showed that the areas of suitability classes are, 4% for highly suitable areas, 32% for moderately suitable areas, 53% for marginally suitable areas, and 11% for not suitable areas.
- Finally, Land use suitability for urban expansion showed that the areas of suitability classes are9% for highly suitable areas, 22% for moderately suitable areas, 34% for marginally suitable areas, and 35% for not suitable areas.
- The current land use was obtained with a high level of detail by applying a supervised classification on a high-resolution multi-spectral Sentinel satellite image. Then, the optimal land use map was compared with the current land use map and the results showed that there is an acceptable similarity and compatibility between them.

  A disadvantage of this method might be in different opinions of experts in giving the appropriate weights to the criteria and in determining the priority of land characteristics, which is a complex process and faces many conflicts between the different sectors of economic, social, and environmental issues, especially for limited land resources regions such as Jordan, which must be utilized carefully to maintain the food security and minimize the damage to the environment.

5. Acknowledgements

The authors acknowledge the ESA for allowing the satellite images for analysis.

References

Abdel Rahman, M. A., Natarajan, A., and Hegde, R. (2016). Assessment of land suitability and capability by integrating remote sensing and GIS for agriculture in Chamarajanagar district, Karnataka, India. The Egyptian Journal of Remote Sensing and Space Science, 19 (1), 125141.

Abdi, A. M. (2019). Land cover and land use classification performance of machine learning algorithms in a boreal landscape using Sentinel2 data. GIScience and Remote Sensing, 120.

Abu-Allaban, M., El Naqa, A., Jaber, M., and Hammouri, N. (2015). Water scarcity impact of climate change in semiarid regions: a case study in Mujib basin, Jordan. Arabian Journal of Geosciences, 8(2), 951959.

Aburas, M. M., Abdullah, S. H., Ramli, M. F., and Asha'ari, Z. H. (2017). Land suitability analysis of urban growth in Seremban Malaysia, using GIS based analytical hierarchy process. Procedia Engineering, 198, 11281136.

Brinkhoff, J., Vardanega, J., and Robson, A. J. (2020). Land Cover Classification of Nine Perennial Crops Using Sentinel1 and2 Data. Remote Sensing, 12(1), 96.

DOS (Department of Statistics), (2018), Jordan in figure, Amman, Jordan. http://dosweb.dos.gov.jo/DataBank/JordanInFigures/2018.pdf . (May. 12,2021).

FAO (Food and Agriculture Organization). (1976), a framework for land evaluation, Rome, Italy.

FAO (Food and Agriculture Organization). (1983), Guidelines: Land evaluation for rainfed agriculture. FAO Soils Bulletin. No. 52, Rome.

Hatten, C. J (1998), improvement of agriculture productivity in arid and semiarid zones of Jordan, visit report of land resources specialist, school of agriculture food and environment, Cranfield University, UK.

Hossain, M. S., Chowdhury, S. R., Das, N. G., Sharifuzzaman, S. M., and Sultana, A. (2009). Integration of GIS and multicriteria decision analysis for urban aquaculture development in Bangladesh. Landscape and Urban Planning, 90(34), 119133.

Jafari, S., (2010). Land Suitability Analysis using Multi-Attribute Decision Making Approach. International journal of environmental science and development, 1(5), 441.

JAZPP (2000), improvement of agriculture productivity in arid and semiarid zones of Jordan: annual report, SEM/O3/628/021. University of Jordan, Amman, Jordan.

Ijam, A., and Tarawneh, E. (2012). Assessing of Sediment Yield for Wala Dam Catchment Area in Jordan. European Water, 38, 4358.

Majumdar, S. (2020). Land Suitability Analysis for Periurban Agriculture Using Multicriteria Decision Analysis Model and Crop Condition Monitoring Methods: A Case Study of Kolkata Metropolitan Area. In IoT and Analytics for Agriculture (pp. 165185). Springer, Singapore.

Makhamreh, Z. (2005). Optical remote sensing and Geo-spatial analysis for assessing and monitoring of land degradation in northern Jordan. Remote Sensing Department, University of Trier, Germany. (Published Ph.D. Thesis).

Makhamreh, Z., M. (2018). Derivation of vegetation density and land-use type pattern in mountain regions of Jordan using multi-seasonal SPOT images: Environmental Earth Sciences 77: 384. https://doi.org/10.1007/s12665-018-7534-z.

Makhamreh, Z. M. (2019). Land degradation vulnerability assessment based on land use changes and FAO suitability analysis in Jordan. Spanish Journal of Soil Science, 9(2).

Mazahreh, S., Bsoul, M., Ziadat, F., and Abu Hamoor, D (2018). Participatory land suitability analysis to identify the optimum land use for a Mountainous Watershed in Jordan. Journal of Engineering Research and Application, Vol. 8, Issue 7 (Part -II), 41-55.

Ministry of Agriculture. (2017), annual statistical report, Amman, Jordan. http://moa.gov.jo/Portals/2017/pdf (May. 12,2021).

MOA (1995). The Soil of Jordan. Report of the National Soil Map and Land Use project, Undertaken by Ministry of agriculture, hunting technical services Ltd. And European commissions. Level one, level two, level three, and JOSCIS manual.

MWI (Ministry of Water and Irrigation). (2018), Jordanian Water Sector, Facts, and numbers, Amman, Jordan. http://waterjo.mwi.gov.jo/Ar/NewsCenter/Pages.aspx (September. 23,2020).

Ngo, K. D., Lechner, A. M., and Vu, T. T. (2020). Land cover mapping of the Mekong Delta to support natural resource management with multitemporal Sentinel1A synthetic aperture radar imagery. Remote Sensing Applications: Society and Environment, 17, 100272.

Park, S (2011), Prediction and comparison of urban growth by land suitability index mapping using GIS and RS in South Korea. Landscape and urban planning, 99(2), 104114.

Proske H, Vlcko J, Rosenbaum MS, Dorn M, Culshaw M, and Marker B (2005) Special-purpose mapping for waste disposal sites. Bull Eng Geol Environ 64(1):1–54.

Ramamurthy, V., Challa, O., Naidu, L. G. K., Kumar, K. A., Singh, S. K., Mamatha, D., and Mishra, B. B. (2020). Land Evaluation and Land Use Planning. In The Soils of India (pp. 191214). Springer, Cham.

RSCN (Royal Society for the Conservation of Nature). (2019), sponsorship opportunities for nature protection programs, Amman, Jordan. https://www.rscn.org.jo/sites/default/files/basic_page_files/RSCN Sponsorship Menu2019-EnglishVersion.pdf (May. 12,2021).

Shalaby, A., Ouma, Y. O., and Tateishi, R. (2006). Land suitability assessment for perennial crops using remote sensing and Geographic Information Systems: A case study in northwestern Egypt, Archives of Agronomy and Soil Science, 52(3), 243261.

Tong, X. Y., Xia, G. S., Lu, Q., Shen, H., Li, S., You, S., and Zhang, L. (2020). Landcover classification with high-resolution remote sensing images using transferable deep models. Remote Sensing of Environment, 237, 111322.

Vazquez-Quintero, G., Prieto-Amparan, J. A., Pinedo-Alvarez, A., Valles-Aragon, M. C., Morales-Nieto, C. R., and Villarreal-Guerrero, F. (2020). GIS-based multicriteria evaluation of land suitability for grasslands conservation in Chihuahua, Mexico. Sustainability, 12(1), 185.

JJEES

JJEES (2022) 13 (3): 168-176
ISSN 1995-6681

Jordan Journal of Earth and Environmental Sciences

The Aquatic Corrosion of International Simple Glass: Corrosion-Rate Trackers and Surface Alteration Layer Evolution at Varying Conditions

Ali Al Dabbas[1,2], Katalin Kopecskó[1*], Rachael Abu-Halimeh[2]

[1]Department of Engineering Geology and Geotechnics, Faculty of Civil Engineering, Budapest University of Technology and Economics BME, Hungary, Műegyetem rakpart 3, Budapest, Hungary,
[2]Jordan Atomic Energy Commission JAEC, Surficial Ores Processing Laboratories, Shafa Badran, Amman, Jordan

Received 1st September 2021; Accepted 3rd March 2022

Abstract

The corrosion of the nuclear-borosilicate matrix in an anaerobic environment is delayed due to the formation of an amorphous gel layer on its glassy interface. The formation of this gel occurs at the saturation of silicic acid. In addition to the in-situ formed iron corrosion products, the metamorphic forms can also delay the gel formation, accelerating the nuclear glass corrosion. Saturated and pure water experimental models with and without Ankerite were incorporated into the standard materials characterization center (MCC) leach test for radioactive waste types at 90 °C. However, a synonymous test was allocated at 25 °C and was conducted among the reaction models. All the batch experiments on International Simple Glass (ISG)were performed at an initial pH of 6.3.

Various techniques for tracking the ISG corrosion rate have been employed and proven to be effective. As a result, the normalized weight loss of Na and Si were efficient trackers for all of the experimental systems/models; the higher the Si concentration, the lower the saturation, and vice versa. Furthermore, Na concentrations were proven to be an effective representation of the ISG corrosion rate, as they were able to produce sound ISG corrosion rate values across the experimental curing durations and circumstances when utilizing a particular conversion factor. Even at saturation, a higher reaction temperature was found to be an effective factor that enhances the ISG corrosion rate.

Keywords: *Ankerite, High-Level nuclear Waste (HLW), International Simple Glass (ISG), Borosilicate glass corrosion rate, Surface AlterationLayer (SAL).*

1. Introduction

Vitrification is considered to be the preferred method for the conditioning and immobilization of High-Level radioactive Waste (HLW) in geological formation repositories before its final disposal. Glass is stable to numerous corrosive parameters, but its durability may be affected over long periods due to essential extrinsic parameters, such as temperature, chemicals, and solvents. Vitrification entails HLW being incorporated in borosilicate glass, making it an inseparable part of the glass matrix, and eventually being discharged into stainless steel containers. Finally, non-recoverable fission products and actinides are trapped in a water-insoluble glass structure, viable for hundreds of millennia [1 – 4].

During this long storage, the direct contact with groundwater reduces the thermodynamic stability of the borosilicate glass turning it into its key elements by dissolution [5, 6]. The nuclear glass matrix behaves as standard glass would in water. Owing to the spread of water across the glass network, which is then accompanied by an ion interaction between the positive protons found in the underlying aqueous solution and alkaline metals within the glass, corrosion of the glass will occur in the saturated silica atmosphere, which sometimes contributes to the development of an amorphous gel coating on the surface; known as the Surface Alteration Layer (SAL) [7 – 10]. Hydration and interdiffusion in the glassy matrix initiate glass dissolution under static conditions. The silicate network is hydrolyzed to form a hydrated glass layer, and the glass dissolves quickly in diluted form; this is the initial phase. The hydrolysis rate slows as the solution becomes silica saturated and a passivating gel forms. Then, secondary phases develop on their surface, slowing the glass alteration rate to a new phase called the residual rate [11 – 14].

The gel is a porous silica-rich hydrated surface layer, generated by the precipitation of silica after it dissolves from the glass network [15 – 17]. The theory behind the gel layer being a glass protection layer is: that it tends to restrict diffusion exchanges between the glass surface and the surrounding aqueous solution, which prevents a thermodynamic equilibrium between the hydrated glass and the bulk solution from being achieved [18].

Ankerite is a complex carbonate mineral ($Ca(Fe, Mg, Mn)(CO_3)_2$), it is either a sedimentary iron corrosion product or a naturally metamorphosed material by-product from the corrosion of the waste steel and heaped HLW containers [19, 20]. Iron-bearing minerals in the repository platform may decelerate silicate saturation, maintain the process of glass dissolution, and affect the formation of several phases containing iron [21]. Iron minerals adversely affect the

* Corresponding author e-mail: ali.al.dabbas@emk.bme.hu

amount of saturation of silicates to reduce or incorporate the porosity of the gel. Therefore, many research studies found them to be prevailing parameters of the glass alteration and prioritized them [22 - 30]. However, during the hydration phase of dissolution, the rapid incorporation of iron would clog the external gel porosity to the gel/Si saturated solution and reduce the alteration rate to minimal values [26, 31, 32].

In this paper, the function of Ankerite on the borosilicate corrosion in saturated and pure-water situations has been studied intensively. Ina previously published study [33], the favorable function of Ankerite on Si sorption under saturated silica conditions has been demonstrated. The current study also investigated the corrosion rate trackers of the aquatic corrosion of ISG and the SAL evolution at varying dissolution conditions; with and without Ankerite.

2. Materials and Sample Preparation

Ankerite

This research employed an Ankerite-rich geological sample from Rudabánya, Hungary. Using a tungsten carbide electrical mortar grinder, the sample was crushed into a powder. Then after, the powder was sieved, and the fraction with a grain size of 75–125 μm was collected.

Afterward, the powder was washed with distilled water and then ethanol before being dried overnight at 105 °C. The Brunauer-Emmett-Teller BET-N_2 method was used to calculate the Specific Surface Area, $SSA_{Ankerite} = 225\ cm^2.g^{-1}$.

A prior investigation on the same material [33 - 35] used Inductively Coupled Plasma - Optical Emission Spectrometry (ICP-OES) to characterize its composition, then identified it using X-Ray Powder Diffraction and elemental analysis (XRD), Figure 1.

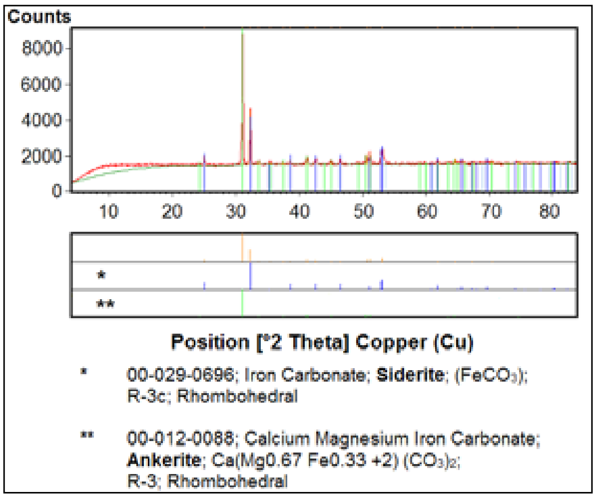

Figure 1. The XRD pattern of a natural Ankerite sample, collected from the mining area in Rudabánya, Hungary [35]

ISG

ISG is often used for testing the durability of HLW glass [36 – 41]. The ISG is a simple glass derived from its composition that aims to be an international standard. It is 6-oxide borosilicate glass with the same elemental ratios as SON68 (an inactive French R7T7 glass reference), and it is widely employed in nuclear research [1].

A 5-inch diamond saw blade was used to cut the ISG ingot into 10*10*2 mm plates (coupons). An oil-based diamond suspension spray and polishing equipment were used to polish each ISG coupon. The Surface Area of each coupon was measured geometrically ($SA=3.1cm^2$), and the BET-N_2 technique was used to determine the additional surface roughness factor of 1.5.

The ISG powder was made by crushing raw ISG monoliths using a tungsten carbide ball mill device, and then sieving and collecting the fraction with a grain size < 45 μm. The powder was cleaned of fine aerosol particles by being soaked in ethanol via vacuum-driven filtration at 0.45 μm and then dried overnight at 100 °C. Equation (1) [26] was used to compute $SSA_{ISG}=2,467\ cm^2.g^{-1}$ geometrically.

$$SSA_{ISG} = \frac{\rho}{3R} \quad \text{.......} \quad (1)$$

where; ρ is the density in $g.m^{-3}$ (= 2.500 $g.cm^{-3}$) and R=10.4 μm is the average radius of a particle, which was determined by a CILAS 1190 LD Particle Size Analyser.

For this initiative, ISG samples were provided by the Savannah River National Laboratory (SRNL) in the United States. The molecular and mass oxides that make up this inactive analog glass are provided in a previous study, Table (1) [35].

Table 1. Common oxide ratios of ISG [35]

Method	Oxide	Mass (%)
ICP-OES	SiO_2	55. 6 ± 5.6
	B_2O_3	16.0 ± 1.6
	Na_2O	13.2 ± 5.1
	Al_2O_3	5.50 ± 1.1
	CaO	5.53 ± 0.6
	ZrO_2	2.98 ± 0.2
ICP-MS	Impurities	~ 0.79 ±0.1
TOTAL (%)		~ 99.6 ± 7.8

3. Methodology

The standard Materials Characterization Center (MCC) leach test for nuclear waste is one of the most regularly used static leach tests [42]. To simulate the saturated and pure-water systems, low and high Surface area to Volume ratios ($S/V_{Coupon}=0.13\ cm^{-1}$ and $S/V_{Powder}=20.55\ cm^{-1}$) were considered by applying the MCC-1 and MCC-3 tests, respectively [7].

Polytetrafluoroethylene (PTFE) containers with a capacity of 30 mL were placed as seven (7) groups in a drying chamber for 3 days, 7 days, 14 days, 28 days, 90 days, 180 days, and 270 days to react. A temperature of 90±2 °C was chosen to expedite the reaction. After adding the ISG and Ankerite to the containers, 24 mL of ASTM Type-I water (with conductivity and resistivity of 0.055 $μS.cm^{-1}$ 18.2 MΩ.cm, respectively) was added. All experimental containers were sealed under argon (Purity = 99.999 %) atmosphere to prevent oxidation reactions, and by adding 10 μL of 0.08 ($g.L^{-1}$) NaOH, the pH was adjusted to 6.3±0.2.

For each ISG+Ankerite experiment the reference trials: (i) with only ISG and (ii) with only Ankerite, were considered. The heated samples were cooled to ambient temperature after the required leaching time, and all samples were centrifuged for 10 minutes at 4,500 rpm. At 25 °C, the pH of the leaching solution was determined immediately for all samples. After filtering the leaching solution using a Millipore filter (0.45 m pore size), 15 milliliters of the filtrate were collected for Inductively Coupled Plasma Mass Spectrometry (ICP-MS) analysis. A special abbreviation has been designed for each trial, according to Table (2).

Table 2. Abbreviations of various trials

Abbreviation	Description
RGC90	Reference Glass Coupon, reaction at 90 °C
RGP90	Reference Glass Powder, reaction at 90 °C
RAP90	Reference Ankerite Powder, reaction at 90 °C
GC90	Ankerite + Glass Coupon, reaction at 90 °C
GP90	Ankerite + Glass Powder, reaction at 90 °C
RGP25	Reference Glass Powder, reaction at 25 °C
RAP25	Reference Ankerite Powder, reaction at 25 °C
GP25	Ankerite + Glass Powder, reaction at 25 °C

By subtracting the identical element concentrations in the reference RAP, the correct element concentrations in the (Ankerite+ Glass) systems were calculated.

4. Results

4.1 Weight Loss (WL) Calculations

To achieve sound readings, the weight loss tests were performed at room temperature. Figure (2) displays the coupons, which reacted in presence of Ankerite, after leaching and provides a bar diagram showing the percentage reduction of weight. The powdered ISG samples developed higher weight loss values than the ISG coupon samples as a consequence of the higher interdiffusion due to their higher S/V ratios. Also, the dissolved silica was shown to re-precipitate on the ISG coupon surface and be incorporated into an amorphous gel layer, contributing to the final mass of the coupon and concluding in a lower recorded WL value. Consequently, weight loss estimates do not reflect the glass corrosion's definite value at the early stages of leaching [7]. In contrast, these measurements are of particular significance when conducting glass dissolution experiments.

Regarding the GC90 system, containing Ankerite, Figure (2) shows that on day 3 the weight loss was at its minimum value, it then continued to double to reach its maximum value on day 270; signaling that the Ankerite incorporation into the SAL decreases gradually over time while the coating layer becomes crystallized in nano-scale [43]. The (evolution/dissolution) mechanism [44, 45] on the alteration layer poses an additional reason for removing the adhered Ankerite, recalling that even when the coupons were washed with ASTM Type-I water for 10 seconds and then dried in the vacuum oven at 50 °C for 24 hours, the red color of the altered coupons is more obvious at low reaction times, as observed in Figure (2).

The ISG reference samples, however, initially exhibited unfavorable behavior, and the loss value reached a maximum, during the first month of reaction, on day 14. It then declined and remained constant. As mentioned earlier, during glass corrosion, many separate steps occur, including reactions, diffusion, and precipitation. During the reaction, the rate determination phase can vary and rely heavily on the test parameters.

The WL analysis provided sufficient primary insight into the ISG corrosion rates. In comparison to Figure (3) later in this article, the WL per unit area of the glass interface might be regarded as an acceptable indication, capable of yielding the same forecast on the subsequent analysis. However, since tracking the boron (B) concentrations in the typical technique for measuring the precise corrosion rate, this method is insufficient. One observation derived from Figure (2) is that the SAL transforms over time from a foam/colloidal structure to a crystal form, this prevents the Ankerite from cohering to the SAL surface.

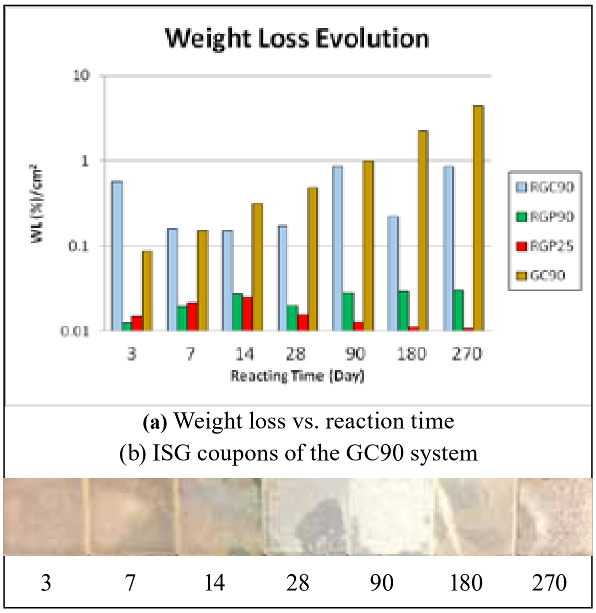

Figure 2. The weight loss per unit area of altered ISG in all systems and the evidence of the formation of amorphous silica in the first hours of a reaction by showing the Ankerite cohering on the SAL of ISG coupon. (a) Chart showing the ISG-weight loss percentage per unit surface area as an indication of the ISG corrosion (b) ISG coupons of the GC90 system after curing. Over time, Ankerite was detaching with (evolution/dissolution) of the SAL

4.2 ISG Corrosion Tracers

The Normalized weight Loss () was calculated using Equation (2) [7] for the main elements resulting from the dissolution of the glass samples (Na, B, Si, Ca, Al); concentrations of Zr were not sufficient for such calculations.

$$NL_i = \frac{m_i}{f_i.SA} \quad \text{(2)}$$

where; : the mass of element i in the leachate, fi: mass fraction of element i in the unleached solid (unitless), and SA: sample geometric Surface Area (m^2).

Boron is commonly used to monitor glass corrosion rates (CR_{ISG}) [7, 46]. Figure (3) shows the corrosion rates for all the experimental systems. The correct boron concentrations were determined in the ISG-Ankerite (GC90, GP90, and GP25) systems by excluding the apparent boron concentrations in the reference (Ankerite-water) systems (RAP90, RAP25) with taking into account the surface area to volume value in each vessel. The ISG corrosion rate in Figure (3)was calculated by applying the following Equations (3 and 4), which were used by Neill et al. [29] for ISG:

$$CR_{ISG} = \frac{d\left(E_{th(B)}\right)}{dt} \quad \text{...} (3)$$

where; CR_{ISG} is ISG corrosion rate ($nm.d^{-1}$) and is the equivalent thickness (altered ISG) of Boron (nm) that can be calculated from the following relation:

$$E_{th(i)} = \frac{NL_i}{\rho_{ISG}} \quad \text{...} (4)$$

where: is the density of ISG (2.5 $g.cm^{-3}$).

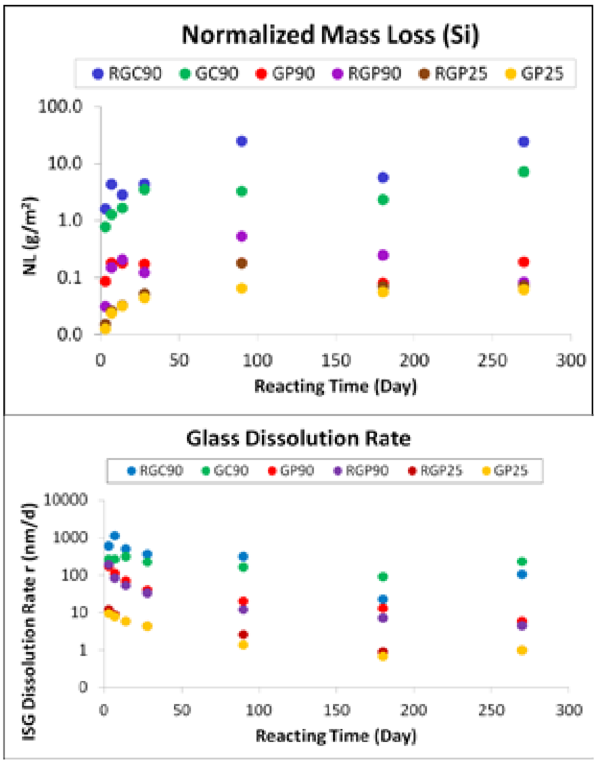

Figure 3. Silicon normalized loss NL_{Si} and ISG dissolution rate CR_{ISG} in all systems

It is apparent that the temperature and S/V ratio have opposite effects on both the NL_{Si} and CR_{ISG}; this is seen to be indirect with S/V, although the presence of Ankerite slightly lowered their values in GC90 and the contrary occurred in GP90. The NL_{Si} increased with time, but the CR_{ISG} was found to decrease with time. (Each point = single experiment)

4.2.1 Silicon Concentrations

In the saturated system, the silicon normalized weight loss (NL_{Si}) values have been seen as the dominant factor of CR_{ISG}, as described in Figure (3). Compared to the ISG-coupon (pure-water) systems, the ISG-powdered (saturated) systems generated significantly lower NL_{Si} results. This implies that once the concentration of soluble silica species in the aqueous phase reaches saturation, no more glass dissolution would occur, and the saturation of amorphous silica may not represent the thermodynamic saturation of the glass network. [15]. The analysis also revealed that the S/V effect is significantly greater than the effect of other parameters (i.e., temperature); however, the NL_{Si} results revealed that the GP90 model was up to ten (10) orders more effective than the GP25 model. It is worth mentioning that Ankerite reference tests have been prepared and leached in the same conditions: pH, time, and temperature for both the ISG/Ankerite and the water systems. The findings of the blank sample were used to promote the calculation of NL_{Si} only arising from ISG corrosion.

The inversely proportional relationship seen in Figure (3) between the period of leaching and the CR_{ISG} may be due to normalized weight transmission through layers formed as glass corrodes or increased concentrations of glass corrosion in the solution. This reduces the driving force of mass transfer, which slows down each reaction that releases these components. In this context, except for Si, the overall normalized weight loss of the main ISG corrosion products (B, Ca, Al, Na) are attached in the Appendix.

The involvement of Ankerite in the ISG coupon 90 °C (GC90) and the ISG powder 25 °C (GP25) systems has lowered the (NL_{Si}) and (CR_{ISG}) values up to 90 days of reaction; the opposite occurred, however, from day 180 of reaction. On day 7 of the reaction, the GP90 glass powder system was the same, suggesting that the higher S/V was forecast to increase the Ankerite impact on ISG dissolution. The previous results show that the rapid precipitation of silicate compounds can cause an increase in ISG dissolution at higher S/V and temperature values with Ankerite presence. However, the concentrations of Ca in ISG powder systems RGP90, and GP90 were below the detection limit (BDL) during the reaction cycle, which may mean that Ca was preferably retained at higher S/V and temperature (Appendix) instead of Na [47], or that gel porosity was possibly clogged [48]. Boron levels have been constantly demonstrated to be higher than silicon levels (Figure 3) typically related to the dissolution of borosilicate glass [7].

In presence of sorptive compounds (i.e., iron corrosion products which are represented in this research by Ankerite) silicon concentrations are generally not consistent with ISG corrosion's behavior due to silica sorption reactions and possible precipitation [7]. This may be justified by Si precipitation (i.e., Mg-Si); nevertheless, it is worth mentioning here that in prior research, Ankerite has been shown to initiate late (at day 90) Mg-Si precipitation and early Si sorption.[33, 35].

4.2.2 Sodium Concentrations

The current experiment has also been used to assess if sodium for the given corrosion stage may be regarded as a tracer factor for the rate of glass corrosion. In Figure (4) extracted from Table (3), the average CR_{ISG} contribution for the whole experiment is summarized and the effect of Ankerite on various systems can be noticed. In particular, Ankerite raised the CR_{ISG} to higher values in the ISG coupon system (i.e., on days 180, and 270). But the overall CR_{ISG} average over the whole treatment period was different. Both stress the above-mentioned assumption about sodium. Therefore, these observations can be stated:

In terms of behavior, the values of NL_{Na} and CR_{ISG} were equivalent.

In ISG powder systems, Ankerite did not affect the CR_{ISG}. (That is, the average value of RGP90 and GP90, as well as the average value of RGP25 and GP25, were nearly identical).

Regardless of the presence of Ankerite, the CR_{ISG} average of the ISG powdered systems at 25 °C was the lowest of all systems, while the CR_{ISG} of the 90 °C powders was higher by 10 orders.

At 90 °C, the CR_{ISG} averages of the ISG coupon systems were the highest of all systems. In addition, the CR_{ISG} was decreased by 10 orders when moving from RGP90 to RGC90 and was decreased by 5 orders when moving from GP90 to GC90.

As a result of the above observation, Ankerite cut the CR_{ISG} in ISG coupon systems in half. (i.e., CR_{ISG} in RGC90 equals 2*CR_{ISG} in GC90).

Table 3. Average normalized loss and average glass corrosion rates at day 270

System	Ankerite Presence	NL_{Na} ($g.m^{-2}.d^{-1}$)	CR_{ISG} ($nm.d^{-1}$)
RGC90	-	1.154 ± 0.192	440.5 ± 17.6
RGP90	-	0.114 ± 0.020	55.98 ± 2.34
RGP25	-	0.012 ± 0.002	5.090 ± 0.22
GC90	Yes	0.686 ± 0.118	224.3 ± 8.96
GP90	Yes	0.123 ± 0.021	62.10 ± 2.58
GP25	Yes	0.013 ± 0.003	4.368 ± 0.215

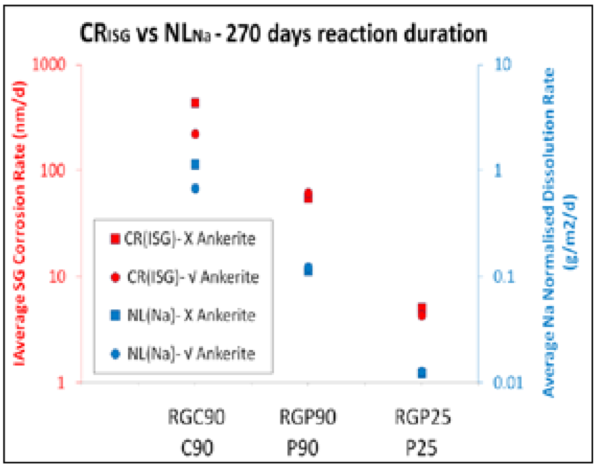

Figure 4. Average Na normalized loss VS Average Glass. *Corrosion Rates at day 270 for all categories. (Each point = average of 7 experiments)*

In this regard, Ebert[7] mentioned that "normalized mass losses of sodium and the pH values at different S/V values show that tests at lower S/V values attain higher sodium releases and higher corrosion rates based on sodium release. Tests at higher S/V generate solutions with higher pH values and higher sodium concentrations but lower glass corrosion rates when expressed as mass glass dissolved per unit area". Throughout the current experiment, the listed details are evidenced by the ISG.

5. Discussion

In light of the above findings, the effect of Ankerite on the rate of glass corrosion in pure-water systems (RGC90, GC90) is significant because it affects the solution's chemistry and hence the rate of glass corrosion via chemical parameters. In comparison to the ISG reference model (RGC90), Ankerite appears to be successful in lowering the ISG corrosion rate primarily by increasing the pH [49] and also by clogging the initial rate [34]. That was true for all corrosion rate observations between days 3 and 90, given that the aforementioned assumption is violated when the system approaches saturation with amorphous silica.

Meanwhile, Ankerite enhanced the corrosion rate slightly more than its reference RGP system in saturated systems, which may be due to the aggressive consumption effect on Si via sorption and precipitation with Fe and Mg [33, 34, 35].

In this paper, the words silica and silica saturation are not used to refer to dissolved SiO_2. In contrast, the more dissolved SiO_2 means more glass corrosion as well as more accumulated silicic acid in the forward stage, this is demonstrated while comparing the evolution of Si with B normalized losses.

Dissolution/precipitation responses were observed between Si and the soluble elements by the diffusion of Ankerite components. That is stressed by Delage et al. and Grambow [50, 51] that glass dissolution is regulated by orthosilicic/silicic acid action in solution in their static leaching studies on French R7T7 non-radioactive reference borosilicate glass in distilled water at 90 °C. Owing to the higher S/V ratio in the powdered ISG experiments, Si concentrations were far higher than in glass coupon systems. However, this work's short time scale limited the requirements, as in ISG coupon systems, silicic acid (H_4SiO_4) saturation was not adequately achieved; however, in ISG powder systems, it was already achieved during the reaction's first hours.

The difference in ISG mass was detected, using an electrical balance, before and after leaching. An alternative method was implied to calculate the mass loss using the values obtained by ICP-MS, by finding the total mass of elements (B, Na, Al, Si, Ca, Zr) transferred to the aqueous solution. The values obtained by both methods were in good agreement and any differences can be attributed to the SAL (evolution/dissolution) weight in (mg). The mass fraction of dissolved X_g glass was represented by Neeway et al. [45], and was calculated by Equation (5).

$$X_g = \frac{NL_i \times S_g}{M_g} \quad \text{.......} \quad (5)$$

where; NL_i is the normalized mass loss for a given period ($g.m^{-2}$), is the surface area of the original glass (m^2) and is the initial mass of the glass (g).

Equation (6) was attained by inserting the normalized loss (NL) formula Equation (2) into the X_g formula Equation (5) for calculating the overall mass fraction of ISG $X_{g(overall)}$ dissolved in solution:

$$X_{g(overall)} = \frac{m_i}{M_g} \quad \text{.......} \quad (6)$$

Figure (5) illustrates calculated and measured weight loss values for all systems except those containing both powdered ISG and Ankerite. Equation (7) is based on the assumption that the difference between the calculated and measured ISG weights results in an estimate of the SAL's (evolution/dissolution) weight. In light of the NL_{Si} in the solution, this layer is mostly silica gel (amorphous silica SiO_2). ISG is primarily composed of the oxides listed in Table (1). At a total concentration of < 1.0 % [38], the ISG's impurities (Cr, P, K, Fe, Ni, Mn, Mg, S, Ti, F, and Cl) are defined. The existence of these impurities was incorporated in the overall uncertainty of 15 % of the estimated SAL's (evolution/

dissolution) weight as a ~ 1.0 % of the total concentration referred to as impurities.

$$W_{SAL} = WL - W_{i(overall)} \quad (7)$$

where; $W_{i(overall)}$ (mg) is the calculated weight of the dissolved elements as obtained by ICP-MS analyses, and WL (mg) is the measured loss in weight in ISG via a Mettler Toledo electrical balance.

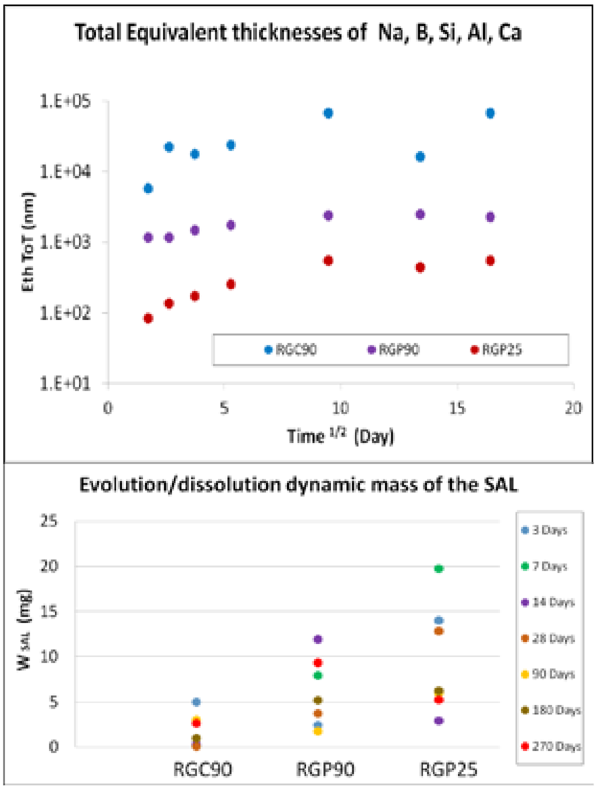

Figure 5. The total equivalent thickness of the ISG corrosion products and the estimated dynamic mass (evolution/dissolution) of the surface alteration layer over time. A ± 15 % uncertainty is considered. (Each point = single experiment).

In the reference powdered glass at 25 °C, RGP25, the maximum (evolution/dissolution) on the SAL was produced. Because of the difficulties in extracting the glass when combined with the Ankerite, it should be noted that these weight reduction measures were only performed on the comparison (reference) glass samples. The highest SAL's dynamic mass of all the systems reached approximately 20 mg in RGP25.

According to the data given, it appears as though a thick silica layer is formed at the interface of the glass coupon as a result of the cooling and drying of an interfacial solution rich in dissolved silica. This solution occurs as the thickness of the SAL develops and aqueous silica can no longer be successfully transferred away from the evaporation/dissolution boundary to the bulk solution. As a result, silicic acid and other glass constituents accumulate at the ISG interface, resulting in aggregation and gelation. As a result, less silicic acid may be removed from the glass, transported, and dissolved into the interfacial suspension or gel, thereby decreasing the surface-controlled dissolving process and favoring interdiffusion. And this may explain and justify the varying rates of weight loss in the case of RGP90 and RGC90.

SAL's dynamic mass (W_{SAL}) differed more in the first 28 days of reaction between the RGP90 and RGC90 models. Higher S/V values appear to intensify the glass alterations during the first aging process independent of Ankerite's existence. This highlights a hypothesis described above that the Ankerite's impact in the first month of reaction should not be considered. Compared to the overall equivalent (altered ISG) thickness ($E_{th(total)}$) of the main ISG elements, which has been calculated for all ISG corrosion products by using Equation (4), the W_{SAL} values had reverse effects and RGP25 showed the highest measurements. The order of the systems concerned is reversely consistent with the order of the specimens in the field of CR_{ISG}; RGP25 < RGP90 < RGC90, which sounds logical according to to experiment observations, based on the capacity for large-scale gel for evolution/dissolution [44, 45].

6. Conclusions

Ankerite has a negligible influence on the rate of ISG corrosion during the initial stage of the reaction. This idea was reinforced by weight loss estimates, which, however, do not accurately reflect the definite value of glass corrosion.

When the concentration of soluble silica species in the aqueous phase approaches saturation; no further glass dissolution occurs. However, sodium normalized mass loss results indicated that pure-water test values result in higher sodium releases and corrosion rates based on sodium release. When stated in terms of glass mass dissolved per unit area, saturated test systems had greater sodium concentrations but lower rates of glass corrosion.

In this study, a new method was used to determine the dynamic mass of the surface alteration layer. This method showed that a high dynamic mass coincides with a low corrosion rate, resulting in low ISG components' equivalent thickness.

Acknowledgment

The authors would like to acknowledge Savannah River National Laboratory (SRNL), USA, for kindly providing the original ISG sample.

They would also like to thank the BME University, Faculty of Natural Sciences (Department of Atomic Physics) for preparing the ISG glass sample by cutting and polishing.

Most of the practical work was carried out at the Surficial Ores Processing Laboratories, and Jordan Uranium Mining Company and the chemical analyses were performed at the Jordan Atomic Energy Commission (JAEC).

Also, the Stipendium Hungaricum Scholarship Programme is highly acknowledged for supporting this study and research work.

Compliance with ethical standards

Conflict of interest: The authors declare that they have no conflict of interest.

References

Gin S, Ryan J, Kerisit S, Du J, Simplifying a solution to a complex puzzle, npj Materials Degradation (2018). doi:10.1038/s41529-018-0057-y

ANDRA, Evaluation of the feasibility of a geological repository in an argillaceous formation, Report Series, France, Dossier, (2005).

World Nuclear Association, 2017, Treatment and conditioning of nuclear waste, World Nuclear Association, 2017

https://www.world-nuclear.org/information-library/nuclear-fuel-cycle/nuclear-wastes/treatment-and-conditioning-of-nuclear-wastes.aspx

World Nuclear Association, 2020, Radioactive Waste Management, World Nuclear Association, 2020.

https://www.world-nuclear.org/information-library/nuclear-fuel-cycle/nuclear-wastes/radioactive-waste-management.aspx

Paul, A. (1977). Chemical durability of glasses; a thermodynamic approach. Journal of Materials Science, 12(11), 2246–2268.

Jollivet P., Frugier P., Parisot G., Mestre J. P., Brackx E., Gin S., & Schumacher, S. (2012). Effect of clayey groundwater on the dissolution rate of the simulated nuclear waste glass SON68. Journal of Nuclear Materials, 420(1-3), 508–518.

https://doi.org/10.1016/j.jnucmat.2011.10.026

Ebert, W L. The effects of the glass surface area/solution volume ratio on glass corrosion: A critical review. United States: N. p., 1995. pp.18-79.doi:10.2172/67461

Bouakkaz R., Abdelouas A., El Mendili Y., Grambow B., Gin S. SON68 glass alteration under Si-rich solutions at low temperature (35–90 °C): kinetics, secondary phases, and isotopic exchange studies, RSC Adv, Vol. 6, 2016, pp. 72616–72633.

https://doi.org/10.1039/C6RA12404F

El Hajj H., Abdelouas A., Grambow B., Martin C., Dion M. Microbial corrosion of P235GH steel under geological conditions, Physics and Chemistry of the Earth, Parts A/B/C, 35 (6-8), 2010, pp. 248–253.doi:10.1016/j.pce.2010.04.007

Gin S. Open scientific questions about nuclear glass corrosion, Procedia Materials Science, Vol. 7, 2014, pp. 163–171.doi: 10.1016/j.mspro.2014.10.022

De Echave T., Tribet M., Jollivet P., Marques C., Gin S., Jégou C., (2018). Effect of clayey groundwater on the dissolution rate of SON68 simulated nuclear waste glass at 70 °C. Journal of Nuclear Materials, S002231151731142X–.

doi:10.1016/j.jnucmat.2018.03.013

Van Iseghem P., Aertsens, M., Lemmens, K., Gin S., Deneele D., Grambow B., McGrail P., Strachan D., Wicks G., McMenamin T., Glamor: A Critical Evaluation of the Dissolution Mechanisms of High-level Waste Glasses in Conditions of Relevance for Geological Disposal INIS-FR-3271; The Sixth International Conference on the Management and Disposal of Radioactive Waste, France, 2004; pp 781−785.

Van Iseghem P., Aertsens M., Gin S., Deneele D., Grambow B., Strachan D., McGrail P., G. Wicks, GLAMOR: How we Achieved a Common Understanding on the Decrease of Glass Dissolution Kinetics, in: A. Cozzi, T. Ohji (Eds.), Environmental Issues and Waste Management Technologies in the Materials and Nuclear Industries Xii, Amer Ceramic Soc, Westerville, 2009, pp. 115-1

Vienna D., Ryan V., Gin S., Inagaki Y., (2013). Current Understanding and Remaining Challenges in Modeling Long-Term Degradation of Borosilicate Nuclear Waste Glasses. International Journal of Applied Glass Science, 4(4), 283–294. doi:10.1111/ijag.12050

Frankel G. S., Vienna J. D., Lian J., Guo X., Gin S., Kim S. H., … Scully J. R. (2021). Recent Advances in Corrosion Science Applicable To Disposal of High-Level Nuclear Waste. Chemical Reviews. doi:10.1021/acs.chemrev.0c00990

Gin S., Neill L., Fournier M., Frugier P., Ducasse T., Tribet M., Abdelouas A., Parruzot B., Neeway J., Wall N., (2016). The controversial role of inter-diffusion in glass alteration. Chemical Geology, 440, 115–123. doi:10.1016/j.chemgeo.2016.07.014

Pierce M., Frugier P, Criscenti J., Kwon D., Kerisit N. (2014). Modeling Interfacial Glass-Water Reactions: Recent Advances and Current Limitations. International Journal of Applied Glass Science, 5(4), 421–435. doi:10.1111/ijag.12077

Gin S., Mestre J.P., (2001). SON 68 nuclear glass alteration kinetics between pH 7 and pH 11.5. , 295(1), 83–96. doi:10.1016/s0022-3115(01)00434-2

Chai L., Navrotsky A.. (1996), Synthesis, characterization, and energetics of solid solution along the dolomite-ankerite join, and implications for the stability of ordered CaFe(CO3)2, American Mineralogist, 81 (9-10), pp. 1141–1147.

https://doi.org/10.2138/am-1996-9-1012

Ellwood B. B., Burkart B., Rajeshwar K., Darwin R. L., Neeley R. A., McCall A. B., … Hickcox C. W. (1989), Are the iron carbonate minerals, ankerite, and ferroan dolomite, like siderite, important in paleomagnetism? Journal of Geophysical Research, 94(B6), 7321. https://doi.org/10.1029/JB094iB06p07321

Bart G., Zwicky H. U., Aerne E. T., Graber T. H., Berg D. Z, Tokiwai M. (1986), Borosilicate glass corrosion in the presence of steel corrosion products, Materials Research Society fall meeting, Boston, MA, USA, 1-5 December 1986, Vol. 18, No. 22,1986, pp. 459–470. https://inis.iaea.org/search/search.aspx?orig_q=RN:18091173

Burger E., Rebiscoul D., Bruguier F., Jublot M., Lartigue J. E., Gin S.. (2013), Impact of iron on nuclear glass alteration in geological repository conditions: A multiscale approach, Applied Geochemistry, Vol. 31, pp. 159–170.

http://dx.doi.org/10.1016/j.apgeochem.2012.12.016

Carriere C., Neff D., Foy E., Martin C., Linard Y., Michau N., Dynes J., Dillmann P.. (2017), Influence of iron corrosion on nuclear glass alteration processes: nanoscale investigations of the iron-bearing phases, Corrosion Engineering, Science and technology, vol. 52, no. S1, 166–172.

https://doi.org/10.1080/1478422X.2017.1306962

Debure M., Frugier P., Windt L. D., & Gin S.. (2013), Dolomite effect on borosilicate glass alteration. Applied Geochemistry, 33, 237-251.

doi:10.1016/j.apgeochem.2013.02.019

Dillmann P., Gin S., Neff D., Gentaz L., Rebiscoul D. (2016), Effect of natural and synthetic iron corrosion products on silicate glass alteration processes, Geochimica et Cosmochimica Acta, Vol. 172, pp. 287–305.

https://dx.doi.org/10.1016/j.gca.2015.09.033

Guo X., Gin S., Liu H., Ngo D., Luo J., Kim S. H., Frankel G. S.. (2020). Near-field corrosion interactions between glass and corrosion-resistant alloys. Npj Materials Degradation, 4(1). https://doi.org/10.1038/s41529-020-0114-1

Jordan N., Marmier N., Lomenech C., Giffaut E., Ehrhardt J. J.(2007), Sorption of silicates on goethite, hematite, and magnetite: Experiments and modeling, Journal of Colloid and Interface Science, 312 (2), pp. 224–229. doi:10.1016/j.jcis.2007.03.053

Michelin A., Burger E., Rebiscoul D., Neff D., Bruguier F., Drouet E., Dillmann P., and Gin S. (2013), Silicate Glass Alteration Enhanced by Iron: Origin and Long-Term

Implications, Environmental Science & Technology, 47 (2), 750-756.

doi: 10.1021/es304057y

Neill L., Gin S., Ducasse T., De Echave T., Fournier M., Jollivet P., WallN. A. (2017), Various effects of magnetite on international simple glass (ISG) dissolution: implications for the long-term durability of nuclear glasses. Npj Materials Degradation, 1(1).doi:10.1038/s41529-017-000

Philippini V., Naveau A., Catalette H., Leclercq S. (2006), Sorption of silicon on magnetite and other corrosion products of iron, Journal of Nuclear Materials, Vol. 348, No. 1-2, pp. 60–69. https://doi.org/10.1016/j.jnucmat.2005.09.002

Aréna H., Rébiscoul D., Podor R., Garcès E., Cabie M., Mestre J.-P., &Godon N. (2018), Impact of Fe, Mg and Ca elements on glass alteration: Interconnected processes. Geochimica et CosmochimicaActa, 239, 420–445. doi:10.1016/j.gca.2018.08.007

Jollivet P., Angeli F., Cailleteau C., Devreux F., Frugier P., Gin S. (2008). Investigation of gel porosity clogging during glass leaching, Journal of Non-Crystalline Solids, Vol. 354,No. 45-46, pp. 4952–4958. http://doi.org/10.1016/j.jnoncrysol.2008.07.023

Kopecskó K., DabbasA. A. (2021).Silicate Sorption on Ankerite from a Standard Silicate Solution. Periodica Polytechnica Chemical Engineering, 65(3).

https://doi.org/10.3311/ppch.16967

Dabbas A. A., KopecskóK. (2021). Corrosion of glass used for radioactive waste disposal influenced by Ankerite, Advanced Aspects of Engineering Research, Vol. 9, Chapter 10 - Book Publisher International.

http://dx.doi.org/10.9734/bpi/aaer/v9/1997F

Dabbas A. A., KopecskóK. (2021). Corrosion of International Simple Glass by Mg-Si Precipitation in Presence of Ankerite, Pollack Periodica.

doi:10.1556/606.2021.00410

Daniel J. Backhouse, Adam J. Fisher, James J. Neeway, Claire L. Corkhill, Neil C. Hyatt, Russell J. Hand, Corrosion of the International Simple Glass under acidic to hyperalkaline conditions, npj Materials Degradation, 2. 29 (2018).

doi:10.1038/s41529-018-0050-5

Guerette M, Huang L, In-situ Raman, and Brillouin light scattering study of the international simple glass in response to temperature and pressure, Journal of Non-Crystalline Solids 411 (2015) 101–105.

https://doi.org/10.1016/j.jnoncrysol.2014.12.028

Kaspar, T. C., Ryan, J. V., Pantano, C. G., Rice, J., Trivelpiece, C., Hyatt, N. C., Smith, N. J. (2019). Physical and optical properties of the International Simple Glass. Npj Materials Degradation, 3(1).doi:10.1038/s41529-019-0069-2

Neill, L., Gin, S., Ducasse, T., De Echave, T., Fournier, M., Jollivet, P., Wall, N. A. (2017). Various effects of magnetite on international simple glass (ISG) dissolution: implications for the long-term durability of nuclear glasses. Npj Materials Degradation, 1(1).doi:10.1038/s41529-017-000

Fournier, M., Ducasse, T., Pérez, A., Barchouchi, A., Daval, D., & Gin, S. (2019). Effect of pH on the stability of passivating gel layers formed on International Simple Glass. Journal of Nuclear Materials.doi:10.1016/j.jnucmat.2019.06.029

Inagaki Y, Kikunaga T, Idemitsu K, Arima T, Initial Dissolution Rate of the International Simple Glass as a Function of pH and Temperature Measured Using Microchannel Flow-Through Test Method, International Journal of Applied Glass Science, 4 [4] 317–327 (2013).https://doi.org/10.1111/ijag.12043

Strachan, D., Turcotte, R. P., & Barnes, B. O. (1982). MCC-1: A Standard Leach Test for Nuclear Waste Forms. Nuclear Technology, 56(2), 306-312.

doi:10.13182/nt82-a32859

Ferrand K., Klinkenberg M., Caes S., Poonoosamy J., Van Renterghem W., Barthel J., Lemmens, K., Bosbach D., Brandt F. Dissolution Kinetics of International Simple Glass and Formation of Secondary Phases at Very High Surface Area to Solution Ratio in Young CementWater. Materials 2021, 14, 1254.

doi.org/10.3390/ma14051254

Gin S., & Frugier P. (2002). SON68 Glass Dissolution Kinetics at High Reaction Progress: Experimental Evidence of the Residual Rate. MRS Proceedings, 757.

Neeway J., Abdelouas A., Grambow B., & Schumacher S. (2011). Dissolution mechanism of the SON68 reference nuclear waste glass: New data in a dynamic system in silica saturation conditions. Journal of Nuclear Materials, 415(1), 31–37.

doi:10.1016/j.jnucmat.2011.05.027

Ebert, W. L., & Mazer, J. J. (1993). Laboratory Testing of Waste Glass Aqueous Corrosion; Effects of Experimental Parameters. MRS Proceedings, 333.

https://doi.org/10.1557/PROC-333-27

Debure, M., Frugier, P., De Windt, L., & Gin, S. (2012). Borosilicate glass alteration driven by magnesium carbonates. Journal of Nuclear Materials, 420(1-3), 347–361.

https://doi.org/10.1016/j.jnucmat.2011.09.032

Jollivet P., Angeli F., Cailleteau C., Devreux F., Frugier P., Gin S. Investigation of gel porosity clogging during glass leaching, Journal of Non-Crystalline Solids, Vol. 354,No. 45-46, 2008, pp. 4952–4958.doi:10.1016/j.jnoncrysol.2008.07.023

Dabbas AA, Kopecskó K. (2022). The Influence of the Saturation on the Rate of ISG Corrosion in Presence of Ankerite. IOP Conference Series: Materials Science and Engineering. (Paper in Press).

Delage F., Ghaleb D., Dussossoy J. L., Chevallier O., & Vernaz E. (1992). A mechanistic model for understanding nuclear waste glass dissolution. Journal of Nuclear Materials, 190, 191–197.https://doi.org/10.1016/0022-3115(92)90086-Z

Grambow, B. (1984). A General Rate Equation for Nuclear Waste Glass Corrosion. MRS Proceedings, 44.https://doi.org/10.1557/PROC-44-15

Appendix

Normalized loss in details for the primary elements (Na, B, Si, Al) in all leaching systems

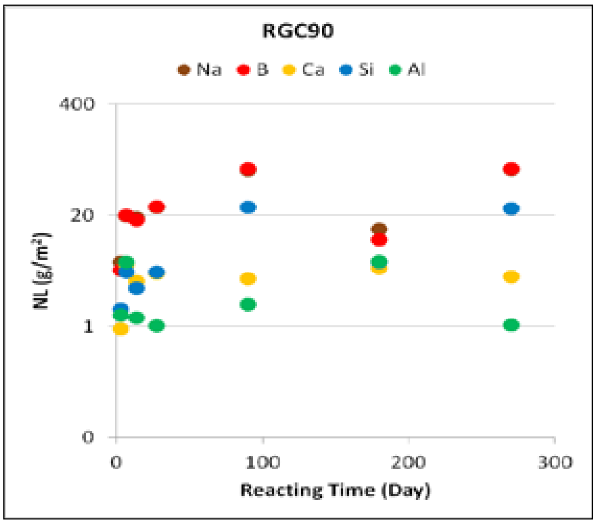

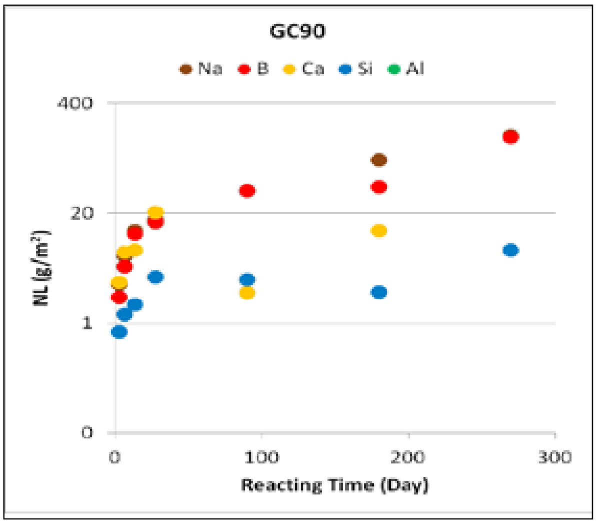

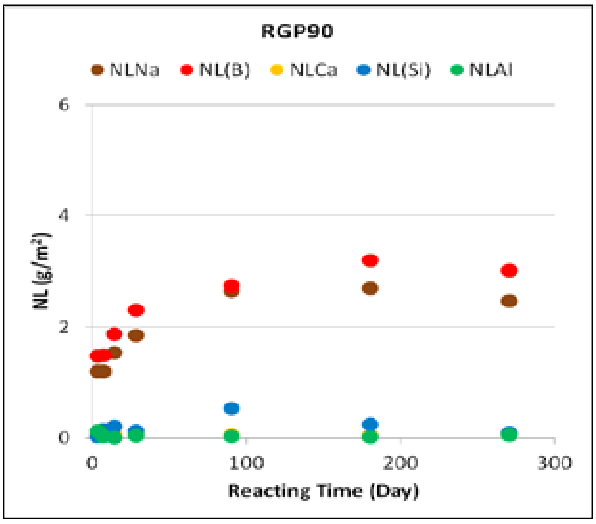

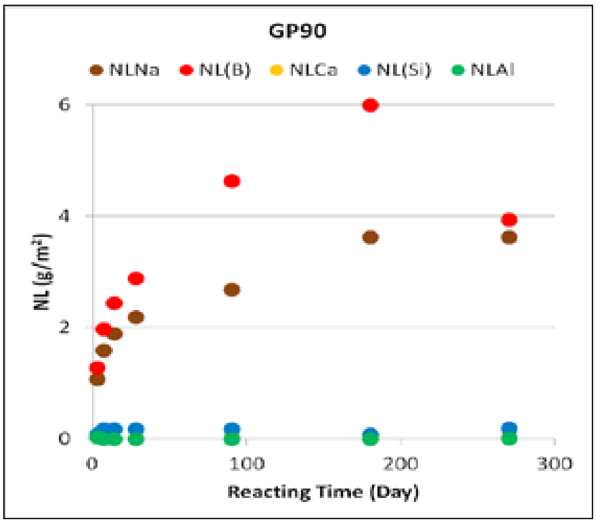

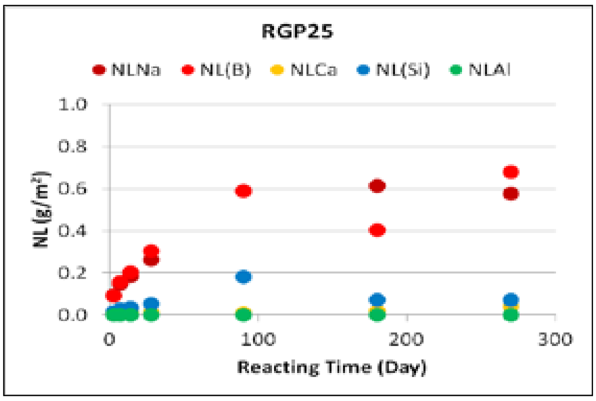

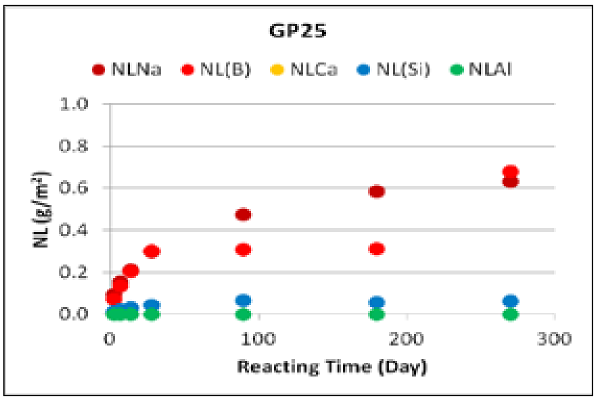

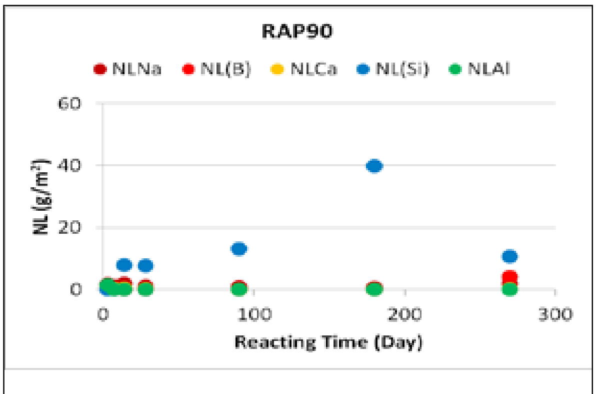

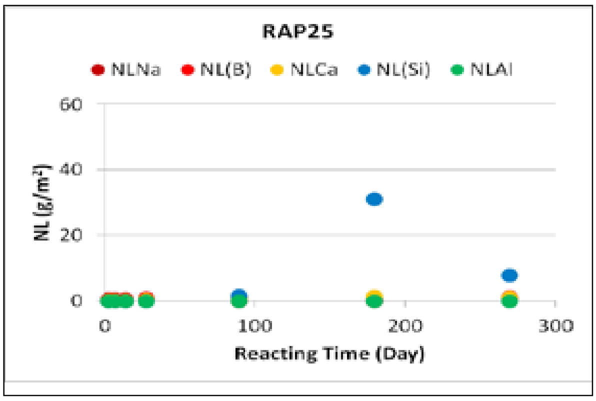

JJEES

Jordan Journal of Earth and Environmental Sciences

JJEES (2022) 13 (3): 177-189
ISSN 1995-6681

Kinematic Analysis of Landslides: A Case Study Along Jerash-Amman Highway, Jordan

Abdullah Diabat[1], Majed Ibrahim[2], Yasmeen Al-Hawareen[3]

[1,3]Earth and Environmental Sciences Department, Al al-Bayt University, Al-Mafraq, Jordan
[2]Information System and Remote Sensing Department, Al al-Bayt University, Mafraq, Jordan

Received 24th September 2021; Accepted 4th March 2022

Abstract

One of the important environmental issues and structural and engineering phenomena in on the earth is the landslide that which are is considered also one of the biggest threats worldwide that hit mountainous and highland areas. Therefore, the current study was carried out in nine measurement stations along Jerash- Amman highway, to analyze the landslides by means ofthrough stereographic projection or kinematic analysis. Results show that the dominant type of the rock slope failure is the wedge failure which is observed in the first five stations of the study area. Stations 1, 2, 5, and 9 showed a toppling failure, while stations 2, 3, 4, and 5 showed planar failure. The circular failure is only found in station 9. Structural control of most of these landslides was inferred through this study.

Keywords: *Landslides, Kinematic analysis, Geological structures, Jerash- Amman highway, Jordan*

1. Introduction

The stability of rock slopes is often significantly influenced by the geological structures of the rock in which the slope is excavated. Geological structures refer to naturally occurring breaks in the rock such as joints and faults, in addition to bedding planes which are generally termed discontinuities. The significance of discontinuities is that they are planes of weakness in the much stronger intact rock, so failure tends to occur preferentially along these surfaces (Wyllie and Mah 2005).

In many research studies with some of the landslides which have been encountered through and after the construction of the Jerash-Amman highway (Fig.1), that occurred through during the very exceptional winter of 1991/1992 which was characterized by dense rain and snowfalls (Al-Homoud and Masanat 1998). However, where it was found that landslides occur when the forces of shear stress exceed the forces of strength in the soil and rock due to many reasons, including the obvious causes such as nature, topography, human intervention, and water flow (Masannat 2014). Many researchs have has been carried out along Irbed-Jerash and/ or Jerash- Amman highway using different methods and techniques (e.g., Dames and Moor ,1993; Al-Basha, 1996; Al-Homoud et al.,1996; Abederahman,1994; Mansour et al.,1997; Saleh,1997; Abederahman,1998; El-Naqa, and Abdelghafoor, 2006; Abederahman,2007; Al-Omari ,2006, 2014; El-Moghrabi, 2016; Al- Hawareen, 2020; Diabat and Abu Rumman 2021).

Cut slopes along the Amman-Jerash highway are composed of highly weathered rock masses and/or alternating sequences of sandy, silty and argillaceous sedimentary rocks. Therefore, several major landslides occurred at different parts along this highway such as rock slides, toppling, slumping, and earth flow (Dames and Moor 1993). Almost all rock slope stability studies should address the structural geology of the site, and such studies have to determine the influence of the discontinuities on stability, which involves studying the relationship between the orientation of the discontinuity and the slope face (Wyllie and Mah 2005). So this study is mainly concentrated on the kinematic analysis to identify possible modes of slope failure in the study area.

The study area is bounded by the coordinates:32°13 to 32° 28N and 35° 85 to 35° 91E and subdivided into nine measurement stations (Fig 1).

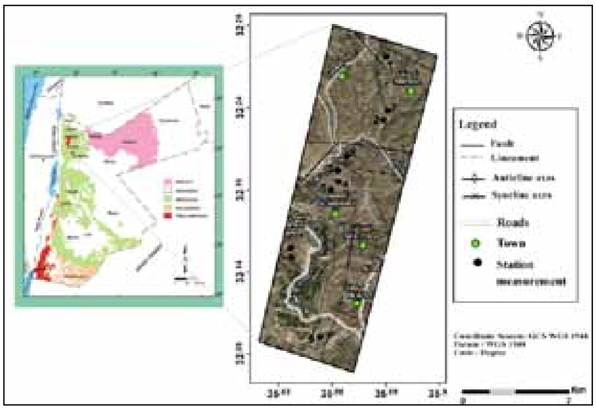

Figure 1. Location map of the study area and satellite image (Explorer 2018)

Most of the study area is mountainous and is a part of the northern highlands of Jordan. It varies in elevation from about 150 m above sea level (A.S.L.) near Zerqa river in the central part of the study area to about 900 m (A.S.L) near Marssa in the southern part (Fig. 2).

* Corresponding author e-mail: adiabat@aabu.edu.jo

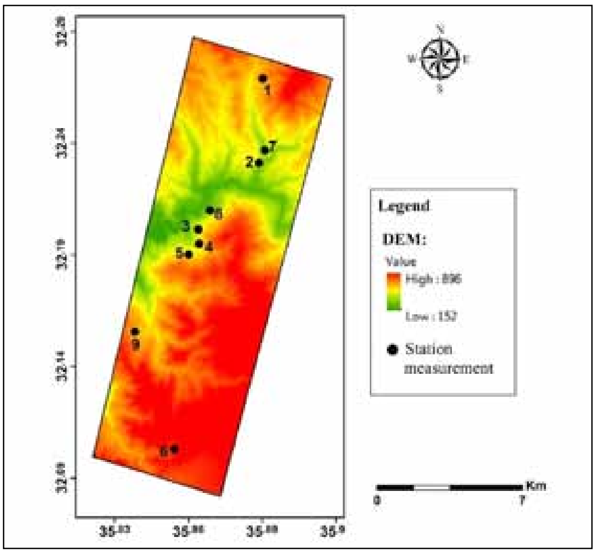

Figure 2. A digital elevation map (DEM) of the study area.

The objectives of this study can be summarized as follow: Determining the orientation and nature of the fracture systems and their relationships with the landslide, collecting relevant field data such as bedding, fractures, and slopes in selected sites to assess stability conditions using kinematic methods.

2. Geological Setting

The following lithostratigraphic units are exposed in the study area (Table1 and Fig. 3):

The study area is located about 20 km east of the Jordan valley fault: the northern segment of the Dead Sea transform fault and about 20-25 km to the north of Amman- Hallabat structure (Fig.4). The southern part of the study area is crossed by part of the NE-SW Wadi Shu'ayb structure. It consists of en echelon folds, monoclinal flexures and faults (Sawariah and Barjous 1993 , Abdelhamid 1993, Abdelhamid 1995). The Zarqa river fault crossed the study area in E-W direction. The fault systems in the study area are oriented E-W, NE- SW, and NW- SE (Fig. 3). The tectonic phases cause incentive drainage, where mass movement is motivated and takes place (Sawariah and Barjous 1993, Abdelhamid 1993).

Table 1. The outcropping lithostratigraphic units in the study area were modified after (Sawariah and Barjous 1993, Abdelhamid 1993, Abdelhamid 1995, Powell 1989)

Group	Formation	Age	Thickness (m)	Lithology
Belqa	Amman Silicified Limestone	Campanian to Maasterichtian	120	Limestone, Chert
	Umm Ghudran	Coniacian to Campanian	15 – 20	Chalk, Chalky marl, and Chalky limestone
Ajlun	Wadi As Sir	Turonian	100 – 125	Massive limestone
	Shu'eib	Turonian	60	Marly limestone
	Hummar	Cenomanian	40 – 60	Dolomitic limestone
	Fuheis	Cenomanian	80	Marl and Marly limestone
	Na'ur	Albian – Cenomanian	180 – 200	Limestone, Dolomitic limestone and marl
Kurnub		Aptian – Albian	250 – 300	Sandstone

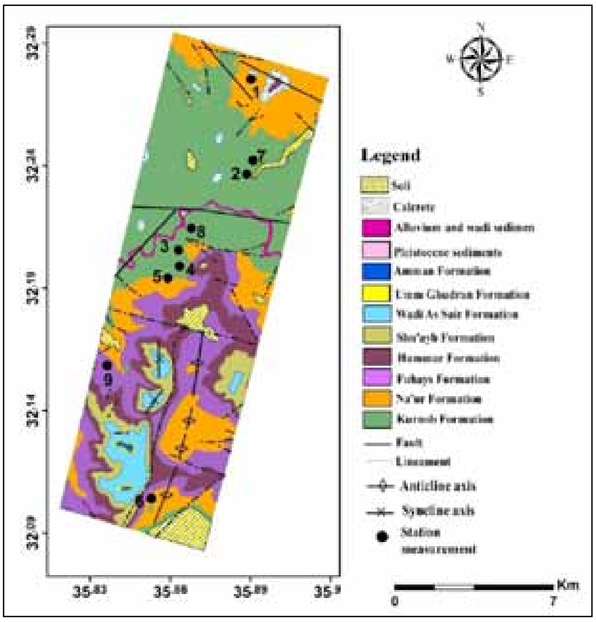

Figure 3. Geological map of the study area (modified after Sawariah and Barjous 1993, Abdelhamid 1993)

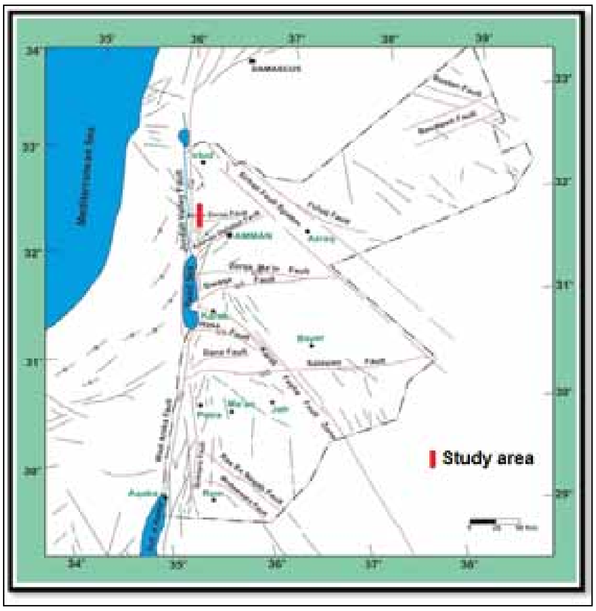

Figure 4. Structural pattern of Jordan (after Diabat and Masri 2005)

3. Methodology

Several field trips were carried out to collect orientation data on discontinuities. A detailed study of the geological features in the selected stations was carried out. Field observations and measurements of the attitude of discontinuities e.g., bedding planes, fractures (faults and joints), in addition to slope faces were directly measured in the field. The measurements of the discontinuities were taken by using a geological compass (CLAR) as dip direction/ dip. The measured discontinuities in the field have been analyzed using stereographic projection software. This helped in determining the pole plot of all measured discontinuities and the contour plot which represents the concentration of all discontinuity's readings (Fig. 5). The rock mass to be able to slide, it must be cohesionless i.e the cohesion between the plane of sliding and the sliding rock mass equal zero. The friction angle of the discontinuities in a rock mass is supposed to be 34 degrees based on Barton (1973) and Jaeger and Cook (1976) as shown in Table 2. The friction angles listed in this table should be used as a guideline only because actual values will vary widely with site conditions. Hoek and Bray (2003) classified rock slope failures into different types. The current study estimated the stability of slopes in nine stations as the same examples shown in figures (5and6).

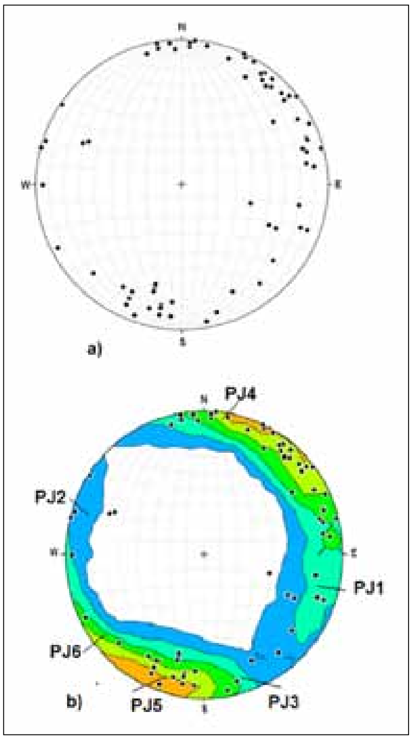

Figure 5. a) Poles of the discontinuities, b) Contour plot of main concentrations of poles.

Table 2. Typical ranges of friction angles for a variety of rock types (after, Barton 1973; Jaeger and Cook, 1976).

Typical rock types	Friction angle range	Rock class
Schists (high mica content), shale, marl	20–27°	Low friction
Sandstone, siltstone, chalk, gneiss, slate	27–34°	Medium friction
Basalt, granite, limestone, conglomerate	34–40°	High friction

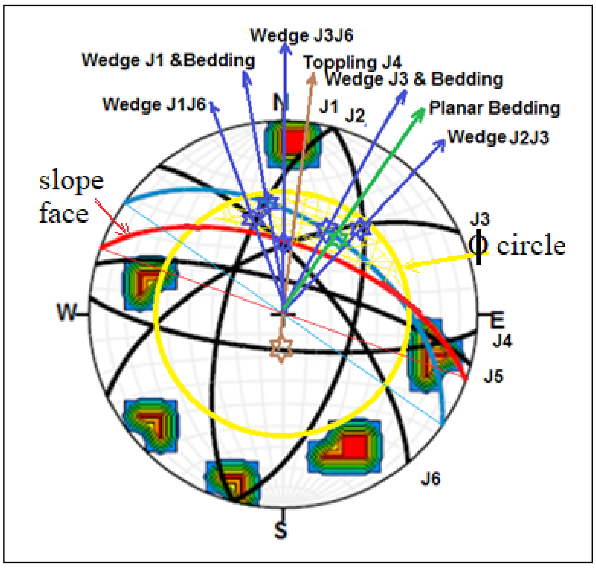

Figure 6. Example of stability estimate of the rock mass in station 5; black great circles represent planes corresponding to centres of pole concentrations of discontinuities probable to planar, wedge, and toppling failures, the blue great circle represents the bedding attitude, the red great circle represents the slope face and the shaded yellow sector represents the unstable area for sliding.

4. Slope stability analysis in the studied stations

The study area is located along Jerash- Amman highway, nine stations were selected based on the discontinuity properties which have indications of the impact on slope stability. These stations are located on the geological map (Fig. 3).

4.1 Station1

This station is located in the city of Jerash, near Jerash University and 40 km north of the capital Amman (Fig. 3). The outcrop is part of the Na'ur Formation, it is highly fractured and highly weathered limestone (Fig. 7).

Figure 7. Highly fractured and weathered rocks in an outcrop of station-1.

Figure 8. Figure (8a) represents the pole plot of all measured discontinuities. The contour plot in Figure (8b) represents the concentration of all discontinuity readings. The fractures and bedding plane (dip/dip direction 05/090) with slope face oriented (65/240) and the supposed friction angle 34° according to Dames and Moore (1993), were kinematically analyzed using stereographic projection (Fig. 9).

Five joint sets were determined and analyzed for stability (Figs 8b and 9); J1(80/075), J2 (80/290), J3 (68/140), J4(80/150), and J5 (88/255). The result shows that probable toppling failure towards WSW (255 °) at J1 (Fig. 9), this is expected because the dip direction of the J1-set is in the opposite direction of the slope face. Figure (9) shows two wedge failure directions along the line of intersections of J2 and J3 (J23), J2 and J4 (J24), respectively towards 40/210° and 60/220°. It is important to note that the wedge sliding along J24 is in its critical case because the intersection point of J2 and J4 lies at the slope face (Fig. 9). Despite the dominance trend of J5 (Figs 8 and 9), the results of the kinematic analysis indicated that it is stable because the dip of discontinuity planes is greater than the slope angle and lying out of the area of probable failure. Figures 10 and 11 show examples of toppling and wedge failures in station 1, respectively.

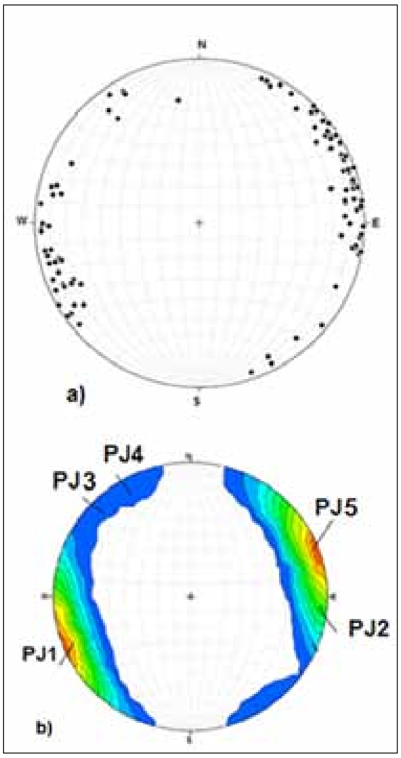

Figure 8. a) Pole plot of the discontinuities, b) Contour plot of main concentrations of poles.

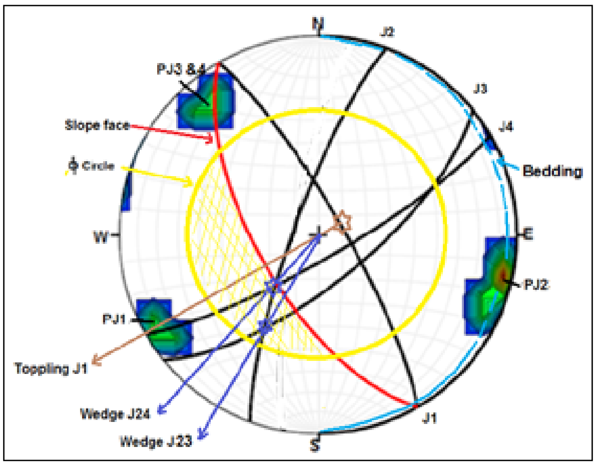

Figure 9. Stability estimates of the rock mass in station1; Great circles representing planes corresponding to centers of pole concentrations of discontinuities probable to toppling and wedge failure. The shaded yellow sector represents the unstable area for sliding.

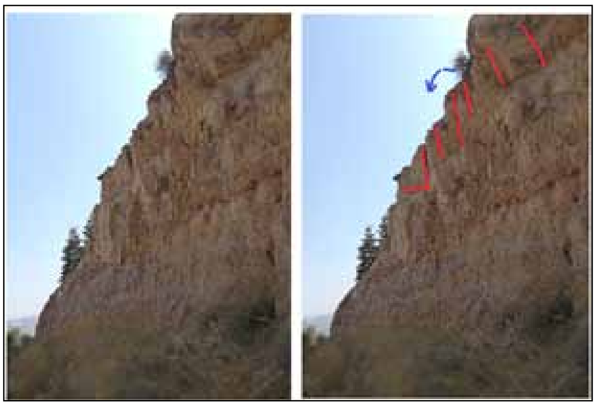

Figure 10. Probability of toppling failure, vertical joints (red lines) show back release surfaces.

Figure 11. Shows wedge failure and the protruding overhanging rocks at the slope face.

4.2 Station2

This station is located 200 meters north of the Zarqa River. It is located at 32° 13. 375'N and 35° 53.536' E (Fig. 3). The outcrop is part of the Kurnub group, medium to thick-bedded white greyish to light brownish sandstone with clay lenses (Fig 12). Figure (13a) represents the pole plot of all measured discontinuities. The contour plot in Fig. (13b) represents the concentration of all discontinuity readings.

The fractures and bedding plane (dip/dip direction 245/25°) with slope face oriented (120/88°) and the supposed friction angle 34° according to Moor (1993), were kinematically analyzed using stereographic projection. Four joint sets were determined and analyzed for stability (Figs. 13b and 14); J1 (60/110), J2 (86/280), J3 (70/150), and J4 (75/ 090). The results show that probable plane sliding along J1 with an attitude of plunge/ plunge direction 60/110 (Fig. 14). Toppling failure towards ESE (100°) at J2 (Fig. 14), is expected because the dip direction of the J2-set is in the opposite direction of the slope face. Fig. 14, also shows a wedge failure along the line of intersection of J3 and J4 (J34) towards 75/125°.

Figure 12. Front view of the Kurnub outcrop with lenses of clay and shale in station 2.

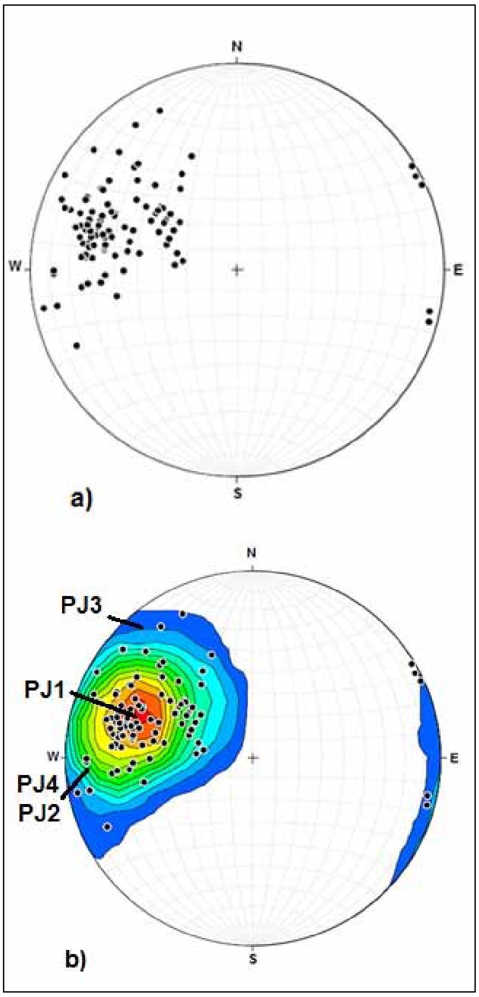

Figure 13. a) Pole plot of the discontinuities, b) Contour plot of main concentrations of poles.

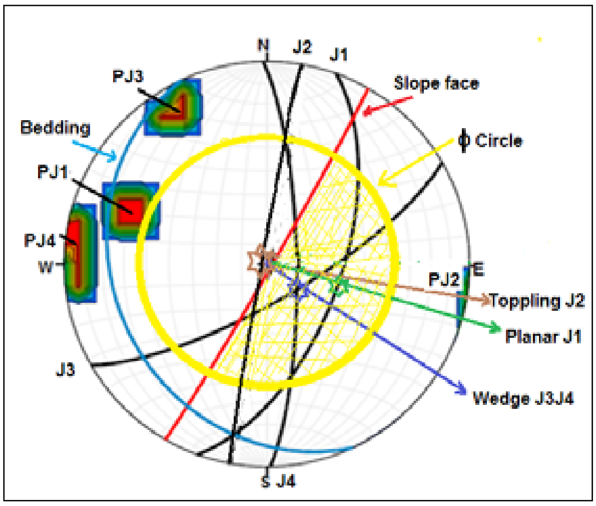

Figure 14. Stability estimates of the rock mass in station-2; Great circles representing planes corresponding to centers of pole concentrations of discontinuities probable to toppling and wedge failure. The shaded yellow sector represents the unstable area for sliding.

4.3 Station 3

This station is located south of Zarqa River and opposite King Talal Dam, 10 km south of Jerash city. It is located at 32° 12. 048'N and 35° 51.932' E (Fig. 3). The outcrop is part of the Kurnub group, massive yellowish to white grey cliffs separated by poorly exposed friable sandstone (Fig. 15). Figure 16a represents the pole plot of all measured discontinuities. The contour plot in Fig. (16b) represents the concentration of all discontinuity readings.

The fractures and bedding plane (dip/dip direction 260/10°) with slope face oriented (270/75°) and the supposed friction angle 34° according to Moor (1993) were kinematically analyzed using stereographic projection (Fig. 17). Three joint sets were determined and analyzed for stability (Figs 16b and 17); J1(70/ 270), J2 (50/ 300) and J3 (50/ 220). The results show that probable plane sliding along J1 with an attitude of 85/ 270 and a wedge failure along the line of intersection of J2 and J3 (J23) towards WNW (60/ 280°).

Figure 15. Very steep slope face towards the highway in the Kurnub outcrop of Station-3.

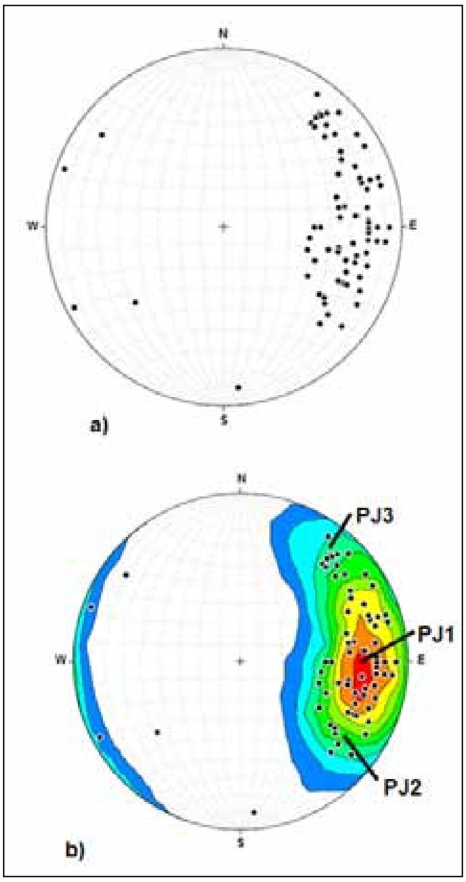

Figure 16. .a) Poles of the discontinuities, b) Contour plot of main concentrations of poles.

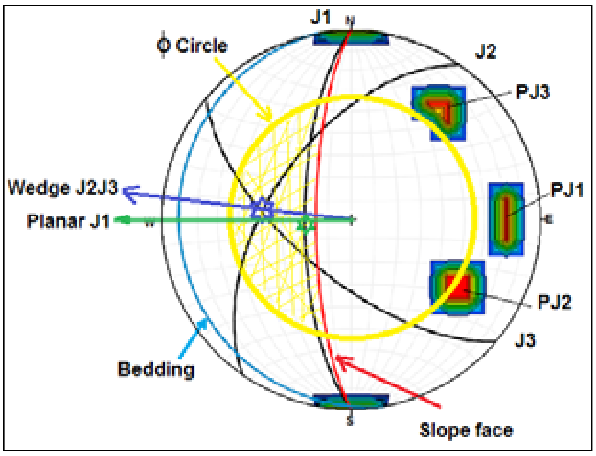

Figure 17. Stability estimate of the rock mass in station-3; Great circles representing planes corresponding to centers of pole concentrations of discontinuities probable to toppling and wedge failure. The shaded yellow sector represents the unstable area for sliding.

4.4 Station 4

This station is located along Jerash-Amman Highway about 15 Km to the south of Jerash. It is located at 32° 11. 713' N and 35° 51.878' E (Fig. 3). The outcrop is part of the Kurnub group, massive yellowish to white grey cliffs separated by poorly exposed friable sandstone (Fig. 18). Figure (19a) represents the pole plot of all measured discontinuities. The contour plot in Fig. (19b) represents the attitude of all concentration discontinuities.

The fractures and bedding plane (dip/dip direction 10/270°) with slope face oriented (270/85°) and the supposed friction angle 34° were kinematically analyzed using stereographic projection (Fig. 20). Six joint sets were determined and analyzed for stability (Figs 19b and 20); J1(80/310), J2 (70/330), J3 (75/050), J4 (75/230), J5 (70/270) and J6 (vertical, strike 140). The results show that a probable plane sliding along J5 toward the west with an attitude of 70/ 270 (Fig. 20) and three wedge failure directions; the first along the line of intersection of J1 and J4 (J1J4) towards WNW (70/ 260°), the second along J2J4 (70/290) and the third along J3J5 (40/330).

Figure 18. Kurnub outcrop in station-4.

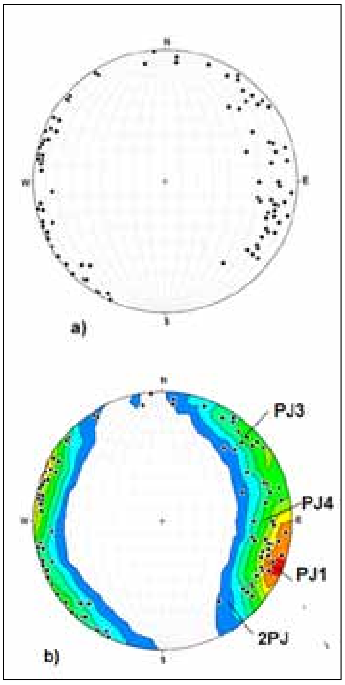

Figure 19. a) Poles of the discontinuities, b) Contour plot of main concentrations of poles.

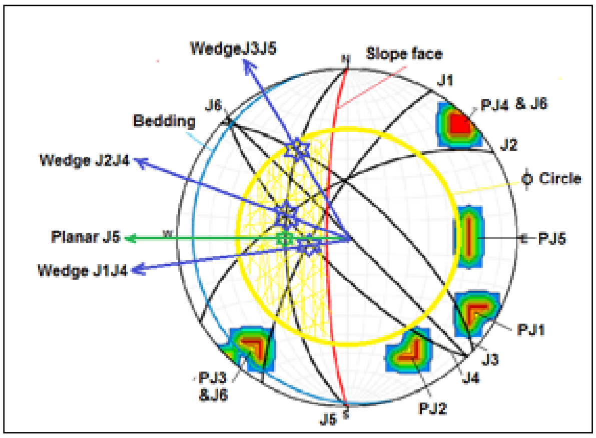

Figure 20. Stability estimate of the rock mass in station-4; Great circles representing planes corresponding to centers of pole concentrations of discontinuities probable to toppling and wedge failure. The shaded yellow sector represents the unstable area for sliding.

4.5 Station5

This station is located along Jerash-Amman Highway about 25 Km south of Jerash.

It is located at 32° 11. 502 'N and 35° 51.621' E (Fig. 3). The outcrop in the study site belong to Na'ur Formation, it consists of thick-bedded limestone forms the vertical cliffs in the area (Fig. 21), highly fractured, limestone alternating with grey to yellow-grey marl. Fig. 22a. represents the pole plot of all measured discontinuities. The contour plot in Fig. 22b represents the concentration of all discontinuity readings.

Figure 21. Vertically jointed Naur limestone cliff (blue lines) probable to topple in station-5

The fractures and bedding plane (dip/dip direction50/ 035°) with slope face oriented (60/ 020°) and the supposed friction angle 34° according to Moor (1993) and (Table 2), were kinematically analyzed using stereographic projection (Fig. 23). Six joint sets were determined and analyzed for stability (Figs 22b and 23); J1(65/ 280), J2 (65/ 100) and J3 (60/ 330), J4 (70/ 185), J5 (70/ 020) and J6 (70/050). The results show that probable plane sliding along bedding planes with an attitude of 50/ 030, because the strike of bedding is sub-parallel to the strike of slope face (Figs 23 and 24), and a toppling failure of J4 towards NNE (010) (Figs 23 and 25). In figure (25) a tension crack acting as a back release surface was observed. Five wedge failure directions are expected; the first is along the line of intersection of J2 J3 (J23) towards (30/ 040), the second is along the line of intersection of J1J6 towards (35/ 342), and the third is along the line of intersection of J3J6 toward the north, the fourth is along the line of intersection of J1 and bedding towards 30/350, and the fifth is along the line of intersection of J3 and bedding towards 40/ 058 (Fig. 23).

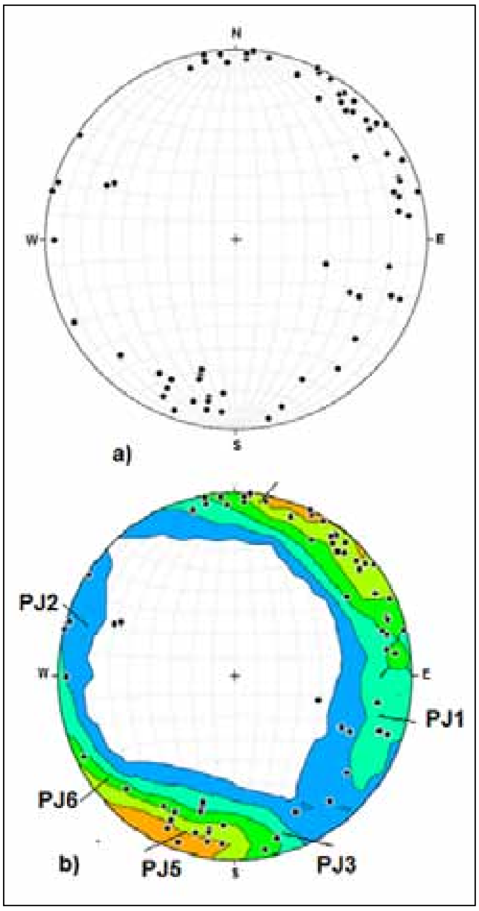

Figure 22. a) Poles of the discontinuities, b) Contour plot of main concentrations of poles.

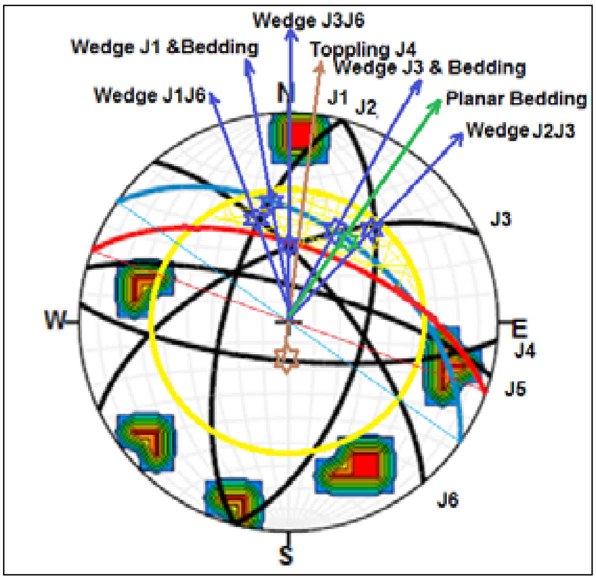

Figure 23. Stability estimate of the rock mass in station-5; Great circles representing planes corresponding to centers of pole concentrations of discontinuities probable to planar, wedge, and toppling failures. The shaded yellow sector represents the unstable area for sliding

Figure 24. Plane sliding in station- 5.

Figure 25. Toppling failure; tension crack (tc) acts as back release surface in station-5.

4.6 Station 6

This station is located along Jerash-Amman Highway about 30 Km from Jerash, near the Salhub village. It is located at 32° 06. 955'N and 35° 51.262' E (Fig. 3). The outcrop in the study site is Na'ur Formation. It consists mainly of hard thick-bedded limestone, dolomite, dolomitic limestone, and also fossiliferous marly limestone with a thin-bedded soft green clay at the base (Fig. 26). Fifty fractures were measured and represented in the rose diagram and shows the main trend of NW-SE (Fig. 27). The attitude of the slope face and bedding planes are parallel and equal 280/30° (Fig. 28). The kinematic analysis of this station, shows that the outcrop was stable and at the critical case for plane sliding because the great circles of the bedding and slope face are less than the friction angle and located out of the friction circle (Fig. 28). The measured joints in this station do not affect the sliding as their strikes are making an angle about 60 with bedding and the intersection line is out of the friction circle (Fig. 28).

Although the dip angle of bedding planes are not exceeding 30 to 35°, landslides have occurred. This station represents an ideal example of an active man-made landslide failure, the outcrop was stable before cutting the foothill during the construction of the highway in the 1990s. The cutting process of the foothill led to increasing the shear forces against the normal and resistance forces, and creating tension cracks a few meters in depth and width (Fig. 29). The thick-bedded limestone in Naur Formation, and the presence of some thin marl beds which has high susceptibility of water absorption and seepage during the rainfall led to lubricate and facilitate the plane sliding (Fig. 30).

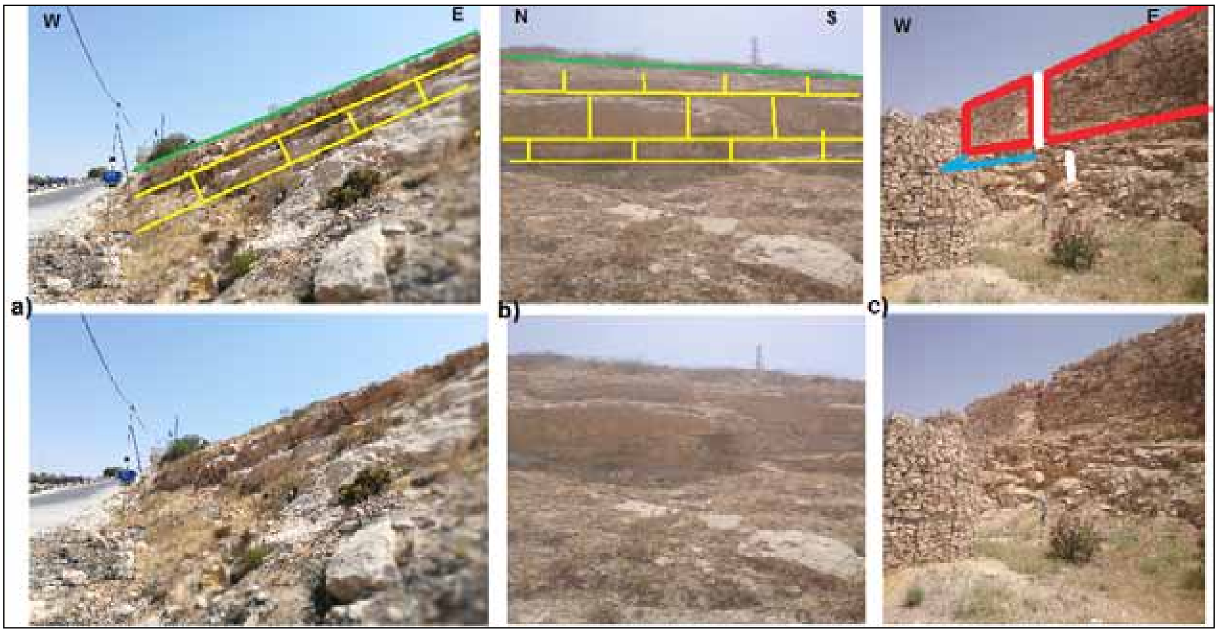

Figure 26. Side view of stable rock mass unaffected by cutting, b) Front view, c) Sliding rock mass has been affected by the direct cutting of the slope foothill in station-6.

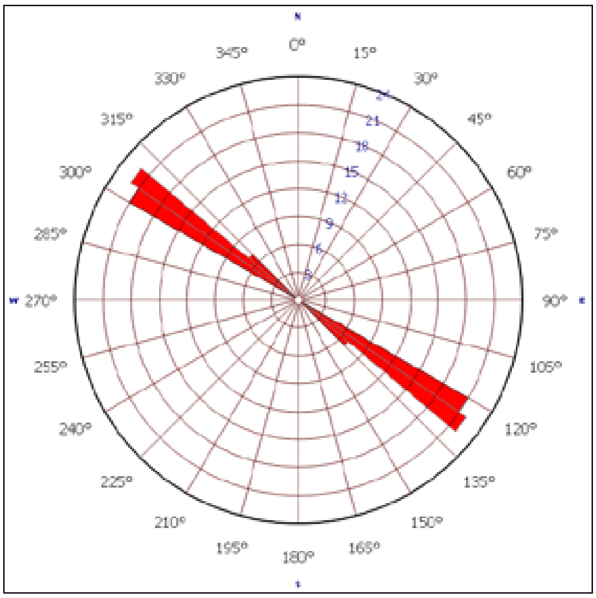

Figure 27. The strike of the main trend of the fractures in station-6.

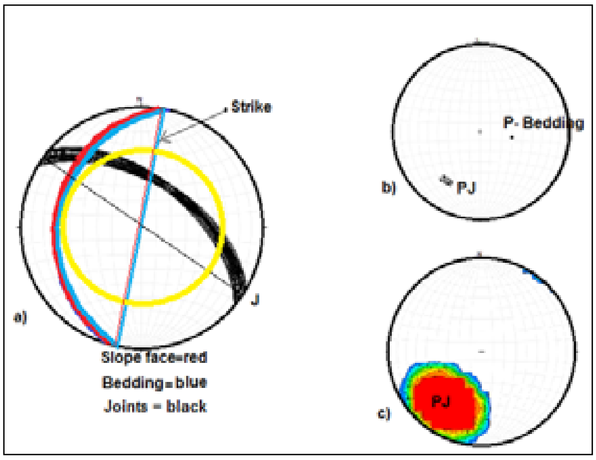

Figure 28. Stereonet diagrams represent the discontinuities (black great circles), slope face (red great circle), and plane sliding along bedding planes (blue great circle) in station 6.

Figure 29. The active landslide along the highway in the Salhub area after cutting the foothill in station-6.

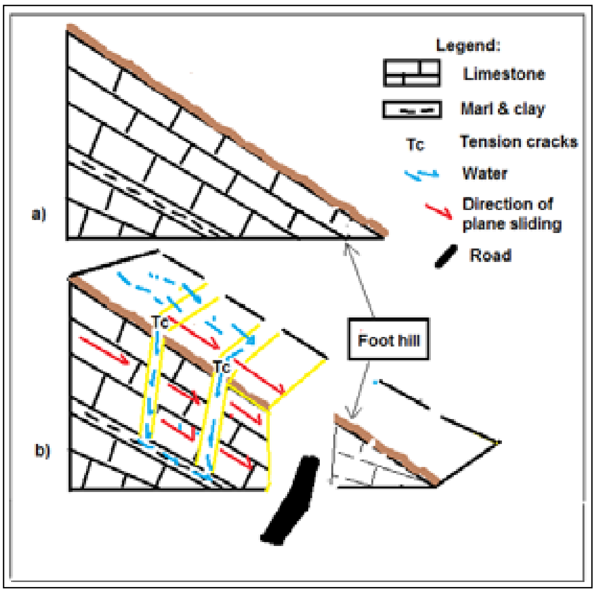

Figure 30. Schematic diagram showing what happened and to shed light on the manmade problem in station 6.

4.7 Station7

This station is located along the old Jerash-Amman road about 2 Km south of Jerash city. It is located at 32° 13. 705'N and 35° 53. 605' E (Fig. 3). The outcrop is part of the Kurnub group, medium to thick-bedded, yellow to dirty white, friable, fine to medium grained, quartzitic, massive and cross-bedded, interbedded with shale beds and clay lenses (Fig. 31). It was difficult to take orientation data measurements in this station because it characterized by friable sandstone and has highly weathered and fractured rock blocks. It also has a steep slope, therefore rock falls and toppling is probable in this station (Fig. 32).

Figure 31. Front view of the outcrop with lenses of clay in station 7.

4.8 Station 8

This station is located about 500 m south of Zarqa River. It is located at 32° 12. 343'N and 35° 52.251' E (Fig. 3). The outcrop is part of the Kurnub Group, which is characterized by highly weathered and friable sandstone. It was difficult to take orientation data measurements from this station. It is characterized by a steep slope with a smooth surface, which led to easier fall down limestone blocks from the Na'ur Formation above (Fig. 33).

Figure 32. Side view of the Kurnub outcrop in station-7, it is yellow to dirty white, friable sandstone (red circle), highly weathered, and highly fractured (red ellipses). The block highlighted blue will topple, the black stars show the topple and slide the block from location 1 to 2.

Figure 33. Kurnub outcrop in station- 8; a) side view, b) front view.

4.9 Station 9

This station is located along Jerash-Amman Highway about 25 Km south of Jerash. It is located at 32° 9.76'N and 35° 50.835' E (Fig. 3).The outcrop in the study site is Fuheis Formation, which is dominated by marls and marly nodular limestone. It also consists of soft, friable marls intercalated with lenses of calcareous--mudstone, thin beds of nodular and fossiliferous limestone. The outcrop is highly fractured in all directions, and highly weathered (Fig. 34). The high density of the fractures and the cohesionless of these fractures led to the circular failure as there is no preferred orientation for them (Fig. 35). Some fractures with preferred orientation NNW-SSE to N-S are also present in this station (Fig. 36). These fractures (J1) beyond the rock mass act as back release (tension cracks), and will be topple in this station (Fig. 36). The kinematic analysis of this station is shown in (Fig. 37).

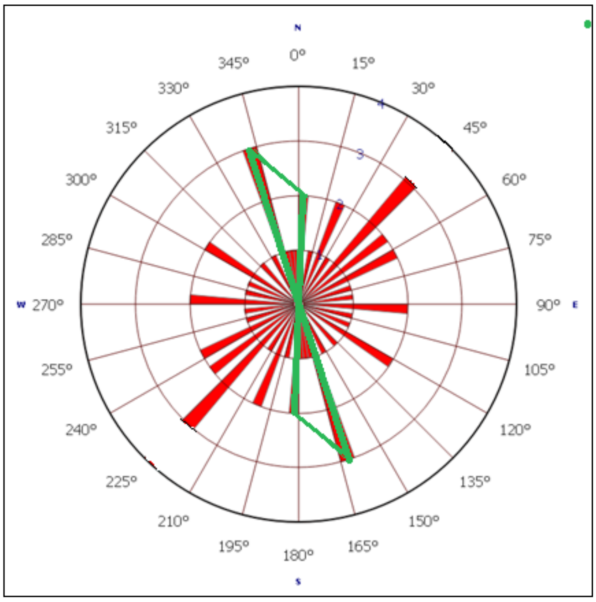

Figure 34. Strike measurements of randomly (no preferred orientation) oriented fractures in station-9; the green marked trend represents the toppling fractures set.

Figure 35. The outcrop shows the circular failure in station- 9.

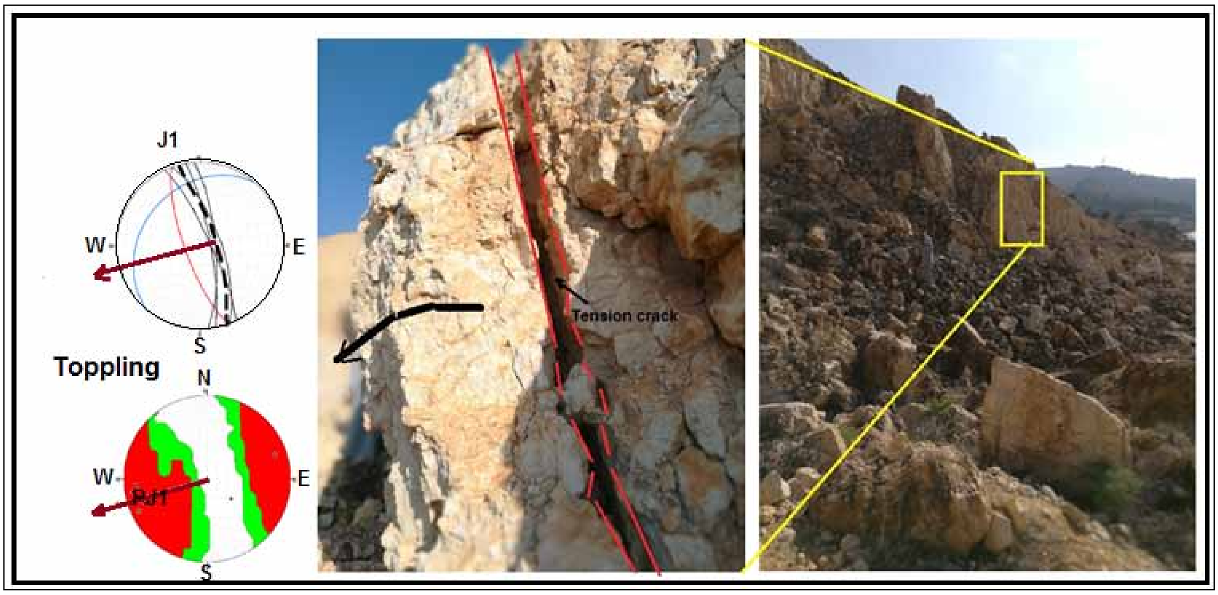

Figure 36. Toppling failure along J1 towards WSW (see the tension crack acts as back release surface) in station-9.

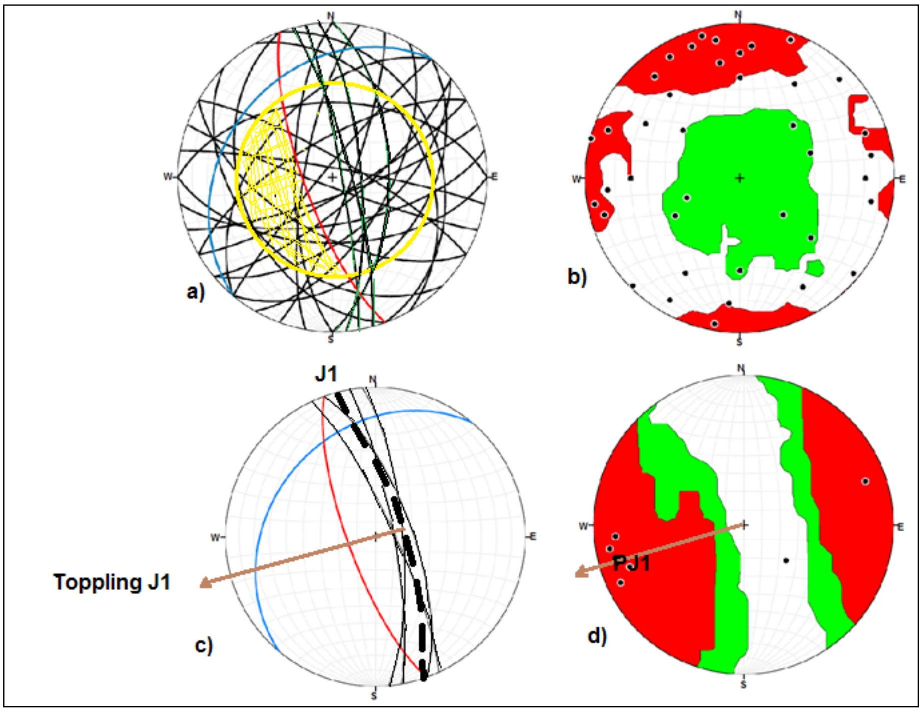

Figure 37. a) Stereographic projection (great circles) of the fractures, b) Poles of the fractures (no preferred orientation), c) Toppling failure along J1 towards WSW, d) poles of J1 (PJ1).

5. Discussion

5.1- Kinematic analysis

The study area is located along Jerash–Amman highway. The formations that outcrop in the study area are of Cretaceous (Fig. 3). The data were collected from nine measurement stations of the study area based on the discontinuity properties which have indications of the impact on slope stability.

Based on the kinematic analysis; there are five major joint sets (dip/ dip direction) that can be identified in Station1. Their attitudes are as follows: J1(80/075), J2 (80/290), J3 (68/140), J4(80/150), and J5 (88/255). While in Station-2 four major joint sets can be identified in this site with attitudes as follows: J1(60/110), J2 (86/280), J3 (70/150), and J4 (75/ 090). In Station-3 three major joint sets were identified with attitudes as follows: J1(70/ 270), J2 (50/ 300), and J3 (50/ 220). In Station-4 six major joint sets can be identified with attitudes as follows: J1(80/310), J2 (70/330), J3 (75/050), J4 (75/230), J5 (70/270), and J6 (vertical, strike= 140), and in station-5 six major joint sets were also identified with attitudes of J1(65/ 280), J2 (65/ 100), J3 (60/ 330), J4 (70/ 185), J5 (70/ 020) and J6 (70/050).

Station-6 which represents a major active landslide was analyzed through this study to show an ideal example (of mistake) of the active man-made landslide failure, that happened during road construction. In Station-7 it was difficult to take measurements of data orientation because it is characterized by friable sandstone and has highly weathered and fractured rock blocks. In Station-8 it was also difficult to take measurements of data orientation because it is characterized by a steep slope with a smooth surface and highly weathered rocks.

Station-9 has highly fractured rocks which resulted in a circular failure, whereas some fractures with preferred orientation in NNW-SSE to N-S resulted in toppling. These fractures (J1) beyond the rock mass act as the back release (tension cracks) and will lead to toppling. The results of the kinematic analysis in the study area show that the wedge failure in stations 1, 2, 3, 4, and 5 between joints (J2 and J4, J2 and J3), (J3 and J4), (J2 and J3), (J1 and J4, J2 and J4, J3 and J5), (J1 and J6, J1 and bedding, J3 and J6, J3 and bedding, J2 and J3). Toppling failure in stations 1, 2, 5, and 9 between the joint sets J1, J2, J4, and J1, respectively. Plane failure in stations 2, 3, 4, and 5 along the joint sets J1, J1, J5, and bedding, respectively. Whereas, circular failure was only observed in station 9. Based on the results of the current study the landslides were delineated and displayed on the land sat and on the geological map of the study area (Fig. 38).

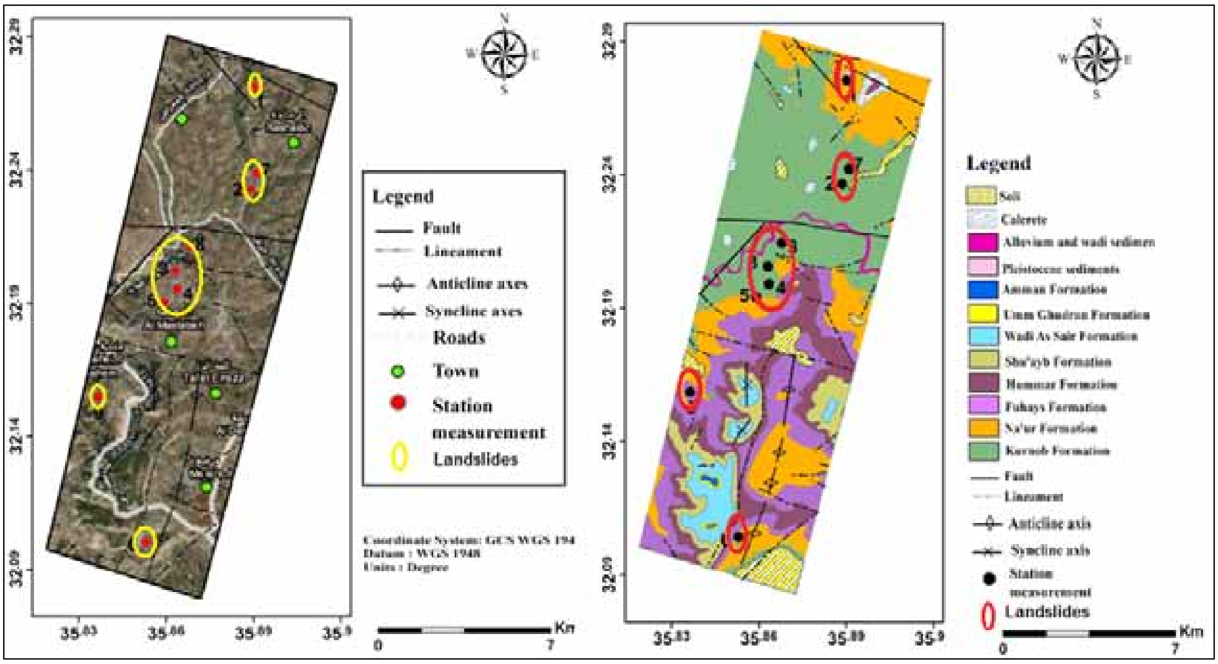

Figure 38. The delineated landslides (red and yellow ellipses) displayed on the land sat satellite image(Explorer 2018)and geological map, respectively.

5.2 Relationship between the measured fractures and the landslides in the study area

All measured microfractures with a total of 500 readings were represented in a rose diagram (Fig. 39). From the figure it can be inferred that the main trend is generally NNE - SSW. It is observed that the strike of the main trend of the fractures in stations 2, 3, and 4 (NNE to N) is parallel to sub-parallel to the strike of the slope face. In stations 1 and 5, the minor trends (NNW to NW) are sub-parallel to the slope face. In station-6 the fractures are oblique to slope face at about 45 degrees. In station-9 it is parallel to the toppling planes only in the NNW-SSE direction. This indicates the major role of the structures in rock landslides, particularly those related to planar, and toppling failures as they are sub-parallel to slope faces.

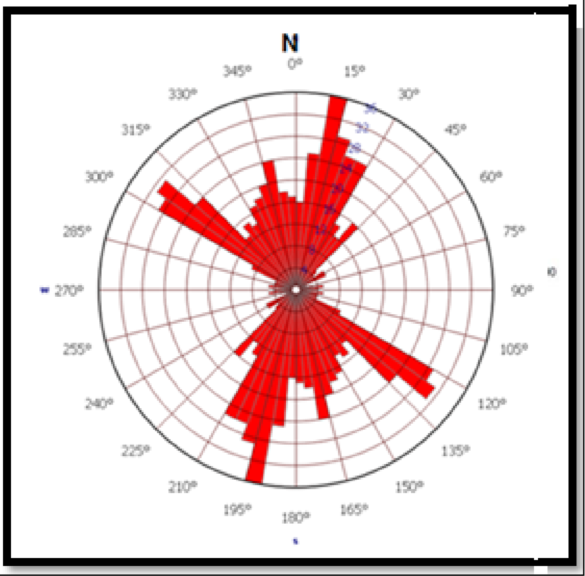

Figure 39. Strike measurements of all measured fractures in the study area

6. Conclusions

This study has pointed out and elaborated the kinematic analysis of slope stability in the study area. Results show that wedge failure in stations 1, 2, 3, 4, and 5 between joints (J2 and J4, J2 and J3), (J3 and J4), (J2 and J3), (J1 and J4, J2 and J4, J3 and J5), (J1 and J6, J1 and bedding, J3 and J6, J3 and bedding, J2 and J3). Toppling failure in stations 1,2,5 and 9 along the joint sets J1, J2, J4, and J1, respectively. Plane failure in stations 2, 3, 4, and 5 along the joint sets J1, J5, and bedding, respectively. In addition to circular failure in station 9. The 500 fracture measurements show a major NNE- SSW trend, and minor trends NNW- SSE, and NW- SE, which often are sub-parallel to slope faces. It is observed that the strike of the main trend of the fractures in stations 2, 3, and 4 (NNE to N) is parallel to sub-parallel to the strike of the slope face. This creates the most dangerous rock landslides in the study area, particularly those related to the planar and toppling failure. The dominant type of rock slope failure in the study area is wedge failure followed by toppling and planar failure. This enhances the role of the geological structures in land sliding. The study area has artificial (man-made) cut steep slopes in some stations, which led to landslide failure.

References

Abdelhamid, G. 1993. "Geological map of Jarash scale 1:50,000, sheet no. 3154-I." Natural Resources Authority, Amman, Jordan.

Abderahman, N. (2007). Evaluating the influence of rate of undercutting on the stability of slopes. Bulletin of Engineering Geology and the Environment, 66(3), 303-309.

Abderahman, N. S. (1998). Landslide at km 56.4 along the Irbid-Amman Highway, northern Jordan. Environmental Geosciences, 5(3), 103-113.

Abederahman, N. 1994. Rock Falls in The Zarqa River, Northern Jordan.Abhath AL-Yarmouk, Pure Since, and Engineering, 3 (2): 111-122.

Al-Basha, S. 1996. Geomechanical Characterization of Rock Slopes Along Amman-Jerash-Irbid. Highway. Unpublished M.Sc. Thesis, University of Jordan, Amman, Jordan.

Al- Hawareen, Y. 2019. Integrate structural analysis and clay mineral investigations monitor landslide: A case study (Jarash-Amman Highway), Unpublished M.Sc. Thesis, Al al-Bayt University, Mafraq, Jordan.

Al-Homoud, A. and Masanat, Y. 1998. "A classification system for the assessment of slope stability of terrains along highway routes in Jordan." Environmental Geology 34 (1):59-69.

Al-Homoud, A., Khoury, H., and Al-Omari, Y. (1996). Mineralogical and engineering properties of problematic expansive clayey beds causing landslides. Bulletin of the International Association of Engineering Geology-Bulletin de l'AssociationInternationale de Géologie de l'Ingénieur, 54(1), 13-31.

Al-Omari, A. 2014. The integrated application of geophysical techniques for the characterization of active landslides: A case study from Salhoub Landslide, Jordan. Unpublished M.Sc. Thesis, Yarmouk University, Irbid, Jordan.

Al-Omari, Y. 2006. “Fossil and recent landslides in central and north Jordan.” Unpublished MSc thesis, University of Jordan, Amman.

Barton, N. (1973). Review of a new shear strength criterion for rock joints. Engineering Geology, 7(4), 287-332.

Dames and Moor, 1993. "Geotechnical studies, Irbid-Jerash-Amman Highway " Submitted to Jordanian Ministry of Public Works and Housing, Amman, Jordan, (Unpublished report).

Diabat, A. and Abu Rumman, W. 2021. Rock Slope Stability Assessment Using Kinematic Analysis of the Limestone Quarries in Al Huson-Shatana Area, Jordan. Iraqi Geological Journal, 54 (2A), 11-33

Diabat, A. and Masri, A. 2005. "Orientation of the principal stresses along Zerqa-Ma'in Fault." Mu’tah Lil-Buhuth wad-Dirasat 20 (1), 57-71.

El-Moghrabi, M. 2016. Multi-Approach Evaluation of Landslide Susceptibility Along Jerash - Amman Highway. M.Sc. Thesis, University of Yarmouk, Irbid, Jordan.

El-Naqa, A., Abdelghafoor, M. 2006. Application of SINMAP terrain stability model along Amman-Jerash-Irbid highway, North Jordan. Electronic Journal of Geotechnical Engineering, 11(Bunde B): 2-19.

Explorer, USGS Earth. 2018. US Geological Survey Earth Explorer.

Hock, E. and Bray, J. W. 2003. "Rock Slope Engineering, " Revised 4th Edition, the Institution of Mining and Metallurgy, London. Pp. 23-45, pp.153-175,

Jaeger, J. C., and Cook, N. G. W. (1976) Fundamentals of Rock Mechanics, 2nd edn. Chapman and Hall, London, UK, 585 pp.

Mansour, Z., Mustafa, H., Abederahman, N. 1997. Geological and geotechnical studies of three main slides along Jerash-Amman highway. Abhath AL-Yarmouk, Pure Science and Engineering, 6(1): 79-104.

Masanat, Y. 2014. "Landslide hazards: geotechnical aspects and management policies." Jordan Journal of Civil Engineering 159 (3175):1-22.

Powell, J. 1989. "Stratigraphy and sedimentation of the Phanerozoic rocks in central and southern Jordan." Bulletin 11, Geology Directorate, Natural Resources Authority (Ministry of Energy and Mineral Resources) Amman, H K of Jordan.

Saleh, K. 1997. Geotechnical study of landslides on the road to Jerash Amman. Unpublished M.Sc. Thesis, Yarmouk University, Irbid, Jordan.

Sawariah, A, and Barjous, M. 1993 "Geological Map of Suwaylih Scale 1:50,000, Sheet no. 3154-II." Natural Resources Authority, Amman, Jordan.

Wyllie, D., Mah, C. 2005. Rock slope engineering: civil and mining. Taylor and Francis Group. London and New York.

JJEES

JJEES (2022) 13 (3): 190-198
ISSN 1995-6681

Jordan Journal of Earth and Environmental Sciences

Plants of Saline Coastal and Inland Sabkha Areas as Indicators of Environmental Conditions in Southern Jordan

Ikhlas Alhejoj[1*], Klaus Bandel[2],
Elias Salameh[1], Mohammad Al-Gharaibeh[3], Jwan Ibbini[4]

[1]The University of Jordan, Department of Geology, 11942, Amman, Jordan
[2]Universität Hamburg, Department of Geologisch-Paläontologische, Hamburg, Germany
[3]Jordan University of Science and Technology, Department of Plant Production, Irbid, Jordan
[4]The Hashemite University, Department of Land Management and Environment, Zarqa, Jordan

Received 26 September 2021; Accepted 5 March 2022

Abstract

In this study, plants of the coastal and inland saline Sabkhas and their indicator values of the arid regions of South Jordan (Taba Oasis and Aqaba coast) were discussed. Plants which that tolerate salty ground display a quite distinct character regarding their systematic composition at the different localities and distribution in Jordan. Most plants species which that thrive in the Gulf of Aqaba were considered fast fast-growing halophytes growing along the Gulf of Aqaba in a salty environment.

Zonation was recorded in the Taba wetland with low biodiversity due to high environmental stress. Taba plants were dominated by different salt-tolerant, heat heat-stress-tolerant, and drought drought-resistant plant communities. Plants in dry environments were being affected by human development activities and climate change. In Jordan, with its arid climate, most plant species were sensitive to environmental changes so that small changes in water availability and salinity due to climatic conditions were reflected in changes in occurrence, distribution, and richness of native plant communities.

The study builds baseline knowledge of the environmental conditions of both the Aqaba and Taba areas to serve future evaluations of changes taking place in these areas due to human activities. It is thought ofto be seriously taken by policy-makers in order to safely plan future developments in orderto minimize actions leading to detrimental environmental changes resulting from human settlements, industry, and others related anthropogenic activities.

Keywords: *Halophytes, saline-alkaline tolerance, environmental indicators, wetland, climate change*

1. Introduction

Plants in wetland and coastal areas are of economic and ecological values, including; their roles in natural water purification from sediments, pollutants, and nutrients; Some of these wild plants are edible and some are used in traditional medicinal treatments; they can combat desertification by fixing sand dunes and preventing wind erosion; they can provide forages for grazing animals; they can be a keystone by providing wild animals food, shelter and nesting place and therefore helps in ecosystems integrity and enhance biodiversity in such harsh(Whigham et al., 1988; Kuusemets and Mander, 1999; Crumpton, 2001; Reed and Carpenter, 2002).

Several types of ecosystems under different environmental conditions are characterized by distinct plant communities that can be used to identify and evaluate their integrity (Fort and Freschet, 2020; Squires and van der Valk, 1992). Many studies confirmed that plants are powerful indicators of environmental conditions given their rapid response to environmental changes that reflect accumulative long and short time changes in the ecosystem, including water turbidity, nutrient enrichment, and organic and chemical pollutants (Craft and Richardson, 1998; Wardrop and Brooks, 1998; Bayouli et al., 2021). The other reason to use them as bioindicators is their immobility as organisms and their occurrence in all wetlands. The taxonomy of the floral species of Jordan was well described and identified by Zohary (1973), Albert et al. (2004), AL-Eisawi (1998), and others. Wetlands, dry lands, and aquatic bodies in Jordan, have characteristic sets of plant species, which sometimes provide good indicators of environmental conditions. For example, Azraq Sabkha with salt-tolerant indicator species includes the flora Spergularia media, Suaeda vera, Tamarix passerinoides, and Spergularia marina (Alhejoj et al., 2015). Additionally, Al Khateeb (2018) studied the use of wild plants as a pollution bioindicator to assess their geno-toxicity.

Jordan is situated in the transition zone between arid and semiarid bioclimates and although the distance between the northern and the southern borders is only about 400 km, the annual rainfall can be as high as 600 mm in the north-western mountains and as low as 50 mm in the southern and eastern desert regions (MoWI and DOM open files). The strong spacial variation in the climate results in conspicuous changes in the vegetation and in the composition of the flora over relatively short distances (Zohary, 1973). Jordan is also the meeting place of four major phytogeographic regions: the Mediterranean (subhumid and semiarid Mediterranean), the Irano-Turanian (arid Mediterranean), the Saharo-Arabian and the Sudanian regions (Zohary, 1973;

* Corresponding author e-mail: i.alhejoj@ju.edu.jo

Al-Eisawi, 1985, 1996; Albert et al., 2004; Muhaidat et al., 2018). In the bioclimatic analyses by Al-Eisawi (1985, 1996), nine subdivisions are considered that fall under four main bioclimatic regions, representing a gradient of decreasing precipitation and increasing temperature: (I) subhumid Mediterranean bioclimate; (II) semiarid Mediterranean bioclimate; (III) arid Mediterranean bioclimate; and (IV) Saharan Mediterranean bioclimate. These bioindicators are faced by several problems including: soil salinity, deep groundwater levels, and temporal rapidly changing rainfall and temperatures. Salinity and climate change are worldwide environmental issues and are the main factors affecting plant species diversity and occurrences.

The main objective of this study is to discuss the use of plants as indicators of the prevailing environmental conditions in the coastal area of Aqaba and the Sabkha of Taba in southern Jordan (Fig.1). In addition, this study will discuss and correlate the occurrences of the same plant species in other areas in Jordan.

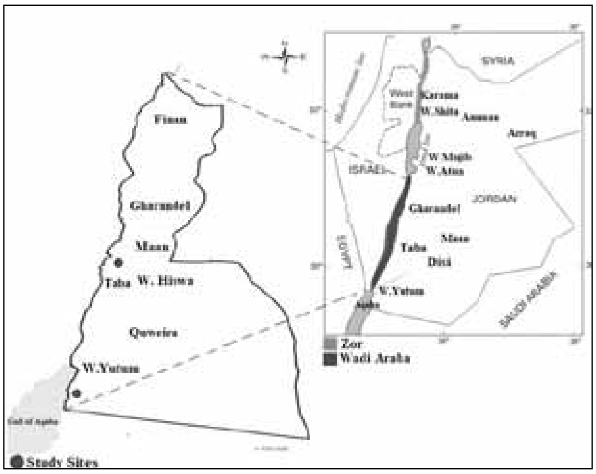

Figure 1. Location map of the studied sites in Southern Jordan. 1. The coastal area of the hotel complex and the Royal Diving Club in Aqaba. 2. The Sabkha of Taba in Wadi Araba.)

2. Methodology

This study builds on the intensive field and laboratory work, collection of samples and their analyses and identification in the field and in the laboratory, interpreting analytical results, and reporting.

3. Discussion of Field and Laboratory Findings

3.1 Coastal plants of The Gulf of Aqaba

The Gulf of Aqaba lies in the southernmost part of Jordan with an ashore length of 26 km. It is the only access of Jordan to the open sea where most import and export activities of the country take place, such as oil, and exports such as phosphate rocks, potash, fertilizers, cement, bromine, magnesium, and other industrial products. The resulting liquid and solid wastes of household and industrial activities are still being disposed of after modest treatment porting. In addition, the shore of Aqaba is a touristic attraction for inland and outland tourism.

The climate in the area is hyper hyper-arid with a a long long-term average precipitation of 30 mm/yr with daily maximum temperatures rising in summer to more than 40^0C degrees (June to August), that which can reach up to 48^0C. Potential evaporation rates reach around 4000 to 4400 mm/yr. (DOM open files).

Plants growing on salty grounds display distinct characteristics regarding their systematic composition in the different climatic zones in Jordan.

Thus a quite specific flora composes the community that had grown next to the Gulf of Aqaba on the uppermost sandy beach that had been separated from the lower beach by an earth wall during construction works (Fig.2). This barrier prevented the flood water of the rare rains in the area falling during the end of March 2014 to simply flow off into the sea and rather to collect in a shallow pond. Rain The rain had fallen one week before our survey, after that the weather became dry and sunny as it is usual for that area. The collected had diluted the salt crust of the soil that had accumulated here during the extended dry period before the raining. The water seeping into the ground moistened it before evaporating, and a dense plant cover grew only in those parts of the small pond that held water and remained moist for a sufficient time to allow the plants to grow. In the last puddles crust of salt formed when the water evaporated.

The plants studied on the 23rd of March 2014 thus reached their size and usually also the flowering and fruiting stage within a time of about 10 days.

Figure 2. Growth zone near the beach of the southern part of the Gulf of Aqaba. The depression near the dam held water which that became so salty that plants could not grow in it.

Albert et al (2004) reviewing data provided by Zohary (1973) suggested that the shore area may have a flora influenced by salinity. *Atriplex halimus, Sueada aegyptiaca, Suaeda monoica, Tamarix negevensis, Tamarix tetragyna,* but also *Typha angustata* were recorded and sandy soils should have *Salsola baryosma, Traganum nudatum, Alhagi maurorum* and *C. cretica* growing on them. But based on field observations, the flora encountered here has a quite different composition. *Tamarix* was not noted at all and probably had no time to grow, and *Traganum* may have been among the young plants encountered by us.

In the area a community of quite a different composition was encountered, *Atriplex holocarpa* with globular green fruits in its upper part is observed. Within the Chenopodiaceae a tendency of efficient uptake of ions and storing them in distinct parts of the plant has developed. High salt concentrations in some cells thus decrease the salt present in the other cells.

A. halimus saltbush is common in Jordanian desert (Albert et al., 2004). But for this first time documented, *A. holocarpa* with greenish globular fruits live in the salty ground of Aqaba (Fig.3A).

While most of the plants encountered us were in full flower, *Opophytum forsskalii* was present only as juvenile and thus had to continue to grow to flower and form seeds, the others had reached maturity and were in the seed production and ripening stage.

Also, the white flowering *Anthemis haussknechtii* with hairy leaves was commonly encountered, but less than *A. holocarpa*. Al- Eisawi (1998, fig. 130) noted that this plant grows in the desert, and we found it also in the dry bed of Wadi Yutum which drains Mudawwara area into the Red Sea at Aqaba. According to Feinbrun-Dothan (1978), its growing environment is the mountain area above 800 m. But *A. haussknechtii* is found on the salty moist ground in Aqaba.

The characteristic *Aaronsohnia factorovskii* with yellow composite flowers with only disc floret and no ray floret is relatively common. Both composite flowers also grow in the desert e.g.: Wadi Yutum, and were observed here in flower on the same day when they were observed in Aqaba.

O. forsskalii can be found commonly in the company of, *Sclerocephalus arabicus* and *Aizoon canariense* (Fig.3B). Of these, *Sclerocephalus* also grows in the not salty desert Wadi Yutum. Especially *A. canariense* is characteristic of the salty soil on the beach of the Gulf of Aqaba in Jordan. A similar environment on the salty flats of the brackish Karama Reservoir in the Jordan Valley has a similar *Mesembryanthemum*. *Aizoon* prefers to grow in moist and high salinity sandy ground.

The thistle *Centaurea sinaica* can be recognized by its spiny involucres and still without flowers, occurring rarely, while other thistles are missing. *C. sinaica* as noted by Al-Eisawi (1998) has the stem right above the basal rosette branching as is the case in the juvenile plant we found growing on the salty ground near the beach of the Gulf of Aqaba. Otherwise, the plant has been described to grow on cultivated land and waste fields in the highlands of Jordan.

Along the ridge of sand separating the salty area that held the shallow pond during the rain flood, the small bush *Halocnemum strobilaceum* has grown and here also *Amaranthus albus* was found. *Anabasis setifera* forms larger bushes, and *Chenopodium ambrosioides* is one of the larger plants here with large stands of flowers of rather indistinct small size. This bush-like growth also follows former water canals.

Figure 3. A. Characteristic plant of the population A. holocarpa with O. forsskalii and with salt in a dried-out puddle. B. A. canariense together with O. forsskalii, Chenopodium species, and Arnebia hispidissima.

Among the Brassicaceae four species are present, the most characteristic is the almost *Zilla spinosa* forming thorny bushes with bluish flowers, *Eruca sativa* with larger veined flowers and its relatives *S. septulatum* with yellow flower and *D. harra* of the same character as flowering also in the dry bed of Wadi Yutum. *E. sativa* can not only tolerate relatively dry ground as on the slopes of the Zor in the Jordan Valley but can also grow on the salty ground, as here near the beach at the Gulf of Aqaba. *D. harra*, and *S. septulatum* grow in similar environments in the Jordan Valley probably here also sometimes with salinity higher than usual due to the high evaporation rates. *Z. spinosa* likes hot moist places, also when they are not salty. But they also grow on the dry ground of Wadi Yutum, following the moisture here after floods.

The small clover *Tetraena simplex* with small yellow flowers grows flat on the soil and is found in other salty places in Jordan as well (Al Khateeb et al., 2010; Muhaidat et al., 2018). The other member of the Leguminosae family *Astragalus crenatus* grows elsewhere close to the ground but has purple flowers; both tolerate salty ground but are also found elsewhere.

O. forsskalii was present during March with its characteristic thick leaves but without flowers. Characteristic also is the yellow *Arnebia hispidissima*, bushes of *Ochradenus baccatus* forming plants with a woody base and many green branches with small leaves and yellow small flowers. But all these plants grow also around puddles after strong rains in the Eastern desert in Jordan. *Trichodesma Africana* from the Boranginacea family and Sclerocephalus from the Caryophyllacea family grow here as they do on the sand in Wadi Yutum but here on the Gulf next to flowering *A. canariense* and juvenile *O. forsskalii*, both are typical halophytes.

The yellow composite *Picris cyanocarpa* is present here as well as in desert places near dried-out puddles. Its fruits are attached to a pappus and fly off with the wind. The plant grows in the desert and it grows also on the salty ground near Aqaba beach together with *A. canariense* (Fig.4A).

Among the monocotyledons only the lily *Asphodelus tenuifolius* occurs rarely while it commonly occurs on dry stony ground in the Jordan Valley. It is an annual or short-lived perennial herb growing with a hollow stem up to 70 centimeters tall. The root system has a series of tuber-like parts at the base of the stem (Feinbrun-Dothan, 1986; Al-Eisawi, 1998). The inflorescence consists of widely-spaced flowers which are generally white or very pale pink with a neat central longitudinal stripe of brown to reddish-purple (Al-Eisawi, 1998). This is the smaller of the two species of the genus from Jordan and was found in a rather dry environment as well as near River Zarqa spring and also among the plants in Aqaba. Thus it tolerates salty ground but is usually found outside of that also in quite dry areas (Alhejoj et al., 2014). Only three glasses were noted in this small specialized flora. Of these *Polypogon monspeliensis* has a characteristic fluorescence and *Hordeum marinum* is common. *Dichanthium annulatum* grows at irrigated places and ditches as well as banks of water reservoirs in the Jordan Valley. *D. annulatum* also grows along the Gulf of Aqaba even in the salty environment (Fig.4B).

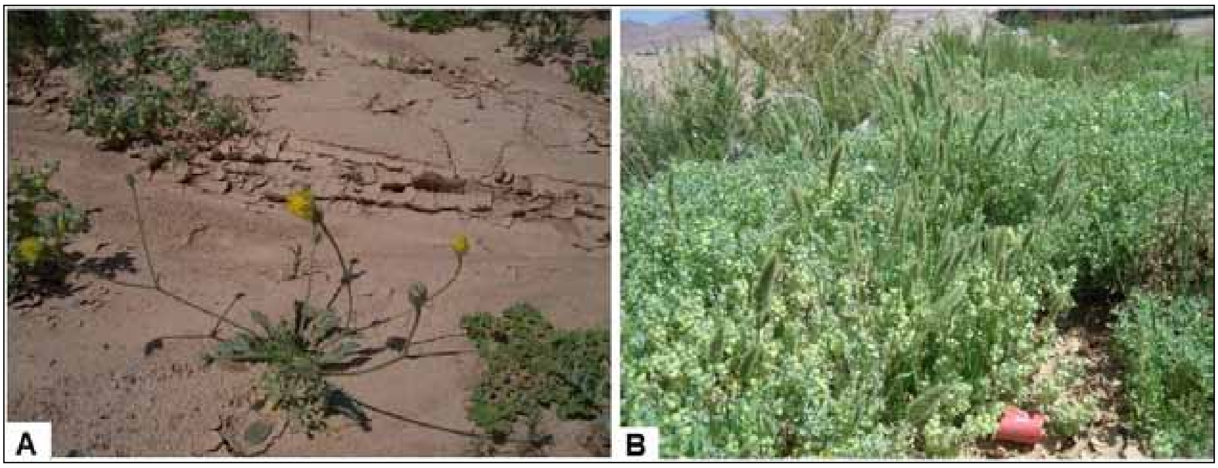

Figure 4. A. *Picris cyanocarpa* next to *A. canariense*. B. *P. monspeliensis, H. marinum, and D. annulatum* from the salty ground at Aqaba growing jointly with *A. holocarpa* and in the same environment as *Z. Spinosa* and *A. setifera* growths.

3.2 Taba Sabkha

Wetland flora includes all different types of vegetation that live in water or sediments which become periodically deficient in oxygen as a result of excessive water content (Cowardin et al., 1979).

The Sabkha of Taba is located in the southern Wadi Araba near Gharandal, about 32 km north of the Gulf of Aqaba. It occupies an area of about 55 km^2 in southern Wadi Araba. The area is characterized by its hyper-arid climate with an average annual rainfall of 30 mm. The daily highest temperature can reach 48◦C. The average rainfall over the eastern mountains is up to 250 mm/year; flood water flows westwards via numerous wadis to Wadi Araba including the Sabkha of Taba.

In Wadi Araba, the Sabkha of Taba is permanently saturated with water with saline, hydric, and peat soils. Hydric soil, resulting in anaerobic (low oxygen) conditions. Plants with aerenchyma tissues often dominate such environments which allow atmospheric oxygen to be transported to their roots (Justin and Armstrong, 1987; Keddy, 2010). Oxygen concentration in wetlands depends on several factors, including soil temperature, chemical reduced elements, and organic matter content (Gambrell and Patrick, 1978). Additionally, Taba soil is covered by salt crusts, which result from the high evapotranspiration rate which exceeds the yearly precipitation by more than 100 fold. The salty surface crusts consist of evaporate minerals (gypsum, and halite) formed due to salt accumulation of evaporation from low salinity shallow groundwater entering the Sabkha from the fan seeping westwards through the Sabkha and from low precipitant with high evaporation.

Taba wetland represents an environment in which evaporation is much higher than the water that is added to the shallow depression during the rare winter floods and that of the springs which issue onto the flat from its eastern margin, that water seems to originate from sporadic recharge along the mountain range that separates Wadi Araba and Taba area from the Disi flats. Here the possible connection between Disi and Wadi al Hiswa lay in the area northwest of the town of Quweira to Wadi Araba near Taba (Bandel and Salameh, 2013). The rising mountain chain that accompanies the eastern margin of southern Wadi Araba seems to cut off that connection. But there are still ways for the groundwater to reach the Wadi Araba. The springs at the margin of the Sabkha have, most probably, their origin in Disi.

Taba in Wadi Araba is a typical Sabhka having a characteristic succession of its vegetation as reported by Albert et al. (2004) and our observations confirm. The Taba swamp dry lake can be considered as one of the historic outlets of the Disi groundwater basin before its capture by headword erosion of Wadi Yutum into Aqaba (Bandel and Salameh, 2013).

Taba plant species consist of, *C. cretica,* an alkali weed that grows at the margin of the dry oases near the road. *C. cretica* of the Convolvulaceae has been indicated by Zohary

(1973) to live in a dry salty environment, as was also stated by Feinbrun-Dothan (1978, pl. 46) and repeated by Al-Eisawi (1998, fig.233). *C. cretica* was encountered to also grow and flower in the lower Wadi Shita, north northeast of the Dead Sea on the salt-free ground, whereas, near Taba, the ground contains some salt. *C. cretica* with rose-colored flowers were also found along the dry margin of Mujib River together with *A. halimus, Suaeda aegyptiaca, Alhagi maurorum,* and the grasses *Aeluropus littoralis, Desmostachya bipinnata.* Among the halophytes recorded from the shore of the Red Sea of Saudi Arabia *C. cretica* has also usually been determined.

Next to the Cressa belt, at the base of fans coming from the mountains, bushes of Acacia grow, and on the other side of this grow zone towards the Sabkha *P. dactylifera* is the dominant tree (Figure 5. A). Albert et al (2004) noticed that *Acacia* (near the salty ground) sometimes stores salt in their leaves. When the sun is intense, small leaves and folding of leaves help Acacia against becoming too hot as does a thick cover of hairs that reflects the sunlight. Acacia is present on dry slopes in the Araba and it also occurs near streams in the hot Jordan Valley, here often jointly with the similar *Prosopis*. When flowering, many insects and also a bird with narrow crooked beak come to harvest nectar. *A. tortilis* grows in extremely arid conditions up to 20 m in height. The plant tolerates high alkalinity, drought, high temperatures, sandy and stony soils, and sandblasting. Fruits are often eaten and excreted seeds have a better chance to germinate than such fallen out of the dry fruit. When having passed the digestive system they are within the excrements and thus have a better start for growth than the single seeds, which are often collected by insects for food.

Next to the dried salt flat with its mud cracked cover and thin salt crusts in former puddles a rim of vegetation consisting of palm trees, and *Tamarix* bushes along with *Phragmites* reeds form together dense thickets at the margin of the Sabkha. A zone follows with the loose growths of *J. rigidus, T. nilotica, T. tretragyna,* and quite characteristically *N. retusa* follows (Figure 5. B). *N. retusa* also forms small thicket islands further towards the mud-cracked flats of the Sabkha with no flora around them and no plants on the mud flat due to higher salinity and precipitation of gypsum-halite crust (Figure 6. A, B).

P. dactylifera, date palm, occurs commonly in Jordan, in the wild, and as a fruit tree. When fully grown it ranges from 5 to 15 m forming a tree with a single woody stem. The leaves are compound, pinnate, spiny and about 3 m long. Their flowers have a compound and spiked arrangements and usually appear during the springtime (Zohary, 1973; Al-Eisawi, 1998). The date palm grows near all the springs on the slopes of the Dead Sea. The trunk is surrounded from the ground upward, by a spiral pattern of leaf bases and in not attended trees the dry leaves remain attached forming a protective veneer.

P. dactylifera is an important culture plant in the Sahara-Arabian region, resembling in its importance the olive in the Mediterranean area (Zohary and Hopf, 1994). *Phoenix* tolerates alkaline conditions and also grows with moderately salty water, but high salt content has a negative effect and lowers the quality of the fruit (Morton, 1987). Kharusi et al (2017) stated that soil tolerances of up to 2400 µS/m. Brackish and freshwater springs along the steep slopes of the Dead Sea are usually quite well recognized by the date palm which is usually accompanied by *Phragmites australis*, as is also the case at Taba.

N. retusa is a salt-tolerant shrub or bush that grows to 2.5 m, although it is usually less than 1m in height. It has tiny, white to green, fragrant flowers, and small edible red fruit. *N. retusa* was recognized by Zohary (1972, pl. 371) as living in the saline desert and recognized by us in Taba salt pen-lake. It has woody stems with many hanging branches which carry succulent leaves and sharp brownish horns. The leaves are simple, triangular, and alternate with one leaf at each node. The small whitish flowers bear five petals and 15 stamens and the plants flower in March and April. *N. retusa* inhabits salty and dry environments and can live in poor soil quality. It also grows on sand and stony soil near water which at Wadi Atun has a salinity of more than 2000 µS/cm.

J. rigidus is the same reed as that growing near the western pool at Azraq with less salinity in the ground. Its inflorescences are about 60 cm high and its leaves have very acute apices. It grows in salt marshes and saltwater pools near oases. It is also found near springs in Jordan often together with *Juncus acutus*. Feinbrun Dothan (1986, pl.186, 187) noticed the mix of both species, especially in saline soils.

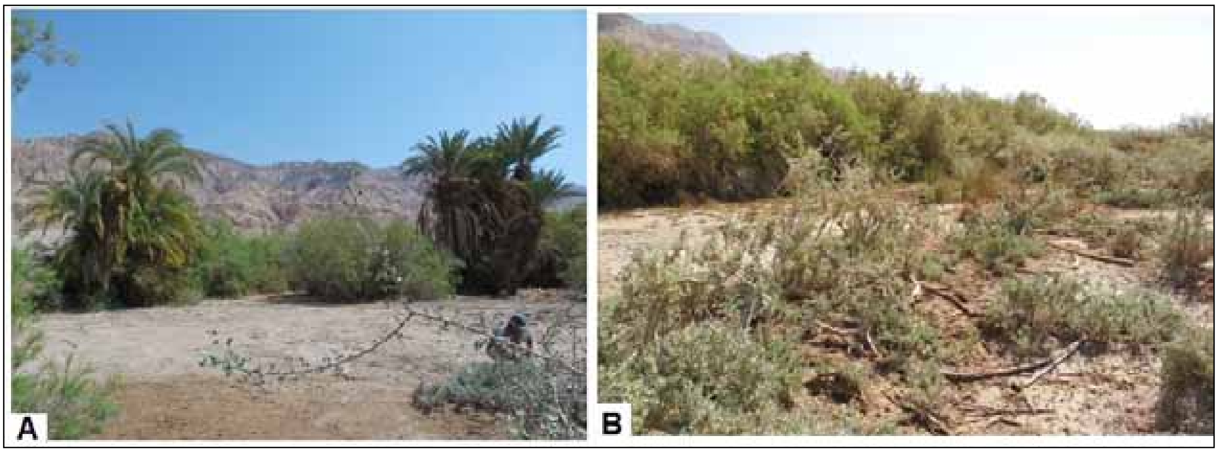

Figure 5. A. The Sabkha of Taba with *Phoenix* tree on the salty soil (2014) B. *N. retusa* community with *Tamarix* bushes in March 2014.

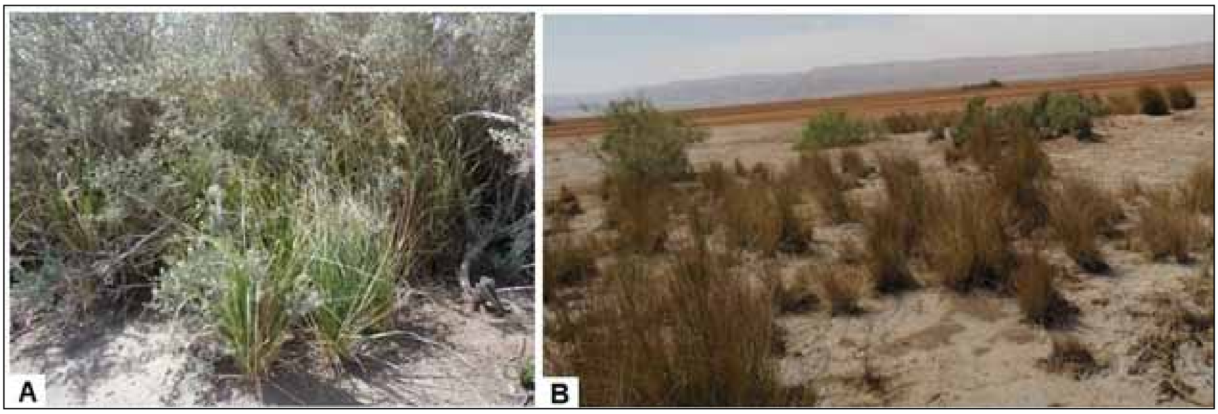

Figure 6. A. *N. retusa* with *Juncus arabicus*. B. *N. retusa and J. rigidus* together with *Tamarix* trees in a mud salt flat, no plants are found in the central part of Taba.

4. Results

The studied plants have been found to tolerate salty ground on both the shore of the Gulf of Aqaba and the Taba wetland, but they are quite distinct from each other. On the shore of the Gulf of Aqaba, plants grew after heavy rain on the salty ground on a slightly inclined field next to the beach, separated from the Sea by a small earthen wall. The most characteristic plants in Aqaba are *Atriplex holocarpa, A. haussknechtii, and A. factorovskii* which are relatively common in the Jordan desert. The thick green fleshy leaves of *O. forsskalii* can be found commonly with *S. arabicus* and *A. canariense*. Of these, *Sclerocephalus* also grows in the not salty desert of Wadi Yutum. Especially *A. canariense* is characteristic to the salty soil on the beach of the Gulf of Aqaba, while the similar environment of the salty flats of the brackish Karama reservoir has similar Mesembryanthemum. *A. canariense* prefers to grow on soils in places of puddles becoming increasingly saltier due to evaporation, thus a salt crust covers the sandy bottom. Along the ridge of sand separating the salty area from the shallow pond, the small bush *H. strobilaceum* and *A. Albus* have grown. *A. setifera* forms larger bushes, and *C. ambrosioides* is one of the larger plants here with large stands of flowers of rather indistinct small size. Among Brassicaceae four species are present, *Z. spinosa*, *E. sativa*, *S. septulatum,* and *D. harra*. The small *T. simplex* and *A. crenatus* grow commonly on the salty ground. *O. forsskaolii* is present with *A. hispidissima*, bushes of *O. baccatus*. *T. Africana* of the Boraginaceae and Sclerocephalus of the Caryophyllacea grow here as they do on the sand in Wadi Yutum but here on the Gulf next to flowering *A. canariense* and juvenile *O. forsskaolii*, both are typical halophytes.

Many plants in dry areas have been found in both saline and non-saline environments such as *S. arabicus, Z. Spinosa, D. harra, Trigonella stellata, A. fistulosus, T. Africana, A. crenatus*, *P. cyanocarpa*, *E. Sativa* and thorny plant of *C. sinaica* (Table.1).

Taba wetland has a characteristic set of plant species, which provide the best indicators of the very drought-resistant species and saline-alkali environmental conditions. These include the flora *N. retusa, J. rigidus, T. nilotica, T. tretragyna, Phragmites australis*, and *C. cretica*. They are of high drought tolerance and can grow without shallow soil water due to the depth of their roots. In the Sabkha of Taba salt-tolerant plants grow on muddy soil with salt crust as is also found in the surrounding Karama Reservoir lake that contains salty water. The formation of the salt crust led to reducing evaporation rate (Xinhu and Fengzhi, 2019).

Table 1. Summary of plant species indicating salinity in the study area.

Species	Family	Site	Environment	Level of Salinization	Habits
Atriplex holocarpa	Amaranthaceae	Aqaba beach, Dead sea valley	Coastal sandy or gravelly, dry, salt-crusted soils	High	Annual herb
Anabasis setifera	Amaranthaceae	Aqaba beach	Coastal sandy, mostly dry	High	Perennial shrub
Halocnemum strobilaceum	Amaranthaceae	Aqaba beach	Coastal sandy soils	High	Perennial shrub
Amaranthus albus	Amaranthaceae	Aqaba beach	coastal sandy soils	High	Annual herb
Chenopodium ambrosioides	Chenopodiaceae	Aqaba beach	Sandy, salty soils	High	Annual herb
Chenopodium murale	Chenopodiaceae	Aqaba beach	Coastal sandy soils	High	Annual herb
Tetraena simplex	Zygophyllaceae	Aqaba beach	Coastal sandy soils	High	Annual to perennial herb
Zilla Spinosa,	Brassicaceae	Aqaba beach, Wadi Yutum	Sand or gravelly soil	Low to high	Annual herb
Eruca sativa	Brassicaceae	Aqaba beach, Wadi Yutum, and Jordan Valley	Coastal dry sandy or gravelly soils	Low to high	Annual herb

Species	Family	Site	Environment	Level of Salinization	Habits
Sisymbrium septulatum	Brassicaceae	Aqaba beach	Coastal sandy soils	Low -High	Annual herb
Diplotaxis harra	Brassicaceae	Aqaba beach, Wadi Yutum	Sandy, gravelly soil	Low to high	Annual herb
Anthemis haussknechtii	Asteraceae	Aqaba beach, Wadi Yutum	Sandy, gravelly soil	Low to high	Annual herb
Aaronsohnia factorovskii	Asteraceae	Aqaba beach, Wadi Yutum	Coast, desert sandy, gravelly soil	Low to high	Annual herb
Centaurea sinaica	Asteraceae	Aqaba beach	Coastal sandy wet soils	Low to high	Annual herb
Picris cyanocarpa	Asteraceae	Aqaba beach	Coastal sandy soils		Annual herb
Opophytum forsskalii	Aizoaceae	Aqaba beach	Coastal salt–crusted sandy soils	Very high	Perennial herb
Aizoon canariense	Aizoaceae	Aqaba beach, Karama	Coastal salt – crusted sandy, rocky soils	Very high	Annual herb
Ochradenus baccatus	Resedaceae	Aqaba beach	Sandy, rocky and dry soils	Low - moderate	Perennial shrub
Astragalus crenatus	Fabaceae (Leguminosae)	Aqaba beach	Costal sandy soil, freshwater wetlands	Low - High	Annual herb
Trigonella stellata	Fabaceae (Leguminosae)	Aqaba beach	Coastal sandy soil and desert	Low - High	Annual herb
Trichodesma Africana	Boraginaceae	Aqaba beach	Coastal sandy soils	Low - High	
Arnebia hispidissima	Boraginaceae	Aqaba beach	Coastal sandy soils	Low- Moderate	Annual herb
Asphodelus tenuifolius	Asphodelaceae	Aqaba beach	Dry, sandy, or rocky grounds	Low - High	Annual herb
Sclerocephalus arabicus	Caryophyllaceae	Aqaba beach, Wadi Yutum	Dry sandy, gravelly soil	Low - High	Annual herb
Nitraria retusa	Nitrariaceae	Taba Sabkha, Dead Sea area (Wadi Atun)	Sandy or rocky with salt crusted and poor soil quality.	Low- High	Perennial shrub
Tamarix nilotica,	Tamaricaceae	Taba Sabkha	Dry, sandy, or rocky grounds	Low - High	Tree
Tamarix tretragyna	Tamaricaceae	Taba Sabkha	Sandy or gravelly and dry soil	Low - High	Tree
Cressa cretica	Convolvulaceae	Taba Sabkha, Mujib	Dry sandy and rocky salty alkaline soil	High	Annual herb
Acacia tortilis	Fabaceae	Taba Sabkha	margins of sabkha Dry, alkaline, sandy, stony soils	Low - Moderate	Tree
Phoenix dactylifera	Arecaceae	Taba Sabkha	margins of Sabkha with alkaline, sandy, and stony soils	Low- Moderate	Tree
Juncus rigidus	Juncaceae	Taba Sabkha, Azraq	Sandy soil near oases and around water pools	Low - High	Perennial herb
Polypogon monspeliensis	Poaceae	Aqaba beach	Coastal wet sandy soils	Low - High	Annual beard-grass
Hordeum marinum	Poaceae	Aqaba beach	Coastal wet sandy soils	Low -High	Annual grass
Dichanthium annulatum	Poaceae	Aqaba beach, Jordan Valley	Coastal wet sandy soils	Low - High	Perennial grass
Phragmites australis	Poaceae	Taba Sabkha	Wet, alkaline, sandy, stony soils	Low - High	Annual reed

5. Conclusions

Plant occurrence and distribution are mainly affected by soil and water types and composition, and by the prevailing climatic conditions such as temperature and rainfall. Climate change is affecting the habitats of several plant species because they are sensitive to salinity and dryness, immobile, and adapted to their specific environment so that they respond to climate change within short periods. A wide range of salinity stress management, monitoring, and mitigation strategies are required to deal with such impacts. Remote sensing and GIS techniques can be used as useful tools for developing soil salinity prediction models in areas experiencing soil salinization (Alqasemi et al., 2021). In addition, Shrivastava and Kumar (2015) study support the use of microorganisms as effective methods for soil salinity alleviation by developing stress-tolerant crop varieties through genetic engineering and plant breeding.

In South Jordan arid to hyper-arid climate with very low rainfall, extremely high evaporation rates, and saline water and soil prevail. Many wild plants that can live in non-saline, moderate, or high saline environments cannot survive such an extremely saline environment. For example, in the Karama area, *Tamarix* bushes grew on the shores of the dam lake in a moderate saline environment but, they dried out because of increasing salinity levels and drought (Fig. 7).

On the other hand, plant species are threatened by human development activities, especially along the coastal area of Aqaba, increasing pollution, erosion, and sedimentation. Even the study site near the shore has been destroyed by the building of new tourist hotels. All of these factors can lead to biodiversity loss of ecosystems.

Both the Wadi Araba and Aqaba areas of Jordan have been declared developmental areas and the government of Jordan allocated millions of dollars for that development. Nonetheless, it is feared that not enough consideration is being given to the potential negative impacts of such development on the environmental conditions there including the biodiversity and especially native plant species.

This study documents the plants tolerant to extremely saline soils and water which have, until now, not been recorded for the studied locations. An example of what can happen is the disappearance of plants in the central part of the Sabkha in Taba due to increasing salinity to an extent, that even salt-tolerant plant species cannot survive the changing environmental conditions.

Figure 7. Dead Tamarix bushes on the dry salty cracked ground on the shore of Karama dam lake.

Acknowledgments

The research was funded by the Deanship of Academic Research, the University of Jordan.

References

Abed, A.M. (2002). An overview of inland sabkhas in Jordan: The Taba Sabkha, southern Wadi Araba. Bart Boer, Sabkha Ecosystems. Kluwer, 83–97. The Netherlands. Google Scholar

Abel, G. H., and MacKenzie, A. J. (1964). Salt tolerance of soybean varieties (*Glycine max* L. Merrill) during germination and later growth. Crop Science., 4, 157–161

Alhejoj, I., Bandel, K., and Salameh, E. (2014). *Macrofaunal* and *floral species* in Jordan and their use as environmental bio-indicators, University of Jordan press.

Alhejoj, I., Bandel, K., and Salameh, E. (2015) Floral Species as Environmental Quality Indicators in Jordan: High Salinity and Alkalinity Environments. Journal of Environmental Protection, 6, 494-514.

Al Kharusi, L., Assaha, D., Al-Yahyai, R., and Yaish M. (2017). Screening of date palm *(P. dactylifera* L.) cultivars for salinity tolerance. Forests.8:136.

Al Khateeb, W. M., R. M. Muhaidat, N. Odat, A. Sawaie, J. N. Lahham, and A. El-Oqlah. (2010). Interactive effects of salinity, light, and temperature on seed germination of Zygophyllum simplex L. (Zygophyllaceae). International Journal of Integrative Biology 10: 9–13

Albert, R., Petuschnig, B., and Watzka, M. (2004). Zur Vegetation und Flora Jordaniens. Denisia 14: 133-220.

Al-Eisawi, D.M. (1996). Vegetation of Jordan. UNESCO— Regional Office for Science and Technology for the Arab States, Cairo, p. 266.

Al-Eisawi, D. (1985). Vegetation in Jordan in A. Hadidi Studies in History and Archaeology of Jordan Vol.ii.pp. 45-57. Dep. of Antiquities Amman, H.K.J.

AL-Eisawi, D. (1998). Field Guide to Wild Flowers of Jordan and Neighboring Countries. Jordan Press Foundation Al Rai, Amman, 296488.

Al-Eisawy, D. (1996). Fifty Years Vegetation of Jordan. Regional Office for Science and Technology for the Arab States, UNESCO, Cairo.

Alqasemi, A., Ibrahim, M., Fadhil Al-Quraishi, A. M., Saibi, H., Al-Fugara, A., and Kaplan, G. (2021). Detection and modeling of soil salinity variations in arid lands using remote sensing data: Open Geosciences, vol. 13, no. 1, pp. 443-453.

Bandel, K., and Salameh, E. (2013) Geologic Development of Jordan-Evolution of Its Rocks and Life. Deposit No. 690/3/2013 of the National Library, Amman, 278 p.

Barko, J.W., and Smart, R.M. (1979). The nutritional ecology of *Cyperus esculentus*, an emergent aquatic plant, grown on different sediments. Aquatic Botany 6:13-28.

Bayouli, I., Bayouli, H.T., Dell'Oca, A., Meers, E., Sun, J. (2021). Ecological indicators and bioindicator plant species for biomonitoring industrial pollution: Eco-based environmental assessment, Ecological Indicators 125,107508.

Cowardin, L.M., Carter, V., Golet, F.C., and LaRoe, E.T. (1979). Classification of Wetlands and Deepwater Habitats of the United States. Washington, DC, U.S. Department of the Interior, U.S. Fish and Wildlife Service.

Craft, C.B., and Casey, W.P.)2000(. Sediment and nutrient accumulation in the floodplain and depressional freshwater wetlands of Georgia, USA. Wetlands 20:323–332.

Crumpton, W.G. (2001). Using wetlands for water quality improvement in agricultural watersheds; the importance of a watershed scale approach. Water Science and Technology 44:559-564.

Dahamsheh, A., and Aksoy, H. (2007). Structural characteristics of annual precipitation data in Jordan. Theoretical and Applied Climatology. 88, 201–212.

Feinbrun-Dothan, N. (1978). Flora Palaestina, vol 3. Israel Academy of Sciences and Humanities, Jerusalem

Fort, F., and Freschet, G. (2020). Plant ecological indicator values as predictors of fine-root trait variations. Journal of Ecology, Wiley, 2020, 108 (4), pp.1565-1577.

Grattan, S. R., and Grieve, C. M. (1999). Salinity-mineral nutrient relations in horticultural crops. Scientia Horticulturae., 78, 127–157.

Grieve, C.M., Grattan, S.R., and Maas, E.V. (2012). Plant salt tolerance. In: Wallender, W.W. and Tanji, K.K. (eds.) ASCE Manual and Reports on Engineering Practice No. 71 Agricultural Salinity Assessment and Management. 2nd Edition. ASCE, Reston, VA. p. 405-459.

Grootjans, A.P., Ernst, W.H., and Stuyfzand, P.J. (1998). European dune slakes Strong interactions of biology, pedogenesis, and hydrology. Tree13:96-100

Justin, S. H. F. W., and Armstrong, W. (1987). The anatomical characteristics of roots and plant response to soil flooding. New Phytologist 106: 465–95.

Keddy, P.A. (2010). Wetland Ecology: Principles and Conservation (2nd edition). Cambridge University Press, Cambridge, UK.

Koyro, H.W. (2003). Study of potential cash crop halophytes by a quick check system: Determination of the threshold of salinity tolerance and the ecophysiological demands, in Cash crop halophytes: Recent studies, H. Lieth and M. Mochtchenko, eds., Kluwer Academic Publishers, Norwell, Mass., 5–17.

Kuusemets, V., and Mander, Ü. (1999). Ecotechnological measures to control nutrient losses from catchments. Water Science. Technol. 40(10): 195–202

Lavorel, S. (2013). Plant functional effects on ecosystem services. Journal of Ecology 101: 4–8.

Morton, J. (1987). Passionfruit. In Morton, J., Ed., Fruits of Warm Climates, Florida Flair Book, Miami, 320-328.

Muhaidat, R., Brake, M.H., Al Zoubi, M. et al. (2018). Integrating morphological characters, molecular markers, and distribution patterns to assess the identity of *Blepharis* species from Jordan. Botanical Studies. 59, 18.

Muhaidat R, McKown AD, Al Zoubi M, Bani Domi Z, Otoum O. (2018). C4 photosynthesis and transition of Kranz anatomy in cotyledons and leaves of Tetraena simplex. American Journal of Botany 105: 822–835

Philippi, T.E., Dixon, P.M., and Taylor, B.E. (1998). Detecting trends in species composition. Ecological Applications 8:300-308.

Salisbury, F. B. (1995). Units, symbols, and terminology for plant physiology, Utah State University, Logan, Utah.

Spence, D.H.N. (1982). The zonation of plants in freshwater lakes. Advanced Ecological Research 12:37-125.

Shrivastava, P., and Kumar, R. (2015). Soil salinity: A serious environmental issue and plant growth promote bacteria as one of the tools for its alleviation. Saudi journal of biological sciences, 22(2), 123-131.

Squires, L., and van der Valk, A.G. (1992). Water-depth tolerances of the dominant emergent macrophytes of the Delta Marsh, Manitoba. *Canadian Journal of Botany* 70:1860-1867.

Stromberg, J.C., and Patten, D.T. (1996). In-stream flow and cottonwood growth in the eastern Sierra Nevada of California, USA. Reg Rivers Res Manage 12:1-12.

Suding, K.N., Lavorel, S., Chapin, F.S., Cornelissen, J.H.C., Diaz, S., Garnier, E., Goldberg, D., Hooper, D.U., Jackson, S.T. and Navas, M.L. (2008). Scaling environmental change through the community-level: a trait-based response-and-effect framework for plants. Global Change Biology, 14: 1125–1140.

Templer, P., Findlay, S., and Wigand, C. (1998). Sediment chemistry associated with native and non-native emergent macrophytes of a Hudson River marsh ecosystem. Wetlands 18:70-78.

Ungar, I. A. (1998). Are biotic factors significant in influencing the distribution of halophytes in saline habitats?" Bot. Rev., 64, 176–199 Verlag Eugen Ulmer, Stuttgart: 33-204.

Wardrop, D.H., and Brooks, R.P. (1998). The Occurrence and Impact of Sedimentation in Central Pennsylvania Wetlands. Environmental Monitoring and Assessment 51, 119–130

Whigham, D. F., Chitterling, C., and Palmer, B. (1988). Impacts of freshwater wetlands on water quality: A landscape perspective. Environmental Management 12: 663-671.

Xinhu, L., and Fengzhi, S. (2019). The Effect of Flooding on Evaporation and the Groundwater Table for a Salt-Crusted Soil, Water, 10.3390/w11051003, 11, 5, (1003).

Zohary, *M*. (*1972*). *Flora* Palaestina. *Part 2*, Text *Platanaceae to Umbelliferae*. Israel Academy of Science and Humanities, Jerusalem, 656.

Zohary, M. (1973). Geobotanical Foundations of the Middle East. Volumes 1 & 2. Gustav Fischer Verlag, Stuttgart & Swets & Zeitlinger, Amsterdam.

Zohary, D., and Hopf, M. (1994). Domestication of plants in the old world. 2nd ed. — Oxford Science Publications, Clarendon Press, Oxford: 1-279.

JJEES

JJEES (2022) 13 (3): 199-214
ISSN 1995-6681

Jordan Journal of Earth and Environmental Sciences

Assessment of Surface Water Resources Based on Different Growth Scenarios, for Borkena River Sub-basin, Awash River Basin, Ethiopia

Hasen Hussien[1], Zerihun Asmelash Samuel[2], Andualem Shigute Bokke[3], Abreham Bekele Bayu[4*]

[1]Faculty of Civil and Environmental Engineering, Jimma Institute of Technology, Jimma University
[2]Faculty of Civil and Environmental Engineering, Jimma Institute of Technology, Jimma University
[3]Faculty of Civil and Environmental Engineering, Jimma Institute of Technology, Jimma University
[4]School of Chemical Engineering, Jimma Institute of Technology, Jimma University

Received 17 January 2022; Accepted 12 March 2022

Abstract

The total annual river flow at the Awash Kombolcha sub-basin of the Borkena river station was estimated to be 4.6 billion cubic meters by 2019-2030. The current average annual flow at the exit measurement station is 544.5Mm^3 of the water resources available in the study area. The monthly peak flow of the Borkena River occurs from July to September. In addition, the highest monthly average flow is in August and the lowest is in June, with values of 150.7 million m^3 and 6.1 million m^3 respectively. WEAP model performance or model calibration was simulated between 1998 and 2018 and quantitative statistics were calculated for each previously observed flow coefficient of determination, R2, Nash Satcliff efficiency, etc. Percent bias, evaluated using PBIAS), then R2 = 0.988 and NSE = 0.70 PBIAS = 0.8 results. Assuming a relatively low reserve flow of over 92% corresponding emission analysis concept of 142 million population was considered as input. The performance balance of the model is 2019 demand data and simulated flow data at the Khemiessy exit supply. In the 2030 average growth scenario, the herd of livestock increased again by 1,610,161 to 1,776,937, with a corresponding growth rate of 0.7% per annum of 81.9 million m^3. This means that annual water usage has increased by 90.5% compared to the current scenario. Other optional implants such as rainwater harvesting, surface water harvesting, and groundwater need to be booked to meet the peak demand for dry months where the availability of surface water resources in these scenarios is felt in all water utilization sectors.

Keywords: *Awash River Basin, Borkena River, WEAP, Surface Water, CROPWAT 8.0*

1. Introduction

1.1. Background

Water is a basic necessity for the maintenance of life and the development of society, and the demand for water has increased rapidly over the years as the population grows, including urbanization, economic growth, industries, agriculture, and livestock (Cosgrove and Loucks, 2015). Population growth and economic development are constantly putting pressure on water resource ecosystems (Xiao et al., 2014). There is also a strong positive correlation between water demand and urbanization or population growth. Ethiopia has 12 major river basins, nine of which flow out except the Awash River basin, the Rift Valley Lake, and the Great Rift Valley, and all other rivers are cross-border, northwest, west, and southeast of the country (Tadese et al., 2020). The Awash River is located on the western plateau of Addis Ababa near Ginch on the central plateau of Ethiopia, at an altitude of about 3000 m. To assess the impact of demand scenario analysis to improve surface water availability and water resource planning and monitoring, the Awash basin has six planned areas: upstream Awash Coca, Awash Awash, Awash Haridebi, and Awash Adaitu. , Awash Terminal, is divided into Eastern Submersibles. -Basin (Belayneh, 2018). The Awash Koka sub-basin includes the Awash Kuntre, Mojo, and Akaka rivers. Awash in the lower reaches of Awash includes the Keletawerenso and Awashalva rivers 1 and 2, and the lower reaches of Awashharidebi include the Kesemkebena, Ankova, Negesogera, Awadi, and Gedevasa Wetlands. The lower reaches of the Awash River Terminal include the Mile and Logia Rivers (Kerala, 2019). Desertification has already begun in the lower and central parts of the Awash River basin. At the top, deforestation and sedimentation have increased over the last 30 years (Tufa, 2021; Kebede,2013).

As more water is drawn from the river, it can lead to dramatic ecological changes and environmental flow that endanger the Borkena River in the habitat and human life of the Awashkom Borkena subbasin (Belachew, 2019). Increasing water demand will reduce the availability of surface water available to users in the dry season, and water conflicts in catchment areas will continue to increase. Unless water resources are properly managed. In particular, at the Awash Kombolcha Borkena Subbasin on the Borkena River in north-central Ethiopia, a relatively large number of large production facilities have been shut down, all located

* Corresponding author e-mail: abrishchem@gmail.com

along two major tributaries of the Borkena River (Morris, 1923). In addition, Awash city is currently selected as the most important industrial corridor in northern Ethiopia. Therefore, it is clear that the availability of relevant surface water and the risk of pollution will increase in the future to meet demand. The existing industries around Awash city dump waste into rivers (Baker, 2012). In addition, the report obtained from the Awash city administration explains that many farmers and businesses have long used the river for irrigation (Zainab, 2011). As a result, no studies have been conducted on the theme of assessing surface water availability and water demand to improve water resource planning and livelihoods in the study area (Singh et al., 2014). Recent studies have shown that climate change, socio-economic activity, population growth, water pollution, and large-scale water withdrawals are the main challenges that have changed the natural water balance of the Borkena River (Bezabih and Mosissa, 2017).

Poor management of water resources, increased competing water demand for self-sufficiency, and lack of strong management and coordination between sectors are expected to exacerbate the water scarcity challenge in catchment areas (Kahil et al., 2015). This means that proper planning and development of water resources are needed. This requires empirical evidence of current and future surface water availability and demand in the Kombolcha basin of the Borkena River. This study fills this gap and provides sufficient information on water supply and demand in river basins that are important to decision-makers in the water sector. Studies show that the main challenges faced by climate change, socio-economic activity, population growth, water pollution, and the naturally altered hydrological regime of the Borkena River are the extraction of large amounts of water (Francés et al., 2017).

The objective of this research was to assess surface water resources based on different growth scenarios, for Borkena River sub-basin, Awash River Basin, Ethiopia. As Ethiopia is heavily affected by global surface water fluctuations, it is very important to anticipate future needs for better awareness and better preparation to mitigate the associated surface water scarcity. The question is whether the future impact of supply and demand imbalances on hydrology in the Awash Kombolcha Borkena subbasin of the Borkena River is another purpose of this research paper, as there is no research on this topic in this area.

2. Materials and Methods

2.1. Description of Study Area

Geographically, the Awash Kombolcha Sub Basin lies between 1154573.2 meters to 1249931.1 meters north and 550396.7 meters to 603.9526 Km east in UTM coordinates, with an altitude range of 1394 to 3513 meters above sea level, with a total area of 1258. It is 4km^2. The Awash Kombolcha Sub Basin in the Borkena basin is named after the city of Kombolcha, located in the north-central part of Ethiopia, just southeast of Dessie, Amhara. The Borkena River crosses the town of Kombolcha in the basin, flowing east and west. As shown in Figure 1, most factories are located close to the middle of the city near these tributaries (Yohannes and Elias, 2017).

2.2. Population

Awash Kombolcha Sub-Basin has 12 woreda and 91 kebeles including Kombolcha, Kemisie, Albuko, Dessie, Chaffie golana dawe, Kutaber, Ancharo, gisheRabel, Tehulederie Anstokian Gemez, Artuma, and Harbu/Kalu are woredas or towns found in the study area. The towns or woredas in this study area are known for their high animal and human population density with different ethnic groups and religions. According to the data obtained from the Ethiopia Central static agency, the current population of the Woreda in the study area is estimated at 1,734,366 of which 544,111are urban and the remaining 1,190,255 are rural, which is 54.3% of the total population in this area (Teklehaymanot, 2017).

2.3. Rainfall and Climate

Rainfall and temperature are the prime factors in determining the climate and therefore the distribution of vegetation types (Fax et al., 2017). The study area is characterized by two rainy seasons (quasi-bimodal rainfall pattern). The main or the longer rainy season is during Kiremt extends from (June- September) which supports the major crop production while the small or the shorter rainy season is during Belg extends from (March-May) and allows minor crop production (Fax et al., 2017). The physiographic characteristics of the study area include an altitude of 1394 up to 3513 meters above sea level (Shumet and Mengistu, 2016). The area receives a mean annual rainfall of 710.94 mm at the Upper Part Kombolcha Station to 648.6 mm at the lower part of Kemisie station with annual average maximum and minimum temperatures of 27.1^{o}C and 11.6^{o}C at Kombolcha and 32.9^{o}C and 13.2^{o}C at Kemiessie, respectively.

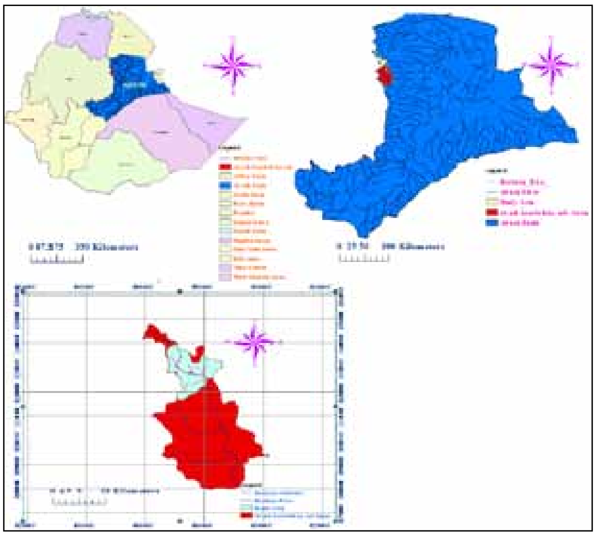

Figure 1. The drainage system and location of the study area

2.4. Data Collection

The sources of the data are the Ministry of Water, Irrigation and Energy, the Ethiopian Mapping Authority, the National Meteorological Service, and documents. Water demand data for each sector were collected from the Ethiopian Water Sector Development Master Plan based on (Shumet and Mengistu, 2016). The required measurement data include precipitation, maximum and minimum air temperature, solar radiation, wind speed, and daily relative humidity. If any of these data are not available, most likely, estimate the required output using the WEAP and Crop Wat modeling program. This data for the remaining stations are loaded at dawn from the global weather data for SWAT. Monthly observational data are required for entry (WEAP) as headwater flows into the study area. These data are taken from the hydrology department of the ministry of water, irrigation, and energy for the period 1998 - 2018. The discharge data is collected and sorted according to the requirements of the model (WEAP). A digital elevation model (DEM) is any digital representation of a terrain surface and is specifically made available as a raster or regular grid of point elevations. The watershed of the Borkena River has been delineated and river networks have been driven from the DEM with a resolution of 90 m x 90 m.

2.4.1. Hydro-meteorological data Analysis

In the analysis of hydrological data, the stations were required to have daily records for the required period of observation (1998-2018) years. Sometimes a particular flow gauge was not functional for a part of a month or year. It then becomes necessary to fill in missing records. In this thesis, arithmetic means the value of the entire period was used to fill the missed records for the stations with less than 10 percent missed records while for the stations having greater than 10 percent of missed records normal- ratio method was used as per Table 1 using excel Extension software named XLSTAT 2018 version.

Table 1. Description of the streamflow recording stations with percentage missed

Station Name	Latitude	Longitude	Recorded period	Missing %
Borkena at swamp outlet	10:38: 0 N	39:56: 0 E	1998 – 2018	3.32%
Borkena at Nr. Albuko	11: 3: 0 N	39:44: 0 E	1998 – 2018	14.43%
Borkena Rr.Nr.kombolcha	11:13: 0 N	39:37: 0 E	1998 -2018	4.39%

Failure of a rain gauge or the absence of an observer from a station causes a brief interruption of rainfall recordings at the station. These gaps must be filled before precipitation data can be used for analysis. The surrounding stations located in the study area help to supplement the missing data on the hydro-meteorological similarity hypothesis of the station group. , and the inverse distance method. This method is used when the normal annual rainfall of the indicator stations differs by more or less than 10% from the deficient station. The precipitation of the surrounding index stations was calculated as an arithmetical and normal ratio o the annual precipitation using the following equations 1 and 2. rainfall recording stations with percentages of missed values are shown in Table 2.

$$\mathrm{Pm} = \sum_{i=1}^{n} \left(\frac{\mathrm{Nm}}{\mathrm{Ni}}\right) \mathrm{Pi} \quad \text{.......} (1)$$

$$Pm = \frac{p1+p2+p3......+pn}{n} \quad \text{.......} (2)$$

Table 2. Description of the rainfall recording stations with percentage missed value

S/No	Station Name	Longitude (E)	Latitude (N)	Area (Km^2)	Missing (%)
1	Dessie	39.63	11.12	136.014	10.81%
2	Maybar/Ancharo	39.63	11.05	131.771	16%
3	Combolcha	39.72	11.08	261.995	13.05%
4	Kemissie	39.87	10.72	190.195	4.43
5	Albuko	39.7142	10.8139	538.409	16.7
	TOTAL			1258.38	-

A consistent record is one in which the characteristics of the record do not change over time. Adjusting for metric consistency involves estimating an effect rather than a missing value. The consistency of precipitation profiles at selected stations is usually checked by dual-mass curve analysis. If the relevant conditions for recording a station, the precipitation data undergo a significant change throughout the recording time, there will be inconsistencies in the precipitation data from this station. This inconsistency can be distinguished from when significant changes have taken place. If a significant change in the mode of the curve is observed, it should be corrected using Equation 3.

$$\mathrm{Pcx} = \mathrm{Px} * \frac{\mathrm{Mc}}{\mathrm{Ma}} \quad \text{.......} (3)$$

Uniformity is an important issue for detecting data variability. In general, when the data is homogeneous, it means that the data measurements are made with both the same equipment and the same environment. However, it is a difficult task when dealing with precipitation data because it is always caused by changes in measurement techniques and monitoring procedures, environmental characteristics and structures as well as the location of the precipitation station. One of the methods to check the uniformity of the selected stations in the study area is to record the rainfall without dimensions and draw a graph to compare the stations with each other. The monthly spacetime precipitation values for each station can be calculated using Equation 4.

$$Pi = \frac{Pi,av}{Pav} * 100 \quad \text{.......} (4)$$

Where:

Pi is the dimensionless value of the monthly rainfall at station i, Pi, av is the average monthly rainfall over the years for station i, and Pav is the average annual rainfall for the station when the precipitation regimes are the same or vary in a range they can consider as uniformity.

2.5. Estimation of Areal Rainfall

The rain gauge is a one-time measurement only. In practice, however, hydrological analysis requires knowledge of precipitation over an area. Several approaches have been designed to estimate surface precipitation from Isohyetal point measurements: isohyets are lines connecting locations of equal rainfall intensity across a watershed. In this research, the aging method is used to determine the average rainfall over the whole area since the rain measurements are uniformly distributed. Surface precipitation in the study area is calculated using Equation 5.

$$Pav = \frac{P1+P2+P3+P4----------+Pn}{n} \quad \text{.........................} (5)$$

Where, P_{av} average areal rainfall (mm), P_1, P_2, P_3, P_n precipitation of station 1, 2, 3...n, respectively. In this method, the sums of each gauge are inversely proportional to the sample size of the rain gauge station.

2.6. Water Supply Data

2.6.1. Stream Flow

Flow streams should be continuously recorded to accurately assess surface water availability. Flow records that represent natural history and hydrology unaffected by humans are the basis for watershed hydrological modeling (WMO). Flow data is collected from the office of the Ethiopian Ministry of Water, Irrigation, and Energy, and flow discharge is an important aspect of the modeling of flows. Data available for the rivers were obtained from three gauging stations namely, Borkena at swamp outlet Nr Kemmisie, Borkena at Nr. Albuko, BorkenaRr. Nr.Kombolcha. The mean monthly flow data from this gauge station were used for the WEAP model shown in Figure 2.

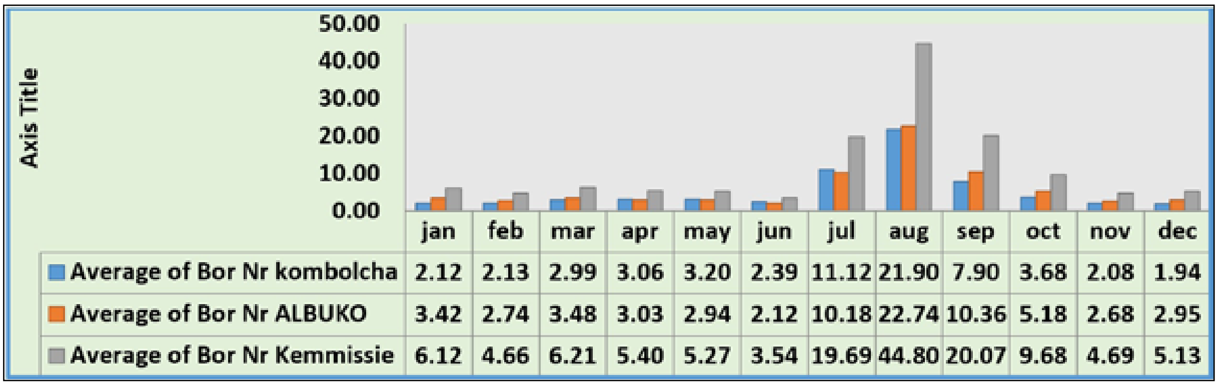

Figure 2. Average streamflow of Borkena River in a different station (Gummadi et al., 2018)

2.6.2. Rainfall and Temperature

Rainfall and temperature are the prime factors in determining the climate and therefore the distribution of vegetation types (Subramoniam et al., 2013). There is a strong correlation between climate and biomass in the study area to quantify current surface water availability to analyze demand scenarios for the future. The study area is characterized by two rainy seasons (quasi-bimodal rainfall pattern). The physiographic characteristics of the study area include an altitude of 1394 up to 3513 meters above sea level (Polidori and El, 2020; (Gummadi et al., 2018). The area receives a mean annual rainfall of 710.94 mm at the Upper Part Kombolcha Station to 648.6 mm at the lower part of Kemisie station with an annual average maximum and minimum temperature of 27.1 C° and 11.6 C° at Kombolcha and 32.9 C° and 13.2 C° at Kemiessie, respectively in the present study figures 2 and 3.

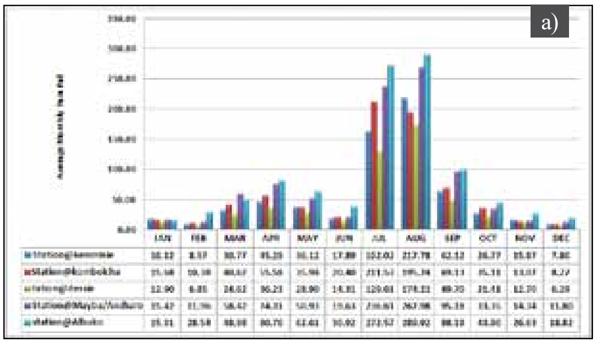

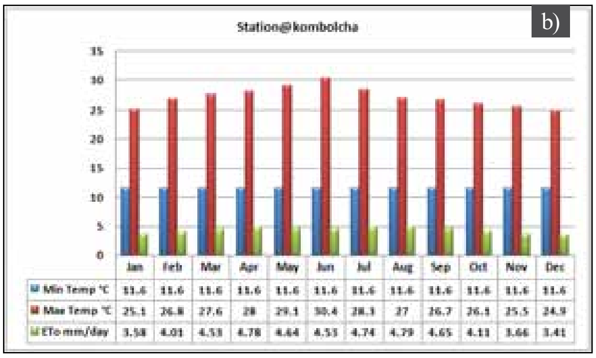

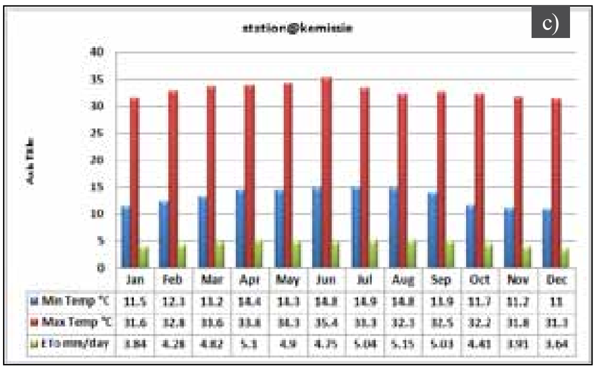

Figure 3. a) Average monthly Rainfall of all stations in the study area b) Average monthly Max and Min temperature of Kombolcha station in the study area c) Average monthly Max and Min temperature of Kemiessie station in the study area

2.7. Materials

2.7.1. GIS for Watershed delineation

Determination of the study area boundary and stream delineation was done using the spatial analyst tool in ArcGIS version 10.4.1, using various thematic maps such as topography, drainage, and land cover/use.

2.7.2. CROPWAT

The CROPWAT 8.0 software was used in calculating crop water requirements. This software uses monthly averages of the climatic parameters. The ETo is calculated using the Penman- monteith method and effective rainfall is estimated by the FAO formula. The software provides data on crops such as Kc, growing stage, rooting depth, and soil moisture as defaults.

2.7.3. Water Evaluation and Planning

Water assessment and planning software was selected for this study. The WEAP model essentially calculates the mass balance of sequential flows along with a river system, taking into account withdrawals and inflows. The elements that make up the water demand system and their spatial relationships are featured in the model. In this thesis, WEAP is used because it has an integrated approach to simulate both natural and engineering components such as reservoirs, international groundwater discharge, and water demand and supply, this can provide water planners with a more complete view of the range of factors that must be taken into account in managing water resources for current and future uses. In Ethiopia, WEAP was exactly performed in 2016 to assess competitive irrigation and water demand scenarios in the Didessa Sub-Basin (Adgolign et al, 2016).

2.8. Methods Analyzed

The water system simulation model helps to understand the relationship between available water resources and the demand for these resources under current and future development scenarios. Basin modeling using WEAP involves the following steps i) Define study area and period ii) Create current account iii) Generate scenarios iv) Evaluate scenarios. With WEAP, the first Current Account of the water system under study is created. Then, one or more simulation scenarios are developed with alternative hypotheses about future development. Situations can answer many types of "what if" questions. The simulation of the model is structured as a set of scenarios with monthly time steps. WEAP21 solves the problem of water allocation through linear programming to maximize the satisfaction of a demand node constrained by water availability, demand priority, the priority of source of supply, and how close the supply is.

2.8.1. Catchment's delineation

The river system has been mathematized using the Arc View GIS layer. The runoff from the catchment nodes in WEAP21 represents the head flow of the streams. In this study, arithmetic means the method is used to generate the aerial precipitation over the catchment. Precipitation in the area was estimated using the arithmetic mean for the selected period from 1998 to 2018 (of the eight rain stations in the basin, only five have complete monthly rainfall data). from 1998 to 2018). Monthly mean of potential monthly evaporation. The Penman-Monteith method is recommended as the only standard method for determining and calculating the Reference Evaporation is generated using Crop Wat while the Kc coefficient is obtained from Crop Wat. Geometric population growth and precipitation method (simplified coefficient method) were used in WEAP. The Rainfall Flow (simplified coefficient) method in WEAP21 was used to simulate the catchment (flow) process. This method determines land use by the crop factor, Kc, catchment area, and effective precipitation while climate is determined by reference precipitation and transpiration, ETo.

2.8.2. Cropwat 8 model setup

CROPWAT is a decision support system developed by the FAO Department of Land and Water Development for irrigation planning and management. The Food and Agriculture Organization (FAO) CropWat8 model was used to simulate the seasonal irrigation pattern observed with different growing seasons in the region. The measured data of the study area was used to generate the actual evaporation (ETo), Kc, and the actual rainfall of the study area and the monthly irrigation demand ratio to be used as the entry for the WEAP model.

2.8.3. WEAP Model

The WEAP model was developed by the Stockholm Environment Institute (SEI) and can be downloaded from www.weap21.org. It is a general-purpose multi-reservoir simulation program that determines the optimal water allocation for each time step on the fundamentals of water balance calculations. The model provides a comprehensive, flexible, and user-friendly framework for policy planning and analysis. According to (SEI), WEAP integration is listed as follows i) GIS-based drag and drop graphical interface ii) Physical simulation of water demand and supply iii) Additional simulation model: variables created users create, model equations and link to spreadsheets and other models iv) Scenario manageability v) Homogeneous modules on hydrology, water quality and watershed finance vi) Developed by the American Center for the Stockholm Environment Institute Integrated Model of Watershed Hydrology and Planning. The advantage of WEAP (Water Evaluation and Planning) is a software tool for integrated water resources planning. It provides a comprehensive, flexible, and user-friendly framework for policy analysis. Its disadvantage is that building a model requires data, time, modeling skills, and patience.

2.9. Model Evaluation Statistics

The quantitative statistics used to evaluate the performance of the model are the coefficient of determination (R2), the efficiency of the Nash-Sutcliffe model (NSE), and the percentage deviation (PBIAS)

2.9.1. Coefficient of determination (R2).

The coefficient of determination (R2) describes the years' congruence between the simulated and observed data. R2 describes the proportion o the observed data variance explained by the model. R2 ranges from 0 to 1, gives higher values, sh less error variance. Rs values greater than years 0.5 are considered acceptable (IOPConf, 2017). The calculation of R2 is presented as follows.

$$R^2 = \left[\frac{\sum_{i=1}^{n}(\text{yisim} - \check{y}\text{sim})(\text{yiobs} - \check{y}\text{iobs})}{\sqrt{\sum_{i=1}^{n}(\text{yisim} - \check{y}\text{sim})^2 \sum_{i=1}^{n}(\text{yiobs} - \check{y}\text{iobs})^2}}\right] \text{.. (6)}$$

Were, Yi, Obs: the ith stream of observations, Jim: the ith simulation stream, ўobs: the average value of the observed stream, ўisim: the average value of the simulation stream.

2.9.2. Percent bias (PBIAS)

Percent bias (PBIAS) measures the average tendency of simulated data to be larger or smaller than the observed data. The optimal value of PBIAS is 0.0, with low amplitude values indicating an accurate simulation of the model. A positive value indicates the estimated bias of the model, and a negative value indicates the acceptable estimated bias for the model (IOPConf, 2017). PBIAS is calculated as shown below.

$$Percentage\ BIAS = \left[\frac{\sum_{i=1}^{n}(yiobs - yisim)}{\sum_{i=1}^{n} yiobs} * 100\right] \text{... (7)}$$

2.9.3. Nash-Sutcliffe efficiency (NSE)

Nash Sutcliffe Efficiency (NSE) is a normalized statistic that determines the relative magnitude of residual variance ("noise") to the variance of measured data ("information") (IOPConf, 2017). NSE tells how closely the histogram of the observed versus simulated data matches the 1:1 line. NSE ranges from −∞ to 1 (including 1), NSE 1 is the optimal value. Values between 0.0 and 1.0 are generally considered to be an acceptable performance level, while values etlt; 0.0 indicates that the observed mean is a better predictor than the simulated value, indicating unacceptable performance (IOPConf, 2017). NSE is calculated as shown below.

$$NSE = 1 - \left[\frac{\sum_{i=1}^{n}(yiobs - yisim)^2}{\sum_{i=1}^{n}(yiobs - yisim)^2}\right] \text{........................... (8)}$$

Were,

Yi, Obs: the ith observed streamflow, yiSim: the ith simulated streamflow

2.10. Reference Scenario and Model Configuration

Reference scenarios are baseline scenarios that use real-world data to help you understand the best estimates during the study period. In this scenario, an existing dataset from the study area was used. This data entry in WEAP is structured according to the schematic structure of the survey boundaries and is the basic scenario for the following scenarios and the required sub-scenarios. This happened in the next step (Shumet and Mengistu, 2016). The model was initially configured to simulate a base year or current situation scenario that could reliably determine water availability and demand. What if scenario analysis is set up and the simulation runs from 2019 to 2030. The scenario is based on the data from the previous scenario. Therefore, the following scenarios formed the basis of the reference scenario development of reference scenarios (2020-2030).

2.11. Scenario Analysis and Model Development

2.11.1. Current account of water demand

Current water billing sectors are identified in the study area to simulate the water demand available in the current account balance between these sectors. The categories of demand are household, agriculture, livestock, environment, and industry. The input data request for the WEAP model was created by adding a GIS-based raster map and vector map to the projection area, and the background vector data was added from the shapefile format. This format was created by the ArcGIS 10.4.1 software when the area was opened and the year, time steps, and units were set. In this survey, the current balance of payments for the year (2019) in the start year scenario until the end of 2030, the time stepper year is set to 12, and the time step limit is set to "based on the calendar month". January. The year of the current account is selected as the basis of the model and all system information (such as supply and demand data) is included in the performance balance. Performance accounts are the dataset from which scenarios are created. In the "Current Scenario", the current account data will be transferred to the entire project up to (20202030). The flow path is drawn in WEAP by clicking the Flow symbol in the element window. WFAP has a module for modeling hydrological processes. The hydrological model is semi-theoretical, continuous-time, semi-distributed, and deterministic. Since the model is semi-theoretical, it must be calibrated to verify the model's performance. To develop the structure of the model, the entire study area was divided into five (5) hydrological basins (according to available hydrological data) and six (6) possible demand sites taking into account the needs of the population. domestic and non-domestic demand. In addition, it has three (3) flow measurement points and five rain gauge stations located in the study area. Next, the structure of the model is developed by taking into account relevant factors, including the river (flow), demand location, transmission link, watershed, and flow discharge, for steps of monthly time from 2020 to 2030. Figure 4: is a diagram of the model showing the topology of a network of WEAP nodes stacked with several GIS layers. Hence, several scenarios have been developed and identified in the model to study surface water problems and water problems that may arise shortly.

A demand site is best defined as a collection of water users who share a common physical distribution system, all of whom are located in a defined area, or who share a common point of primary supply and priority system. The water demand per site is calculated with the total volume/area which is the annual water demand per unit area (m^3/ha) or per person/population / as well as monthly variations. The schematic illustrations are provided in Figure 4.

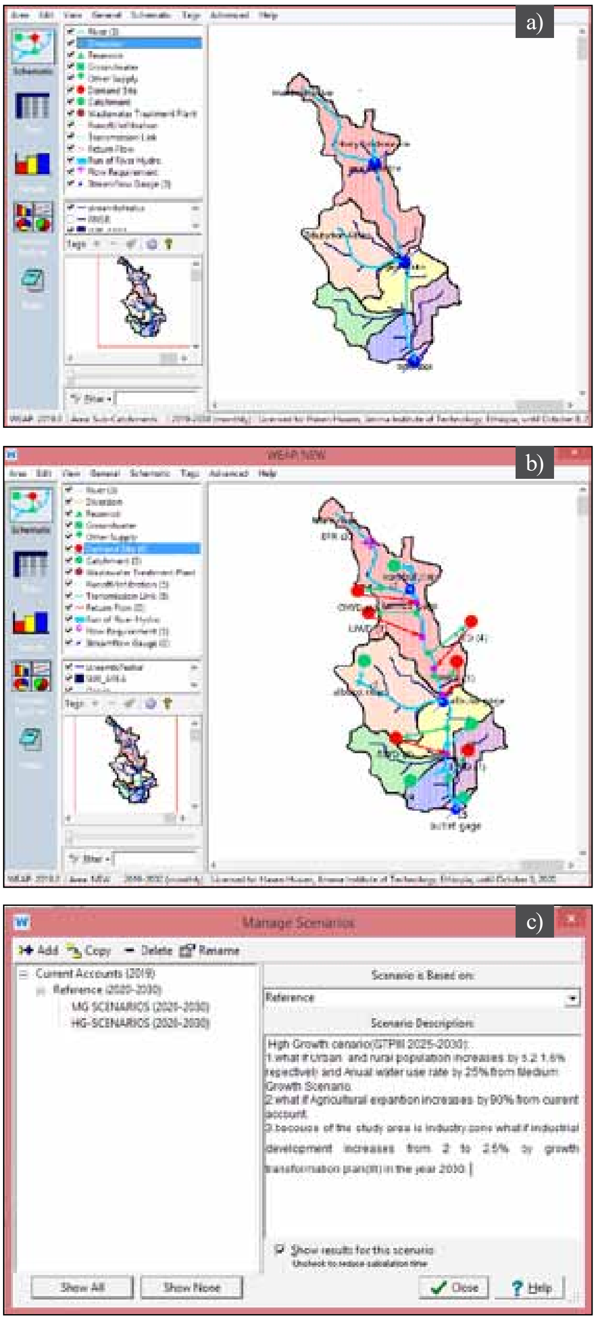

Figure 4. a) Data input into WEAP interface and Catchment boundary in WEAP model development b) Schematic illustration of the Awash Kombolcha sub-basin of Borkena watershed in WEAP c) Creation of Scenarios in WEAP

2.11.2. Current scenarios

The base scenario is also known as the default scenario set from current accounts, it represents the basic definition of the current system including the specification of first-year supply and demand data. First, the monthly study stimulates the likelihood of system growth without intervention (Aung et al., 201). In this study, the current scenario applied to the Borkena river situation analysis does not have any development of the system, except for the population growth rate of 7, and 1.3% per year, respectively. In urban and rural areas and the average annual growth rate of livestock is estimated at 0.7%.

2.11.3. Medium Growth (MG) scenario

After analyzing the possible impact in current scenarios WEAP was configured in medium growth scenarios, these scenarios are to evaluate the impact of a population growth rate and extended Agricultural area for the study area. The medium growth (MG) scenario is assumed considering the urban population growth rate increase from 4.7 to 5% per annum and rural population growth rate of 1.8% and livestock population 0.85% and agricultural land expansion by 6.6% which reach 11,326 ha to 23,680 ha in the medium Growth Scenario as obtained from the Awash city administration.

2.11.4. Higher growth (HG), scenario

The socio-economic development activities in the Awash River Basin such as investment in agricultural development through irrigation, land conversion by pastoral groups, and the expansion of industries due to expansion of output markets and macro-economic policy support are expected to be the major drivers of land degradation challenges. This process can be strengthened in association with the expansion of urbanization and population growth which will add pressure on water, land, and related resources in the basin (ABA, 2017). Agricultural growth is assumed to be 7.6%, it reaches 23.680 ha to 35,450 ha it shows a 90% increment when comparing from current scenario industrial growth 2 to 2.5 % by Growth transformation plan (III) by the year 2030.

2.11.5. Environment flow

In the annual discharge of the river Borkena, it is assumed that the current amount of river flow will be constant for up to three scenarios, also the minimum environmental flow requirement will be constant in the three scenarios since there is no reliable projection in the study it can be increased or reduce in the environmental flow.

3. Results and Discussion

3.1. Surface Water Availabilities

3.1.1. Stream Flow

The available data for the Awash Kombolcha sub-basin of the Borkena river watershed, 20-year data were taken to estimate the river flow at Swamp outlet near Kemiessie, which is the outlet of the sub-basin. The total river flow at this station has been estimated at 4.6 BCM by 2019-2030 but the current average annual at the outlet gage station has been estimated to be 544.5Mm^3 of the available water resource in the study area by (2019). The higher flows for 2019, 2020, 2021, and 2022. The peak monthly flow in the Borkena River is occurring from July to September, furthermore, the highest monthly average flow occurs in August and the lowest occurs in June with values of 150.7 and 6.1 M m^3 respectively. The annual and monthly streamflow data is illustrated in Figure 5 and Table 3.

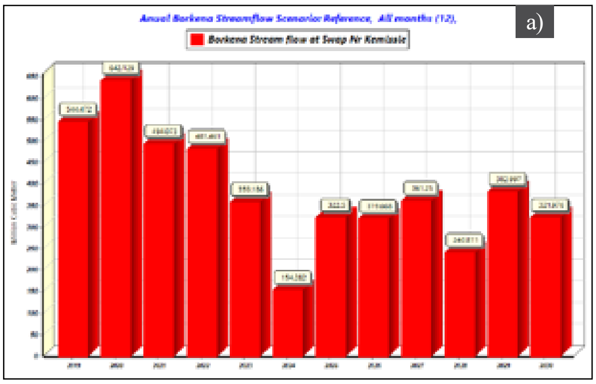

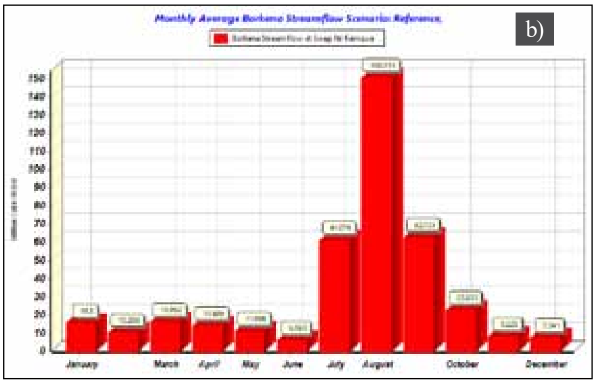

Figure 5. a) Annual Streamflow data at swamp outlet (2019-2030) b) Monthly average Streamflow data at swamp outlet (2019-2030)

Table 3. Annual and monthly Borkena Stream Flow (MCM) at Swamp outlet Nr Kemiessie

Year 2019-2030	Annual streamflow (Mm^3)	Monthly Current-2019	monthly streamflow (Mm^3)
2019	544.47	Jan	15.3
2020	642.13	Feb	10.26
2021	494.07	Mar	15.95
2022	481.46	Apr	13.81
2023	359.19	May	11.1
2024	154.28	Jun	6.063
2025	322.5	Jul	61.08
2026	319.67	Aug	150.7
2027	361.25	Sep	62.73
2028	240.81	Oct	22.83
2029	383	Nov	8.225
2030	321.98	Dec	7.341
Sum	4624.8	-	385.4

3.1.2. Precipitation over the Kombolcha sub-basin of Borkena River

The results show that the Borkena basin's Kombolcha sub-basin receives an estimated 63.3 MCM of rainfall per year. Table 4 relays what could improve rainwater harvesting in the study area. The highest monthly rainfall occurs from July to September and decreases from March to May. In addition, the highest average monthly rainfall in the region occurs in July and the lowest in February with values are 13.58 and 1.11 M m3 respectively. The precipitation of the five basins shows significant spatial and temporal variations.

Table 4. Observed Precipitation Monthly Average (MCM) in kombucha Sub-basin

Month	c1	c2	c3	c4	c5	Sum
Jan	2.68	2.31	2.25	1.60	0.11	8.95
Feb	1.99	1.56	1.52	0.92	0.07	6.05
Mar	1.49	1.80	1.29	1.17	0.05	5.79
Apr	0.84	0.43	0.21	0.67	0.03	2.17
May	1.99	1.41	0.84	1.65	0.07	5.96
Jun	1.01	1.24	1.38	0.57	0.04	4.23
Jul	2.32	1.03	1.14	0.98	0.07	5.54
Aug	0.66	0.80	0.40	0.54	0.02	2.42
Sep	1.43	1.06	0.65	0.86	0.05	4.04
Oct	0.72	1.20	0.88	0.63	0.03	3.46
Nov	1.56	1.69	1.24	2.00	0.05	6.54
Dec	2.24	2.24	1.18	2.41	0.08	8.15
Sum	18.93	16.76	12.96	14.01	0.66	63.32

Note; C1, C2, C3, C4, and C4 are catchment 1, catchment 2, and catchment 3. catchment4 and catchment5. The water balance of simulations shows that on average, 27.8 % of rainfall contributes to the surface and subsurface flow and 72.2% is evapotranspiration.

3.1.2.1. Runoff generated from precipitation

The runoff generated from the rainfall of the study area has been estimated using the water balance, the rainfall-runoff method in the WEAP model. As a result of the calculations, based on the Rainfall-Runoff method in WEAP, it was found that the total annual surface runoff from given precipitation in the Study area is 17.60 (MCM) Table 5: which is 27.8 % of total surface water availability from precipitation of different station in the study area.

Table 5. Runoff Monthly Average (MCM) in Awash kombucha Sub-basin.The water balance of the study area is indicated in Figure 6.

Year	Runoff from C1 to Kombol river	Runoff from C2 to the Main river	Runoff from C3 to the main river	Runoff from C4 to the main river	Runoff from C5 to the main river	Sum
Jan	0.96	1.02	0.25	0.21	0.03	2.46
Feb	0.72	0.68	0.17	0.12	0.02	1.70
Mar	0.54	0.79	0.14	0.15	0.01	1.63
Apr	0.30	0.19	0.02	0.09	0.01	0.61
May	0.72	0.62	0.09	0.21	0.02	1.66
Jun	0.36	0.55	0.15	0.07	0.01	1.14
Jul	0.83	0.45	0.13	0.13	0.02	1.56
Aug	0.24	0.35	0.04	0.07	0.01	0.71
Sep	0.51	0.46	0.07	0.11	0.01	1.17
Oct	0.26	0.53	0.10	0.08	0.01	0.97
Nov	0.56	0.74	0.14	0.26	0.01	1.71
Dec	0.81	0.99	0.13	0.31	0.02	2.25
Sum	6.81	7.38	1.43	1.82	0.16	17.60 Mm^3

Note; C1, C2, C3, C4, and C4 are catchment 1, catchment 2 and catchment 3, catchment 4, and catchment 5

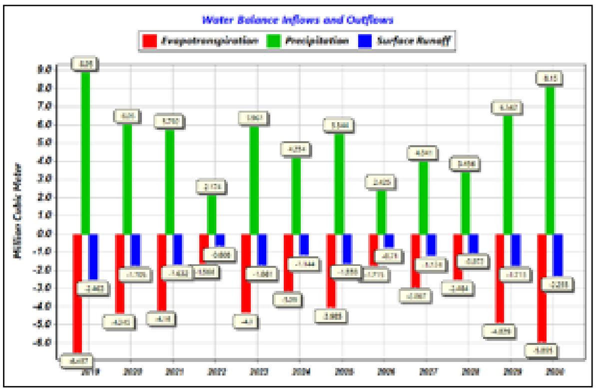

Figure 6. Water Balance of the study area (MCM)

3.2. Model Calibration

The calibration of the WEAP model for this study was based on discharges at the Borkena Wetland measuring stations near Kemissie, it was carried out between 1998-2018, and the results of the WEAP simulation are completely dependent on the quality of the data. Inputs such as hydrological and meteorological data. Model accuracy was assessed using Quantitative statistics (coefficient of determination, R2; NashSutcliffe efficiency, NSE and percent bias, PBIAS) calculated for each set of historical and model lines. simulated observations in the period 1998-2018, then I obtained the results as R2 = 0.988 Figure 7 and Table 7: and NSE = 0.70, PBIAS = 0.8, we can observe that the simulated and observed flows in the Borkena river at the measuring station, there is a good correspondence between the simulated and observed discharge values, the results show that The simulation adapts well to the observed data and the performance of the model is perfect and provides a good estimate as indicated in figure 7 and Table 6.

Table 6. Stream low at Gage station (observed Vs Simulated)

Year	Simulated	observed
2019	471.9849	544.4721
2020	572.1683	642.1291
2021	431.5058	494.0732
2022	419.3256	481.4614
2023	276.5615	359.1855
2024	97.25155	154.2819
2025	258.7808	322.5001
2026	235.1602	319.6679
2027	260.9561	361.2496
2028	183.9549	240.8115
2029	297.2647	382.9974
2030	232.2037	321.9756

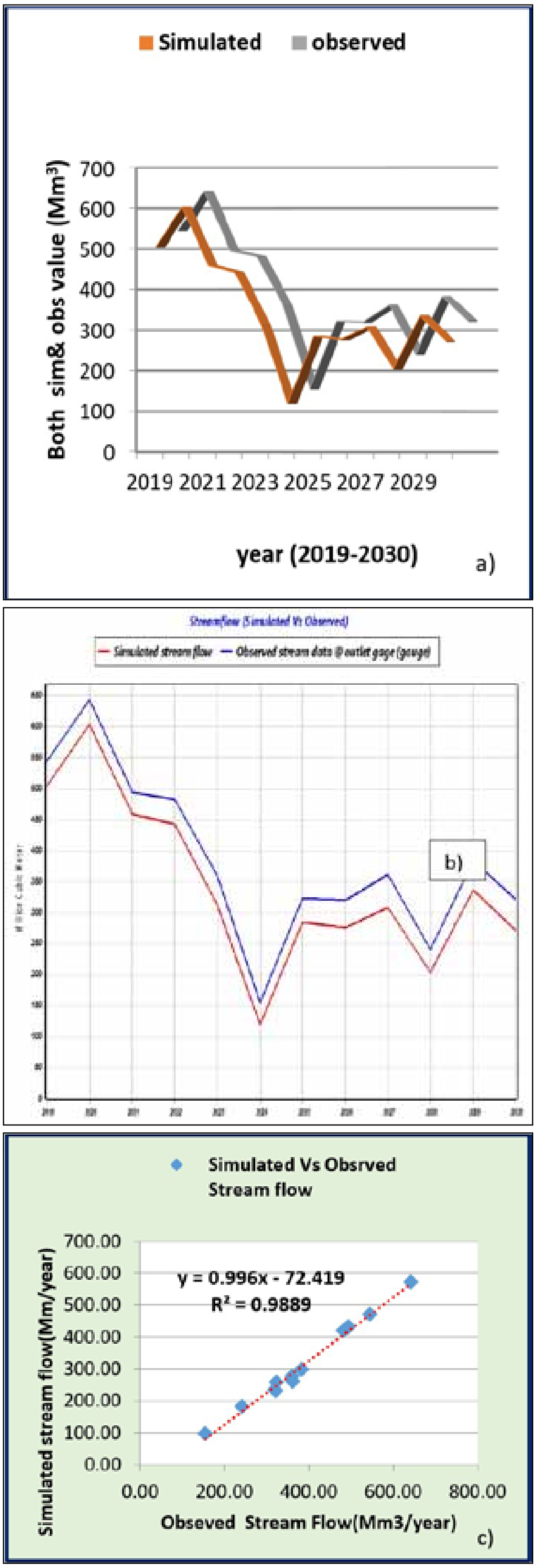

Figure 7. a) Observed and simulated streamflow in Borkena River (output from WEAP model) b) Observed and simulated streamflow in Borkena River c) Factor of determination (R2) for observed simulated Vs stram flow rate.

3.3. Environmental flow requirements

To maintain the ecological services as well as the natural channel habitat associated with the historic flow regimes of the Broken River, a certain reserve flow has to be maintained and could be considered as a sectoral demand on its own. The basic time unit used in preparing a flow duration curve was determined by sorting average monthly discharges for a period of record from the largest value to the smallest, involving a total of n values. The sorted monthly traffic values are assigned a rank (M) starting with 1 for the maximum value, and the probability of excess (P) is calculated by assuming a relatively low discharge exceeding 92% (with a corresponding discharge of 12 Mm3/year or Q92% = .50 m3/s) for the WEAP input in the Awash sub-basin of the Borkena Basin only. This area should not be overlooked, using the weak concepts of flow analysis shown in Table 7 and Figure 8.

Table 7. Flow duration curve of Borkena River at swamp outlet Near Kemiessie

Month	Q (Mm^3/YEAR)	FRANK(M)	N+1	P=100(M/N+1)	
Aug	1443	1	13	8%	30
Sep	663	2	13	15%	30
Jul	651	3	13	23%	30
Oct	335	4	13	31%	30
Mar	226	5	13	38%	30
Jan	223	6	13	46%	30
Apr	200	7	13	54%	30
May	196	8	13	62%	30
Dec	192	9	13	69%	30
Nov	178	10	13	77%	30
Feb	177	11	13	85%	30
Jun	142	12	13	92%	30

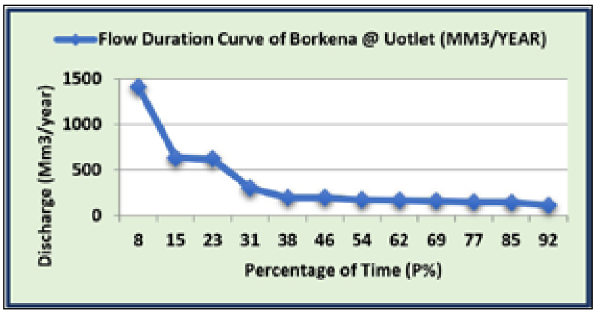

Figure 8. Flow Duration Curve for minimum Environmental Flow Requirement

3.4. Modeling of Water Demand for all scenarios

3.4.1. Current Scenario

The model current account was developed using demand data from 2019 and the Kemiessie store flow (supply) simulation data is 553. Mm3. The study area has at least six consumer needs, urban water demand, rural water demand, agriculture, livestock, industrial waste,r demand, and baseline water demand. Table 8: summary of model results for the current account (water consumption). These results indicate that utilization is low relative to the population in the flooded Kombolcha sub-basin. The total current water consumption in the study area is estimated at 390. 7 MCM per year. Thus, the amount of water extracted in the flooded Kombolcha sub-basin represents about 70.6% of the total available water in the region, or 553. Mm^3 per year. By comparing water requirements with available surface water resources, in the flooded Kombolcha sub-basin only 70.6% of the water available in the area is available for consumption. This scenario achieves an entire project-specific (2019), current data for the entire period with no changes imposed, and serves as a point of comparison for other scenarios where changes are performed for system data

Table 8. Average monthly Water Consumption of all demand node current accounts (Mm^3)

Month	AWD	CIWD	IWD	LWD	RWD	UWD	EFR	Sum
	1,1326ha	-	-	1,610,161	1,190,255	544,111	-	-
19-Jan	0.2	0	0.34	6.29	1.1	1.69	5.30	14.92
19-Feb	0.49	0	0.3	5.68	0.99	1.52	4.13	13.11
19-Mar	0.49	0	0.34	6.29	1.1	1.69	6.02	15.93
19-Apr	0.26	0	0.32	6.09	1.06	1.63	0.19	9.55
19-May	0.23	0	0.34	6.29	1.1	1.69	3.18	12.83
19-Jun	0	0	0.32	6.09	1.06	1.63	0.05	9.15
19-Jul	0	0	0.34	6.29	1.1	1.69	52.88	62.30
19-Aug	0	0	0.34	6.29	1.1	1.69	111.67	121.09
19-Sep	0.04	0	0.32	6.09	1.06	1.63	62.67	71.81
19-Oct	0.29	0	0.34	6.29	1.1	1.69	27.08	36.79
19-Nov	0.31	0	0.32	6.09	1.06	1.63	3.21	12.62
19-Dec	0.32	0	0.34	6.29	1.1	1.69	0.63	10.37
Sum	2.63	0	3.96	74.07	12.93	19.87	277.01	390.47

3.4.1.1. Unmet demand, demand coverage, and demand reliability for Current-scenarios

This study considered unmet demand, coverage, and demand reliability. Unmet demand is the amount of unmet requirements for each demand location and coverage is from 0% (no water) delivered to 100% (full requirement delivery). Reliability is a measure of how often or likely a system is in a satisfactory condition that meets certain criteria.

A) Unmet demand, demand for Current-scenarios (2019)

Unmet demand is defined as the amount of water that cannot be physically supplied from a river during a particular period of the year. This situation can be exacerbated in the future due to increased demand for water if no action is taken. Simulations using WEAP show requirements for April-June and November-December. As shown in figures 9 a) and b), a channel map similar to the case where rainfall occurs in the second half of the season, peak runoff occurs from July to October, and runoff is still fairly low from April to June and November to December. So it's difficult to achieve them which is shown in Figures 9 a) and b).

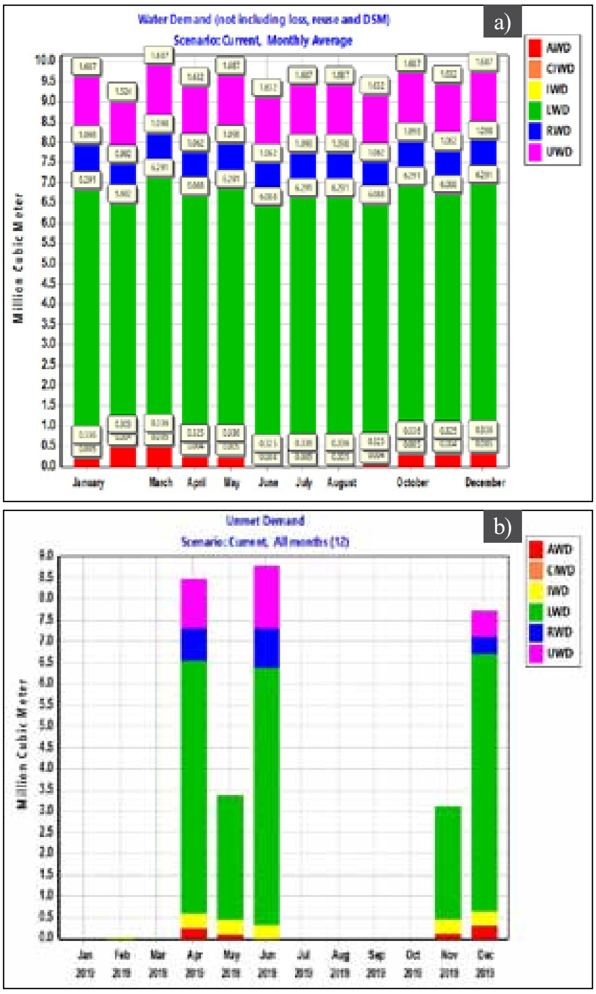

Figure 9. a) Current Monthly average water demand of all sectors in demand node b) Current Monthly average unmet demand of all nodes

B) Demand site coverage (%) for Current-scenarios (2019)

In the case of all Sectors in demand nodes are note covered 100% except July to October. While the other month over the year notes fully covered example from April to June average percent of coverage is 31.07% (unmet demand, 20.7 Mm^3) and from November to December percent of coverage is 42.7% (unmet demand, 10.8Mm3) which is the total unmet demand 20.7+10.8 = 31.46, this variation is clearly shown in the study area based on the result from WEAP model. Here, seasonal variations of rainfall lead to varying flow from each catchment in the study area as shown in Figure 9.

C) Demand site Reliability (2019)

The demand reliability in the current -Scenario for all demand sites does not reach 100% because available surface water is highly dependent on precipitation so this precipitation variation under the study area leads to demand reliability or dependability on available surface water is decreased. The demand reliability of all demand sites is shown in table 9.

Table 9. Demand site Reliable percentage for current -Scenario

Demand site Reliable Reference Scenario	AWD	CIWD	IWD	LWD	RWD	UWD
Percent (%)	62.50	55.56	54.17	55.56	75.00	75.00

3.4.2 Reference Scenario (20202030-)

Reference Scenario (2020-2030) represents the changes that are likely to occur in the future without intervention in new policy measures; it only increases with population growth. The population growth rate is 4.7% for urban and 1.3 rural% and for livestock is an average of 0.7 % annually. While assuming that similar trends of the streamflow situation will exist in the future. Hydrological conditions, Industrial and commercial, and institutional water demand are assumed unchanged into the future in this scenario. Climate change scenarios and their impact on surface water resources in this study are hard to be taken into account due to the limitations of climate data as shown in Table 10.

Table 10. Water Consumption (MCM) of the Reference Scenarios 2020_2030

Year	AWD	CIWD	IWD	LWD	RWD	UWD	EFR	Sum
2020	2.77	0.05	4.1	74.07	13.09	20.12	13.01	127.21
2021	2.94	0.05	4.25	74.07	13.26	20.38	8.53	123.48
2022	3.12	0.05	4.4	74.07	13.44	20.64	13.09	128.81
2023	3.33	0.05	4.56	74.07	13.61	20.91	10.17	126.7
2024	3.55	0.05	4.73	74.07	13.79	21.18	8.4	125.77
2025	3.8	0.05	4.9	74.07	13.97	21.46	5.36	123.61
2026	4.07	0.05	5.07	74.07	14.15	21.74	39.77	158.92
2027	4.37	0.05	5.26	74.07	14.33	22.02	89.57	209.67
2028	4.7	0.05	5.45	74.07	14.52	22.31	40.15	161.25
2029	5.07	0.05	5.65	74.07	14.71	22.6	13.57	135.72
2030	5.47	0.05	5.85	74.07	14.9	22.89	5.43	128.66
Sum	43.19	0.55	54.22	814.77	153.77	236.25	247.05	1549.8

The analysis of the result shows that there is not a significant change in the demand within the area when comparing this reference scenario with the scenario of the current account and is around 8.7 % of the total surface water availability in the study area. Therefore, there is a significant increase in livestock, rural and urban demand, due to the population in this area highly depending on livestock.

3.4.2.1. Unmet Demand and Demand coverage in Reference Scenario (20202030-)

The simulation with WEAP suggests that the unmet demand for this scenario shows significant change when comparing the current account, the requirements for Jan to June, and November to December. Still, the change followed similar to hydrographs during the rainy season that has a peak flow in July to November with flows higher shortage in the month Jan to June and November to December with the corresponding value of total demand coverage (%) and demands unmet is 46.52% of coverage and unmet demand 384.7 MCM as shown in Figure 10.

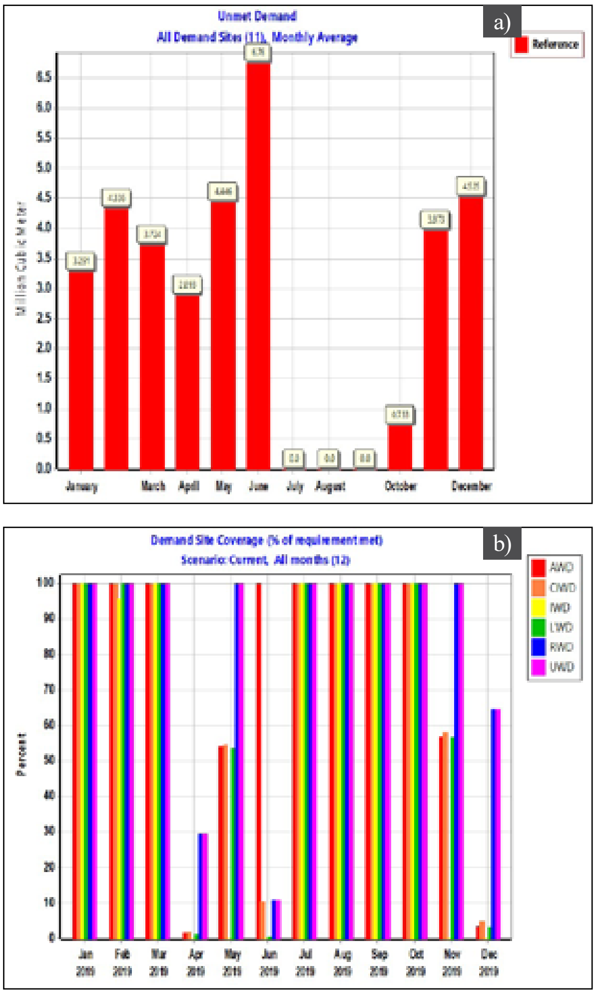

Figure 10. a) All Demand site coverage in (%) current scenario b) Unmet Demand for all nodes in Reference Scenario (2020-2030)

3.4.3. Medium growth up to 2030

Assuming a general medium growth scenario for 2030, where again livestock populations are increased by 1,610,161 to 1,776,937 with the corresponding value of average growth rate of 0.7% annual water used to be 81.9Mm^3. This means the annual water use rate is 90.5% increment shown when we compared the current scenario. The population rate in the study area has grown to almost a 5% annual increase from 544,111 to 930,615 and a 1.8% annual increase by 1,190,255 to 1448323 for urban and rural respectively (in 2030). Environmental flow demands stay constant (annually 247.05 Mm^3 for the Borkena River) as given in Table 11.

Table 11. Water demand of all demand nodes based on medium scenarios

Year	AWD	CIWD	IWD	LWD	RWD	UWD	EFR	Sum
2020	2.93	0.05	4.11	75.41	13.4	21.89	13.01	130.8
2021	3.3	0.05	4.28	76.77	13.88	24.14	8.53	130.95
2022	3.73	0.06	4.45	78.16	14.39	26.61	13.09	140.49
2023	4.24	0.06	4.63	79.57	14.91	29.34	10.17	142.92
2024	4.83	0.06	4.82	81.01	15.45	32.35	8.4	146.92
2025	5.52	0.06	5.01	82.47	16.01	35.66	5.36	150.09
2026	6.33	0.06	5.22	83.97	16.59	39.32	39.77	191.26
2027	7.3	0.06	5.43	85.48	17.2	43.35	89.57	248.39
2028	8.45	0.07	5.65	87.03	17.82	47.79	40.15	206.96
2029	9.81	0.07	5.87	88.6	18.47	52.69	13.57	189.08
2030	11.43	0.07	6.11	90.21	19.14	58.09	5.43	190.48
Sum	67.87	0.67	55.58	908.68	177.26	411.23	247.05	1868.34

It must be highlighted at this point again, that there are extremely trends of demand in livestock development and hence assumes quite high-water demand and has envisioned correspondingly high absolute abstractions from the rivers, these at some point might surpass the available river flows in this scenario for the Borkena river for instance in the total water demands of 1868.34Mm^3 have been abstracted from the total annual streamflow of 4625 Mm^3, and 2757 Mm^3 is reaming to the river.

3.4.3.1. Unmet Demand for Medium Growth Up To 2030

The unmet water demand is much higher in this scenario, the dry season demands and supplies are not balanced, however, the analysis shows that the situation of the unmet water demand monthly has been selected (Jan to June) and (Oct to Dec). Average monthly projections for river flows were selected as the highest unmet water demand in June. The result in this scenario shows that still considering the flow at the Kemiessie outlet of gauge station, the unmet demand during June is hence projected as 64.4Mm3 for Borkena River. The total unmet water demand is 515.2 Mm^3 corresponding to its demand coverage of 38.8%. Due to the agricultural, population, and livestock developments and demand variation on monthly flow are achieved in the medium growth scenario. Hence the dry season water demand is relatively high as compared with the rainy season. But extending the Socio-economic development in these scenarios with the increasing agricultural, industrial, commercial, and institutional development as result the remaining surface water availability above in 4.4.3 will be sufficient based on wet seasons but in dry months over the year demand is greater than the supply due to the available water resource is highly dependent on seasonal rainfall as shown in Figure 11.

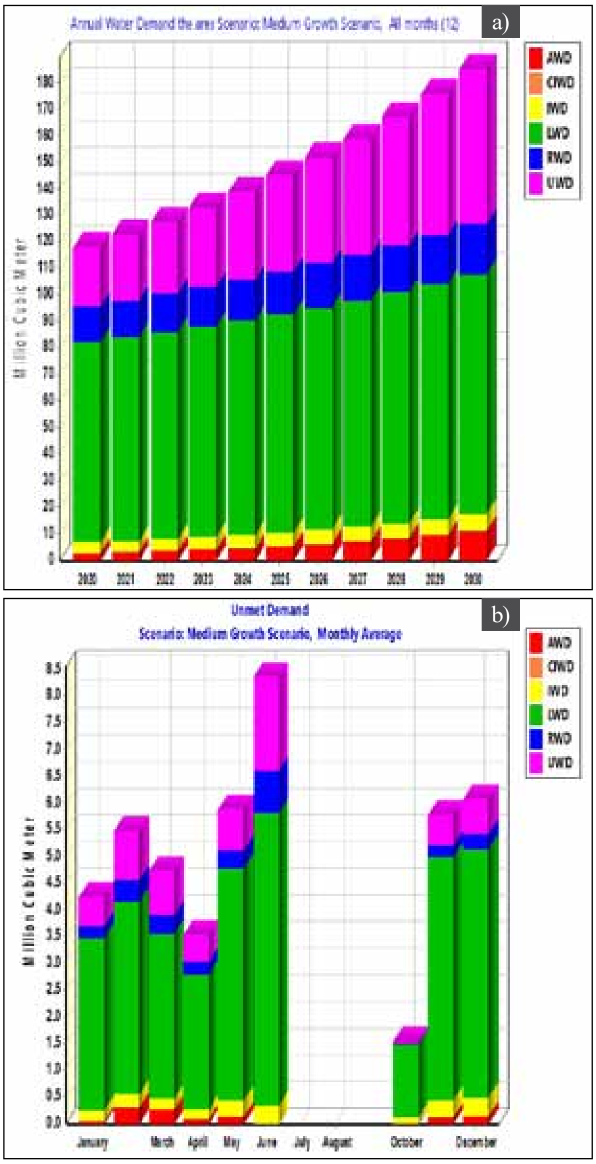

Figure 11. a) Water demand of all demand nodes based on medium scenarios b) Unmet water demand based on medium scenarios

In the flooded Kombolcha catchment of Volkena, urban, rural, livestock, and agricultural water demand account for about 33.86% of total surface water availability, while industrial and commercial water demand accounts for about 1.22 of water demand. About 32.4% of the total average annual demand in the study area is highest in the months (January-June) and (October-December). The medium-growth scenario shown in Figure 12 shows a tendency to increase faster than the base value. This is highly dependent on local precipitation, which will significantly reduce the availability of water in the future, impacting economic and environmental conditions. And its surrounding area catchment area is shown in Figure 12.

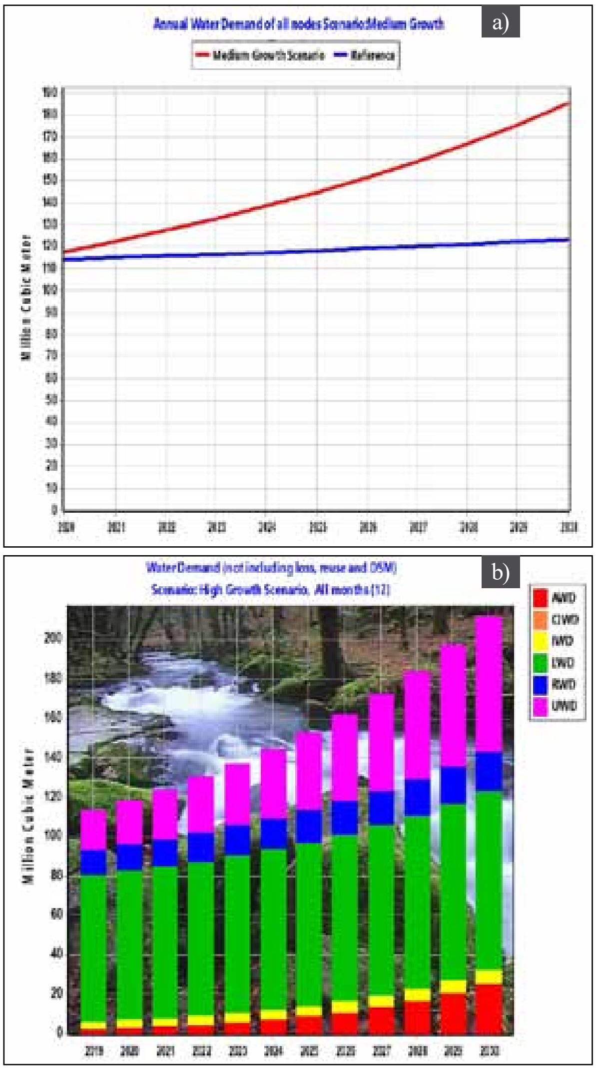

Figure 12. Comparison of Annual water demand for all nodes between medium growth and reference Scenario b) all scenarios in annual water demand

3.4.4 High growths up to 2030

The result in this scenario also shows that still considering the flow at the Kemiessie outlet of gauge station, the unmet demand during June is hence projected as 68.8Mm3for Borkena River, and the total unmet water demand is 572.6 Mm^3 corresponding to its demand coverage of 30.9%, due to the population density and large livestock size extremely expose in a surface water shortage for the other socio-economic developments scenario except for rainy season tables 12,13, 14 and Figure 13.

Table 12. Water demand of all demand nodes based on High scenarios

In (Mm3)	AWD	LWD	RWD	UWD	CIWD	IWD	EFR	Total
Annual Activity	35,450ha	1,786,648	1,479,933	1,011,649	-	-	-	
Water demand	122.86	914.26	181.75	457.58	0.66	59.2	247.05	1983.3MCM
Unmet demand	572.6Mm^3							

Table 13. Comparison of water demand, unmet demand, and coverage

All Scenario	(Total Available surface water resource (MCM) 2019-2030)) = 4625 MCM	water used from Available (MCM)	Available water remaining Storage (MCM)	Unmet demand (MCM) Observed during (Jan to June) & (Oct to Dec)	Demand Coverage (%) Observed during (Jan to June) & (Oct to Dec)
Current account by 2019	544.5	390.5	154	31.5	73.77
Reference 2020-2030	4080.3	1549.81	2530.49	384.7	46.52
Medium Growth up to 2030	4080.3	1868.35	2211.95	515.2	38.8
High Growth up to 2030	4080.3	1983.32	2096.98	572.6	30.9

Table 14. Comparison of water demand for all scenarios

All Demand site	current data by 2019	Reference scenario up to 2030	Medium Growth up to 2030	High Growth up to 2030
AWD	2.62	43.19	67.87	122.82
CIWD	0.05	0.59	0.66	0.66
IWD	3.95	54.21	55.58	59.20
LWD	74.07	814.74	908.68	914.26
RWD	12.93	153.77	177.25	181.75
UWD	19.86	236.25	411.25	457.58
EFR	277.00	247.05	247.05	247.05
Sum	390.48	1549.81	1868.35	1983.32

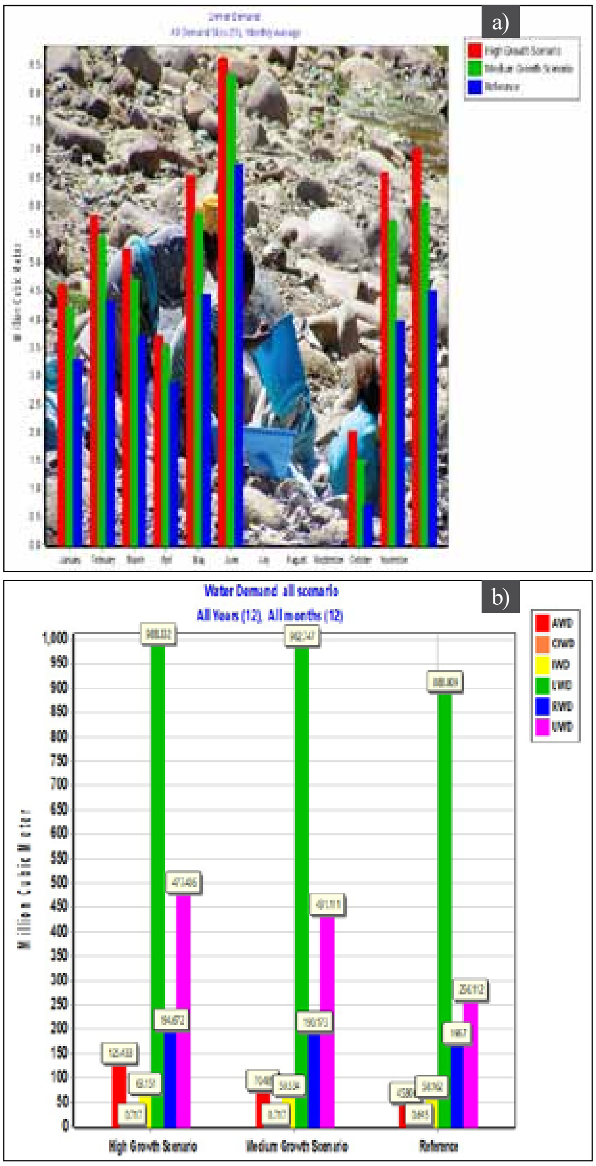

Figure 13. Unmet Demand of all Scenarios in the study area b) summary of total water demand by 2030 scenarios

3.5. Water resource and optional adaptation measures

Ethiopia is currently experiencing significant natural and socio-economic changes that are changing the availability and needs of water resources. Due to its geography and climate, Ethiopia has always been characterized by high hydrological variability. It was exacerbated by the almost complete lack of reservoirs and highly sensitive watersheds (Beatrice et al., 2015). Climate change is expected to increase uncertainty and extremes in meteorological patterns and increase precipitation variability (Beatrice et al., 2015). In addition, the remarkable economic growth and population growth of the last decade require a lot of good water resources, causing known pollution problems. Nevertheless, Ethiopia's water sector is still characterized by poorly integrated plans, and the allocation of water resources is not based on competing demands or a systematic understanding of water availability. This has already led to conflicts, as shown in the case of the Awash River basin between upstream, middle, and downstream water users (Beatrice et al., 2015). WRM's existing legal and political framework has already fixed the basic principles of Integrated Water Resources Management (IWRM). But; needs updates and enhancements. Also, catchment plans by the Embryonic River Basin Authority (AWRBA) remain weak. The establishment of a "sufficient" institution (WRM) in Ethiopia is hampered by a lack of knowledge about resource conditions, usage patterns, and the impetus for change. Lack of on-site capacity and skills to plan water distribution and assess impact. Etc. (Beatrice et al., 2015).

Agricultural demand comprises irrigation of large plots and formal schemes. Therefore, only scaled irrigation is represented in this sector. Within the WEAP model, the irrigation water demand varied inter-annually or monthly based on rainfall. During wet years the irrigation demand reduces and during dry years it increases (Pousa,2019). Agricultural irrigation demands have been calculated by simulating the demand node on WEAP and the CropWat8 model of the Food and Agriculture Organization (FAO) was used to simulate the observed seasonal pattern of irrigation with different cropping seasons in the area. Metrological data were used to estimate net evaporation (ETo), Kc and effective rainfall from the study area, and monthly share of irrigation demand.

3.5.1 Scenarios adaptation measures

Table 14 and Figure 13 above show that the region's only demand coverage (%) for all sectors is monthly (7), as precipitation in this region is characterized by a rainy season / long bimodal precipitation pattern. It indicates that it will be filled from month to September), which means less / shorter rainy season. The low/short rain months from March to April cannot meet the demands of all sectors, even if the environmental flow requirements of the study area are required. Precipitation patterns such as October, November, December, January, February, May, and June are dry. For this reason, other optional implants such as rainwater harvesting are needed surface water harvesting to meet the peak demand for dry months where the availability of surface water resources in these scenarios is felt in all waters. And use the sector where you need to book groundwater together. However, this combination of surface and groundwater may improve and address problems related to water scarcity (January-June) and (November-December), satisfying demand and efficient use. Groundwater nourishes the surface, although it should be considered an important strategy. Water needs to be improved and used for catchment management through integrated large-scale management. The results of this study clearly show that in all scenarios there is an oversupply on the supply side during the rainy season in the sub-collection area, and an integrated approach to water resource development in the sub-collection area is taken. To avoid the use of water in the dry season, it is necessary to meet the water demand of all sectors and respond to competition and conflict. Sub-basin water resources required great demand for current water resources in the morning, such as the Jara River and wetlands, to properly manage water. This supply-side surplus must also be secured during the rainy season throughout the year to meet future water demand if harvested carefully. One of the main objectives of this study is to assess the availability of surface water in terms of supply and demand systems in the Awash-Kombolcha sub-basin of the Bokanea River. The result of this study is to transfer supply and demand forecasts up to 2030 to assess the possible impacts of future scenarios related to surface water availability. Stakeholders and civil society participation in water management and conservation efforts need to be facilitated through education and capacity building, making policy processes more transparent and collaborative. Suggested that integrated river basin management is included as an important element of an efficient and effective strategy to address water scarcity, especially in dry months, through the use of increasingly scarce resources in the study area. It's an exaggeration to do. It provides a wide range of opportunities for all stakeholders, including the general public, to share their views and influence results. Raise awareness at the basin level and develop various preventive and mitigation measures against floods and droughts. Build consensus and public support for results. Build stakeholder involvement. Ensuring flood management plans for river basins with extensive public support. Ensure the sustainability of plans and related decisions. Strengthen the resilience of flood-prone communities.

4. Conclusion

The overall purpose of the study is to perform surface water availability and demand analysis for water resource planning in the flooded Kombolcha catchment of the Bokanea catchment. This has been elaborated by using the WEAP approach (water assessment and planning tool). It was that. Based on the results of the survey, the following conclusions were drawn. The availability of surface water sub-basin is (544.5 Mm3 emissions), and under current water demand conditions, pet and livestock water demand, the average annual emissions at the Samp Exit measurement station near Khemiessy are. It is 17.3 m3 / s. 106.9 million m3 is the largest consumer of surface water, followed by agriculture, trade, industry, and 6.6 million m3, with an environmental requirement of 142 million m3. Currently, the total annual water demand in the basin accounts for 20.85% of the total surface water available, which is sufficient to meet the site's total water demand during the rainy season. Analysis and simulation of surface water availability and demand in the flooded Kombolcha sub-basin of the Bokanea River have limited data availability through the basic functions of WEAP, without the use of a link between groundwater analysis and climate change. It was executed. In this study, a scoring model was used to operate on the WEAP underwater catchment scale and monthly time steps. The survey period was 2019-2030. The calculation of evaluation model was performed by calculating the overall model of the reference scenario, which is a failure scenario, generated using the current account information for the study period (2019-2030). The year of the current account is selected as the base year for the valuation model. In this survey, all current account data are relevant for 2019. The adaptation methods regarding water harvesting and flood control can be achieved by providing all stakeholders, including the public, with full opportunities to share their views & influence the outcome; raising awareness at the basin level & developing a host of preventive & mitigation measures against floods & droughts. Build consensus & public support for the outcomes; build stakeholders' commitment; ensure implementation of basin flood management plans with full public support; ensure the sustainability of plans & associated decisions, and build the resilience of flood-prone communities.

Acknowledgments

The authors want to express their sincere thanks to the Awash City Administration for sharing the data used in this study. There is no conflict of interest in this work. This research was not supported by any funding institution.

Acronyms

AWD	Agricultural water demand
CIWD	Commercial and institutional water demand
EFR	Environmental flow requirement
IWD	Industrial water demand
LWD	Livestock water demand
RWD	Rural water demand
UWD	Urban water demand

References

ABA. (2017) Awash River basin integrated participatory watershed management strategic & detail action plan, Awash basin Authority, Adis Abeba, Ethiopia.

Adgolign, T.B., Rao, G.V.R. and Abbulu, Y., 2016. WEAP modeling of surface water resources allocation in Didessa Sub-Basin, West Ethiopia. Sustainable Water Resources Management, 2(1), pp.55-70.

Aung, Z.W., Dietrich, I.J. and van der Heijden, I.S. (2014) Water supply options for the growing megacity of Yangon-scenarios with the WEAP model (Doctoral dissertation, Ph.D. thesis, University of Hannover).

Baker, J.L. ed. (2012) Climate change, disaster risk, and the urban poor: cities building resilience for a changing world. World Bank Publications.

Beatrice Mosello, Roger Calow, Josephine Tucker, Helen, Parker, Tena Alamirew, Seifu Kebeded.et. al. (2015) Tesfay Alemseged, Assefa Gudina (2015). Building Adaptive water resources management in Ethiopia, Publications, 203 Blackfriars Road, London SE1 8NJ, Tel. +44 (0) 20.

Belachew, E.Z. (2019) Estimating combined loads of diffuse and point-source pollutants into the Borkena River, Ethiopia. CRC Press.

Belayneh Y.(2018) The Effect of Lake Beseka Discharge on Irrigation Water Quality of Awash River (Doctoral dissertation, ASTU).

Bezabih, B. and Mosissa, T. (2017) Review on distribution, importance, threats, and consequences of wetland degradation in Ethiopia. International Journal of Water Resources and Environmental Engineering, 9(3), pp.64-71.

Cosgrove WJ, Loucks DP.(2015) Water management: Current and future challenges and research directions. Water Resources Research. 2015 Jun;51(6):4823-39.

Fan X, Ma Z, Yang Q, Han Y, Mahmood R. Land use/land cover changes and regional climate over the Loess Plateau during 2001–2009. Part II: interrelationship from observations. Climatic Change. 2015 Apr;129(3):441-55.

Francés, G.E., Quevauviller, P., González, E.S.M. and Amelin, E.V. (2017) Climate change policy and water resources in the EU and Spain. A closer look into the Water Framework Directive. Environmental Science & Policy, 69, pp.1-12.

Gummadi, S., Rao, K.P.C., Seid, J., Legesse, G., Kadiyala, M.D.M., Takele, R., Amede, T. and Whitbread, A. (2018) Spatio-temporal variability and trends of precipitation and extreme rainfall events in Ethiopia in 1980–2010. Theoretical and Applied Climatology, 134(3), pp.1315-1328.

International of postgraduate Conference (2017) Application of Water Evaluation and Planning Model for Integrated Water Resources Management: Case Study of Langat River Basin, Malaysia, publisher, IOP Conf. Series: Materials Science and Engineering 210 (2017) 012024 doi:10.1088/1757-899X/210/1/012024.

Kahil, M.T., Dinar, A. and Albiac, J. (2015) Modeling water scarcity and droughts for policy adaptation to climate change in arid and semiarid regions. Journal of Hydrology, 522, pp.95-109.

Kebede S. (2013) Groundwater occurrence in regions and basins. In Groundwater in Ethiopia; (pp. 15-121). Springer, Berlin, Heidelberg.

Kerala AS.(2019) Assessment and Modeling of Surface Water Quality Dynamics in Awash River Basin, Ethiopia (Doctoral dissertation, Addis Ababa Institute of Technology, School of Chemical and BioEngineering, Addis Ababa University.

McGinnis, M.D. and Ostrom, E. (2014) Social-ecological system framework: initial changes and continuing challenges. Ecology and Society, 19(2).

Morris, C. ed.(1923) Winston's Cumulative Loose-leaf Encyclopedia: A Comprehensive Reference Book (Vol. 6). John C. Winston Company.

Polidori, L. and El Hage, M.(2020) Digital elevation model quality assessment methods: A critical review. Remote sensing, 12(21), p.3522.

Pousa, R., Costa, M.H., Pimenta, F.M., Fontes, V.C., Brito, V.F.A.D. and Castro, M., 2019. Climate change and intense irrigation growth in Western Bahia, Brazil: The urgent need for hydroclimatic monitoring. Water, 11(5), p.933.

Shumet A, Mengistu K. (2016) Assessing the Impact of Existing and Future Water Demand on Economic and Environmental Aspects (Case Study from Rift Valley Lake Basin: Meki-Ziway, Sub Basin), Ethiopia. Int J Waste Resour 6: 223. doi:10.4172/2252-5211.1000223.

Singh, P., Gupta, A. and Singh, M., 2014. Hydrological inferences from watershed analysis for water resource management using remote sensing and GIS techniques. The Egyptian Journal of Remote Sensing and Space Science, 17(2), pp.111-121.

Subramoniam, S.R., Joseph, M., Bera, A.K. and Sharma, J.R. (2013) Role of Earth Observation (EO) Technologies in Dryland Management towards Adaptation to Climate Change. Annals of Arid Zone, 52(1), pp.7-15.

Tadese, M., Kumar, L., Koech, R. and Kogo, B.K. (2020) Mapping of land-use/land-cover changes and its dynamics in Awash River Basin using remote sensing and GIS. Remote Sensing Applications: Society and Environment, 19, p.100352.

Teklehaymanot T. An ethnobotanical survey of medicinal and edible plants of Yalo Woreda in Afar regional state, Ethiopia. Journal of Ethnobiology and Ethnomedicine. 2017 Dec;13(1):1-26.

Tufa KN.(2021) Review on Status, Opportunities, and Challenges of Irrigation Practices in Awash River Basin, Ethiopia. Agrotechnology; 10:207.

Worqlul, A.W., Collick, A.S., Rossiter, D.G., Langan, S. and Steenhuis, T.S. (2015) Assessment of surface water irrigation potential in the Ethiopian highlands: The Lake Tana Basin. Catena, 129, pp.76-85.

Xiao-jun W, Jian-Yun Z, Shahid S, Xing-hui X, Rui-min H, Man-ting S. (2014) Catastrophe theory to assess water security and adaptation strategy in the context of environmental change. Mitigation and Adaptation Strategies for Global Change;19(4):463-77.

Yohannes, H. and Elias, E. (2017) Contamination of rivers and water reservoirs in and around Addis Ababa City and actions to combat it. Environ Pollut Climate Change, 1(116), p.8.

Zainab, E. (2011) Assessment of the impact of industrial effluents on the quality of irrigation water and changes in soil characteristics: the case of Kombolcha town. Irrigation and Drainage, 60(5), pp.644-653.

Zainab, E. (2011) Assessment of the impact of industrial effluents on the quality of irrigation water and changes in soil characteristics: the case of Kombolcha town. Irrigation and Drainage, 60(5), pp.644-653.

JJEES

JJEES (2022) 13 (3): 215-222
ISSN 1995-6681

Jordan Journal of Earth and Environmental Sciences

Integrated Geophysical Study for Delineation of Structures Favorable to Uranium Mineralization in Al-Amerat, Sultanate of Oman

Narasimman Sundararajan*, Bernhard Pracejus, A Ebrahimi, Talal Al Hosni and Jaber Al Neseiri

Department of Earth Science, Sultan Qaboos University, Muscat, Sultanate of Oman

Received 16 February 2021; Accepted 21 January 2022

Abstract

The spectroscopic results of the acquired Gamma-ray have indicated a moderately high concentration of radioactive minerals showing ~100 ppm of Uranium and ~1000 ppm of Thorium in the placer deposit in Amerat, near Muscat Sultanate of Oman. To identify the extension and structural parameters of the Formation, the area was further investigated with very low frequency electromagnetic (VLF-EM) and magnetics surveys along five profiles of approximately 200 m long 20 m apart (10 m measurement intervals). In-phase and quadrature components of the VLF-EM signal were recorded at two different transmitter frequencies (15.1 kHz and 16.4 kHz) as well as the total magnetic field. Processing and interpretation were carried out by well-known methods such as Euler deconvolution, Fourier spectral analysis, and also by Hilbert transform technique. Magnetics data resulted in a depth in the range of 5-20 m by Euler deconvolution and 6-12 m by Fourier spectral analysis whereas the VLF-EM signals have resulted in a depth in the range of 7.2 m-10.4 m by Karous and Hajelt (KH) filtering. On the other hand, the Hilbert transform technique estimated both the depth and width of the subsurface source in the range of 9.2 – 24 m and 19.5 – 66.5 m respectively. Thus, the overall analyses of geophysical data have revealed the possible Uranium bearing structures as deep as 5-24 m from magnetics and VLF-EM methods.

Keywords: *In-phase component, Uranium, Thorium, Fraser filter, Karous-Hjelt current density, Gamma spectroscopy.*

1. Introduction

Spectrometry is a well-established analytical technique that has been widely used for elemental composition analysis. A relatively recent development has been the availability of sophisticated digital instrumentation, which can be used for both direct in situ non-destructive analysis of samples also is readily transportable to field sites for use in a mobile laboratory style of operation (Povinec et al., 2005). Gamma-ray spectrometry is a surveying technique that allows the calculation of the heat produced during the radioactive decay of Potassium, Uranium, and Thorium within rocks (IAEA, 2003).

VLF-EM is a rapid, simple, and economical tool among all geophysical devices with the capability of being carried out on rough topographic areas. The device receives signals from 42 military navigation stations across the world and is a well-established technique for Uranium and other mineral exploration (Sharma et al., 2014). The subsurface targets of specific surveys are often small-scale structures buried at shallow depths (Karous and Hjelt, 1983). In addition, the magnetics method which is equally popular in mineral exploration is also an efficient and economical geophysical technique. Ramesh Babu et al. (2007) have successfully applied the magnetic method in association with the VLF-EM technique in delineating Uranium deposits in the Proterozoic basins of Raigarh district, India.

In Amerat, near Muscat, Sultanate of Oman, the investigation for uranium was carried out using the geophysical methods discussed above. In the study area, the slightly metamorphosed siliciclastic Amdeh Formation belongs to the Ordovician and is ~1700 m thick, outcropping in the Wadi Qahza area of Muscat. This geological section contains two small placer deposits, which represent a succession of shallow marine siliciclastic shelf facies, measuring around 3400 m in overall thickness. The Formation is characterized by well-bedded quartzite exhibiting tabular cross-beds and contorted bedding structures that were specifically investigated with a Gamma-ray spectrometry technique.

The initial investigation based on Gamma-ray spectroscopy has revealed a moderate concentration of Uranium as much as 100 ppm and Thorium around 1000 ppm with minor traces of Potassium near the Amerat area of Muscat, Sultanate of Oman. Further, to establish the spatial location of the structures that host these radiometric anomalies were investigated by magnetic as well as VLF-EM techniques, and then processed and interpreted results approximately yield a depth to subsurface source in the range of as 5-24 m are presented.

* Corresponding author e-mail: raajanns@hotmail.com

2. Geology of the study area

The study area is a small hilltop highly uneven terrain covering an area of less than 200-300 square m encompassing the coordinates 23°17'57.6" N and 58°22'10.1" E. The heavy minerals of these placers dominantly consist of ilmenite ($FeTiO_3$), anatase (TiO_2), and zircon ($ZrSiO_4$). Hematite (Fe_2O_3) and apatite ($Ca_5(PO_4)_3F$) are relatively rare, although hematite stains reveal their presence through red internal reflections, and the presence of apatite is reflected through increased phosphorous levels. The oldest rocks of the eastern Hajar Mountains are exposed in the cores of two large anticlinal structures (e.g., Béchennec et al., 1993), the Jabal Akhdar and the Saih Hatat Domes, which formed during the Late Cretaceous during obduction of the Semail Ophiolite (Glennie et al., 1973, 1974; Searle and Malpas, 1980; Lippard et al., 1986; Searle and Cox, 1991; Hacker, et al., 1996; Goffé et al., 1998). The Amdeh Formation is an autochthonous unit and was exposed to gentle metamorphism, in which quartz-rich sandstones were transformed into the "Amdeh Quarzite" (Am4). This metamorphism may predate ophiolite obduction, probably during the Hercynian orogeny (Glennie et al., 1974; Beurrier et al., 1986). Exposures of the Amdeh Formation are restricted to the Saih Hatat Dome (Wadi Qahza is the study area in its western part of the dome encompassing 23°17'57.6" N and 58°22'10.1" E).

The Amdeh Formation represents a succession of shallow marine siliciclastic shelf facies, measuring at least 3400 m in overall thickness (Lovelock et al., 1981), in which Am4 is characterized by well-bedded quartzites exhibiting tabular cross-beds and contorted bedding structures. Am4 accumulated in a rapidly subsiding coastal environment during the Ordovician (Lovelock et al., 1981). There are also mafic intrusions of unknown age in this formation (Oterdoom et al., 1999). The source rocks for the placer deposits that contain ilmenite (>50%) > anatase > zircon > tourmaline (Knox, 2006) > monazite (Knox, 2006), hematite (<1%), and apatite (<1%), may be found in metamorphic and acidic plutonic rocks of the Omani basement, which may have shed detritus from exposed rift shoulders. The location of the study area as well as the geological map are shown in Figure 1.

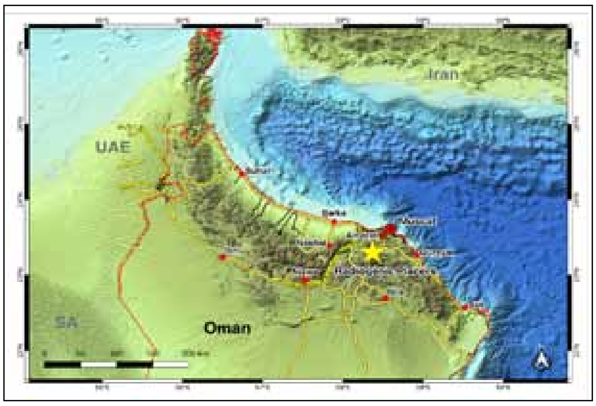

Figure 1. a. The location of the study area is Amerat near Muscat, Sultanate of Oman

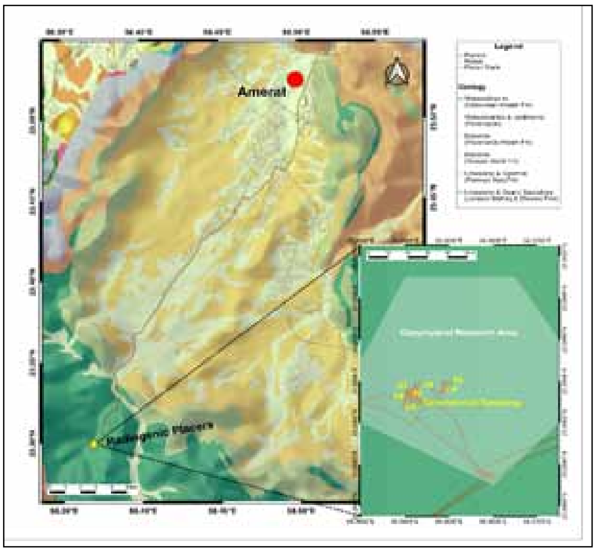

Figure 1. b.The geology of the study area with geophysical traverses.

Figure 1. (a) Location of the study area (b) and geological map.

3. Methodology

The magnetic method is a fast and simple technique that is extremely useful in mineral exploration. There are some renowned processing steps for processing and interpretation of magnetic data. Euler deconvolution (ED) and spectral analysis are widely used in potential field anomalies such as magnetic, gravity, electric, and electromagnetic fields to evaluate the depth and other parameters of the causative sources. Initially, the ED was proposed by Thompson (1982) and later extended by Reid et al. (1990), and improved by Keating (1998) and Mushayandebvu et al. (2004). ED has a wide range of applications (Gerovska and Araúzo-Bravo, 2003) and the popularity of this elegant method is due to its simplicity and ease of implementation and hence its choice for a quick initial analysis. Further, the radially averaged power spectral analysis has a wide range of applications in geophysical data processing and is perhaps the most common in potential field data for estimation of depth and other parameters of the subsurface geophysical structures (Hinich and Clay, 1968; Bhattacharyya and Leu, 1977).

Very low frequency electromagnetic (VLF-EM) is yet another useful technique with a wide range of applications in geological mapping and environmental issues as well as in mineral exploration. The VLF method uses 42 powerful remote radio transmitters across the world for military communications at frequencies range 15 to 30 kHz. Generally, the interpretation of the VLF-EM signal is based on qualitative analysis particularly based on Fraser and K-H filtering (Fraser, 1969; Karous and Hjelt, 1983) which are routinely used in many applications including Uranium exploration (Ramesh Babu et al., 2007). In the recent past, Sundararajan et al. (2011) have used the method of Hilbert transform as a semi-quantitative analysis of in-phase and out-of-phase components for the estimation of depth to the source.

4. Data Acquisition and Interpretation

The various geophysical data were acquired using a BGO Super RS-230 spectrometer, a G-859 mining magnetometer, and a portable VLF-EM receiver along 5 traverses of each 200 m at a measurement interval of 10 m and line interval of 20 m comprising a small area. Contour images of Uranium, Thorium, and Potassium concentrations along the indicated principal profile (PP) are shown in Figure 2. Further, the recorded Gamma-ray spectroscopic concentration of Uranium, Thorium, and Potassium along the principal profile (PP) is shown in Figure 3. A combination of Uranium, Thorium, and Potassium was used to create a ternary image, as shown in Figure 4.

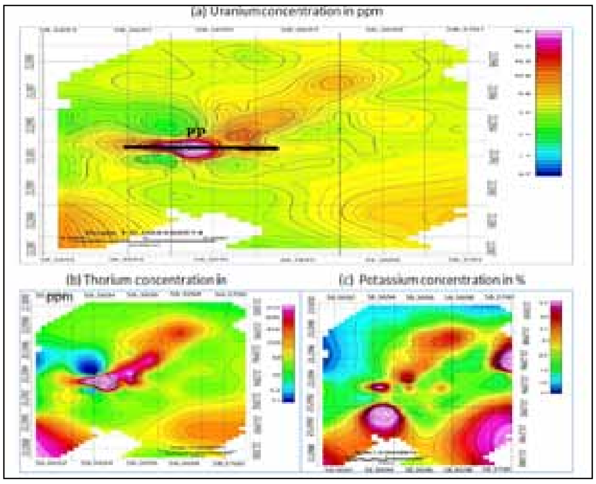

Figure 2. Contour map of (a) Uranium (b) Thorium and (c) Potassium concentrations recorded by Gamma-ray spectrometer.

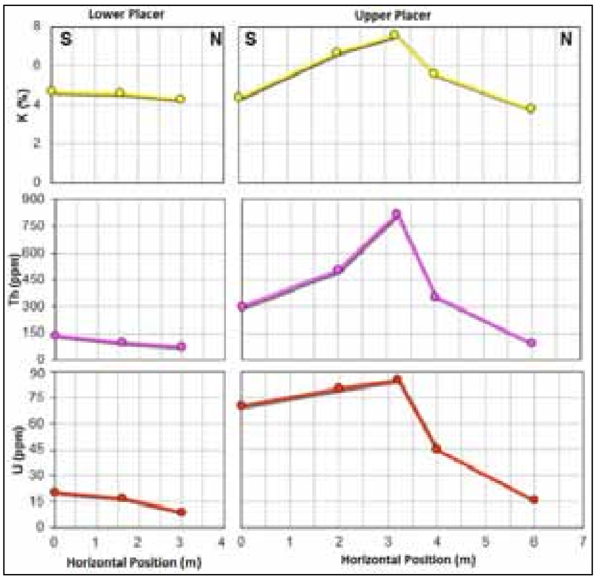

Figure 3. Recorded Gamma-ray spectroscopic concentration of Uranium, Thorium, and Potassium along the principal profile (PP).

Furthermore, the contoured map of a total magnetic field, as well as the amplitude of analytical signal that can delineate the subsurface target, are shown in Figures 5 (a and b). The depth to subsurface structures from magnetic anomalies was estimated based on two well-known methods such as spectral analysis and Euler Deconvolution (ED) which are shown in Figures 5 (c and d). Also, the in-phase component at two different transmitter frequencies indicate the spatial location of subsurface conductors and are shown in Figure 6 (a-b). The contour map of Fraser filtered in-phase and quadrature components for both transmitter frequencies of 15.1 kHz and 16.4 kHz are shown in Figure 7 (a-d). The signal was also subjected to Hjelt filtering (current density) which yields the depth to the source given in Figure 8 (a-f). In addition, the in-phase component of VLF-EM signals is used for Hilbert transform analysis to derive the depth to the source as well as width. All the five traverses (L1, L2, L3, L4, and L5) at transmitter frequency 15.1 kHz and L3 and L4 at transmitter frequency 16.4 kHz were subjected to Hilbert transform analysis and are shown in Figures 9 (a-g). For each traverse, the Hilbert transform of the in-phase component, and amplitude of the analytic signal that aids in the precise spatial location of the subsurface target were computed and shown in Figure (a-g). Further, the Hilbert transform of the principal profile (PP) of the VLF-EM in-phase component at a transmitter frequency of 15.1 kHz was also computed and shown in Figure 10. The depths to subsurface structures derived from magnetic and VLF-EM fields are shown in Table 1. Also, the depths derived from the Hilbert transform of in-phase components of all five traverses as well as the principal profile(PP) of the VLF-EM signal are given in Table 2. A brief procedural description of methods used in the interpretation of data is discussed hereunder.

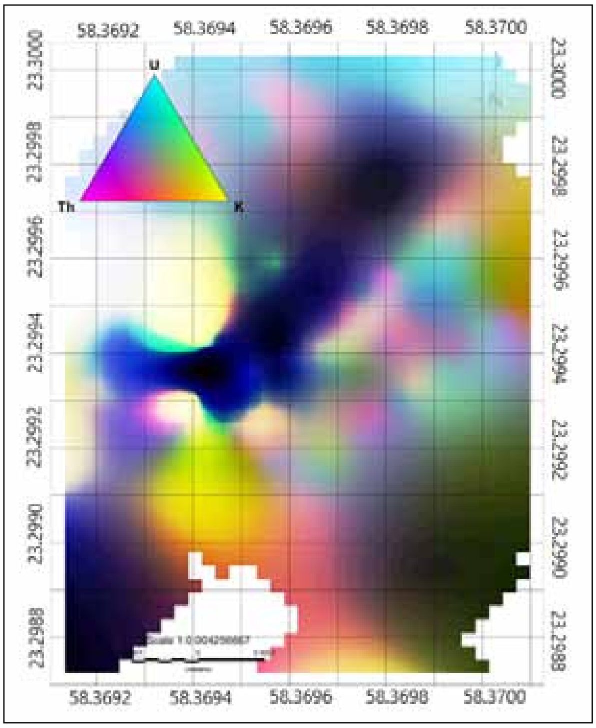

Figure 4. Ternary image of Uranium, Thorium, and Potassium

Table 1. The estimated depth of subsurface structures (in meters) from magnetic and VLF-EM fields.

Method	Magnetic	VLF-EM
Euler Deconvolution	5-20 m	-
Spectral Depth	6-12 m	-
Karous-Hjelt Depth	-	7.2-10.4 m

Table 2. The estimated depth of subsurface structures (in meters) was acquired by applying the Hilbert transform to VLF-EM signals.

Traverse/Transmitter Frequency →	15.1 kHz		16.4 kHz	
	Width(m)	Depth(m)	Width(m)	Depth(m)
L1	19.5	14		
L2	46	-		
L3	27.5	9.2	66.5	10.5
L4	35	-	27	9.5
L5	29.5	20.2		
Principal Profile of In-phase Component	35	24	-	-

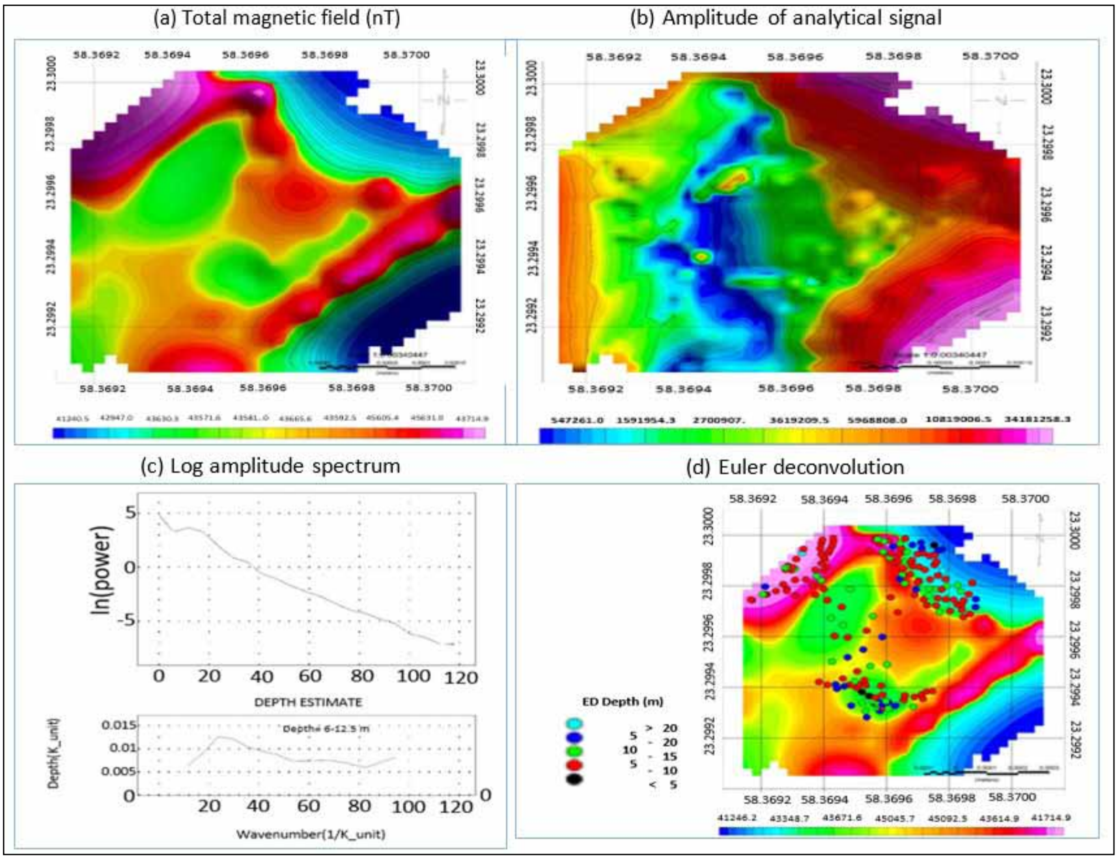

Figure 5. (a) Total magnetic field (nT) and (b) amplitude of the analytical signal of the magnetic field. Depth to subsurface structures by (c) Spectral analysis and (d) Euler Deconvolution

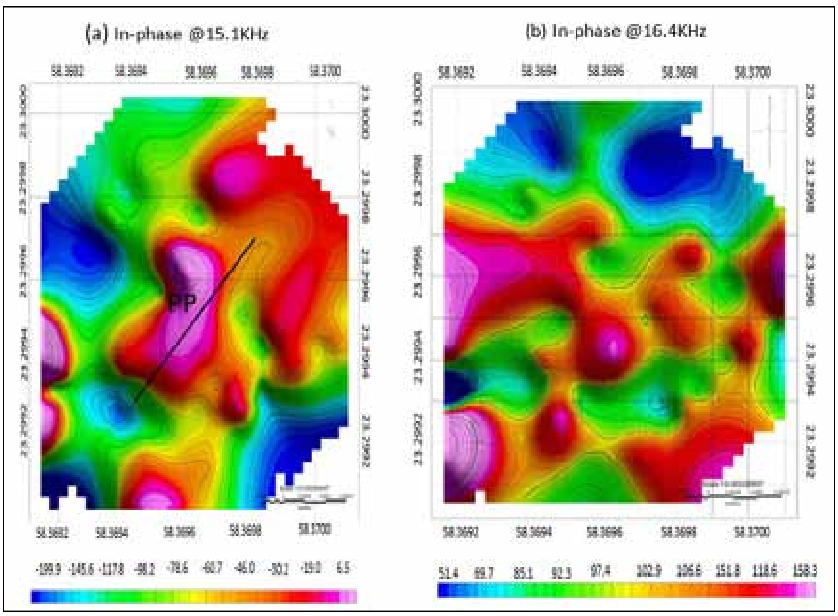

Figure 6. Contour image in-phase component of VLF-EM signal for transmitter frequencies of (a) 15.1 kHz and (b) 16.4 kHz.

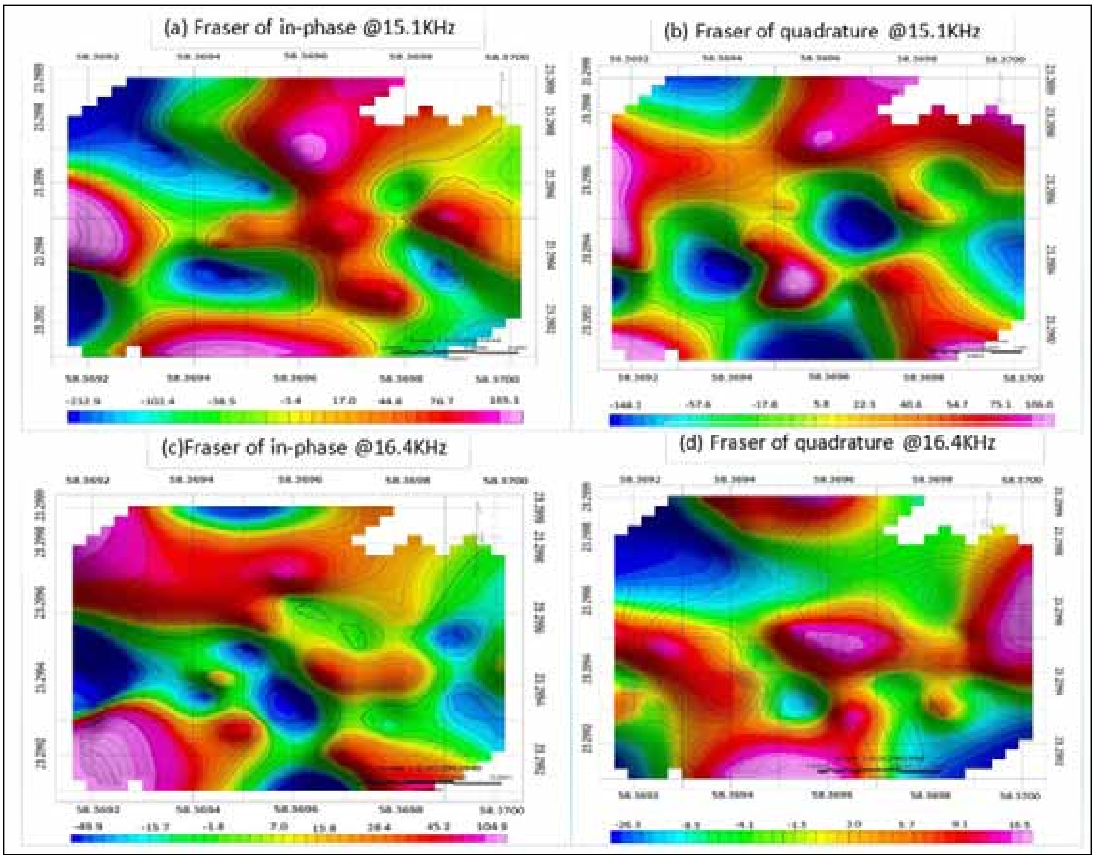

Figure 7. Contour map of Fraser filtered a) in phase and b) quadrature at transmitter frequency of 15.1 kHz, and c) in-phase and d) quadrature at transmitter frequency of 16.4 kHz.

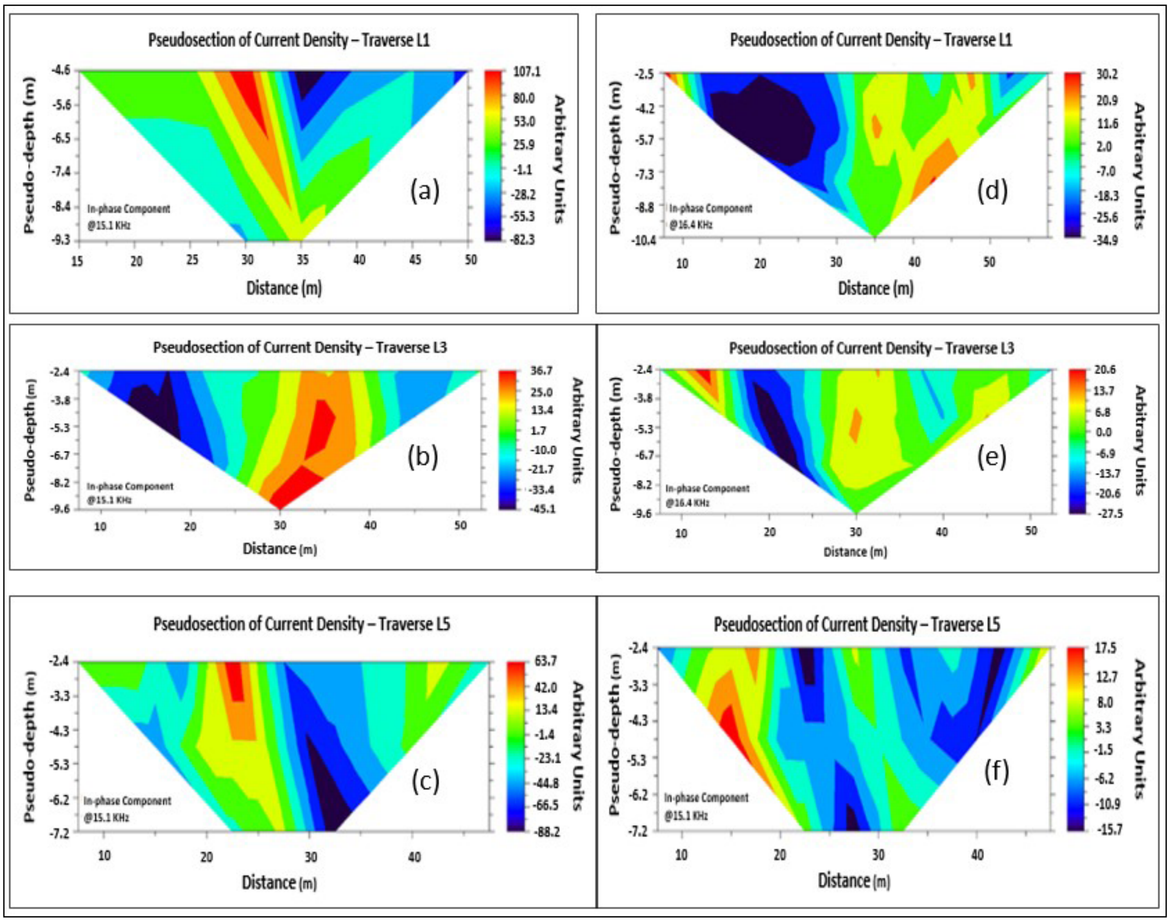

Figure 8. (a) Pseudosection of the current density of K-H filtering of traverses L1, L3, and L5 for transmitter frequencies of 15.1 kHz (a-c) and 16.4 kHz (d-f)

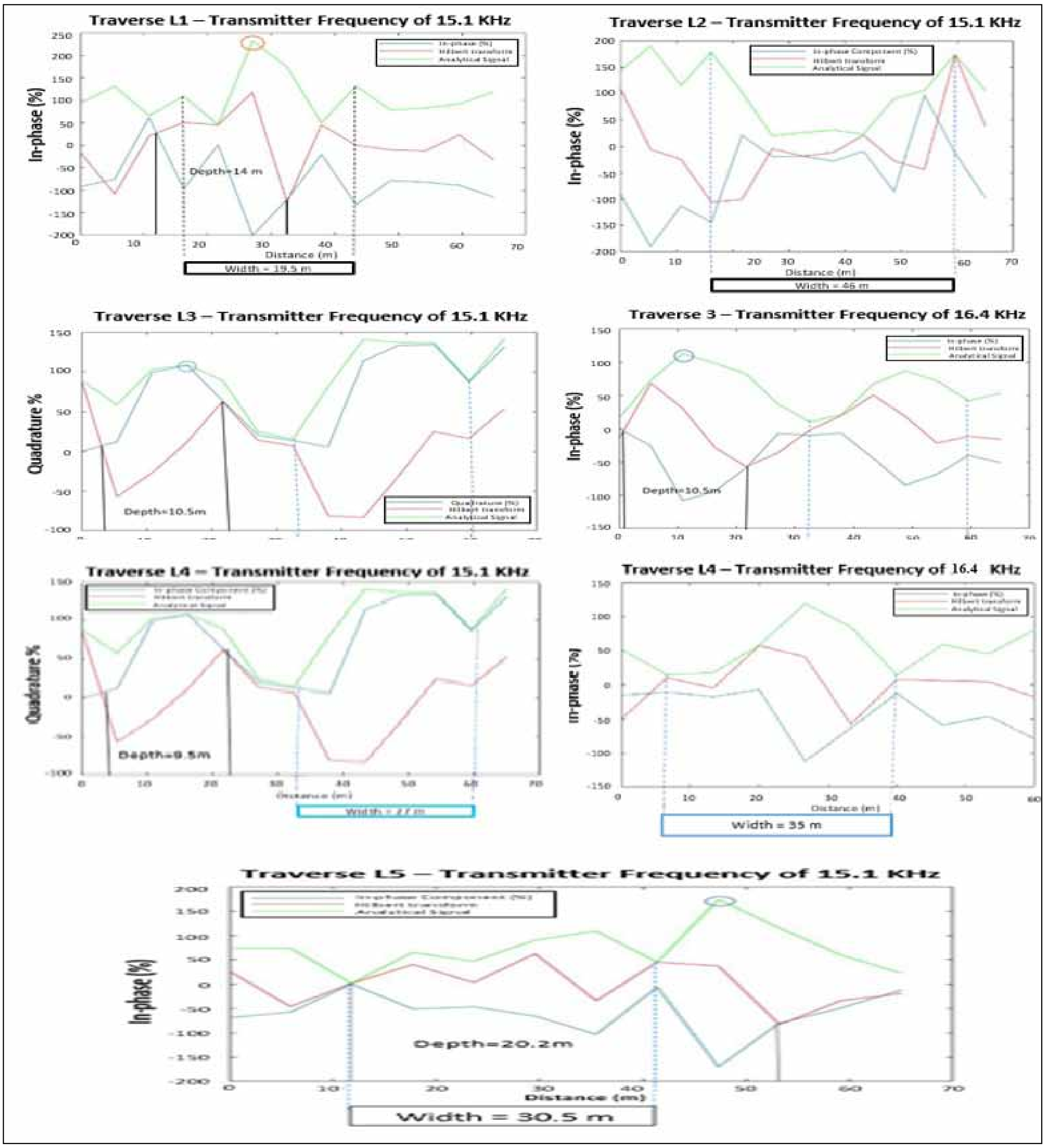

Figure 9. Hilbert transform (HT) analyses of VLF-EM signals of L1-L5 (a) HT of in-phase at a frequency of 15.1 kHz, (b) HT of in-phase of L2 at frequency 15.1 kHz, (c) HT of L3 at frequency 16.4 kHz, (d) HT of quadrature component of L3 at frequency 15.1 kHz, (e) HT of n-phase of L4 at frequency 15.1 kHz, (f) HT of quadrature component of L4 at frequency 15.1 kHz, and (g) HT of in-phase of L5 at frequency 15.1 kHz.

In general, KH (Karous-Hjelt) filtering is a forward modeling tool for depth determination either from measured in-phase (IP) or quadrature (OP) component of VLF-EM signal at a range of measurement intervals between measurement points (Karous and Hjelt, 1983, Sundararajan et al, 2007). Further, the interpretation is made simply based on a software VLF2DMF (A program for 2-D inversion of multifrequency VLF-EM data). On the other hand, depth from magnetics data is derived by a well-known method called Euler deconvolution (ED) using Geosoft. It is one of the elegant tools to estimate depth from potential field data, particularly magnetics on the horizontal location of an anomalous source, and requires the spatial location of the measurement points and structural index, a parameter to be assumed depending on the nature and shape of the anomaly (Thompson, 1982, Ebrahimi et. al, 2019).

In Fourier or Hartley spectral analysis (Fourier transform and Hartley transforms yield the same amplitude spectra), the log amplitude spectrum A(ω) of the total magnetic field results in a straight line, and the slope of such straight line yields the depth to source (Sundararajan et al, 2019). Further, the Hilbert transform of in-phase component of VLF-EM signal IP(x) can be computed using Matlab and then the amplitude of analytical signal can be obtained (Sundararaja and Srinivas, 2010, Ebrahimi et al 2019) as

$$A(x) = \mathrm{SQRT}\left[\, IP(x)^2 + H(x)^2 \,\right]$$

where H(x) is the Hilbert transform of IP(x). The amplitude A(x) attains its maximum over the center of the subsurface target. If the width of the target is larger than the depth, the amplitude results in a minimum at the center of the target and two maxima on either side of the minimum. The distance between the two maxima gives the width of the target as shown in Figure 10. Further, the depth to the subsurface source can be determined as a function of abscissae of the point of intersection of IP(x) and its Hilbert transform wherein if there is a single point of intersection that corresponds directly to depth and in the case of two or more, the average yields the depth (Sundararajan and Srinivas, 2010).

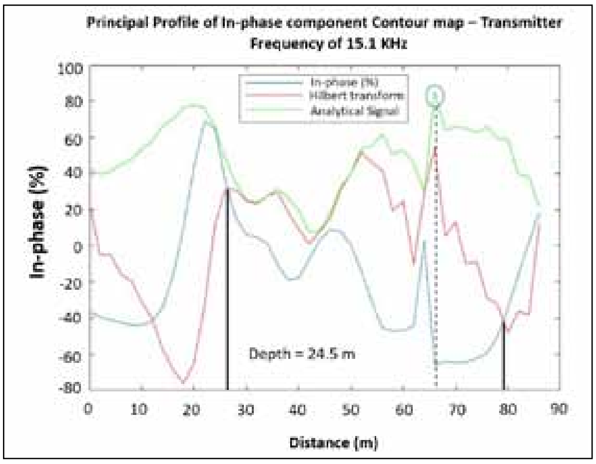

Figure 10. Hilbert transform analysis of an in-phase component of the principal profile.

5. Results and Discussion

Generally, the concentration of essential radioelements (Uranium, Thorium, and Potassium) expressively differs with the lithology of the study area and in the present study Figure, 2 reflects according to rock units such as metamorphic siliciclastic and placers. Also, the maximum variation of Uranium is seen in pink and red as shown in Figure 2a. Elevated Uranium and Thorium concentrations are more clearly shown in Figure 3, which corresponds to the values recorded along the principal profile (PP). The Uranium and Thorium concentrations along the principal profile (PP) are as high as 100 ppm and 900 ppm respectively.

The depth to the subsurface source obtained from magnetic anomalies by different methods such as radially average spectral analysis and Euler deconvolution agree well with each other. The estimated depth of subsurface structures ranges from 6-12 m by radially averaged power spectral analysis (Figure 5c) and 5-20 m by Euler Deconvolution (Figure 5d) respectively. On the other hand, the depth to source is obtained from the in-phase component of VLF-EM data by K-H filtering at two different transmitter frequencies viz. 15.1 kHz and 16.4 kHz range 7.2 m -10.4 m [Figure 8 (a-f)] and are presented in Table 1.

Further, the Hilbert transform analysis of the in-phase component of the VLF-EM signal has resulted in the depth as well as the width of the subsurface structure at both transmitter frequencies range 9.2 m -20.2 m [Figure 9 (a-g)] and 19.5m - 66.5 m. In addition, the principal profile yields the depth and width by HT analysis as 35 m and 24 m respectively at a transmitter frequency of 15.1 kHz which is somewhat close to the depth and width obtained from traverse L5 as shown in Table 2. It may be noted that the results obtained from spectral analysis(depth) and the Hilbert transform technique (depth and width) are more reliable as these techniques are analytical/quantitative methods in comparison with qualitative methods such as Euler deconvolution and K-H filtering.

6. Conclusions

The integrated geophysical strategy consisting of Gamma-ray spectroscopy, magnetic, and VLF-EM is a proven strategy elsewhere is employed in this study in the exploration of radioactive minerals. Gamma-ray spectroscopy recorded the occurrence of Uranium, however of low grade (<100 ppm) and Thorium moderately a high concentration of around 1000 ppm. The magnetics and the VLF-EM surveys have resulted in the depth of mineralized structures in the range of 5 – 24 m in addition to the width of 19.5 m-66.5m. The study area being small on a hilltop as well as uneven terrain, an extensive heliborne survey may be recommended for covering a wider area that will ensure a highly reliable outcome.

Acknowledgments

The authors wish to record their sincere thanks to Sultan Qaboos University for the strategic grants (SR/SCI/ETHS/12/02) provided to support this investigation.

References

Béchennec, F., Le Métour, J., Platel, J. P., and Roger, J. (1993). Geological map of the Sultanate of Oman. Scale 1: 1.000. 000, with explanatory notes. Directorate General of Minerals, Oman Ministry of Petroleum and Minerals, Muscat.

Beurrier, M., Béchennec, F., Rabu, D and Hutin, G., (1986). Geological map of Rustaq, sheet NF 40-03D, scale 1:100,000, Explanatory Notes. Directorate General of Minerals, Oman Ministry of Petroleum and Minerals, p. 69.

Bhattacharyya, B. K., and Leu, L. K. (1977). Spectral analysis of gravity and magnetic anomalies due to rectangular prismatic bodies. Geophysics, 42(1), 41-50.

Ebrahimi, A., N. Sundararajan and V. Ramesh Babu, (2019). A comparative study for the source depth estimation of very low frequency electromagnetic (VLF-EM) signals. Applied Geophysics, 162, 173-184

Fraser D. (1969). Contouring of VLF-EM data. Geophysics, 34(6), 958-967.

Gerovska, D., and Araúzo-Bravo, M. J. (2003). Automatic interpretation of magnetic data based on Euler deconvolution with unprescribed structural index. Computers and Geosciences, 29(8), 949-960.

Glennie, K.W., Boeuf, M.G.A., Hughes-Clarke, M.W., Moody-Stuart, M., Pilaar, W.F.H. and Reinhardt, B.M., (1973). Late Cretaceous nappes in Oman Mountains and their geological evolution. Am. Assoc. Petrol. Geol. Bull. 57, 5-27.

Glennie, K.W., Boeuf, M.G.A., Highes-Clarke, M.W., Moody-Stuart, M., Pilaar, W and Reinhardt, B.M.,(1974). Geology of the Oman Mountains. Kon. Ned. Geol. Mijnb. Gen. Trans. 31 (1), p. 423.

Goffé, B., Michard, A., Kienast, J.R. and Le Mer, O., (1988). A case of obduction related high P, low T metamorphism in upper crustal nappes, Arabian continental margin, Oman: P-T paths and kinematic interpretation. Tectonophys 151, 363-386.

Hacker, B.R., Mosenfelder, J.L and Gnos, E.(1996). Rapid emplacement of the Oman ophiolite: Thermal and geochronologic constraints. Tectonics 15, 1230-1247.

Hinich, M. J., and Clay, C. S. (1968). The application of the discrete Fourier transform in the estimation of power spectra, coherence, and bispectra of geophysical data. Reviews of geophysics, 6(3), 347-363.

IAEA, (2003). Guidelines for radioelement mapping using Gamma-ray spectrometry data, IAEA-TECDOC-1363, Vienna, Austria, pp. 97.

Karous, M., and Hjelt, S. E. (1983). Linear filtering of VLF dip angle measurements. Geophysical prospecting, 31(5), 782-794.

Keating, P. B. (1998). Weighted Euler deconvolution of gravity data, Geophysics, 63, 1595–1603.

Knox, W. O'B. (2006). Heavy mineral signatures in sandstone samples from the Amdeh Formation (?Cambro-Ordovician) of the Saih Hatat and Hayl al Quwasim inliers, Oman. Unpublished report for PDO (Petroleum Development of Oman) by Knox Stratigraphic, p. 15.

Lippard, S.J., Shelton, A.W., and Gass, I.G. (1986). The ophiolite of northern Oman. J. Geol. Soc. (London) Mem. 11, p. 178.

Lovelock, P, E.R., Potter, T.L., Walsworth-Bell, E.B., and Wiemer, W.M.(1981). Ordovician rocks in the Oman Mountains: the Amdeh Formation. Geol. Mijnb. 60, 487-495.

Mushayandebvu, M. F., Lesur, V., Reid, A. B., and Fairhead, J. D. (2004). Grid Euler deconvolution with constraints for 2D structures. Geophysics, 69(2), 489-496.

Oterdoom, W.H., Worthing, M.A., and Partington, M.(1999). Petrological and Tectonostratigraphical Evidence for a Mid Ordovician Rift Pulse on the Arabian Peninsula. GeoArabia 4, 467-500.

Povinec, P., Commanducci, J., and Levy-Palomo, I. (2005). IAEA-MEL's underground counting laboratory (CAVE) for the analysis of radionuclides in the environment at very low-levels. Journal of radioanalytical and nuclear chemistry, Vol. 263(2), pp. 441-445

Ramesh Babu V, Ram S, Sundararajan. N (2007) Modeling and inversion of magnetic and VLF-EM data with an application to basement fractures: A case study from Raigarh, India. Geophy 72: B133-B140.

Reid, A. B., Allsop, J. M., Granser, H., Millett, A. T., and Somerton, I. W. (1990). Magnetic interpretation in three dimensions using Euler deconvolution. Geophysics, 55(1), 80-91.

Searle, M. and Cox, J. (1991). Tectonic setting, origin, and obduction of the Oman ophiolite. Geol. Soc. of Am. Bull. 111, 104-122.

Searle, M.P., and Malpas, J. (1980). Structure and metamorphism of rocks beneath the Semail ophiolite of Oman and their significance in ophiolite obduction. Trans. R. Soc. Edinburgh 71, 247-262.

Sharma, S. P., Biswas, A., and Baranwal, V. C. (2014). Very Low-Frequency Electromagnetic Method: A Shallow Subsurface Investigation Technique for Geophysical Applications. In Recent Trends in Modelling of Environmental Contaminants. Springer India, 119-141.

Sundararajan, N., M. Narashimha Chary, K.Ramam, Y.Srinivas and G. Nandakumar, (2007). VES and VLF—an application to groundwater exploration, Khammam, India. The Leading Edge, 6, 708-716

Sundararajan, N., and Srinivas, Y. (2010). Fourier–Hilbert versus Hartley–Hilbert transforms with some geophysical applications. J. Appl. Geophys. 71 (4), 157–161.

Sundararajan, N., Babu, V. R., and Chaturvedi, A. K. (2011). Detection of basement fractures favourable to Uranium mineralization from VLF-EM signals. Journal of Geophysics and Engineering, 8(2), 330.

Sundararajan, N, Bernhard Pracejus, Salah Al- Khirbash, Talal K. Al-Hosni, A. Ebrahimi, Ali Al Lazki and Musallam Al-Mushani (2019). Radiometric Surveys for Detection of Uranium in Dhofar Region, Sultanate of Oman. SQU Journal for Science, 24, 36-46.

Thompson, D. T. (1982), EULDPH: A new technique for making computer-assisted depth estimates from magnetic data, Geophysics, 47, 31–37.

JJEES

Jordan Journal of Earth and Environmental Sciences

JJEES (2022) 13 (3): 223-231
ISSN 1995-6681

Impact of the Effluent Characteristics of Industrial and Domestic Wastewater Treatment Plants on the Irrigated Soil and Plants

Mohammad Al-Mubaidin[1], Husam Al-Hamaiedeh[1] and Tayel El-Hasan[2*]

[1] *Civil and Environmental Engineering Department Mutah University, Al-Karak, Jordan*
[2] *Chemistry Department, Mutah University; Al-Karak, Jordan*

Received 1st September 2021; Accepted 27th March 2022

Abstract

Treated wastewater (TWW) reuse became a common practice and a significant component of the water budget in Jordan due to the shortages in available water sources. TWW is being diluted with harvested rainwater to improve its quality for its subsequent reuse for irrigation. However, the reuse of TWW without dilution may pose an adverse effect on the irrigated soils and plants. This study investigates the effect of TWW reuse for irrigation on soil and plants. The TWW in this study is the effluents of domestic and industrial wastewater treatment plants namely Mutah-Al-Mazar (MMWWTP) and Al-Hussein II Industrial City (HICWWTP). The TWW from both plants has been tested for several quality parameters (pH, EC, BOD_5, COD, TSS, TDS, NO_3^{-2}, PO_4^{-3}, Cl^-, Na, K, Cu, Fe, Pb, and Cd). The obtained results have been compared with the allowable limits specified by the Jordanian standard for reclaimed WW reuse. Concentrations of the measured elements were below the allowable limits except for lead and cadmium. The average concentrations of lead and cadmium in TWW from HICWWTP were 0.65 mg/L, and 0.035 mg/L respectively. Whereas the concentrations of these elements in the TWW from MMWWTP were 0.58 mg/L, and 0.047 mg/L respectively. The allowable limit for these elements according to the Jordanian standard for the use of treated wastewater in irrigation is 0.2 mg/L and 0.01 mg/L respectively. Soil and plant samples irrigated with TWW from both plants and control samples irrigated with fresh water were tested for (pH, EC, Fe, Cu, Pb, Cd, K, and Na). The results showed that there was no difference in the chemical properties of soil and plant samples irrigated with fresh water and those irrigated with TWW. Therefore, this study concluded that the reuse of TWW for irrigation did not have adverse effects on the properties of the irrigated soils and plants.

Keywords: *Wastewater, Treatment plants, Heavy metals, Soil pH, Irrigation*

1. Introduction

Jordan suffers from a severe water shortage in its water resources. The water situation is one of the most important and strategic challenges facing Jordan. The per capita water availability has decreased from 3,600 cubic meters per year in 1946 to <100 cubic meters per year in 2017 (MWI, 2017). The per capita consumption is below the level of the global water poverty line (1000 m^3 / capita/year) and represents less than 15% of the global per capita rate (The Ministry of Water and Irrigation, 2015). Jordan is characterized by limited renewable and non-renewable water resources, where about 94% of Jordan's area is desert and dry land which has a long-term rainfall of about 100 mm and an evaporation rate of 93 % (Ministry of Water and Irrigation, 2015). Recently water crisis has been exacerbated by the impact of climate change, low rainfall, lack of alternative water sources, and sudden population displacements. Matouq et al. (2013), had predicted of escalating climate change impact on Jordan in the coming decades especially in lowering the rainfall which may reach 80 mm in the central and eastern regions of Jordan. Moreover, the annual population increase besides the improved living standard and decline in water quality due to depletion of many sources also lead to an increase in water scarcity. It is estimated that the average rate of water consumption by Jordanian individuals could increase by 50-60% by 2025, which will strain scarce water resources Ministry of Water and Irrigation, (2015). Therefore, Jordan has classified as one of the poorest countries in terms of water availability in the world, which form the biggest challenge for decision-makers and sustainable development in Jordan.

Despite all the difficulties in that facing the Jordanian water sector, the percentage of the population served by the public drinking water network is 97% and by the sewage network is 67%. To overcome the above-mentioned challenges, applying good planning programs for water resources to balance the current and future needs is of high importance. One of the available alternatives which can bridge the gap between supply and demand is the reuse of reclaimed wastewater, specially treated domestic wastewater mainly for agricultural purposes to save more fresh water for domestic purposes.

In Jordan, most of the TWW is being used for irrigation. TWW contributed approximately 13% of the water budget of Jordan in 2015 (Ministry of Water and Irrigation 2015). Wastewater is 99.9% water and 0.01% concentrations of suspended and dissolved organic and inorganic solids (Aljbour et al., 2021a and b). Many researchers had studied the impact of using TWW of different sources for irrigation on the environment mainly on the irrigated plants and soil.

* Corresponding author e-mail: tayel@mutah.edu.jo

Al-Hamaiedeh and Bino (2010) studied the effect of the reuse of treated grey water for irrigating olive trees and some vegetative crops, the results showed that salinity, sodium adsorption ratio (SAR), and organic content of soil increased as a function of time, therefore they recommended that the soil should be leached with fresh water. The chemical properties of the irrigated olive trees and vegetable crops were not affected, while the biological quality of some vegetable crops was adversely affected. However, the reuse of TGW for irrigation in home gardens showed an adverse effect on public health and safety in terms of breeding of flies and Unpleasant odors (Al-Hamaiedeh, 2010). Mohawesh et al., (2019) investigated the effect of olive mill wastewater (OMW) application on soil properties and wheat growth performance under rain-fed conditions, the results showed that the application rate of OMW at 60 $m^3 ha^{-1}$could improve significantly wheat growth without significant negative impact on soil properties. Another study (Mohawesh et al., 2020), investigated the sustainable controlled land application of OMW to enhance soil properties and improve barely production under rain-fed conditions, the results revealed that no harmful effect of OMW application for all application rates on growth parameters of barely as well as soil properties.

Baker (2007) studied the use of untreated WW for irrigation, the results showed that WW quality parameters are extremely above the permissible limits for WW reuse in irrigation and vary spatially and temporally. Reuse of untreated WW in irrigation showed clear effects on the top soil texture, total carbon and total nitrogen amounts, and the accumulation of heavy metals in soil profile especially arsenic, cadmium, and lead. The study concluded that it is a danger to use untreated WW for irrigation.

TWW is considered the main non-conventional source of water in Jordan. The strategy of the Ministry of Water and Irrigation approved the use of 133 million m^3 of TWW in 2015 (Ministry of Water and Irrigation, 2015). This amount is projected to reach 250 million m^3 in 2050 as a result of the increasing demand and the heavy stress on groundwater resources (Ministry of Water and Irrigation, 2004).

This study aims to study the effect of the reuse of TWW from domestic influent wastewater treatment plants (MMWWTP) and industrial influent wastewater treatment plants (HICWWTP) on the quality of irrigated plants and soils.

1.1 Study area settings

Mutah – Al-Mazar wastewater treatment plant (MMWWTP) is located in Al-Karak Governorate; it treats domestic WW since 2014. The plant includes an activated sludge system, it is a design capacity of 7060 cubic meters per day with a polishing pond. The treated wastewater from the plant is used to irrigate the feed and the remainder is disposed to the nearby valleys. The present average daily flow rate is 800 m^3/day, the organic design load = 673 mg/L, and the actual organic load = 1120 mg / L (Ministry of Water and Irrigation, 2015). Al-Hussein II Industrial City WWTP (HICWWTP) is one of the small WWTPs in Al- Karak governorate (Fig. 1).

The plant treats industrial wastewater generated mainly from textile fabrics and the food industry since 2000. The plant design capacity is 1500 m^3 / day, the present average daily flow rate is 500 m^3 / day. It includes an activated sludge system as secondary treatment, part of the TWW from the plant is used for fodder irrigation and the remainder is disposed to the nearby valleys.

This study aims to evaluate the suitability of TWW produced in the two WWTPs in the Al-Karak governorate for irrigation and study the impact of long-term irrigation with TWW on the characteristics of the irrigated soil and plants.

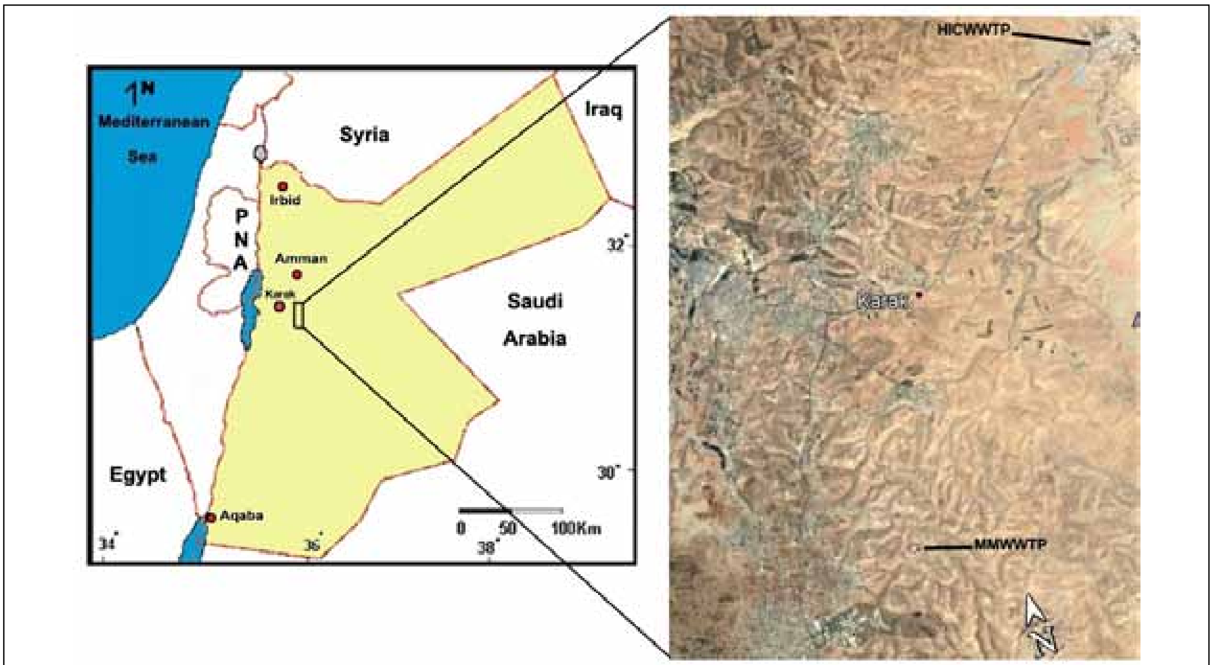

Figure 1. Location map showing the two studied WWTP's in Al-Karak province

2. Methodology

Fifteen TWW samples were taken from the middle depth of the TWW receiving channel for two successive months (April and May) from the studied WWTP's. The volume of the samples collected was 10 liter, the samples were kept in a polyethylene container, transported to the laboratory, and stored at 4˚C as outlined by (Kulikowska and Klimiuk, 2008) to be tested for different parameters as suggested by the Standard Methods of Chemical Analysis (Tatsi et al., 2003) and the standard conservation methods for the examination of water and wastewater (APHA, 1998).

Fifteen TWW samples have been tested for main quality parameters (pH, EC, BOD_5, COD, T SS, TDS, Cl^-, PO_4^{-3}, NO_3^{-2}, Cu, Fe, Pb, Cd, Na, and K). Water sample analyses were conducted according to the Standard Methods for the Examination of Water and Wastewater, (Barid and Bridgewater, 2017). The average values for each parameter were compared with the Jordanian standard for reclaimed wastewater reuse. The total dissolved solids (TDS) for each sample was determined as the mass of the dissolved solid normalized to the volume of water filtered. The value of TDS was measured according to the standard method 2540C (Barid and Bridgewater, 2017). The total suspended solids (TSS) for each sample was determined as the mass of the suspended solid normalized to the volume of water filtered. The value of TSS was measured according to the standard method 2540D. The water samples were analyzed for NO_3^{-2}, Cl^- and PO_4^{-3} following the standard method 4110B. Using an Ion Chromatography Analyzer (IC) (761 compact IC, Metrohm AG, Ionenstrasse, Herisau, Switzerland). The BOD_5 and COD were analyzed following the standard methods 5210-B and 5220-B respectively. Total Nitrogen TN was determined by calculating the sum of organic and inorganic nitrogen.

Fifteen soil and plant samples irrigated with these TWW from both WWTP's were collected. Soil samples were taken before the start of the rainy season from a selected site, fifteen soil samples were taken based on the specific protocols and tools. Where each sample was collected from three pits that dogged each site at two depth intervals of 0- 30cm, and 30-60 cm. A portion of soil from each depth was taken and then all were mixed up until homogenization. Samples were then labeled to show the depth and location. Control soil samples from similar soil not irrigated with TWW were taken from a nearby location.

The soil samples were dried at 105 °C for 2 hours, sieved in a 2 mm mesh sieve, and grinded by using a soil mill. From each sample, 500 gm was filled in a plastic bag and labeled. The soil acidity pH and electrical conductivity (EC) had analyzed by mixing 1:5 ratios of soil and de-ionized water following the procedure of (Blakemore et al. 1987). To determine the heavy metals contents (Fe, Cu, Pb, Cd, Ni, K, and Na), the soil leaching procedure had done as follows: 2 g of soil sample was mixed with 10 ml of 2 M HNO_3 solution, shaken and ultra-sonicated for4 h, then it was filtered using 45-µn Whitman filter paper according to (El-Hasan, 2002; and Fialova et al. 2006). The solution was then transferred into 25-ml polyethylene bottles, filled up with distilled water exactly to 25 ml, then stored in the refrigerator until the analysis time. The concentrations of heavy metals Fe, Cu, Pb, Cd, Ni, K, and Na) in the soil samples were determined by using Flame Atomic Absorption Spectrophotometer (AA-7000, Shimadzu Scientific Instruments, Japan) according to the Standard Method 3111 B.

The pH values of all soil samples were measured according to the standard method SM 4500 H+B (Greenberg, 2005) by preparing 1:5 (Soil: Water) suspensions. The suspensions were prepared by shaking 10 g air-dry soil < 2 mm in 50 ml deionized water in a rotating shaker for 1 h at 15 rpm. The obtained pH values (pH meter 315i, WTW GmbH, Weilheim, Germany) were recorded when the equilibrium (stability in the reading) was reached while stirring with a mechanical stirrer (El-Hasan and Al-Tarawneh, 2020), (Al-Hamaiedeh and Maaitah 2011).

The EC values of all soil samples were measured according to the standard method SM 2510. The soil EC was determined by shaking a 1:2.5 (w/w) ratio of soil and deionized water. The mixture was homogenized for 30 min at 15 rpm using a horizontal shaker and then left at room temperature until the soil settled down before EC measurement. The conductivity of the supernatant liquid was determined using the conductivity meter without disturbing the settled soil (Conductivity meter 4310, JENWAY, UK) (El-Hasan and Al-Tarawneh, 2020).

The alfalfa samples were taken from the same sites where soil samples were taken from both WWTP's. After drying the samples in the oven at a temperature of 105 ±2 C° for 2 hrs and grinding the samples then were digested in Aqua regia, 0.5 g of alfalfa leaves were added to 10 ml of Aqua regia solution (Garnaud et al. 1999). The bottle was heated on the hotplate and then the distilled water is added to the bottle to complete its volume to 100 ml, then filtered using 0.45-micrometer cellulose nitrate filters. The plant was tested for heavy metals (Cu, Pb, Cd, and Fe) and was measured by Flame Atomic Absorption Spectrophotometer (AA-7000, Shimadzu Scientific Instruments, Japan) according to Standard Method 3111 B. Standard solutions with concentrations of 0.05, 0.1, 0.2, 0.5, and 1 ppm from these elements by standard method 3111 B were prepared and used for calibration. In all analyses triplicate measurements were done for each sample; the error was within ± 5%.

3. Results and Discussion

3.1. HICWWTP

The TWW effluent from (HICWWTP) which is used for irrigation of Alfalfa is about 300 m^3/day. Its chemical and physical characteristics and the maximum allowable limits for these parameters stated in the Jordanian Standard Specification for reuse of Industrial reclaimed wastewater (Jordanian Standard JS202:2007) are shown in Table (1). Alfalfa is a field crop that was compared with the Jordanian specifications for industrial wastewater reuse for irrigation of field crops. Jiries et al. (2004) have shown that industrial wastewater effluent generated from phosphate mining effluent water fell within the allowable limit and could be used for crop irrigation.

3.2. MMWWTP

The TWW of MMWWTP, which is about 550 m^3/day, its chemical and physical characteristics, and the maximum allowable limits for these parameters according to Jordanian

Standard Specification for reuse of reclaimed domestic wastewater (Jordanian Standard JS 893:2006) are shown in Table (2).

From the data presented in Tables (1 and 2), it can be seen that all quality parameters for the treated Industrial WW in HICWWTP and treated domestic WW in MMWWTP are below the allowable limits that are present in the Jordanian standard for reclaimed WW reuse except the concentrations of cadmium and lead.

As for heavy metals in treated wastewater, there was a high concentration of lead and cadmium in the effluent of both plants, the average value of the concentration of lead in treated wastewater at HICWWTP is 0.65 and at MMWWTP is 0.575, which is greater than the allowable limits in the Jordanian specifications for reclaimed WW reuse 0.2.

The average concentration of Cadmium in treated wastewater at HICWWTP was 0.035 and at MMWWTP was 0.043 which exceeds the allowable limits in the Jordanian specifications for reclaimed WW reuse 0.01 as shown in Fig. (2). Cadmium is a toxic heavy metal present in wastewaters from a variety of industries and its harmfulness come from its ability to accumulate in the human body if it enters through contaminated water or food chain (Dojlido and Best, 1993). Cadmium is predominantly found in rechargeable batteries for domestic use (Ni-Cd batteries), in paints, and in photography. The main sources of urban wastewater are diffuse sources such as food products, detergents, and body care products, stormwater (Ulmgren, 2000a, and Ulmgren, 2000b). Therefore, the sources of Pb and Cd might be the paints, pigments used in the cloths, and treatment materials in textile industries.

Table 1. Chemical and physical characteristics of treated wastewater used for irrigation from HICWWTP

ID	Parameter	April 2018	May 2018	**Average**± SD	Jordanian Standard	Unit
1	pH	6.98	7	0.014±6.99	6-9	-
2	EC	1360	1300	42.42±1330	700-3000	µs/cm
3	BOD_5	15	15	0003.15±	300	mg/l
4	COD	45	45	0.003±45	500	mg/l
5	TSS	20	20	0.02±20	300	mg/l
6	TDS	880	850	21.21±865	2000	mg/l
7	^{-}Cl	340	340	0.05±340	400	mg/l
8	PO_4	1.96	1.94	0.014±1.95	30	mg/l
9	NO_3^-	12.5	11.7	0.57±12.1	70	mg/l
10	Cu	B.D	B.D	B.D	0.2	mg/l
11	Fe	0.21	0.27	0.0.04±0.24	5	mg/l
12	Pb	0.57	0.73	0.11±0.65	0.2	mg/l
13	Cd	0.027	0.043	0.01±0.035	0.01	mg/l
14	Na	126.35	116.03	7.3±121.19	230	mg/l
15	K	4.60	3.56	4.08±0.74	-	mg/l

B.D ≡Below Detection Limit = 0.1 mg/l; Standard Deviation

Table 2. Chemical and physical characteristics of treated wastewater used for irrigation from MMWWTP

ID	Parameter	April 2018	May 2018	**Average**± SD	Jordanian Standard	Unit
1	pH	7.7	7.5	7.6±0.07	6.9	-
2	EC	1850	1785	1817.5±22.98	700-3000	µs/cm
3	BOD_5	26.5	20	23.25±2.3	300	mg/l
4	COD	168	114	141±19.09	500	mg/l
5	TSS	24	24	24±0.003	300	mg/l
6	TDS	1209	1165	1187±15.56	1500	mg/l
7	^{-}Cl	-	-	-	400	mg/l
8	PO_4	NA	NA	NA	30	mg/l
9	NO_3^-	4	4.4	4.2±0.28	70	mg/l
10	Cu	B.D	B.D	B.D	0.2	mg/l
11	Fe	0.5	0.61	0.55±0.04	5	mg/l
12	Pb	0.52	0.62	0.57±0.03	0.2	mg/l
13	Cd	0.041	0.047	0.043±0.003	0.01	mg/l
15	Na	206.24	197.56	201.9±3.07	230	mg/l
15	K	39.76	28.94	34.35±3.82	-	mg/l

B.D ≡Below Detection Limit = 0.1 mg/l; NA: Not analyzed; SD: Standard Deviation

The concentration of Copper and Iron in treated wastewater was within the permissible limit in the Jordanian specifications of the both WWTPs, the concentration of the copper in treated wastewater at HICWWTP and MMWWTP are below the detection limit (0.1 mg/l), and also the concentration of the iron in treated wastewater at HICWWTP was 0.245 and at MMWWTP is 0.55.

On the other hand, the concentration of sodium in TWW was within the allowable limits in the Jordanian specifications for reclaimed WW reuse in both WWTPs (230), it was in the HICWWTP 121.9 and at MMWWTP 201.9. The risk is high in lead and cadmium because they are toxic heavy metals if they exceed their permissible concentration. Lead increase in wastewater is due to pipes used in the water distribution system or from dry cell batteries or welding process or released from fossil fuels (Thornton et al. 2001).

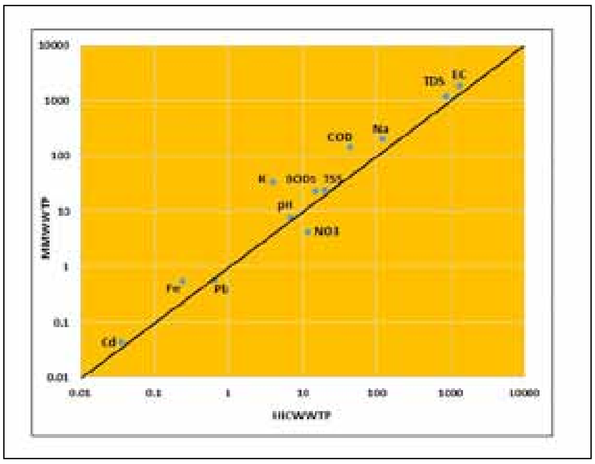

Figure 2. 1:1 ratio plotting showing the comparison between TWW from the two studied WWTP's

3.3. Results of Soil Analysis

Three locations were selected for sampling from each area that was irrigated with treated wastewater from both plants and two samples from each location for different depths. Samples were tested for (pH, EC, Cu, Fe, Pb, Cd, Na, K, and Total Nitrogen). Table (3) shows the chemical characteristics of soil samples irrigated by treated WW generated from HICWWTP and MMWWTP, the comparison between the two WWTP's illustrated in Fig. (3).

The pH results presented in Table (3) and Fig. (3) show that soil in both locations is alkaline where pH is around 9. The HICWWPT soils are slightly more alkaline values than MMWWTP soils, which can be explained by the that pH of MMWWTP effluent water is slightly less alkaline than HICWWPT effluent water as shown in Fig. (2). Moreover, there is no big difference between upper and lower soils pH value. These results are consistence with other studies on Jordanian soils (El-Hasan, 2002; Hararah et al. 2012; El-Hasan and Lataifeh, 2002 and 2013, El-Hasan and Al-Tarawneh, 2020). The pH in the soil is rarely to be a problem by itself, but it is an indication of soil conditions such as the mobility of heavy metals and the availability of special ions that increase or decrease the pH value (Sposito, 2008)

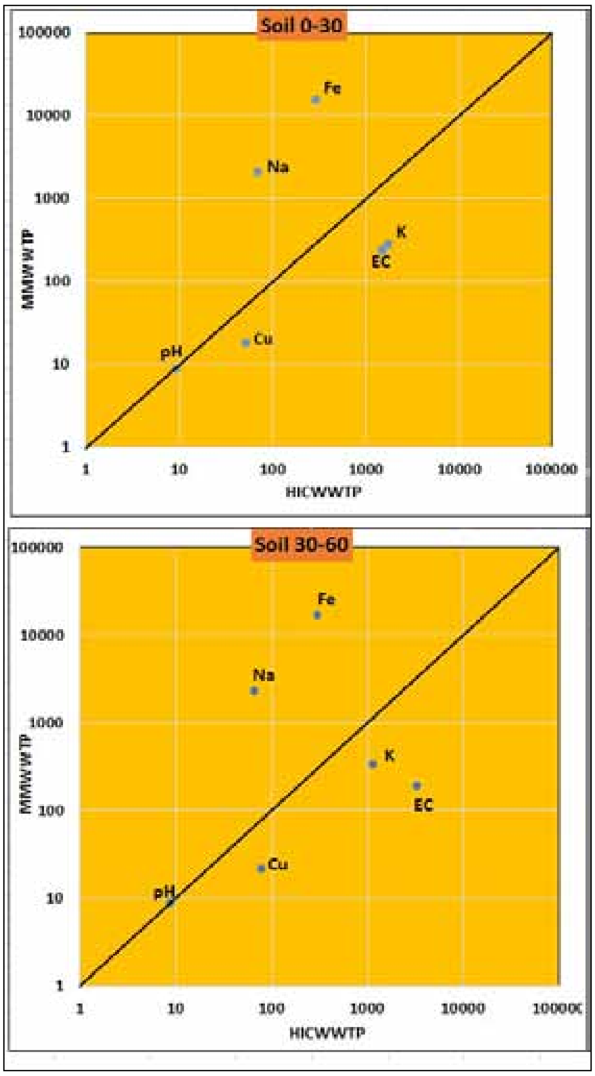

Figure 3. 1:1 ratio plotting's showing the comparison between the soils at both studied WWTP's within the upper and lower soils.

Table 3. Summary table showing the average values of the soil parameters after irrigation with TWW from both studied WWTP's.

Parameter	Depth (cm)	Unit	HICWWTP	MMWWTP
pH	0-30	-	9.09	8.74
	30-60		8.80	8.78
EC	0-30	µs/cm	1491.3	240.8
	30-60		3253.6	194.4
Cu	0-30	mg/kg	52.0	18.2
	30-60		77.3	22.1
Fe	0-30	mg/kg	294.7	15518
	30-60		301.3	17038
Pb	0-30	mg/kg	BD	204.8
	30-60		BD	215.3
Cd	0-30	mg/kg	BD	3.55
	30-60		BD	5.09
Na	0-30	mg/kg	70.2	2121
	30-60		65.4	2305
K	0-30	mg/kg	1736.7	284
	30-60		1143.3	338.7
Total N	0-30	mg/kg %	3.78	2.94

BD: Below Detection Limit

Electrical Conductivity (EC) is a measure of salt concentration in the soil; crops exhibit a spectrum of responses under salt stress (Shrivastava and Kumar, 2015). The EC of the soil is directly related to salinity where salinity usually refers to the presence of soluble salt in the soil. Salinity not only decreases the agricultural production of most crops, but also, affects soil physicochemical properties, and the ecological balance of the area. The impacts of salinity include low agricultural productivity, low economic returns, and soil erosions (Hu and Schmidhalter, 2004). A productive soil's EC should be below 150 µs/cm (Reid and Dirou, 2004). The pH of the soil probably affects salt solubility and soil moisture content. Alkaline soils will have a lower amount of soluble salt (Mohd-Aizat et al. 2014).

The EC values in soil samples from HICWWTP has very higher than the EC values that should be in productive soil, Table (3), there EC values were (1491.3 and 3253.6 µs/cm) for upper and lower soils Fig. (3), whereas, the soil samples from MMWWTP has much lower EC values (240.8 and 194.4 µs/cm), Fig. (3). Which might have attributed to the different input water types, where HICWWTP input is mainly industrial water, but the MMWWTP is domestic water.

3.3.1 Heavy Metal Accumulation

Results of analysis for copper, iron, lead and cadmium for soil samples of the depths (0 – 30) cm and (30 – 60) cm were evaluated. Copper is one of the most valuable and prevalent metals used in the industry and it's important for good health (Minnesota Department of Health, 2018), but higher concentrations can cause harmful health effects, especially for infants. From the results shown in Table (3), the Cu concentration in upper soil ranges (from 48 mg/kg to 132 mg/kg), and in lower soils, it ranges (from 9.7 mg/kg to 42.6 mg/kg). Copper in wastewater comes from industrial sources such as alloy manufacturing and heat exchangers and households such as pipes and tips. Therefore, it is being higher in soil irrigated by industrial wastewater effluents (HICWWTP) than in the soils irrigated by domestic wastewater effluents (MMWWTP) as shown in Figs. (3 a and b).

In both sites, there is no difference in copper values in soil samples and control samples. Most of the copper values in the soil samples are within the allowable level of copper for agricultural soil (2-50) mg/kg) (Reid and Dirou, 2004). There is no cumulative effect of copper in the soil as a result of irrigation with TWW.

Iron is considered one of the most abundant micronutrients in surface soils (Fageria et al. 2002), Iron is an essential element needed by all organisms for growth and development. Because iron becomes toxic at higher concentrations, the concentration of iron in the plant should be monitored (Agafonov et al. 2016). Iron is a catalyst needed to form chlorophyll, which is why the symptoms of iron problems appear as changes in plant color (Rout and Sahoo, 2015).

From the results that are shown in Table (3), the concentration of iron in the soil from HICWWTP samples ranges (from 252 mg/kg to 356 mg/kg. Whereas, is very high in soils from MMWWTP samples (13560 mg/kg to 35548 mg/kg). It is clear from Fig. (3 aand b) that the upper and lower soils of MMWWTP bear a very high iron concentration than HICWWTP, which might be attributed to the soil iron content not related to Fe in the irrigated wastewater, as evident from its high concentration in both upper and lower soil. Moreover, Tables (1and2) showed that Fe contents in effluent wastewater from both WWTP are very low, and it is far below the allowable limits. There is no difference in the concentration of iron in soil samples irrigated with TWW from both WWTP's and control soil samples. This indicates that there is no accumulation of iron because of irrigation with TWW.

Lead is toxic to plants and human beings; Pb is less toxic to plants than mercury and copper. Lead is found in paint and it's also used in several alloys, flashing solder, and some batteries. Lead is released during the combustion of fossil fuels and many manufacturing processes produce or release lead (Dojlido and Best, 1993). Soil may become contaminated with Pb if it is exposed to any of these substances or processes or if water runoff from such substances infiltrates the soil, mining activity may also lead to lead contamination.

The Pb concentration in the soil samples from HICWWTP was below the detection limit (BD). All values appeared below the permissible lead values in the soil, (35 mg/Kg) (Reid and Dirou, 2004), this indicates the lack of accumulation of the element in the soil due to using TWW for irrigation. Whereas, it's an average of 204.8 mg/kg and 215.3 mg/kg in the upper and lower soil from MMWWTP site Table (3). Despite that, the TWW from both sites has Pb concentrations slightly above the permissible limit Tables (1and2), however, the irrigated soils at HICWWTP in BD mean no accumulation effect. But for MMWWTP the Pb values could be from lithogenic sources as in the case of Fe.

Cadmium is very toxic and its harmfulness comes from its ability to concentrate in the human body if it enters through contaminated water or food chain (Dojlido and Best, 1993). One of the potential causes of the appearance of cadmium in the soil is the use of phosphate fertilizers, sewage sludge, and industrial usage (Dojlido and Best, 1993).

The cadmium concentration in the soil samples irrigated from HICWWTP was below detection limits in upper and lower soils, Table (3). These results showed that despite Cd being slightly above the permissible limits in the wastewater effluents from HICWWTP, however, there is no value for cadmium in soil. This indicates that the element is not accumulated in the soil and not affecting the soil, we cannot confirm whether the values allowed in the soil are permissible or not (1 mg/Kg) (Reid and Dirou, 2004). Whereas, the soil from MMWWTP has average concentrations of 3.55 mg/kg and 5.09 mg/kg for upper and lower soil. The TWW effluent from MMWWTP has Cd slightly above the permissible limit (Table 2). The concentration of cadmium in the soil is higher than the normal existing amount of cadmium in the soil (1 mg/kg) (Reid and Dirou, 2004), but the concentration of cadmium in control samples is higher than the concentration of cadmium in the soil samples that irrigated with treated wastewater, this indicates so there is no cumulative effect of Cadmium on the soil as a result of irrigation with treated wastewater. Moreover, soil leaching with rain water during the wet season is the main reason behind the low concentrations of heavy metals in the soil, and subsequently in the irrigated plants.

3.3.2 Sodium

Sodium content is a very important factor in plant irrigation. The roots absorb sodium from the soil and transport it to the leaves, where it accumulates and can cause damage (Castro et al. 2011). From the results that are shown in Table (3), the minimum concentration of sodium in soil samples was 21.32 mg/kg while the maximum was 91.06 mg/kg.

The concentration of sodium in soil samples is lower than the appropriate quantity of concentration of sodium in the agricultural Soil (230 mg/Kg) (Reid and Dirou 2004), also the small difference between the concentration of sodium in the soil samples irrigated with TWW and concentration of sodium in the control samples indicates that the concentration of sodium in the soil is unaffected by irrigation with TWW.

From the results that are shown in Table (3), the minimum concentration of sodium in soil samples was 1480 mg/kg while the maximum was 2976 mg/kg. The concentration of sodium in the soil is higher than the normal amount of sodium found in soil (230 mg/kg) (Reid and Dirou, 2004), and the concentration of sodium in control samples is less than the concentration of sodium in the soil samples that were irrigated with TWW this is a result of using treated wastewater in irrigation.

3.3.3 Potassium

Potassium concentration in wastewater is not known to cause adverse effects on plants or the environment. It is an essential macronutrient and affects positively soil fertility, crop yield, and quality (FAO, 2003). From the results that are shown in Table (3), the minimum concentration of potassium in soil samples HICWWTP was 550 mg/kg while the maximum was 1796 mg/kg, there is a small increase in the values of potassium in control samples compared to soil samples that irrigated with TWW, this possibly occurs due to plant uptake of potassium from the soil. As for MMWWTP soils, the Potassium minimum concentration was 132 mg/kg while the maximum was 504 mg/kg Table (3). There was no effect on the concentration of Potassium in the soil due to irrigation with TWW because there was no difference in the concentration of Potassium in the soil samples that were irrigated with treated wastewater and control samples.

Figure (3) showed that Potassium in soils irrigated with TWW from HICWWTP is higher than in the soil irrigated with TWW from MMWWTP, the average K content was 4.08 and 34 mg/kg for TWW from MMWWTP and HICWWTP respectively (Tables 1 and 2). This might be due to the difference in the influent water sources. There is no risk of Potassium concentration in soil because the appropriate level of Potassium concentration in soil is above 195 mg/kg (Reid and Dirou, 2004).

3.3.4 Total Nitrogen

Nitrate levels fluctuate widely, depending on the rainfall season; agronomists generally like to see a level of 10 mg/kg or more in pasture soils, and a level greater than 20 mg/kg in horticultural crops soil (Reid and Dirou, 2004).

Total Nitrogen (TN) content in the upper soil samples (0-30 cm) from HICWWTP ranges from 0.34% (1.68 mg/Kg) to 0.76% (3.78 mg/Kg) and it falls within the required allowable level of the soil. More studies and more samples are needed to study the effect of using TWW for irrigation on nitrogen in the soil. Meanwhile, the total Nitrogen content in soil upper soil samples (0-30 cm) samples from MMWWTP ranges from 0.34% (1.82 mg/kg) to 0.59 % (2.94 mg/kg) and falls within the normal level of the nitrogen content of the soil. The results showed that there is slightly higher TN in the soils irrigated by TWW from HICWWTP than those irrigated by TWW from MMWWTP as shown in Table (3). This might be attributed to the nature of the soil rather than TWW characterization. Therefore, there is no solid evidence for the increased nitrogen content in the soil due to the use of TWW. The high percentage of nitrogen in one soil sample to that of soil control samples because the Alfalfa plant is a natural source of nitrogen (Wikiarmer, 2017).

3.4 Results of Plant analysis

The control plant is the same type of plant that was irrigated with TWW (Alfalfa), it was irrigated with fresh water and was taken from a nearby farm. Table (4) shows the chemical characteristics of plant samples irrigated by TWW from MMWWTP, and HICWWTP and the chemical characteristics of the control sample.

Table 3. Chemical characteristics of plants samples

ID	Cu mg/kg	Fe mg/kg	Pb mg/kg	Cd mg/kg	Na mg/kg	K mg/kg
HICWWTP	62	414	B.D	B.D	50.66	1974
MMWWTP	B.D	10820	242.1	6.48	4076	26752
Control plant	B.D	8996	212	7.7	4580	12900

B.D ≡Below detection limit = 20 mg/kg

From Table (4) the concentration of copper in the plant irrigated with TWW from HICWWTP is higher than its concentration in the plant irrigated with TWW from MMWWTP and the sample irrigated with fresh water.

While the concentration of iron, lead, cadmium, sodium, and potassium in the plant irrigated with TWW generated from both WWTP's are below their concentration in the Control plant that is irrigated with fresh water.

It is noticed that heavy metals concentration in the plant from the two studied WWTP are identical to their counterpart soil samples., as Cd and Pb were below the detection limits in the plant from HICWWTP and similarly the soil samples from the same WWTP are below detection limit too. Despite that TWW from HICWWTP has noticeable Pb and Cd Concentrations Table 1). The same trend was found between the plant and soil of MMWWTP, where Cd and Pb are noticed in soil and plant heavy metal concentration Table (4). This is inconsistent with MMWWTP TWW that have considerable concentrations of heavy metals (Table 2). This confirms that there is no effect of TWW on the plants' uptake due to lower accumulation. And that the plant chemistry is reflecting the original soil chemical composition. More investigation should be made to explain why the uptake of copper by alfalfa took place from TWW from HICWWTP while this did not happen to the plant that was irrigated with TWW from MMWWTP.

4. Conclusions

The results of TWW analysis produced from HICWWTP and MMWWTP showed that its quality is comply well with Jordanian standards for reclaimed WW reuse for restricted irrigation. The results showed that the quality of treated wastewater for irrigation, whether it was generated from domestic or industrial influent wastewater is safe because the chemical characteristics of the irrigated plant with treated wastewater at HICWWTP and MMWWTP were below the allowable limits for the irrigation of plant with fresh water. TWW produced from both WWTP's is recommended for fodder plantations such as (Alfalfa). Also, there is no adverse effect on the irrigated soil's chemical characteristics, which might be due to the low accumulation rate because of a short time interval of application and lower heavy metal concentrations in the produced TWW. In addition to the leaching with rainwater in the wet season which prevents contaminant accumulation. Although, the reuse of TWW for irrigation did not show any adverse effect, however continuous monitoring of irrigated soil and plant units is highly recommended to ensure high treatment efficiency. Frequent analysis of both irrigated plants and soils should be conducted to monitor the long-term heavy metal accumulation

Acknowledgment:

This research was financially supported by the Deanship of Scientific Research – at Mutah University. The authors are grateful to the staff of Prince Faisal Center for their efforts in the sample analytical procedures.

References

Agafonov, O., Selstø, C. H., Thorsen, K., Xu, X. M., Drengstig, T., and Ruoff, P. (2016): The Organization of Controller Motifs Leading to Robust Plant Iron Homeostasis. PLOS one: 11(1), e0147120.

Al-Hamaiedeh, H., and Bino, M. (2010): Effect of Treated Greywater Reuse in Irrigation on Soil and Plants. Desalination. 256(1-3): 115-119. Al-Hamaiedeh, H., (2010): The Impact of Greywater Reuse in Irrigation on Public Health and Safety, Electronic Journal of Geotechnical Engineering. 15:1131-1138.

Al-Hamaiedeh, H., and Maaitah, O. (2011): Treatment of oil polluted soil using electrochemical method, Alexandria Engineering Journal. 50(1):105-110.

Aljbour, S.H., El-Hasan, T., Al-Hamaiedeh, H., Hayek, B., Abu-Samhadaneh, K. (2021a): Anaerobic co-digestion of domestic sewage sludge and food waste for biogas production: A decentralized integrated management of sludge in Jordan. Journal of Chemical Technology and Metallurgy. 56(5,):1030-1038.

Aljbour, S.H., El-Hasan, T., Al-Hamaiedeh, H., Hayek, B., Abu-Samhadaneh, K., Al-Momani, S., and Aburawa, A. (2021b): Anaerobic Co-digestion of Domestic Sewage Sludge with Food Waste: Incorporating food waste as a co-substrate under semi-continuous operation. Journal of Ecological Engineering. 22(7):1-10. https://doi.org/10.12911/22998993/137442.

APHA (1998) Standard Methods for the examination of water and wastewater American Public Health Association. 874pp.

Baird, R., and Bridgewater, L. (2017): Standard methods for the examination of water and wastewater. 23rd edition. Washington, D.C.: American Public Health Association.

Baker, M. S. (2007): Wastewater Characteristics and the Impact of its Use in Irrigation on Soil: the Case of Faria Catchment (Doctoral dissertation).

Blakemore, L.C., Searle, P.L., Daly, B.K. (1987): Methods for the chemical analysis of soils. NZ Soil Bureau Scientific Report 80.

Castro, E., Mañas, M. P., and Heras, J. D. L. (2011): Effects of Wastewater Irrigation on Soil Properties and Turfgrass Growth, Water Science and Technology. 63(8): 1678-1688.

Dojlido. Jan R., Best Gerald A. (1993): Chemistry of Water and Water Pollution, Ellis Horwood Limited.

El-Hasan, T. (2002): Urban Geochemistry: Heavy Metals Distribution on the Soils of Relatively Heavy Industrial City of Sahab, Central Jordan. Mu'tah Lil-Buhuth wad-Dirasat, Pure Sciences.17 (3): 49-67.

El-Hasan, T., and Al-Tarawneh, A. (2020): Heavy metal contamination and distribution within the urban soil cover in Mutah and Al-Mazar Municipal area, Jordan Journal For Earth and Environmental Sciences (JJEES). 11(3): 202-210.

El-Hasan, T., and Lataifeh, M. (2003): Environmental Magnetism: The Implication of Initial Magnetic Susceptibility and Saturation Magnetization for Detecting Roadside Pollution in Arid Regions. Dirasat, Pure Sciences. 30 (2):191-202.

El-Hasan, T., and Lataifeh, M. (2013): Field and Dual Magnetic Susceptibility Proxies Implication for Heavy Metal Pollution Assessment in the Urban Soil of Al-Karak City, South Jordan. Environmental Earth Sciences. 69(7): 2299-2310.

Fageria, N. K., Baligar, V. C., and Clark, R. B. (2002): Micronutrients in Crop Production, In Advances in Agronomy. 77:185-268..

FAO (2003): User's Manual for Irrigation with Treated Wastewater, FAO Regional Office for the near east, Cairo.

Fialova, H., Maier, G., Petrovsky, E., Kapicka, A., Boyko, T., and Scholger, R. (2006): Magnetic properties of soils from sites with different geological and environmental settings. J. Appl. Geophys. 59:273–283.

Garnaud, S., Mouchel, J.M., Chebbo, Ghassan, and Thevenot, D.R. (1999): Heavy metal concentrations in dry and wet atmospheric deposits in Paris district: comparison with urban runoff. The Science of the Total Environment. 235: 235-245.

Hararah, M.A., Al-Nasir, F.; El-Hasan, T. and Al-Muhtaseb, A.H. (2012): Zinc adsorption-desorption isotherms: Possible effects on the calcareous vertisol soils from Jordan. Environmental Earth Sciences. 65:2079-2085.

Hu, Y., and Schmidhalter, U. (2004): Limitation of salt stress to plant growth. HOCK, E. Plant toxicology. 4:191-224.

IWA (2018): Wastewater: The Reuse Opportunity, International Water Association.

Jiries, A., El-Hasan, T., Al-Hiwati, M., and Seiler, K. P., (2004): Evaluation of the Effluent Water Quality Produced from Phosphate Mines in Central Jordan. Mine Water and the Environment. 23 (3): 133-137.

Jordanian Standard JS 202:2007: Jordan Standard for Industrial reclaimed wastewater. http://www.jsmo.gov.jo/En/EServices/Standards/Pages/stdDetails.aspx?mfn=2639

Jordanian Standard JS 893:2006: Jordan Standard for Water-Reclaimed domestic wastewater. http://www.jsmo.gov.jo/En/EServices/Standards/Pages/stdDetails.aspx?mfn=2601

Kulikowska, D. and Klimiuk, E. (2008): The effect of landfill age on municipal leachate composition. Bioresource Technology. 99(13): 5981-5985.

Manoj Kumar Jindal, Deepak Meshram, Shubham Shravan, Abhishek Shrey, Monesh Sahu, and Ravi Mannade. (2016): Treatment of Wastewater and Reuse in Irrigation System Int. J. of Adv. Res. 4 (11).

Matouq, M.; El-Hasan, T.; Al-Bilbisi, H.; Abdelhadi, M.; Hindiyeh, M.; Eslamia, S. and Duheisat, S. (2013): The Climate change implication on Jordan: A case study using GIS and Artificial Neural Networks for weather forecasting. Journal of Taibah University for Science. 7:44-55.

Ministry of water and irrigation (2004): National Water Master Plan, Ministry of water and irrigation. Unpublished report, P97.

Ministry of water and irrigation (2015): Jordan Water Sector Facts and Figures 2015, Ministry of water and irrigation.

Minnesota Department of Health (2018): Copper in Drinking Water, https://www.health.state.mn.us/communities/environment/water/docs/contaminants/copperfactsht.pdf.

Mohawesh, O., Al-Hamaiedeh, H., Albalasmeh, A., Qaraleh, S.; Haddadin, M. .(2019): Effect of Olive Mill Wastewater (OMW) Application on Soil Properties and Wheat Growth Performance Under Rain-Fed Conditions Water, Air, and Soil Pollution

Mohawesh, O.; Albalasmeh, A.; Al-Hamaiedeh, H.; Qaraleh, S.; Maaitah, O.; Bawalize, A.; Almajal, D. (2020): Controlled Land Application of Olive Mill Wastewater (OMW): Enhance Soil Indices and Barley Growth Performance in Arid Environments, Water Air and Soil Pollution 231(5):214-225.

Mohd-Aizat, A., Mohamad-Roslan, M. K., Sulaiman, W. N. A., and Karam, D. S. (2014): The Relationship between Soil pH and Selected Soil Properties in 48 Years Logged-Over Forest. International Journal of Environmental Sciences. 4(6): 1129.

MWI (2017): Jordan Water Sector: Facts and numbers, Ministry of water and irrigation. Unpublished report, P24.

Reid, G., and Dirou, J. (2004): How to interpret your Soil Test, Adapted from Soil Sense leaflet 4/92, Agdex 533. New South Wales Department of Primary industries. http://web.archive.org/web/20150421044903/http://www.dpi.nsw.gov.au/agriculture/resources/soils/testing/interpret Accessed on 1/10/2018.

Rout, G. R., and Sahoo, S. (2015): Role of Iron in Plant Growth and Metabolism. Reviews in Agricultural Science. 3:1-24.

Shrivastava, P., and Kumar, R. (2015): Soil salinity: a serious environmental issue and plant growth promoting bacteria as one of the tools for its alleviation. Saudi journal of biological sciences. 22(2):123-131.

Sposito Garrison (2008): The Chemistry of Soils, Oxford University Press.

Tatsi, A.A., Zouboulis, A., Matis, K.A., and Petros Samaras (2003): Coagulation–Flocculation Pre-Treatment of Sanitary Landfill Leachates. Chemosphere 53(7):737-744.

Thornton, I., Butler, D., Docx, P., Hession, M., Makropoulos, C., McMullen, M.and Smith, S. (2001): Pollutants in Urban Waste Water and Sewage Sludge, Luxembourg: Office for Official Publications of the European Communities.

Ulmgren, L. (2000): Stockholm Water Company. Wastewater Treatment and Steps Taken in Practice for Reducing Sludge Contamination in Stockholm, Sweden, Paper presented 27–28 March 2000, at the Conference Traitamiento de lodos dedepuradora:su minimización, valorización y destino final.

Wikifarmer, (2017): Alfalfa plant information, Wikifarmer editorial team. https://wikifarmer.com Accessed on 16/10/2018

المملكة الأردنية الهاشمية

صندوق دعم البحث العلمي

الجامعة الهاشمية

المجلة الأردنية
لعلوم الأرض والبيئة

JJEES

مجلة علمية عالمية محكمة

المجلد (١٣) العدد (٣)

http:// jjees.hu.edu.jo/

ISSN 1995-6681

المملكة الأردنية الهاشمية صندوق دعم البحث العلمي الجامعة الهاشمية

JJEES

المجلة الأردنية لعلوم الأرض والبيئة

المجلد (13) العدد (3)

مجلة علمية عالمية محكمة تصدر بدعم من صندوق دعم البحث العلمي

ISSN 1995-6681 jjees.hu.edu.jo أيلول 2022